

Technische Universität Kaiserslautern  
Fachbereich Chemie

**Structure and reactivity of solvated  
transition metal ions and complexes**

Am Fachbereich Chemie der Technischen Universität Kaiserslautern  
zur Erlangung des akademischen Grades „Doktor der Naturwissenschaften“  
genehmigte

Dissertation  
(D386)

vorgelegt von  
Dipl.-Chem. Anita Lagutschenkov

Betreuer: Prof. Dr. G. Niedner-Schatteburg

Tag der wissenschaftlichen Aussprache: 22. September 2008



Die vorliegende Arbeit wurde in der Zeit von Juli 2003 bis August 2008 im Fachbereich Chemie der Technischen Universität Kaiserslautern unter der Betreuung von Prof. Dr. G. Niedner-Schatteburg angefertigt.

Datum des Antrags auf Eröffnung des Promotionsverfahrens: 08.01.2007

Tag der wissenschaftlichen Aussprache: 22.09.2008

Promotionskommission:

Vorsitzender: Prof. Dr.-Ing. S. Ernst

1. Berichterstatter: Prof. Dr. G. Niedner-Schatteburg

2. Berichterstatter: Prof. Dr. M. Gerhards



O glücklich, wer noch hoffen kann,  
aus diesem Meer des Irrtums aufzutauchen!  
Was man nicht weiß, das eben brauchte man,  
und was man weiß, kann man nicht brauchen. (Faust)

Goethe

Faust 1, Vor dem Tor



---

## Contents

<b>0. Abbreviations</b>	<b>III</b>
<b>1. Introduction</b>	<b>1</b>
<b>2. Methods</b>	<b>7</b>
2.1 Experimental methods	7
2.1.1 Ion generation: Electrospray ionization and laser vaporization	7
2.1.3 Infrared multiphoton dissociation spectroscopy with the free electron laser at the Centre Laser Infrarouge Orsay	21
2.2 Theoretical methods	24
2.3 References	33
<b>3. The spectroscopic signature of the "all-surface" to "internally solvated" structural transition in water clusters in the n=17–21 size regime</b>	<b>37</b>
3.1 Introduction	37
3.2 Summary of the results	39
3.3 Conclusions	43
3.5 References	45
<b>4. Infrared spectrum of <math>\text{NH}_4^+(\text{H}_2\text{O})</math>: Evidence for mode specific fragmentation</b>	<b>47</b>
4.1 Introduction	48
4.2 Summary of the results	49
4.3 References	55
<b>5. Beyond the harmonic approach: Calculation of anharmonic frequencies of protonated and deprotonated carboxylic acid homologues, from oxalic acid to adipic acid</b>	<b>57</b>
5.1 Introduction	57
5.2 Computational details	60
5.3 Results and discussion of the computational results	61
5.4 Summary and conclusions	78
5.5 References	79

---

<b>6. Preliminary experimental and quantum chemical studies for IRMPD and IR matrix isolation spectroscopy of dioxygen containing nonheme iron(III) catecholate complexes</b>	<b>81</b>
6.1 Introduction	81
6.2 Measurements with ESI-FT-ICR-MS	83
6.3 Density functional calculations	88
6.4 Summary and outlook	97
6.5 References	99
<b>7. Complexes of vanadium and vanadium oxides with organic solvents: FT-ICR-MS study and IRMPD spectra compared to ab initio calculations</b>	<b>101</b>
7.1 Introduction	101
7.2 Experimental details	102
7.3 Computational details	103
7.4 Results and Discussion	104
7.4.1 IRMPD spectra of vanadium oxide acetonitrile complexes	104
7.4.2 IRMPD spectra of vanadium oxide methanol complexes	117
7.4.2 IRMPD spectra of vanadium oxide ethanol complexes	128
7.5 Summary and outlook	134
7.6 References	139
<b>8. Energetics and reaction pathways of intramolecular reductive nitrile coupling of monocationic group 3 through 7 transition metal acetonitrile complexes</b>	<b>143</b>
8.1 Introduction	143
8.2 Computational details	146
8.3 Results and discussion	147
8.4 Summary and outlook	160
8.5 References	161
<b>9. Summary</b>	<b>167</b>
<b>10. Zusammenfassung</b>	<b>171</b>
<b>11. List of Publications</b>	<b>175</b>
<b>12. Acknowledgment</b>	<b>177</b>
<b>13. Curriculum Vitae</b>	<b>179</b>



---

### Abbreviations

B3LYP	Becke three parameter hybrid Lee Yang Parr correlation functional
BLYP	Becke Lee Yang Parr correlation functional
CAD	collision activated dissociation
CC	coupled cluster
CCSD(T)	coupled cluster with single and double and perturbative triple excitations
CE	capillary electrophoresis
CID	collision induced dissociation
CGF	contracted Gaussian function
CLIO	Centre Laser Infrarouge d'Orsay
CPMD	Car-Parrinello molecular dynamics
DFT	density functional theory
DZVP	double-zeta valence plus polarization
ECP	effective core potential
ESI	electrospray ionization
FEL	free electron laser
FFT	fast Fourier transform
FT-ICR-MS	Fourier transform ion cyclotron resonance mass spectrometry
FWHM	full width at half maximum
GGA	generalized gradient approximation
GTO	Gaussian-type orbital
HF	Hartree-Fock
HPLC	high performance liquid chromatography
HWHM	half width at half maximum
IR	infrared
IRMPD	infrared multiphoton dissociation
IVR	internal vibrational relaxation
LDA	local density approximation
LVAP	laser vaporization (source)
MALDI	matrix assisted laser desorption ionization
MD	molecular dynamics
MICRA	mobile ion cyclotron resonance analyzer

MP2	second order Møller-Plesset perturbation theory
MS	mass spectrometry
PA	proton affinity
PEEK	polyetheretherketone
PES	potential energy surface
RF	radio frequency
RI	resolution of the identity
S/N	signal to noise ratio
SCF	self consistent field
SORI	sustained off resonance irradiation
STO	Slater-type orbital
Tp'	trispyrazolylborate
TZVP	triple-zeta valence plus polarization
UV	ultraviolet
VIS	visible
ZPE	zero point energy

## 1. Introduction

The concepts of solvation and dissolution are crucial for the understanding of all those chemical reactions that take place in the liquid phase. When solvated, an atom or molecule – the solute – is embedded into a large number of solvent molecules. Interactions between the solute and the solvent can range from weak van der Waals forces and hydrogen bonds to strong ionic interactions. Depending on the strength of interaction the solute enforces a short range order on the first layer of the surrounding solvent molecules. While solvation describes a certain state of matter, the term dissolution is commonly used for the description of the solvation process and the underlying dynamics.

The most common and most abundant liquid solvent is water. Thus it does not come as a surprise that water is involved in almost any process that is of importance in biology, pharmacology and medicine. Under physiological conditions any ion is either hydrated or bound in a chelate complex. Metal ions are of special interest, as they occur in a large variety of proteins, in animals as well as in plants. Metalloproteins like hemoglobin with an iron-containing heme group and the magnesium-containing chlorophyll are essential to sustain life. The coordination and solvation of metal ions by ligands and the strength of the interactions are responsible for the uptake and release of dioxygen and therefore for the whole process of respiration. When we look at the biochemistry within cells, we can also find the concept of solvation in a wide range of processes in which a change of the solvation state takes place. Upon diffusional transfer through membranes an ion has to get rid of its solvent shell. Similar constraints hold for the active transport by ion-pumps like the sodium/potassium pump. Thus a detailed knowledge of structures of such systems, their interactions and the strength of bonds between solvent and solute is essential and worth being investigated.

This thesis presents various molecular systems, in which the concept of microsolvation is of special interest. Microsolvates are neutral or ionic atoms or molecules which are surrounded by a finite number of solvent molecules. The microsolvates' intrinsic physical properties strongly depend on the number of ligands and change significantly upon addition or removal of single solvent molecules. However, solvated transition metal ions are more commonly labelled as complexes in the gas phase than as microsolvates. Catalytic activities of such complexes vary significantly depending on the number of solvent molecules that coordinate to the transition metal or its oxides. Possible intramolecular reactions<sup>1</sup> will be

investigated in this work by a combination of experimental infrared multiphoton dissociation (IRMPD)<sup>2-4</sup> and advanced quantum chemical methods.

Within a microsolvate it is possible to observe the gradual transition from so called contact ion pairs to solvent separated ion pairs with growing number of ligands. Further prominent examples of size dependent gradual transitions in microsolvates are given by the transformation of an elemental metal to a solvated metal ion and a solvated electron, e.g. in  $[\text{Mg}(\text{H}_2\text{O})_n]^+$ , which incorporates the structural motif of a solvent separated ion pair  $[\text{Mg}(\text{H}_2\text{O})_{n-m}^+ \text{e}^-(\text{H}_2\text{O})_m]^{2+}$  for large values of  $n$ .<sup>5</sup> Solvated electrons with similar structural motifs can also be found in the anionic system  $[\text{Mg}(\text{H}_2\text{O})_n]^-$ .<sup>6</sup>

It is very complicated to assign single contributions to the total interactions within a solute-solvent system in the condensed phase. In contrast, gas phase data can be compared directly to ab initio calculations. By investigation of the stepwise solvation – adding one solvent molecule at a time – solvent-solvent interactions can be separated from solute-solvent interactions when looking at microsolvates. A useful tool for gas phase studies of microsolvates is mass spectrometry and, if possible, optical spectroscopy, especially infrared spectroscopy, when compared to and supplemented by quantum chemical calculations. Here, microsolvates are produced via electrospray ionization (ESI)<sup>7,8</sup> of ion containing solutions or with laser vaporization of metals<sup>9,10</sup> and subsequent collision reactions with gaseous solvents within FT-ICR mass spectrometers. The most common detection of these generated model compounds is realized by means of mass spectrometry, as they are already ionic. Therefore experiments in the gas phase are a good starting point for fundamental studies and the number of publications in this field is constantly increasing.<sup>11,12</sup>

Microsolvates are also very useful model compounds when investigating aerosol formation in the atmosphere.<sup>13-19</sup> Stepwise solvation of small particles in the air leads to bigger aggregates or clusters. Microsolvates can serve as condensation nuclei in the formation of clouds. In order to develop a deeper understanding of fundamental processes that take place in gaseous atmosphere, it is essential to have a thorough knowledge about the aggregation process of water molecules alone. Size dependent structural changes in water clusters in the size regime of 17 to 21 water molecules will be discussed in this study.<sup>20,21</sup>

This thesis is organized as follows: Chapter two describes the experimental and theoretical methods, which are used in this work.

Chapter three provides a closer look at the most common solvent in living matter – namely water. It contains an ab initio study of pure water clusters of well defined size.

Geometry features of water clusters show an unexpected alternation in the investigated size regime from  $n = 17$  to 21.<sup>20,21</sup> Although water is a ubiquitous and a well investigated substance, there are still surprises and the number of related publications is continuously increasing.<sup>22-24</sup>

The thesis proceeds in chapter four with a fundamental study on a mono hydrate of the ammonium cation. Infrared multiphoton dissociation (IRMPD) spectra of various hydrated molecular ions had been recorded in the 1990s and published.<sup>25-27</sup> The spectrum of the hydrated ammonium remained unpublished due to the lack of a conclusive interpretation. Today molecular systems of this size can be treated with more sophisticated ab initio methods that were not at hand in those times. Only through the calculation of anharmonic frequencies on a perturbation theory level the IRMPD spectra of hydrated ammonium obtained a conclusive interpretation.<sup>28</sup>

The fifth chapter deals with the calculation of structures and anharmonic frequencies of dicarboxylic acids in various charge states. Dicarboxylic acids are utilized by the polymer industry in large volumes, as e.g. adipic acid in the production of nylon. Protonated and deprotonated adipic acid are supposed to yield cyclic structures in the gas phase. Thus the redshifted O–H stretch band of the proton bridge should be observable, similar to related proton bound systems investigated recently.<sup>29</sup> However, IRMPD measurements did not show the expected O–H stretch band, which can be rationalized by anharmonic shifts and/or broadening. Thus the harmonic and anharmonic frequencies of adipic acid are calculated in parallel to a Car-Parrinello molecular dynamics results from Kwang Kim and coworkers which will be published soon. Furthermore, this work presents the calculation of the harmonic and anharmonic frequencies of the homologous series of dicarboxylic acids from oxalic acid to adipic acid.

A particular example of metal containing enzymes is presented in chapter six. The combined mass spectrometry and ab initio project deals with the description of model compounds for the non-heme iron containing 1,2 catechol dioxygenases.<sup>30</sup>

The solvation of ionic transition metal oxides, infrared multiphoton dissociation spectra of vanadium oxides solvated by organic compounds like acetonitrile, ethanol and methanol is presented in chapter seven. Challenges in the description by ab initio methods in case of V=O bonds will also be addressed.

Chapter eight of this work includes the ab initio description of pure solvated metal ions contrasting the more complex solvation of metal oxides. As has been shown in the example of niobium acetonitrile complexes,<sup>1</sup> the dependence on the number of ligands

observed in IRMPD experiments can be described with density functional theory. This work gives a systematic density functional study through group III to group VII transition metal acetonitrile complexes with coordination number  $n = 4, 5$ . Furthermore it contains the computed reaction coordinates for the intramolecular reductive nitrile coupling in all group V complexes as well as the analogous titanium and tungsten complexes.

The thesis concludes by a chapter that summarizes the obtained findings and provides for an outlook on future experiments.

## References

- <sup>1</sup> B. M. Reinhard, A. Lagutschenkov, J. Lemaire, P. Maitre, P. Boissel, and G. Niedner-Schatteburg, *J. Phys. Chem. A* **108** (16), 3350 (2004).
- <sup>2</sup> E. R. Grant, P. A. Schulz, A. S. Sudbo, Y. R. Shen, and Y. T. Lee, *Phys. Rev. Lett.* **40** (2), 115 (1978).
- <sup>3</sup> R. C. Dunbar, *Int. J. Mass Spectrom.* **200** (1-3), 571 (2000).
- <sup>4</sup> M. A. Duncan, *Int. J. Mass Spectrom.* **200** (1-3), 545 (2000).
- <sup>5</sup> B. M. Reinhard and G. Niedner-Schatteburg, *Phys. Chem. Chem. Phys.* **4** (8), 1471 (2002).
- <sup>6</sup> B. M. Reinhard, A. Lagutschenkov, and G. Niedner-Schatteburg, *Phys. Chem. Chem. Phys.* **6** (17), 4268 (2004).
- <sup>7</sup> M. Yamashita and J. B. Fenn, *J. Phys. Chem.* **88** (20), 4451 (1984).
- <sup>8</sup> M. Yamashita and J. B. Fenn, *J. Phys. Chem.* **88** (20), 4671 (1984).
- <sup>9</sup> R. E. Smalley, *Laser Chem.* **2** (1-6), 167 (1983).
- <sup>10</sup> C. Berg, U. Achatz, M. Beyer, S. Joos, G. Albert, T. Schindler, G. Niedner-Schatteburg, and V. E. Bondybey, *Int. J. Mass Spectrom.* **167**, 723 (1997).
- <sup>11</sup> G. Niedner-Schatteburg and V. E. Bondybey, *Chem. Rev.* **100** (11), 4059 (2000).
- <sup>12</sup> M. K. Beyer, *Mass Spectrom. Rev.* **26** (4), 517 (2007).
- <sup>13</sup> H. Wincel, E. Mereand, and A. W. Castleman, *J. Phys. Chem. A* **101** (44), 8248 (1997).
- <sup>14</sup> A. J. Stace, J. F. Winkel, and S. R. Atrill, *Journal of the Chemical Society-Faraday Transactions* **90** (22), 3469 (1994).

- 15 T. Schindler, C. Berg, G. Niedner-Schatteburg, and V. E. Bondybey, *J. Chem. Phys.* **104** (11), 3998 (1996).
- 16 T. Schindler, C. Berg, G. Niedner-Schatteburg, and V. E. Bondybey, *J. Phys. Chem.* **99** (33), 12434 (1995).
- 17 T. Schindler, C. Berg, G. Niedner-Schatteburg, and V. E. Bondybey, *Chem. Phys. Lett.* **229** (1-2), 57 (1994).
- 18 E. E. Ferguson, F. C. Fehsenfeld, and D. L. Albritton, edited by M. T. Bowers (Academic Press, New York, 1979), Vol. 1.
- 19 D. Smith and N. G. Adams, edited by M. T. Bowers (Academic Press, New York, 1979), Vol. 1.
- 20 A. Lagutschenkov, G. S. Fanourgakis, G. Niedner-Schatteburg, and S. S. Xantheas, *J. Chem. Phys.* **122** (19) (2005).
- 21 S. S. Xantheas, G. S. Fanourgakis, K. Kowalski, A. Lagutschenkov, and G. Niedner-Schatteburg, *Abstracts of Papers of the American Chemical Society* **229**, U706 (2005).
- 22 B. Bandow and B. Hartke, *J. Phys. Chem. A* **110** (17), 5809 (2006).
- 23 S. Bulusu, S. Yoo, E. Apra, S. Xantheas, and X. C. Zeng, *J. Phys. Chem. A* **110** (42), 11781 (2006).
- 24 A. Lenz and L. Ojamae, *J. Phys. Chem. A* **110** (50), 13388 (2006).
- 25 M. Okumura, L. I. Yeh, and Y. T. Lee, *J. Chem. Phys.* **88** (1), 79 (1988).
- 26 M. Okumura, L. I. Yeh, J. D. Myers, and Y. T. Lee, *J. Phys. Chem.* **94** (9), 3416 (1990).
- 27 J. M. Price, M. W. Crofton, and Y. T. Lee, *J. Phys. Chem.* **95** (6), 2182 (1991).
- 28 T. Pankewitz, A. Lagutschenkov, G. Niedner-Schatteburg, S. S. Xantheas, and Y. T. Lee, *J. Chem. Phys.* **126** (7), 074307/1 (2007).
- 29 J. R. Roscioli, L. R. McCunn, and M. A. Johnson, *Science* **316** (5822), 249 (2007).
- 30 W. O. Koch and H. J. Kruger, *Angewandte Chemie-International Edition in English* **34** (23-24), 2671 (1996).
- 31 K. R. Asmis, G. Santambrogio, J. Zhou, E. Garand, J. Headrick, D. Goebbert, M. A. Johnson, and D. M. Neumark, *J. Chem. Phys.* **126** (19) (2007).





## 2. Methods

### 2.1 Experimental Methods

The development of soft ionization methods like electrospray ionization (ESI)<sup>1-3</sup> and matrix-assisted laser desorption ionization (MALDI)<sup>4</sup> in recent years has enabled substantial progress in the mass spectrometric characterization of macromolecules, in particular important biopolymers such as proteins and nucleic acids. These methods are described as soft, because the ions can be transferred from solution into the gas phase without fragmentation. Consequently, the high relevance of the new ionization schemes for many areas of chemistry was recognized by the award of the Nobel prize to John Fenn in 2002 for the application of ESI to large (bio-)molecules. This method successfully generates ions of macromolecules with a molecular weight of 100 kDa and beyond directly from solution. Recently ESI has proved to be useful for a direct characterization of complexes containing noncovalent interactions (noncovalently bound complexes)<sup>5-7</sup>. ESI in combination with the FT-ICR-MS (Fourier transform ion cyclotron resonance mass spectrometry) technique is a powerful tool for manifold chemical and biological tasks. Some of the major features of FT-ICR-MS are high accuracy along with exact mass determination, very high mass resolution, and the power to perform MS-MS experiments (in principle MS<sup>n</sup>). Due to the possibility to store the ions and due to their nondestructive detection, MS<sup>n</sup> experiments are feasible.<sup>8</sup>

#### 2.1.1 Ion Generation: Electrospray Ionization and Laser Vaporization

##### Electrospray Ionization Source

In our experimental setup, ions are produced by an Bruker Apollo I ESI source at atmospheric pressure (see Figure 2.1). The applied ESI source consists of a thin needle to spray a sample solution into a spray chamber in order to form droplets and release ions therefrom. A metal coated glass transfer capillary and two subsequent skimmers follow. A radio frequency (RF) hexapole then accumulates the ions.

The exact mechanism of ion formation in the ESI process is still subject of ongoing debate. In one of the proposed mechanisms, ion formation is believed to result from a direct *ion evaporation* process.<sup>9,10</sup> A spray of droplets is produced by electrostatic dispersion from the liquid ejected from the capillary tip. Aided by a heated bath gas (usually nitrogen), the droplets undergo declustering, losing solvent molecules in the process and eventually produce individual ions.

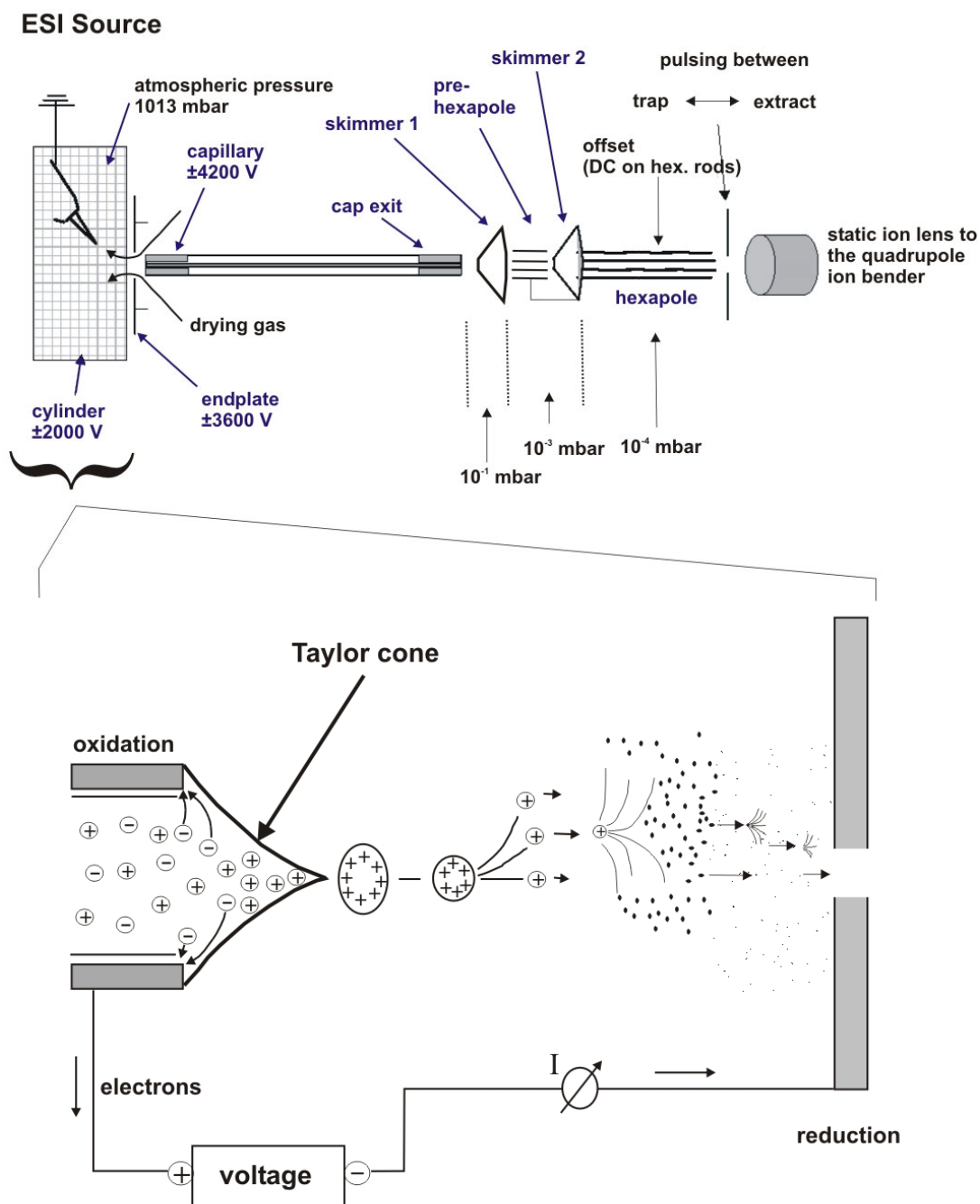


**Figure 2.1:** Scheme of the used Bruker-Apollo I ESI source and of major processes during electrospray ionization. If the spraying needle has a positive potential with regard to the endplate (counter electrode), enrichment of positive charges at the surface leads to destabilization of the meniscus and to formation of a Taylor cone and of a jet emitting droplets with excess of positive ions. Charged droplets shrink by evaporation and split into smaller droplets and finally yield gas phase ions. The gas phase ions enter the transfer capillary through the orifice of the endplate. Ions are collected in the second hexapole, from which they are injected into the ion optics transfer system. (Lower part analogue to Ref. 11)

In another proposed mechanism, the *charged residue mechanism*,<sup>3,12</sup> desolvation of the droplets leads to an increasing charge density on the droplet surface that will eventually cause a coulombic explosion that leads to individual ions. Closer examination of the two models reveals that many observed mass spectral features can be explained with either model.

Whatever the detailed mechanism is, ions form at atmospheric pressure and enter a cone shaped orifice, which acts as first vacuum stage where they undergo free jet expansion. A skimmer then samples the ions and guides them to the mass spectrometer. The formation of multiply charged ions is characteristic for electrospray ionization (typically about one charge per 1000 Dalton).

### Variation of the Bruker Apollo I ESI Source with a Custom-Built PEEK Capillary

Due to the high risk of breaking the glass transfer capillary (cf. Fig. 2.2) in the process of source cleaning, we looked for a robust, low priced alternative.



**Figure 2.2:** Scheme of the metal coated glass transfer capillary used in the Bruker Apollo I ESI source (3D scheme by H. Kampschulte).



**Figure 2.3:** Scheme of the custom-built PEEK transfer capillary (3D scheme by H. Kampschulte).

One possibility is to replace the glass transfer capillary by a capillary made of poly-ether-ether-ketone (PEEK). This material combines good isolating properties with robustness and low price (relative to the glass capillary). The PEEK capillary consists of a rigid, hollow PEEK tube (dark-beige, cf. Fig 2.3), in which a standard, flexible HPLC-PEEK capillary of 0.5 mm inner and 1/16" outer diameter is inserted. Two sealing O-rings are stuck on both ends

in order to ensure vacuum, and stainless steel end caps are on top of both ends. A further advantage of this assembly is that the inner PEEK capillary can easily be exchanged, when it is contaminated.

Due to the low melting point of the PEEK material ( $\sim 150^{\circ}\text{C}$ ), a temperature curve of the current cartridge heating elements was measured in order to determine a calibration curve (cf. Fig 2.4). The upper limit for safe operation,  $T_{\text{max}} = 120^{\circ}\text{C}$ , is reached at  $10\text{ V}/1.7\text{ A}=17\text{ W}$  heating power.

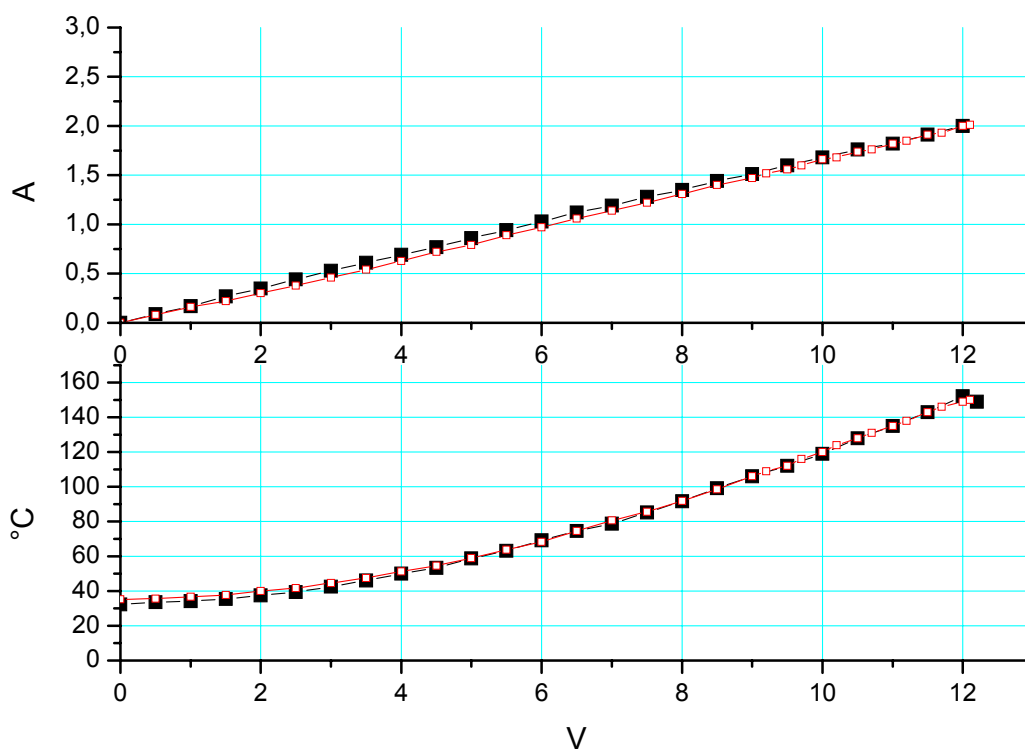


**Figure 2.4:** Temperature curve of the currently used cartridge heating element (Watlow St. Louis, 24 V, 100 W Firerod) when controlled by the external power supply unit (Elektro-Automatik EA-PS 2032-050).

Unfortunately, first performance tests did not yield promising results for ion transfer. When tested with a typical  $10^{-5}\text{ M}$  aqueous L-carnosine solution in positive ion mode, spectra were recorded with both the glass and the PEEK capillary under the same experimental conditions. The same signals were observed but the absolute ion intensity and the signal to noise ratio are much poorer – about one order of magnitude in total ion intensity – when using the PEEK capillary (see Table 2.1 and Fig. 2.6). This finding is even worse in negative ion mode spectra of an aqueous trifluoroacetic acid/sodiumchloride solution. While the glass capillary provides spectra of high resolution and total ion intensities, the PEEK capillary gave (almost) no analyte specific signals. An initially existing ion peak of the deprotonated

trifluoroacetic acid dimer vanished after a few minutes. Repetitions of the experiment gave no signal at all in negative ion mode.

Therefore the exchange of the glass capillary against the PEEK capillary is, if at all, only recommendable in case of measurements in positive ion mode.

**Table 2.1:** Experimental results of ESI spectra measured with glass and PEEK transfer capillary. For each spectrum 64 scans are accumulated.

	Molecule*	m/z exp.	S/N	Resolution	Total ion intensity
Positive ion mode	[Carn-NH <sub>3</sub> +H] <sup>+</sup>	210.09	1066.7	22561.3	7.9*10 <sup>7</sup>
glass capillary	[Carn+H] <sup>+</sup>	227.12	9757.3	20578.6	7.2*10 <sup>8</sup>
	[2Carn+H] <sup>+</sup>	453.23	2001.5	10039.9	1.5*10 <sup>8</sup>
	[3Carn+H] <sup>+</sup>	679.36	511.7	9398.3	1.9*10 <sup>7</sup>
	[4Carn+H] <sup>+</sup>	905.50	253.9	4845.9	1.1*10 <sup>7</sup>
Positive ion mode	[Carn-NH <sub>3</sub> +H] <sup>+</sup>	210.09	65.0	22702.6	3.5*10 <sup>6</sup>
PEEK capillary	[Carn+H] <sup>+</sup>	227.12	862.2	20900.3	4.5*10 <sup>7</sup>
	[2Carn+H] <sup>+</sup>	453.23	153.5	10379.9	8.1*10 <sup>6</sup>
	[3Carn+H] <sup>+</sup>	679.35	26.3	7051.3	1.4*10 <sup>6</sup>
	[4Carn+H] <sup>+</sup>	905.50	20.1	5131.4	1.1*10 <sup>6</sup>
Negative ion mode	[2TFA-H] <sup>-</sup>	226.98	1292.2	20334.1	1.1*10 <sup>7</sup>
glass capillary	[2TFA+Na-H] <sup>-</sup>	248.96	390.0	18619.4	3.6*10 <sup>7</sup>
	[3TFA+2Na-H] <sup>-</sup>	384.93	271.4	11970.3	2.5*10 <sup>7</sup>
	[4TFA+3Na-H] <sup>-</sup>	520.91	168.4	8902.7	1.6*10 <sup>7</sup>
	[5TFA+4Na-H] <sup>-</sup>	656.89	111.9	7132.7	1.1*10 <sup>7</sup>
	[6TFA+5Na-H] <sup>-</sup>	792.86	74.0	5731.7	6.9*10 <sup>6</sup>
Negative ion mode	[2TFA-H] <sup>-</sup>	226.98	36.7	20196.2	9.5*10 <sup>5</sup>
PEEK capillary					

\* Carn denotes a neutral carnosine molecule, TFA stands for a neutral trifluoroacetic acid molecule.

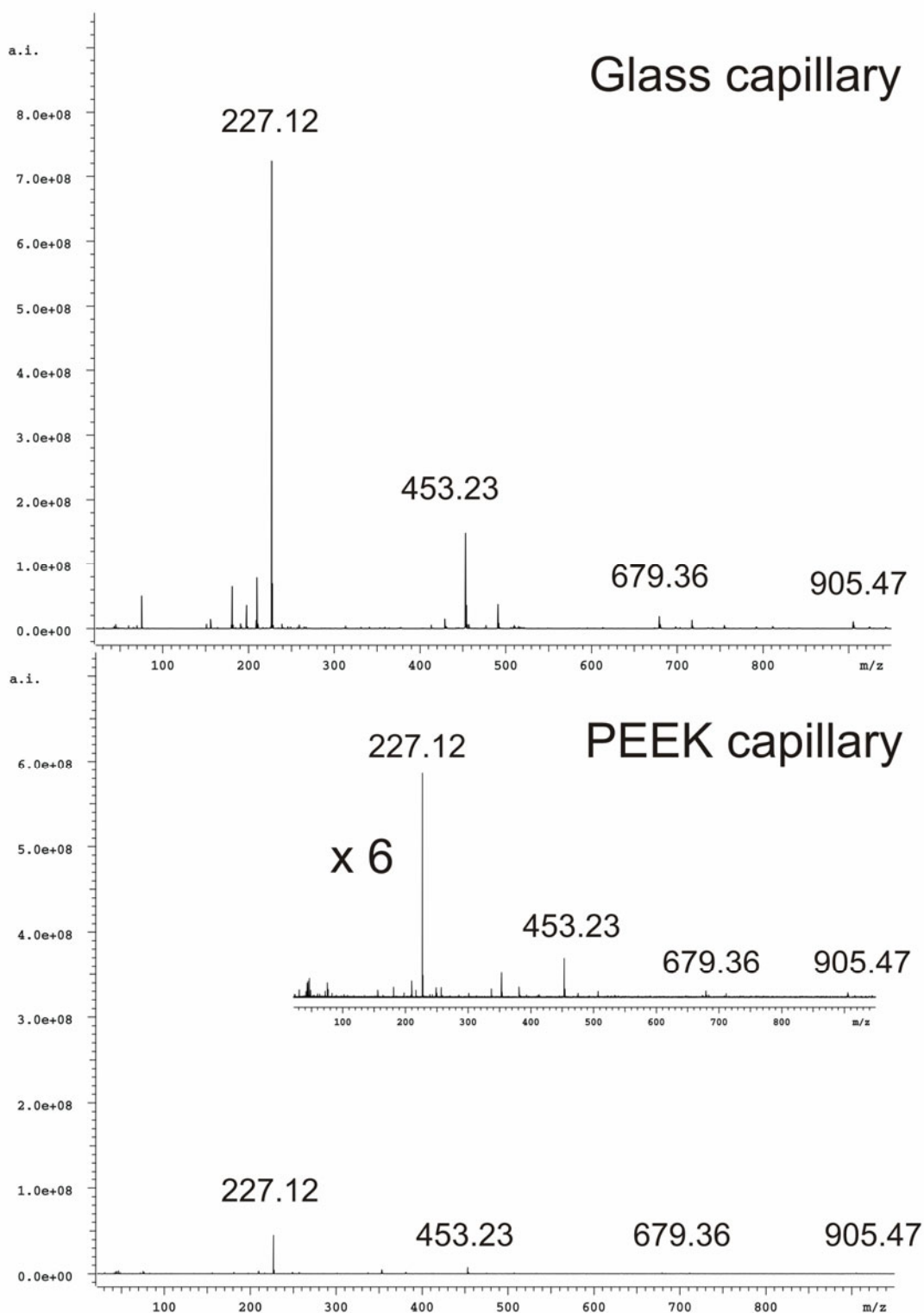


**Figure 2.5:** Comparison of ESI-FT-ICR-MS spectra of aqueous L-carnosine solutions in positive ion mode. The upper panel shows the results of the glass transfer capillary, the lower panel represents the spectrum when using the PEEK transfer capillary ( $T = 120^{\circ}\text{C}$ , cap exit = 120 V) at otherwise identical conditions. Intensities are to scale.

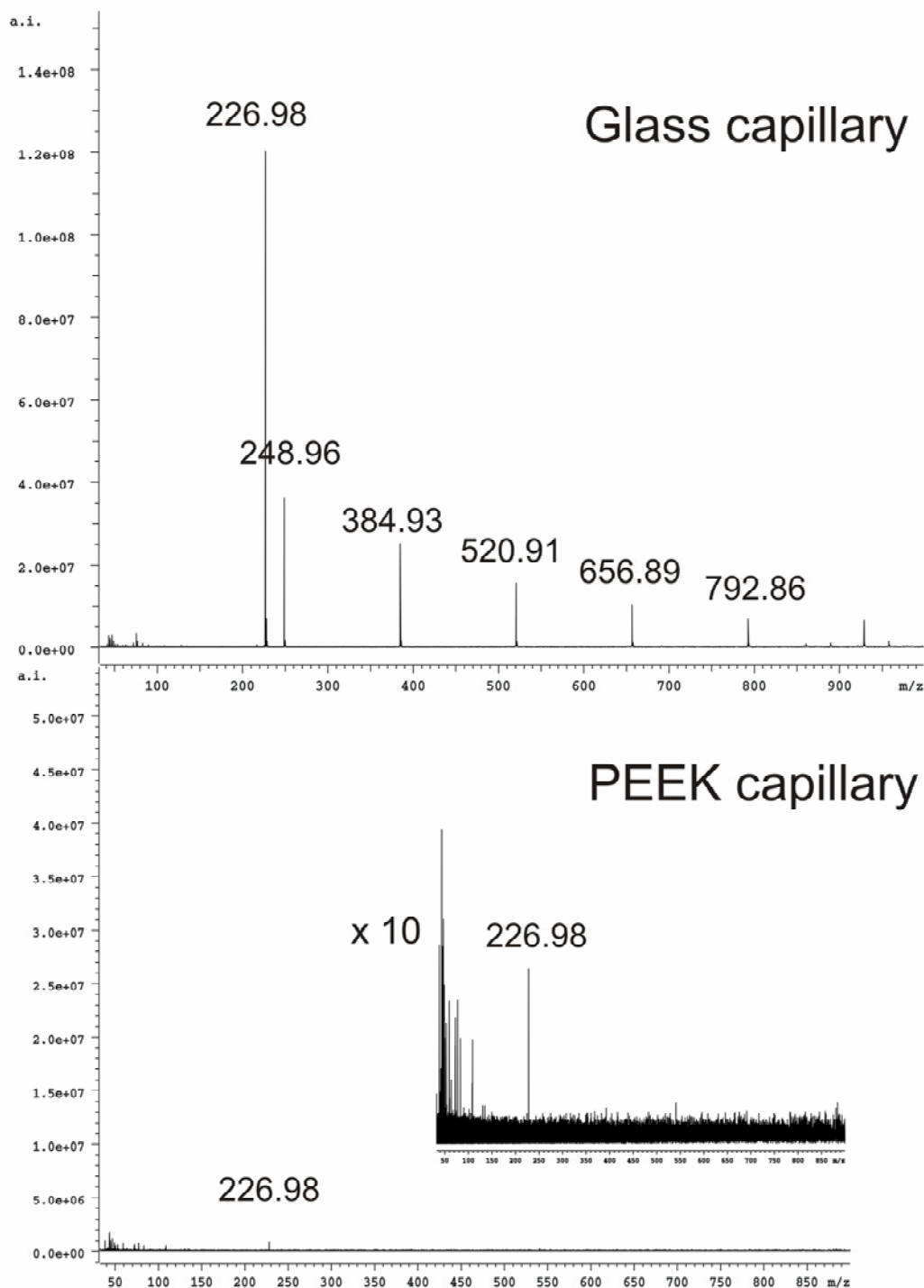


**Figure 2.6:** Comparison of ESI-FT-ICR-MS spectra of aqueous trifluoroacetic acid/sodium chloride solution in the negative ion mode. Upper panel shows the results of the glass transfer capillary, lower panel represents the spectra when using the PEEK transfer capillary ( $T = 120^{\circ}\text{C}$ , cap exit =  $-40\text{ V}$ ).

### **Laser Vaporization Source**

The production of metal clusters and metal (cluster) molecule complexes at the Kaiserslautern FT-ICR-MS is accomplished by laser vaporization and (in case of complexes) subsequent reaction with a volatile reactant. The laser vaporization source (LVAP) is a pulsed disk type design according to the design invented by Smalley.<sup>13</sup> It consists of a home-made piezoelectric valve,<sup>14</sup> a rotating target unit and expansion channels of variable length. The focused 532 nm radiation of a Continuum Surelite Nd:YAG laser operating at 20 Hz is used to induce ablation off the metal target. The formed metal plasma is very hot ( $\gg 1000$  K) and only partially ionized. The plasma is transferred into the expansion channel by a helium carrier gas pulse from the piezoelectric valve and subsequently cooled by supersonic expansion. Depending on the source voltage, gas pulse duration, laser intensity and the type of metal, this leads to the formation of typically singly charged metal clusters of well defined size.

The produced clusters (or single metal ions) are then transferred into the high vacuum region of the mass spectrometer by a quadrupole bender and a system of electrostatic lenses. During storage of the metal (cluster) ions in the ICR cell, the ions can undergo reactions with a gaseous reactant. The reactant can be admitted into the cell through either a leak valve or a pulsed valve.

### **2.1.2 Ion Detection: Fourier Transform Ion Cyclotron Resonance Mass Spectrometry FT-ICR-MS**

#### **The FT-ICR-MS Setup in Kaiserslautern**

Parts of the experimental data in this work are obtained with a modified version of a Bruker APEX III ESI-FT-ICR-MS instrument. This commercially available experimental setup can mainly be divided into five subunits:

- 1) Electrospray ionization source (Apollo I source, Bruker, cf. Sec. 2.1.1)
- 2) Electrostatic ion transfer optics and vacuum system
- 3) Superconducting magnet with a magnetic field of 7 Tesla
- 4) Ion storage and analyzer cell (Infinity ICR cell, Bruker)
- 5) Supply electronics and data recording system



In addition, our ICR in Kaiserslautern is equipped with a quadrupole bender, which either deflects the ions by 90° degrees or guides them without deflection. This enables the simultaneous installation of several (currently three) external ion sources (cf. figure 2.7).

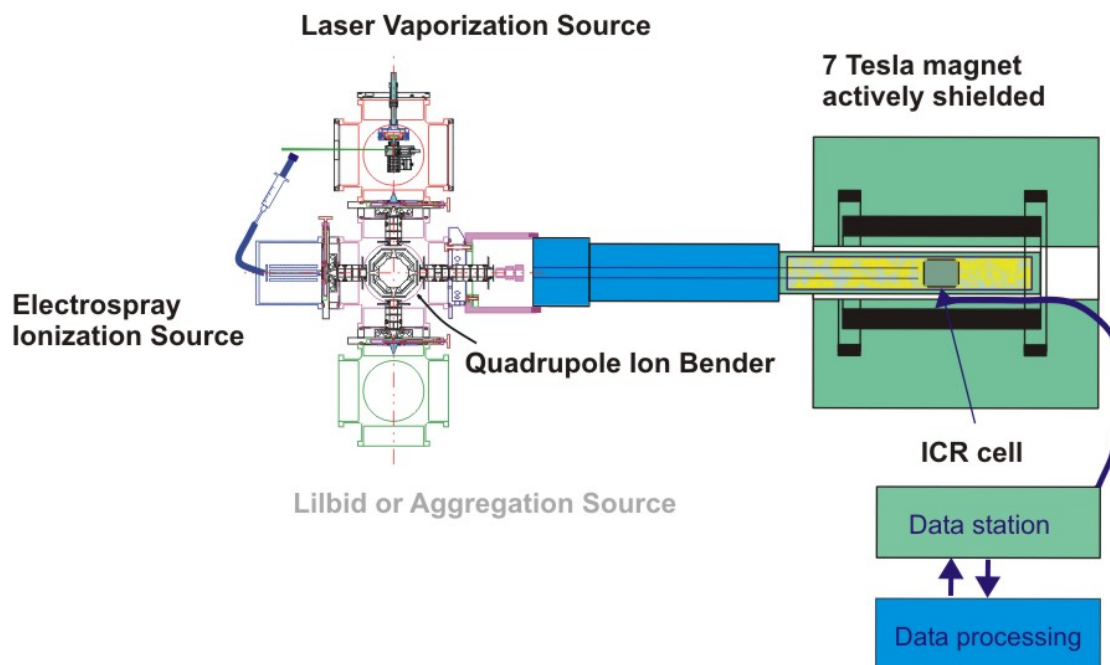


**Figure 2.7:** Schematic drawing of the Kaiserslautern FT-ICR-MS. A commercial Bruker Apex III FT-ICR-MS was modified with a quadrupole bender used as an ion deflector, for quick switching between different ion sources like the electro spray ionization source, the laser vaporization source and the LILBID<sup>15</sup> or aggregation source.<sup>16</sup> Ions generated in one of the sources are transferred to the ICR cell inside the magnet by a system of electrostatic lenses.

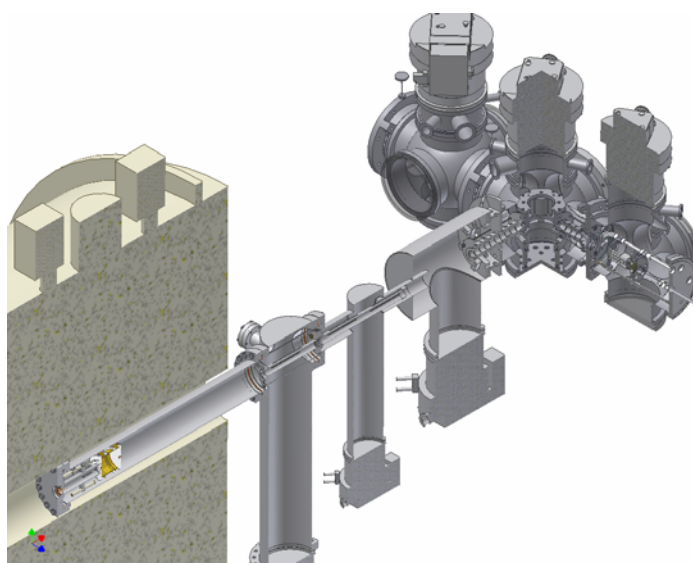


**Figure 2.8:** Cut through a 3 D model of the modified Kaiserslautern FT-ICR-MS (scheme by H. Kampschulte). Left side: 7 Tesla superconducting magnet with ICR cell. Middle: Ion transfer optics. Right side: External ion sources.

### Electrostatic Ion Transfer Optics and Vacuum System

The ions in an ESI ion source are generated under atmospheric pressure. This makes ESI ion sources compatible with separating techniques like high performance liquid chromatography (HPLC) and capillary electrophoresis (CE). For high resolution detection of ions in the cell, a vacuum of about  $10^{-10}$  mbar is required. In the commercial ICR setup this high vacuum is obtained by four differential pumping stages. The capillary region ( $\sim 10^{-1}$  mbar) of the ESI source is pumped by a  $20 \text{ m}^3/\text{h}$  rotary vane pump followed by an Edwards 250 L/s turbo drag pump ( $\sim 10^{-4}$  mbar) in the hexapole ion guide region of the ESI source. The original source chamber ( $\sim 10^{-7}$  mbar), the intersection of the ion bender and the ICR transfer optics, is pumped by a 520 L/s turbomolecular pump backed by a  $20 \text{ m}^3/\text{h}$  rotary vane pump. The transfer stage ( $\sim 10^{-8}$  mbar) is pumped by a 70 L/s turbomolecular pump and the subsequent analyzer region ( $\sim 10^{-10}$  mbar) is pumped by a 500 L/s turbomolecular pump, both backed by a  $10 \text{ m}^3/\text{h}$  rotary vane pump. With higher background pressure in the analyzer cell the resolution decreases, but it is still possible to record mass spectra. The turbomolecular pumps of the transfer stage and analyzer region are shielded against the high stray field of the magnet.

In addition, in our modified setup, the LVAP chamber ( $\sim 10^{-6}$  mbar) is pumped by a 520 L/s turbomolecular pump backed by a  $10 \text{ m}^3/\text{h}$  rotary vane pump. The chamber of the ion bender ( $\sim 10^{-7} - 10^{-6}$  mbar) is also pumped by a 520 L/s turbomolecular pump backed by a  $10 \text{ m}^3/\text{h}$  rotary vane pump.

To transfer the ions into the analyzer cell, ion transfer optics are needed, which guide the ions through electric fields. In order to guide the ion beam against the magnetic mirror effect<sup>17</sup> into the homogenous high field region of the magnet, it is accelerated up to 3.0 keV kinetic energy.

### Superconducting Magnet

The mass range and the mass resolution depend on the magnetic field strength  $B$  of a FT-ICR-MS magnet. Superconducting magnets with magnetic field strength of 3, 4.7, 7, and 9.4 (recently even 12) Tesla are commercially available. Cooling to 4 Kelvin is performed by two Dewars filled with liquid helium and liquid nitrogen. The Kaiserslautern magnet has a field strength of 7 Tesla and is actively shielded.

### Analyzer Cell

Inside the ICR cell, a Bruker *infinity cell*,<sup>18</sup> the ions are trapped, excited and detected. With acceleration out of the ion source, an ion acquires kinetic energy

$$E_{kin} = zV_{acc} = mv^2/2, \quad (2.1)$$

where  $V_{acc}$  represents the potential difference that defines the acceleration region,  $m$  is the mass of the ion,  $z$  the charge state and  $v$  its velocity. Under current conditions the ion possess  $E_{kin} \approx 1$  eV when entering the ICR cell. When entering a homogeneous magnetic field on a trajectory perpendicular to the magnetic field strength  $B$ , the ion experiences a Lorentz force  $F$  that is perpendicular both to  $B$  and  $v$ . The resulting trajectory of the ion in the magnetic field is a circle with radius  $r$  because the Lorentz force just balances the centrifugal force

$$F = zvB = mv^2/r. \quad (2.2)$$

Thus, one obtains the following relationship between the  $m/z$  value of an ion and the magnetic field strength

$$m/z = r^2 B^2 / 2V_{acc}. \quad (2.3)$$

Various trap geometries have been designed. For most applications cubic, tetragonal and cylindrical cells are in use. The ICR cell in use consists of six plates. The analyzer cell lies within the strong magnetic field which is perpendicular to the trapping plates. An electrostatic field is applied to these trapping plates to confine ion motion parallel to the magnetic field. A trapped ion, having an initial velocity  $v$ , will travel in a circular path of radius  $r$  (according to eq.(2.2))

$$r = mv/zB, \quad (2.4)$$

rotating with a frequency  $\omega$

$$\omega = 2\pi/\tau = zB/m. \quad (2.5)$$

The frequency  $\omega$  is called the cyclotron frequency. The ion is kept within the cell by a DC-voltage applied to the trapping plates and can remain trapped for minutes or even hours, provided the pressure in the cell is low enough (high vacuum). To assist ion trapping in the ICR cell, the Caravetti method for enhanced trapping efficiency is used, applying a small potential gradient ('side-kick') perpendicular to the velocity of the ions.<sup>19</sup> Thereby the kinetic energy of the injected ions is converted into cyclotron and magnetron motion perpendicular to the magnetic field. The other two pairs of plates (excitation resp. detection plates) are parallel to the field lines.

According to eq.(2.5), the frequency is inversely proportional to the mass of an ion. Due to the initial spatial distribution of ions, an excitation pulse (radio frequency, RF) is

applied prior to detection, such that all ions with identical cyclotron frequency absorb energy and then move together coherently on a larger orbit radius (cf. Figure 2.9).

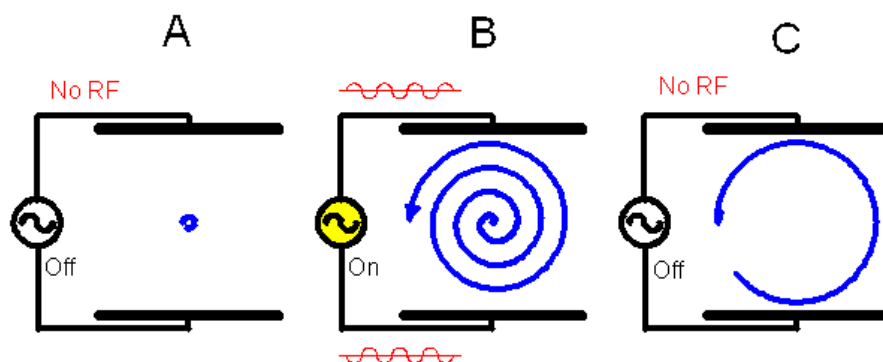


**Figure 2.9:** Activation of ions in the ICR cell to higher, detectable orbits by radio frequency

Actually, the resulting ion cyclotron motion is more complicated than a simple movement on an orbit (cf. Figure 2.10). The cyclotron motion of the ions then induces a current in the detector plates (image current) that is proportional to the number of ions and to the  $m/z$  values of the excited ions.

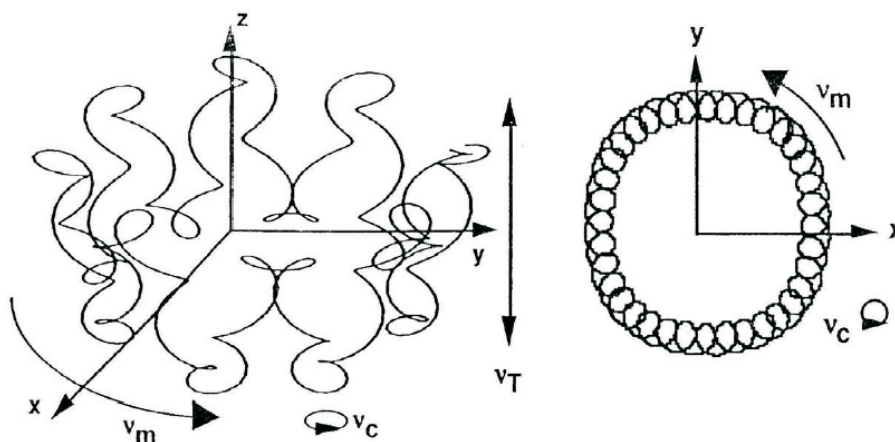


**Figure 2.10:** Resulting ion cyclotron motion in the ICR cell, comprising the three basic oscillations: cyclotron ( $\nu_c$ ), magnetron ( $\nu_m$ ) and trapping ( $\nu_T$ )

### Supply Electronics and Data Recording System

Supply electronics and data recording system consist of frequency synthesizer, pulse generator, signal amplifier, digitizers and a personal computer for controlling the components. The digital excitation and acquisition system (AQS) of the Bruker Apex III is used. Online display of mass spectra with transients up to 1 Mword is performed via fast Fourier

transformation (FFT) by the personal computer (Intel Xeon 2.4 GHz processor, 512 Mbyte RAM).

### **Fragmentation of Ions in the ICR-Cell**

Information about the structure of ionic molecules is difficult to obtain from mass spectra alone, as they describe only the stoichiometrical composition of the molecule and, if the mass resolution is high enough, the isotopic distribution. However, fragmentation of molecules has proved to be a useful tool to get deeper insight in the structural composition of molecules. Mass spectrometers which are able to perform MS/MS experiments allow for an isolation of a so called parent ion. After activation the parent ion undergoes fragmentation and the resulting product ions, the fragments (or daughter ions), are detected. The composition of the fragments then helps to interpret the former parent ion. Sometimes not all fragments are ionic, but as at least one fragment remains which carries the initial charge, the neutral fragments can be inferred by the mass difference between the parent and the product ion.

Fragmentation can be induced by various methods. In collision induced dissociation (CID),<sup>20-23</sup> also called collisionally activated dissociation (CAD), ions gain internal energy through collisions with an inert gas. The ions subsequently fragment via a process of unimolecular decomposition. In general, fragmentation requires sufficient energy to be deposited in the ion such that the vibrational energy in a given bond exceeds its bond strength (threshold effect). The most common variation of this method in use today is called SORI (sustained off resonance irradiation) CID. In SORI CID, the ions are excited not only by collisions with a background gas but also by irradiation of the ions with radio frequencies. These radio frequencies thereby have to be shifted from the resonant frequency by a few Hertz to avoid elimination. If the binding energy between fragments is rather small (e.g. in a complex with weakly bound ligands or in noncovalent complexes), fragmentation can also be induced by blackbody infrared radiative dissociation (BIRD).<sup>24-27</sup> The internal energy of the molecule is increased by absorption of multiple infrared (IR) photons from the thermal blackbody background radiation until the energy suffices to induce bond breaking. These techniques are commonly used today, but it has to be mentioned that further methods exist. For example the elucidation of primary structures of proteins can be achieved by fragmentation of the molecules with a CO<sub>2</sub> laser by absorbing multiple infrared photons.

The FT-ICR-MS is capable to perform MS<sup>n</sup> experiments with or without collision gas. Hence, by variation of a pumping delay, which controls the time that the ions spend in the cell, kinetic measurements can also be accomplished.

### Laser vaporization and Ion Detection with MICRA at the Free Electron Laser CLIO

In our infrared multiphoton dissociation (IRMPD) experiments at the free electron laser CLIO in Orsay, France, we used a compact FT-ICR mass spectrometer prototype based on a 1.24 T permanent magnet, covering a mass range of 10 – 1000 amu.<sup>28</sup> The ion trap of MICRA (Mobile ICR Analyzer) differs from standard FT-ICR cell geometries by its open structure. Two opposite side electrodes, perpendicular to the axis of the magnetic field, are replaced by four interconnected electrodes parallel to it. The open-ended ICR cell of this custom-made ICR provides a good optical access to its center, which is superior to other potential cell designs using grids as side electrodes. Because of the open structure of its ICR cell MICRA is well suited for spectroscopic investigations of ions stored within the cell. Inside the high vacuum region of MICRA a base pressure of the order of  $6.7 \times 10^{-9}$  mbar is maintained by a 70 L/s turbomolecular pump backed by a dry membrane pump.

In the high magnetic field region of the ICR metal cations can be generated via laser ablation from a metal target, which is mounted in the high vacuum chamber of the ICR with a  $45^\circ$  angle to the ICR cell (cf. Fig. 2.11). A Nd:YAG laser beam (Continuum Surelite,  $\lambda = 532$  nm, 10 mJ per 5ns pulse) directed parallel to the axis of the ICR cell is focused on the metal surface and ablates the metal ion.<sup>29</sup> The ablated metal ions are trapped inside the ICR cell and can react with gases injected into the cell via three different pulsed valves.

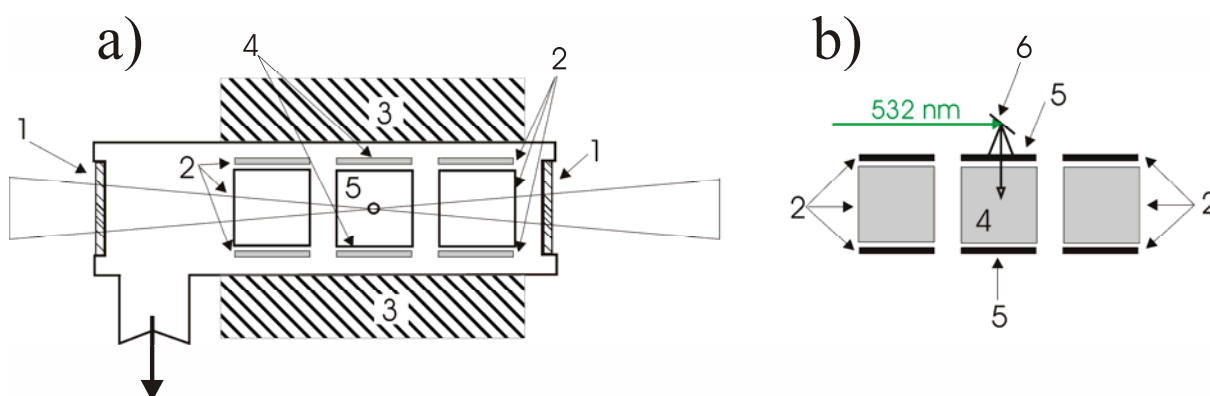


**Figure. 2.11:** Schematic sideview of MICRA (a) and top view of the ICR cell (b) showing the metal target mounted near the ICR cell. Details of experimental setup: (1) ZnSe optical window, (2) excitation plates, (3) permanent magnet, (4) detection plates, (5) trapping plate with hole, (6) metal target.

### 2.1.3 Infrared Multiphoton Dissociation Spectroscopy with the Free Electron Laser at the Centre Laser Infrarouge d'Orsay

Infrared multiphoton dissociation (IRMPD) spectroscopy is a special approach to measure IR spectra of molecules in the gas phase.<sup>30,31</sup> Due to low number densities of ions in the gas phase, a conventional measurement of absorption spectra is difficult or impossible.

This problem can be solved by using high power laser systems in combination with mass spectrometry. In most cases, the ions of interest are transferred to an ion trap (ICR or Paul traps are common). The trapped ions are then radiated with IR photons. If the wavelength of the photons is in resonance with a vibrational mode of the ion, the photons get absorbed and the energy of the ion increases. Due to internal vibrational relaxation (IVR), the additional energy can be distributed into all accessible modes of the ion, unless one bond contains enough energy to break and produce fragment ions, which in turn can be detected in the ion trap. However, the energy uptake through the first resonant absorption process alone might not be sufficient to induce a fragmentation. Due to anharmonicities, the energy uptake through the absorption process is reduced as soon as higher excited states are reached. Nevertheless, the high density of states then might lead to a quasi continuum, in which mixing with other vibrational states occurs and further absorptions finally lead to the dissociative continuum (cf. Fig. 2.12).

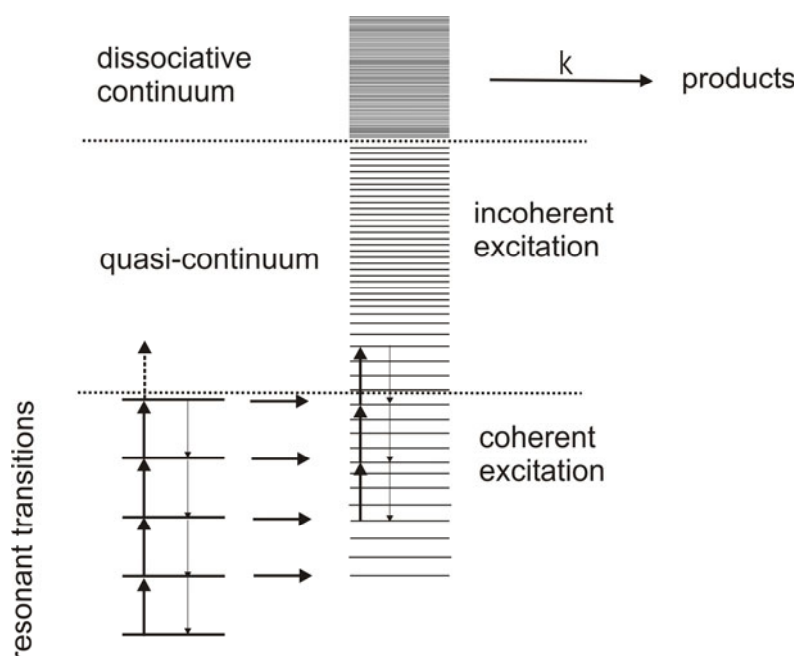


**Figure 2.12:** Scheme of the infrared multiphoton dissociation (IRMPD) at a certain wavelength. The absorption takes place resonantly in a discrete region. The density of states increases with increasing energy and the system reaches a quasi-continuum. If enough energy is present in the system, it reaches a dissociative continuum. For details on the mechanism and transition from coherent to incoherent excitation, see Refs. 32-35.

Experimental IRMPD spectra are obtained by plotting  $P_{\text{frag}}$ , the fraction of the sum of fragment intensities over the total intensities of fragments and parent ion, against the wavelength:

$$P_{\text{fragments}} = -\ln \left( \frac{I_{\text{parent}}}{I_{\text{parent}} + \sum_i I_{\text{fragment}(i)}} \right) \quad (2.6)$$

A limiting factor of the IRMPD method is that the obtained IR spectra only mimic the (calculated) absorption spectra. Some of the modes might be "dark modes", which means that the excitation of these modes does not lead to fragmentation and thus the mode might not be visible in the spectrum. Another point is that the comparability of the IR intensities is also limited by the IRMPD efficiency.

A large variety of neutral and ionic systems has been investigated by IRMPD before.<sup>29,36-43</sup> Depending on the system under investigation, the choice of the applied laser system is crucial. For our systems we needed a laser system with a broad spectral range and high intensity. Therefore we used the free electron laser (FEL) at the Centre Laser Infrarouge d'Orsay (CLIO).

In general, FELs are capable of producing tuneable, coherent, high power radiation, currently spanning wavelengths from millimeters to visible, and ultraviolet to X-ray.<sup>44,45</sup> The FEL can have the optical characteristics of conventional lasers, like e.g. high spatial coherence and near diffraction limited radiation beam. However, it differs from conventional lasers in using a relativistic electron beam as lasing medium as opposed to bound atomic or molecular states. The electron beam produced by an accelerator is sent through a wiggler, which denominates a magnet whose field varies sinusoidally with distance. The electrons radiate and bunch at a resonant wavelength determined solely by the wavelength of the wiggler, the wiggler magnetic field and the electron beam energy. The CLIO infrared FEL at Orsay is a user facility operating in the mid-infrared. Its major components are an electron accelerator, an optical resonator and an undulator, which creates a periodic transverse magnetic field. CLIO's experimental setup is depicted schematically in Fig. 2.13.



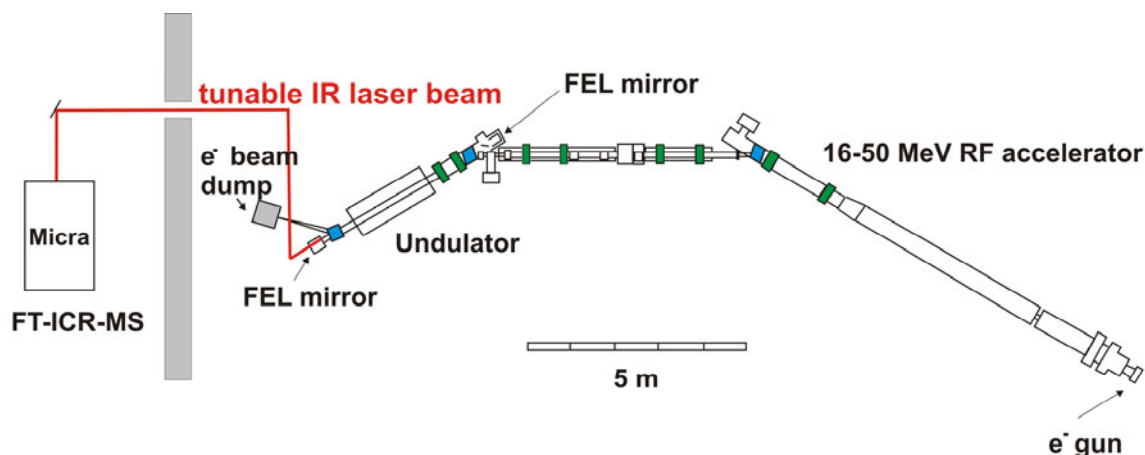


**Figure 2.13:** Scheme of the CLIO FEL coupled to the MICRA FT-ICR-MS.

At each electron energy continuous tunability is obtained over a spectral range  $\Delta\lambda/\lambda \approx 2.5$  without the need to modify any accelerator settings. The FEL temporal structure consists of macropulses about  $8 \mu\text{s}$  long at a repetition rate of 25 Hz, containing typically 500 micropulses a few picoseconds long each, separated by 16 ns. The typical energy content of a macropulse is 25 mJ with a peak power of 20 MW in each micropulse. CLIO emits intense laser radiation in the chemical infrared and is therefore well suited to probe molecular vibrations in gas phase ions by IRMPD spectroscopy. For this purpose CLIO is coupled to the mobile ICR MICRA.<sup>28,29</sup> Characteristic CLIO FEL powers depending on the electron energy are shown in Figure 2.14.

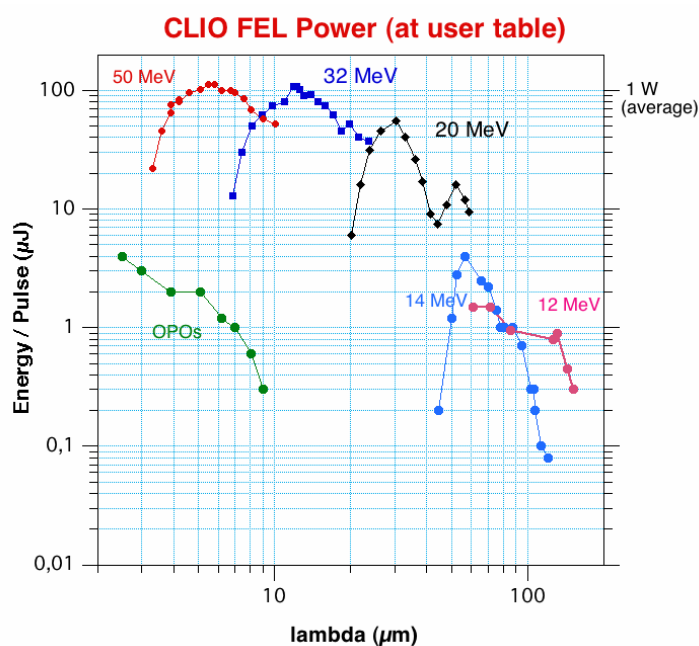


**Figure 2.14:** Average power of the CLIO FEL vs. wavelength for different electron energies.<sup>46</sup>

## 2.2 Theoretical Methods

In the following equations no fundamental physical constants will appear due to the introduction of atomic units. Physical quantities are expressed as multiples of fundamental constants and/or as combinations of such constants. Therefore all equations will appear in a more compact form. Good introductions can be found elsewhere.<sup>47-51</sup>

Most ab initio quantum chemical calculations base on the solution of the time-dependent, non-relativistic Schrödinger equation

$$\hat{H}\Psi = i\hbar\partial\Psi/\partial t \quad (2.7)$$

This equation can't be solved exactly for many particle systems, thus several approximations have to be applied.

In most cases only stationary states are of interest, therefore the first approximation applied is the so-called *separation of variables*. If the Hamilton operator  $\hat{H}$  does not contain the time variable explicitly, the wave function  $\Psi(\vec{r}_i, \vec{R}_A, t)$  can be written as the product of a spatial function  $\Psi(\vec{r}_i, \vec{R}_A)$  and a time function  $F(t)$ , which (after substitutions) results in two equations:

$$\hat{H}\Psi(\vec{r}_i, \vec{R}_A) = E\Psi(\vec{r}_i, \vec{R}_A) \quad (2.8)$$

$$i\hbar\partial F(t)/\partial t = i\hbar dF(t)/dt = EF(t). \quad (2.9)$$

The first of these two equations (2.8) is called the time-independent Schrödinger equation, which is only a function of the spatial coordinates of the electrons ( $\vec{r}_i$ ) and nuclei ( $\vec{R}_A$ ), but no longer a function of time. Next, the time-independent Schrödinger equation can be further simplified by taking advantage of the significant differences between the masses of nuclei and electrons. Because of this mass difference the nuclei move much slower than the electrons and in consequence we can consider – at least to a good approximation – the electrons as moving in the field of fixed nuclei. This is the central conclusion of the *Born-Oppenheimer* (BOA) or clamped-nuclei approximation which leads to a reduction of the so far molecular Hamiltonian to the so-called electronic Hamiltonian,

$$\hat{H}_{elec} = -\frac{1}{2} \sum_{i=1}^N \nabla_i^2 - \sum_{i=1}^N \sum_{A=1}^M \frac{Z_A}{r_{iA}} + \sum_{i=1}^N \sum_{j>i}^N \frac{1}{r_{ij}} = \hat{T} + \hat{V}_{Ne} + \hat{V}_{ee}. \quad (2.10)$$

This Hamiltonian is then used in the Schrödinger equation describing the motion of electrons in the field of fixed nuclei:

$$\hat{H}_{elec} \Psi_{elec}(\vec{r}_i; \vec{R}_A) = E_{elec} \Psi_{elec}(\vec{r}_i; \vec{R}_A) \quad (2.11)$$

Solving this equation for the electronic wave function will produce the effective potential function  $E_{elec}$ , which depends only parametrically on the coordinates of the nuclei and is free of the kinetic energy of the nuclei. It describes the potential energy surface of the system.

$\Psi_{elec}$  itself depends on the electron coordinates, while again the nuclear coordinates enter only parametrically and do not explicitly appear in  $\Psi_{elec}$ .

The total energy of the system  $E_{tot}$  is then the sum of  $E_{elec}$  and the constant nuclear repulsion term

$$E_{nuc} = \sum_{A=1}^M \sum_{B>A}^M \frac{Z_A Z_B}{r_{AB}}. \quad (2.12)$$

In summary we now have the time-independent electronic Schrödinger equation of a many-electron system as

$$\hat{H}_{elec} \Psi_{elec} = E_{elec} \Psi_{elec} \quad (2.13)$$

and the total energy of the system as

$$E_{tot} = E_{elec} + E_{nuc}. \quad (2.14)$$

Now we are faced with the next problem, namely finding and describing (approximate) solutions of the electronic Schrödinger equation. Except for the very simplest cases like  $H_2^+$ , quantum chemists are faced with many-electron problems. Thus the main obstacle here is the electron-electron repulsion term in the electronic Hamiltonian. One approach to this problem is the Hartree-Fock approximation (HF), which will be introduced in the following sections.

### The Hartree-Fock Approximation

To describe the ground state of an  $N$ -electron system, the simplest antisymmetric wave function is a single Slater determinant. By definition a determinant obeys the antisymmetry principle and thus the Slater determinant represents a quantum-mechanical generalization of *Pauli's exclusion principle*.

$$\Psi_0 \approx \Phi_{SD} = \frac{1}{\sqrt{N!}} \begin{vmatrix} \chi_1(\vec{x}_1) & \chi_2(\vec{x}_1) & \cdots & \chi_N(\vec{x}_1) \\ \chi_1(\vec{x}_2) & \chi_2(\vec{x}_2) & \cdots & \chi_N(\vec{x}_2) \\ \vdots & \vdots & & \vdots \\ \chi_1(\vec{x}_N) & \chi_2(\vec{x}_N) & \cdots & \chi_N(\vec{x}_N) \end{vmatrix} \quad (2.15)$$

where  $\Psi_0$  is the ground state wave function and the one-electron functions  $\chi(\vec{x})$  are called *spin orbitals*, and are composed of a spatial orbital  $\phi(\vec{r})$  and one of the two spin functions,  $\alpha(s)$  or  $\beta(s)$ .

$$\chi(\vec{x}) = \phi(\vec{r})\sigma(s), \quad \sigma = \alpha, \beta. \quad (2.16)$$

The spin functions have the important property that they are orthonormal. For computational convenience, the spin orbitals themselves are usually chosen to be orthonormal.

The variational principle states that the best wave function of this functional form is the one which gives the lowest possible energy

$$E_0 = \langle \Psi_0 | \hat{H} | \Psi_0 \rangle \quad (2.17)$$

where  $\hat{H}$  is the full electronic Hamiltonian. The variational flexibility in the wave function (eq. 2.15) is in the choice of spin orbitals. By minimizing  $E_0$  with respect to the choice of spin orbitals, we can derive an equation, called the Hartree-Fock equation, which determines the spin orbitals. The Hartree-Fock equation is an eigenvalue equation of the form

$$\hat{f}(i)\chi(\vec{x}_i) = \epsilon\chi(\vec{x}_i), \quad i = 1, 2, \dots, N. \quad (2.18)$$

$\hat{f}(i)$  is an effective one-electron operator, called the *Fock* operator, of the form

$$\hat{f}(i) = -\frac{1}{2}\nabla_i^2 - \sum_{A=1}^M \frac{Z_A}{r_{iA}} + V_{HF}(i) \quad (2.19)$$

where  $V_{HF}(i)$  is the *average* potential experienced by the  $i$ th electron due to the presence of the other electrons.

The essence of the Hartree-Fock approximation is to replace the complicated many-electron potential in eq. (2.10) by an *effective potential*  $V_{eff} = \sum_i V_{HF}(i)$  in which electron-electron repulsion is treated in an average way.

The HF potential  $V_{HF}(i)$ , depends on the spin orbitals of the other electrons. The HF equation (eq. (2.18)) is nonlinear because of the nature of the Fock operator eq. (2.18) and must be solved iteratively as  $V_{HF}$  depends on the eigenfunctions of  $\hat{f}$ . One procedure for solving the HF equation iteratively is called the self-consistent field (SCF) method.

By making an initial guess (e.g. by an extended Hückel calculation) at the spin orbitals (giving  $\Psi_{trial}$ ), one can calculate the average field seen by each electron and then solve the eigenvalue equation (2.18) for a new set of spin orbitals. Using these new spin orbitals, one can obtain new fields and repeat the procedure until self-consistency is reached (i.e., until the fields no longer change and the spin orbitals used to construct the Fock operator are good approximations of its eigenfunctions). The variational principle now states that the energy as the expectation value of the Hamilton operator  $\hat{H}$  from any guessed  $\Psi_{trial}$  will be an *upper bound* of the true energy of the ground state (because the true energy will never be reached) i.e.,

$$\langle \Psi_{trial} | \hat{H} | \Psi_{trial} \rangle = E_{trial} \geq E_0 = \langle \Psi_0 | \hat{H} | \Psi_0 \rangle \quad (2.20)$$

where the equality holds if and only if  $\Psi_{trial}$  is identical to  $\Psi_0$ .

As noted before, Hartree-Fock theory provides an inadequate treatment of the correlation between the motions of the electrons within a molecular system, especially that arising between electrons of opposite spin. HF theory fulfills the requirement that  $|\Psi^2|$  is invariant with respect to the exchange of any two electrons. By making the wave function antisymmetric, it automatically includes the major correlation effects arising from pairs of electrons with the same spin. This correlation is termed *exchange correlation*. The motion of electrons of opposite spin remains uncorrelated under HF theory. Approaches to include these effects are known as *electron correlation* methods or *post-HF* methods, e.g. the Møller-Plesset perturbation theory.

### Møller-Plesset Perturbation Theory

In 1934, Møller and Plesset proposed a perturbation treatment of atoms and molecules<sup>52</sup> in which the unperturbed wave function is the Hartree-Fock function and as a non-iterative correction higher excitations are added, based on the so-called many body perturbation theory.<sup>47</sup> The perturbation  $\hat{H}'$  is the difference between the true molecular Hamiltonian  $\hat{H}$  and  $\hat{H}^0$  (the Hamiltonian of the HF equation)

$$\hat{H}' = \hat{H} - \hat{H}^0. \quad (2.21)$$

The Møller-Plesset (MP) unperturbed Hamiltonian is taken as the sum of one-electron Fock operators  $\vec{f}(m)$ ,

$$\hat{H}^0 \equiv \sum_{m=1}^N \bar{f}(m). \quad (2.22)$$

Now a parameter  $\lambda$  is introduced, which leads to a unperturbed system for  $\lambda = 0$  and a fully turned on perturbation for  $\lambda = 1$ ,

$$\hat{H} = \hat{H}^0 + \lambda \hat{H}^1. \quad (2.23)$$

The Schrödinger equation for a perturbed state is then

$$\hat{H}\Psi_n = (\hat{H}^0 + \lambda \hat{H}^1)\Psi_n = E_n \Psi_n. \quad (2.24)$$

$\Psi_n$  is the perturbed wave function. Since the Hamiltonian in eq. (2.24) depends on the parameter  $\lambda$ , both the eigenfunction  $\Psi_n$  and the eigenvalue  $E_n$  depend on  $\lambda$ ,

$$\Psi_n = \Psi_n(\lambda, q); \quad E_n = E_n(\lambda), \quad (2.25)$$

where  $q$  indicates the system's coordinates. Both  $\Psi_n$  and  $E_n$  are now expanded in a Taylor series in powers of  $\lambda$  to:

$$\Psi_n = \Psi_n^{(0)} + \lambda \Psi_n^{(1)} + \lambda^2 \Psi_n^{(2)} + \dots + \lambda^k \Psi_n^{(k)} + \dots \quad (2.26)$$

$$E_n = E_n^{(0)} + \lambda E_n^{(1)} + \lambda^2 E_n^{(2)} + \dots + \lambda^k E_n^{(k)} + \dots \quad (2.27)$$

$\Psi_n^{(k)}$  and  $E_n^{(k)}$  are called the  $k$ th-order corrections to the wave function and energy;

$\Psi_n^{(0)}$  respectively  $E_n^{(0)}$  belong to the unperturbed HF ground state wave function  $\Psi_n^0$  and the corresponding energy Eigenvalue  $E_n^0$ .

Substituting equations (2.26) and (2.27) into eq. (2.24) gives

$$\begin{aligned} (\hat{H}^0 + \lambda \hat{H}^1)(\Psi_n^{(0)} + \lambda \Psi_n^{(1)} + \lambda^2 \Psi_n^{(2)} + \dots) = \\ (E_n^{(0)} + \lambda E_n^{(1)} + \lambda^2 E_n^{(2)} + \dots)(\Psi_n^{(0)} + \lambda \Psi_n^{(1)} + \lambda^2 \Psi_n^{(2)} + \dots). \end{aligned} \quad (2.28)$$

Collecting like powers of  $\lambda$  provides

$$\begin{aligned} \hat{H}^0 \Psi_n^{(0)} + \lambda(\hat{H}^1 \Psi_n^{(0)} + \hat{H}^0 \Psi_n^{(1)}) + \lambda^2(\hat{H}^0 \Psi_n^{(2)} + \hat{H}^1 \Psi_n^{(1)}) + \dots \\ = E_n^{(0)} \Psi_n^{(0)} + \lambda(E_n^{(1)} \Psi_n^{(0)} + E_n^{(0)} \Psi_n^{(1)}) + \lambda^2(E_n^{(2)} \Psi_n^{(0)} + E_n^{(1)} \Psi_n^{(1)} + E_n^{(0)} \Psi_n^{(2)}) + \dots \end{aligned} \quad (2.29)$$

The coefficients of like powers of  $\lambda$  in the two series must be equal on each side of eq. (2.28). Equating the coefficients of the  $\lambda^0$  terms yields

$$\hat{H}^0 \Psi_n^{(0)} = E_n^{(0)} \Psi_n^{(0)} \quad (2.30)$$

which is the Schrödinger equation for the unperturbed problem. Equating the coefficients of the  $\lambda^1$  terms gives us

$$\hat{H}^1 \Psi_n^{(0)} + \hat{H}^0 \Psi_n^{(1)} = E_n^{(1)} \Psi_n^{(0)} + E_n^{(0)} \Psi_n^{(1)} \quad (2.31)$$

and for the  $\lambda^2$  terms we have

$$\hat{H}^0\Psi_n^{(2)} - E_n^{(0)}\Psi_n^{(2)} = E_n^{(2)}\Psi_n^{(0)} + E_n^{(1)}\Psi_n^{(1)} - \hat{H}\Psi_n^{(1)}. \quad (2.32)$$

After several transformations one can achieve the desired expression for  $E_n^{(2)}$  in terms of the unperturbed wave functions and energies.

$$E_n^{(2)} = \sum_{m \neq n} \frac{|\langle \Psi_m^0 | \hat{H} | \Psi_n^{(0)} \rangle|^2}{E_n^{(0)} - E_m^{(0)}}. \quad (2.33)$$

By now we are able to determine the second-order correction to the energy. Determination of the third-order correction is much more complicated because it is necessary to know also the first perturbed wave function  $\Psi_n^{(1)}$ , whereas for the second-order it is sufficient to have knowledge about the unperturbed ground state wave function. Apart from being able to include correlation, the second-order Møller-Plesset perturbation theory (MP2) method has the advantage to be size consistent. Disadvantages of this method are the (relative) high computational costs and, as this method is not variational, the risk to calculate an energy that is below the true energy.

### Density Functional Theory

A different quantum chemical approach to describe atoms or molecules is density functional theory (DFT).<sup>51</sup> DFT is based on the evaluation of the electron density as the square of the atomic respectively molecular wave function:

$$\rho = \langle \Psi^* | \Psi \rangle \quad (2.34)$$

In 1964 Hohenberg and Kohn<sup>53</sup> proved that the potential energy  $\hat{V}$  is (up to a constant) determined by the density  $\rho$ . Hence  $\rho$  determines N (number of electrons),  $\hat{V}$ , and  $\hat{H}$ :

$$\hat{V} = E_0 - \{[\hat{T} + \hat{V}_{ee}]\Psi_0\} / \Psi_0 \quad (2.35)$$

The ground state energy  $E_0$  is given by

$$E_0[\rho_0] = \int \rho_0(\vec{r}) V_{Ne} d\vec{r} + F_{HK}[\rho_0], \quad (2.36)$$

which defines the *Hohenberg-Kohn functional*  $F_{HK}[\rho]$  to an arbitrary density  $\rho$  as

$$F_{HK}[\rho] = T[\rho] + E_{ee}[\rho] = T[\rho] + J[\rho] + E_{xc}[\rho], \quad (2.37)$$

where at least the Coulomb part  $J[\rho]$  can be extracted, as it is already well known.  $E_{xc}[\rho]$  is the contribution to the electron-electron interaction containing all the effects of self-

interaction correction, exchange and Coulomb correlation described before in the HF part. The functional for the kinetic energy  $T[\rho]$  also stays unknown for many particle systems.

Kohn and Sham now tackled the problem for the kinetic energy by expressing it in terms of a system with *non-interacting* electrons (analog to the HF method).<sup>54</sup> For such a system the kinetic energy can be exactly expressed as

$$T_s = -\frac{1}{2} \sum_i^N \langle \varphi_i | \nabla^2 | \varphi_i \rangle \quad (2.38)$$

where the spin orbitals, in analogy to equations (2.17) and (2.18), are determined by

$$\hat{f}^{KS} \varphi_i = \varepsilon_i \varphi_i \quad (2.39)$$

with the one-electron Kohn-Sham operator  $\hat{f}^{KS}$  defined as

$$\hat{f}^{KS} = -\frac{1}{2} \nabla^2 + V_s(\vec{r}) \quad (2.40)$$

In order to distinguish these orbitals from their Hartree-Fock counterparts, they are usually termed *Kohn-Sham orbitals*, or briefly KS orbitals.

Now we have to choose the introduced effective potential  $V_s$  such that the density resulting from the summation of the moduli of the squared  $\{\varphi_i\}$  exactly equals the ground state density of the real target system of interacting electrons,

$$\rho_s(\vec{r}) = \sum_i^N \sum_s |\varphi_i(\vec{r}, s)|^2 = \rho_0(\vec{r}) \quad (2.41)$$

By now we still have to take into account that the term for the kinetic energy  $T_s[\rho(\vec{r})]$  is an approximation, for it is the energy of a non-interacting system. Kohn and Sham accounted for that by using the Hohenberg-Kohn functional  $F_{HK}[\rho(\vec{r})]$ ,

$$F_{HK}[\rho(\vec{r})] = T_s[\rho(\vec{r})] + J[\rho(\vec{r})] + E_{XC}[\rho(\vec{r})], \quad (2.42)$$

where  $E_{XC}$ , the so-called *exchange-correlation energy*, includes the residual part of the true kinetic energy. In other words, the exchange-correlation energy  $E_{XC}$  is the functional which contains everything that is unknown.

The expression for the energy of the interacting, real system, highlighting the dependence on the orbitals as indicated in eq.(2.38) and (2.41), is now given as

$$\begin{aligned} E[\rho(\vec{r})] &= T_s[\rho] + J[\rho] + E_{XC}[\rho] + E_{Ne}[\rho] \\ &= -\frac{1}{2} \sum_i^N \langle \varphi_i | \nabla^2 | \varphi_i \rangle + \frac{1}{2} \sum_i^N \sum_j^N \iint |\varphi_i(\vec{r}_1)|^2 \frac{1}{r_{12}} |\varphi_j(\vec{r}_2)|^2 d\vec{r}_1 d\vec{r}_2 + E_{XC}[\rho(\vec{r})] \end{aligned}$$



$$-\sum_i^N \int \sum_A^M \frac{Z_A}{r_{iA}} |\varphi_i(\vec{r}_i)|^2 d\vec{r}_i \quad (2.43)$$

If the exchange-correlation functional would be known exactly, the DFT approach would deliver the true energy, as so far no approximations have been done. Unfortunately, this functional is not known exactly, so we again only get an approximate solution like for HF.

Different approximate functionals are widely used. One of the most often used functionals was the the gradient-corrected Becke88-exchange functional<sup>55</sup> in combination with the Lee-Yang-Parr-correlation functional (BLYP).<sup>56</sup> Today, due to larger computer capacities, the hybrid exchange-correlation functional B3LYP,<sup>56-58</sup> a three parameter functional, is one of the most applied functionals and is used as the standard functional in this thesis.

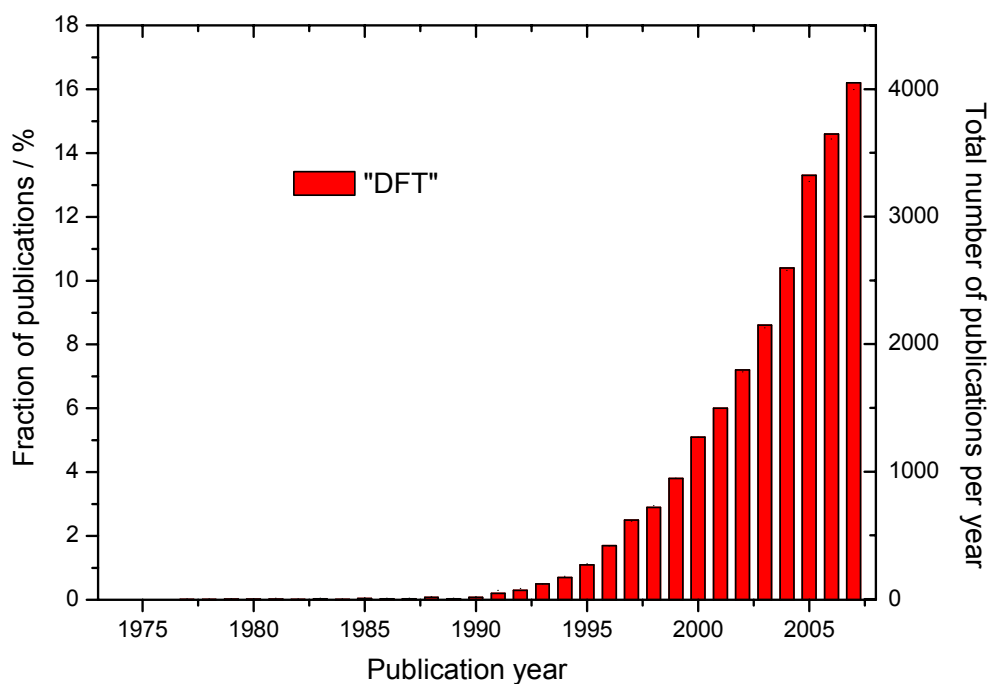


**Figure 2.15:** Temporal development of the number of publications listed in "ISI Web of Knowledge" for the search term "DFT" in the topics section. A similar picture is found when entering "density functional theory" as search term (April 2008). This graph demonstrates the rapidly growing use and importance of DFT calculations.

### Calculation of Anharmonic Frequencies with the VPT2 Approach

For some of the systems studied in this work the calculation of frequencies in the harmonic approximation completely fails. This is due to the strongly anharmonic potential energy curves of e.g. the O–H modes in strong and medium hydrogen bonds.

Anharmonic frequencies<sup>59-63</sup> of the dicarboxylic acids were computed at the MP2/cc-pVDZ level of theory. The calculation follows the conceptual approach of W. H. Miller<sup>63</sup> as coded by V. Barone,<sup>60,61,64</sup> which is based on second order perturbation theory and provides closed form expressions for most of the spectroscopic constants needed for obtaining anharmonic frequencies. Starting from the analytical second derivatives of the electronic energy with respect to the nuclear displacements at a particular level of ab initio level of theory, the third and semi-diagonal fourth derivatives can be obtained by a finite difference approach. This procedure requires the evaluation of  $(2k+1)$  second derivatives for a system with  $k$  normal modes. The anharmonic calculations were carried out using the Gaussian 03 program package (Ref.<sup>65</sup>).

### Basis Sets and Effective Core Potentials

Solving the Hartree-Fock resp. the Kohn-Sham equation (eq.(2.38) resp. eq.(2.39)) demands a representation of the molecular orbitals.<sup>47-51</sup> The linear combination of atomic orbitals approach (LCAO) to create molecular orbitals (MO) was first used for this purpose by Roothaan in 1951.<sup>66</sup> In the LCAO approach a set of  $K$  predefined basis functions  $\{\eta_\mu\}$  is introduced and the orbitals are linearly expanded as

$$\Psi_i = \sum_{\mu=1}^K C_{\mu i} \eta_\mu, \quad i = 1, 2, \dots, K \quad (2.44)$$

with the coefficients  $C_{\mu i}$  as the only variables.

If the set  $\{\eta_\mu\}$  was complete, which would require  $K=\infty$ , every function  $\eta_i$  could be expressed exactly via eq. (2.44). In real applications  $K$  is finite and thus it is important to choose the  $\{\eta_\mu\}$  such that the linear combination provides an approximation of the exact orbitals which is as accurate as possible.

There are several types of basis functions that could be applied to represent molecular orbitals. Two types of basis functions have found common use: the Slater-type function and the Gaussian-type function. Both are atom-centered basis functions.

A typical Slater-type orbital (STO) is expressed as

$$\eta^{STO} = N r^{n-1} e^{(-\zeta r)} Y_{lm}(\Theta, \phi) \quad (2.45)$$

$N$  is a normalization factor which ensures that  $\langle \eta_\mu | \eta_\mu \rangle = 1$ .  $n$  corresponds to the principal quantum number, the orbital exponent is termed  $\zeta$ , and  $Y_{lm}$  are spherical harmonics that describe the angular part of the function. The second type of commonly used basis functions describe the so-called Gaussian-type orbitals (GTO):

$$\eta^{GTO} = Nx^l y^m z^n e^{-\alpha r^2} \quad (2.46)$$

N again is a normalization factor.  $\alpha$  represents the orbital exponent which determines how compact (large  $\alpha$ ) or diffuse (small  $\alpha$ ) the resulting function is.  $L = l + m + n$  is used to classify the GTO as s-functions ( $L=0$ ), p-functions ( $L=1$ ), d-functions ( $L=2$ ), etc.  $x, y, z$  are Cartesian coordinates.

Generally, the use of GTOs is preferred as there are efficient algorithms for providing solutions, but the GTOs fail in the correct description of the cusp behavior as  $r \rightarrow 0$ . To achieve a certain accuracy one usually needs three times as many GTOs as STOs, what would lead to a preference of the STOs. Nevertheless, with the introduction of contracted Gaussian functions (CGF) the GTOs are more favorable. As the product of two primitive Gaussian functions is again one Gaussian function these CGFs can be used to compensate for unaccuracies without severe increase of computational costs.

As trade off between accuracy and computational efficiency Ahlrich's triple-zeta valence plus polarization (TZVP) basis sets<sup>67</sup> were chosen for most of the calculations in this thesis. With the chosen TZVP basis sets the valence electrons are described by at least three contracted gaussians. It was shown before that these basis sets have a very good performance and high accuracy when applied to systems containing water molecules.<sup>68</sup>

In case of second and third transition row elements the core electrons (e.g. 28 core electrons in niobium) are described by an effective-core potential (ECP) which takes into account relativistic corrections.<sup>69</sup> The remaining electrons are again described by a TZVP basis set.

In some chapters of this work also other basis sets like Dunning's (augmented) correlation consistent basis sets<sup>70</sup> and some of Poples basis sets<sup>71</sup> are used.

## 2.3 References

- <sup>1</sup> J. B. Fenn, M. Mann, C. K. Meng, S. F. Wong, and C. M. Whitehouse, *Science* **246** (4926), 64 (1989).
- <sup>2</sup> M. Yamashita and J. B. Fenn, *J. Phys. Chem.* **88** (20), 4451 (1984).
- <sup>3</sup> M. Dole, L. L. Mack, and R. L. Hines, *J. Chem. Phys.* **49** (5), 2240 (1968).

- 4 M. Karas and F. Hillenkamp, *Anal. Chem.* **60** (20), 2299 (1988).
- 5 J. A. Loo, *Mass Spectrom. Rev.* **16** (1), 1 (1997).
- 6 R. D. Smith, J. E. Bruce, Q. Y. Wu, and Q. P. Lei, *Chem. Soc. Rev.* **26** (3), 191 (1997).
- 7 M. Przybylski and M. O. Glocker, *Angew. Chem., Int. Ed. Engl.* **35** (8), 807 (1996).
- 8 A. G. Marshall, C. L. Hendrickson, and G. S. Jackson, *Mass Spectrom. Rev.* **17** (1), 1 (1998).
- 9 J. V. Iribarne and B. A. Thomson, *J. Chem. Phys.* **64** (6), 2287 (1976).
- 10 B. A. Thomson and J. V. Iribarne, *J. Chem. Phys.* **71** (11), 4451 (1979).
- 11 P. Kebarle and L. Tang, *Anal. Chem.* **65** (22), A972 (1993).
- 12 G. Schmelzeisenredeker, L. Butfering, and F. W. Rollgen, *Int. J. Mass Spectrom. Ion Processes* **90** (2), 139 (1989).
- 13 S. Maruyama, L. R. Anderson, and R. E. Smalley, *Rev. Sci. Instrum.* **61** (12), 3686 (1990).
- 14 C. Berg, *Reaktivität von ionisierten Übergangsmetallclustern und solvatisierten Metallionen*, Technische Universität München, 1996.
- 15 W. Kleinekofort, J. Avdiev, and B. Brutschy, *Int. J. Mass Spectrom. Ion Processes* **152** (2-3), 135 (1996).
- 16 H. Haberland, M. Karrais, and M. Mall, *Zeitschrift Fur Physik D-Atoms Molecules and Clusters* **20** (1-4), 413 (1991).
- 17 J. D. Jackson, *Klassische Elektrodynamik*, 2. ed. (de Gruyter, Berlin, New York, 1983).
- 18 P. Caravatti, US Patent No. 4924089 (May 8 1990).
- 19 P. Caravatti and M. Allemann, *Organic Mass Spectrometry* **26** (5), 514 (1991).
- 20 M. B. Comisarow and A. G. Marshall, *J. Chem. Phys.* **64** (1), 110 (1976).
- 21 R. B. Cody and B. S. Freiser, *Int. J. Mass Spectrom. Ion Processes* **41** (3), 199 (1982).
- 22 M. B. Comisarow, *J. Chem. Phys.* **55** (1), 205 (1971).
- 23 A. G. Marshall and D. C. Roe, *J. Chem. Phys.* **73** (4), 1581 (1980).
- 24 D. Tholmann, D. S. Tonner, and T. B. McMahon, *J. Phys. Chem.* **98** (8), 2002 (1994).
- 25 D. S. Tonner, D. Tholmann, and T. B. McMahon, *Chem. Phys. Lett.* **233** (3), 324 (1995).
- 26 R. C. Dunbar, *J. Phys. Chem.* **98** (35), 8705 (1994).
- 27 G. Niedner-Schatteburg and V. E. Bondybey, *Chemical Reviews* **100** (11), 4059 (2000).

- 28 P. Maitre, S. Le Caer, A. Simon, W. Jones, J. Lemaire, H. N. Mestdagh, M. Heninger, G. Mauclaire, P. Boissel, R. Prazeres, F. Glotin, and J. M. Ortega, *Nuclear Instruments & Methods in Physics Research Section a-Accelerators Spectrometers Detectors and Associated Equipment* **507** (1-2), 541 (2003).
- 29 J. Lemaire, P. Boissel, M. Heninger, G. Mauclaire, G. Bellec, H. Mestdagh, A. Simon, S. L. Caer, J. M. Ortega, F. Glotin, and P. Maitre, *Phys. Rev. Lett.* **89** (27) (2002).
- 30 R. C. Dunbar, *Int. J. Mass Spectrom.* **200** (1-3), 571 (2000).
- 31 M. A. Duncan, *Int. J. Mass Spectrom.* **200** (1-3), 545 (2000).
- 32 D. W. Lupo and M. Quack, *Chemical Reviews* **87** (1), 181 (1987).
- 33 R. Marquardt and M. Quack, *Infrared Phys.* **29** (2-4), 485 (1989).
- 34 M. Quack, *Abstracts of Papers of the American Chemical Society* **196**, 147 (1988).
- 35 M. Quack, *Infrared Phys.* **29** (2-4), 441 (1989).
- 36 B. Chiavarino, M. E. Crestoni, S. Fornarini, J. Lemaire, L. Mac Aleese, and P. Maitre, *ChemPhysChem* **5** (11), 1679 (2004).
- 37 B. Chiavarino, M. E. Crestoni, S. Fornarini, J. Lemaire, L. MacAleese, and P. Maitre, *ChemPhysChem* **6** (3), 437 (2005).
- 38 B. Chiavarino, M. E. Crestoni, S. Fornarini, J. Lemaire, P. Maitre, and L. MacAleese, *J. Am. Chem. Soc.* **128** (38), 12553 (2006).
- 39 O. Dopfer, J. Lemaire, P. Maitre, B. Chiavarino, M. E. Crestoni, and S. Fornarini, *Int. J. Mass Spectrom.* **249/250**, 149 (2006).
- 40 R. C. Dunbar, D. T. Moore, and J. Oomens, *J. Phys. Chem. A* **110** (27), 8316 (2006).
- 41 L. MacAleese and P. Maitre, *Mass Spectrom. Rev.* **26** (4), 583 (2007).
- 42 D. T. Moore, J. Oomens, J. R. Eyler, G. von Helden, G. Meijer, and R. C. Dunbar, *J. Am. Chem. Soc.* **127** (19), 7243 (2005).
- 43 N. C. Polfer, J. Oomens, and R. C. Dunbar, *Phys. Chem. Chem. Phys.* **8** (23), 2744 (2006).
- 44 W. B. Colson, E. D. Johnson, M. J. Kelley, and H. A. Schwettman, *Physics Today* **55** (1), 35 (2002).
- 45 H. P. Freund and G. R. Neil, *Proceedings of the Ieee* **87** (5), 782 (1999).
- 46 *Centre Laser Infrarouge d'Orsay* ([http://clio.lcp.u-psud.fr/clio\\_eng/laserSR.html](http://clio.lcp.u-psud.fr/clio_eng/laserSR.html), 2008).
- 47 I. N. Levine, *Quantum Chemistry*, fourth ed. (Prentice Hall, New Jersey, 1991).
- 48 A. Szabo and N. S. Ostlund, *Modern Quantum Chemistry*. (Dover Publications, 1996).

- 49 J. Simons and J. Nichols, *Quantum Mechanics in Chemistry*. (Oxford University Press, 1997).
- 50 J. B. Foresman and A. Frisch, *Exploring Chemistry with Electronic Structure Methods*, second ed. (Gaussian Inc., Pittsburgh, 1996).
- 51 W. Koch and M. C. Holthausen, *A Chemists Guide to Density Functional Theory*, second ed. (Wiley-VCH, Weinheim, 2001).
- 52 C. Moller and M. S. Plesset, *Physical Review* **46** (7), 0618 (1934).
- 53 P. Hohenberg and W. Kohn, *Physical Review B* **136** (3B), B864 (1964).
- 54 W. Kohn and L. J. Sham, *Physical Review* **140** (4A), 1133 (1965).
- 55 A. D. Becke, *Phys. Rev. A* **38** (6), 3098 (1988).
- 56 C. T. Lee, W. T. Yang, and R. G. Parr, *Physical Review B* **37** (2), 785 (1988).
- 57 A. D. Becke, *J. Chem. Phys.* **104** (3), 1040 (1996).
- 58 B. Miehlich, A. Savin, H. Stoll, and H. Preuss, *Chem. Phys. Lett.* **157** (3), 200 (1989).
- 59 W. D. Allen, Y. Yamaguchi, A. G. Csaszar, D. A. Clabo, R. B. Remington, and H. F. Schaefer, *Chemical Physics* **145** (3), 427 (1990).
- 60 V. Barone, *J. Chem. Phys.* **122** (1), 014108 (2005).
- 61 V. Barone, *J. Chem. Phys.* **120** (7), 3059 (2004).
- 62 D. A. Clabo, W. D. Allen, R. B. Remington, Y. Yamaguchi, and H. F. Schaefer, *Chemical Physics* **123** (2), 187 (1988).
- 63 W. H. Miller, R. Hernandez, N. C. Handy, D. Jayatilaka, and A. Willetts, *Chem. Phys. Lett.* **172** (1), 62 (1990).
- 64 V. Barone, *J. Chem. Phys.* **101** (12), 10666 (1994).
- 65 M. J. Frisch, G. W. Trucks, and H. B. Schlegel *et al.*, *Gaussian 03*, Revision C.02, Inc., Wallingford, CT (2004).
- 66 C. C. J. Roothaan, *Reviews of Modern Physics* **23** (2), 69 (1951).
- 67 A. Schafer, C. Huber, and R. Ahlrichs, *J. Chem. Phys.* **100** (8), 5829 (1994).
- 68 M. Sprik, J. Hutter, and M. Parrinello, *J. Chem. Phys.* **105** (3), 1142 (1996).
- 69 D. Andrae, U. Haussermann, M. Dolg, H. Stoll, and H. Preuss, *Theor. Chim. Acta* **77** (2), 123 (1990).
- 70 T. H. Dunning, *J. Chem. Phys.* **90** (2), 1007 (1989).
- 71 R. Ditchfield, W. J. Hehre, and J. A. Pople, *J. Chem. Phys.* **54** (2), 724 (1971).

### 3. The Spectroscopic Signature of the "All-Surface" to "Internally Solvated" Structural Transition in Water Clusters in the $n=17-21$ Size Regime

*The existence of a transitional size regime where preferential stabilization alternates between "all-surface" (all atoms on the surface of a cluster) and "internally solvated" (one water molecule at the center of the cluster, fully solvated) configurations with the addition or the removal of a single water molecule, predicted earlier with the TTM2-F interaction potential, has been confirmed from electronic structure calculations for  $(\text{H}_2\text{O})_n$ ,  $n=17-21$ . The onset of the appearance of the first "interior" configuration in water clusters occurs for  $n=17$ . This trend was previously predicted by the TTM2-F interaction potential and it is confirmed from electronic structure calculations. The observed structural alternation between "interior" and "all-surface" global minima between  $n = 17-21$  is accompanied by a corresponding spectroscopic signature, namely the undulation in the position of the most red-shifted O–H stretching vibrations according to the trend: "interior" configurations exhibit more red-shifted O–H stretching vibrations than "all-surface" ones. These most red-shifted O–H stretching vibrations form distinct groups in the intramolecular region of the spectra and correspond to localized vibrations of donor O–H stretches that are connected to neighbors via "strong" (water dimmer-like) hydrogen bonds and belong to a water molecule with a "free" O–H stretch.*

#### 3.1 Introduction

In the liquid phase water molecules experience, in average, a homogeneous environment in which they possess a maximum coordination number of surrounding water molecules. The need to maximize hydrogen bonding rather than coordination is the factor that determines the optimal structures of the first few water clusters (small number of water molecules, i.e. small cluster size  $n$ ) in which most, if not all, atoms are located on the surface of the cluster. However, at some point the transition from "all-surface" (all molecules at the surface of the cluster) to "interior" structures (one or more water molecules at the center of the cluster, internally solvated) must occur with growing cluster size.

In an earlier study by Hartke,<sup>1,2</sup> two potentials were applied to calculate minimum structures of the first few water clusters ( $n = 2-30$ ). The rigid, pairwise-additive, four-site transferable intermolecular potential<sup>3</sup> (TIP4P) is parametrized in order to reproduce solution

thermodynamical and structural data, whereas the flexible polarizable (many-body) Thole-type model<sup>4</sup> (TTM2-F) has been fitted solely to cluster (mainly water dimer) data obtained from high level *ab initio* electronic structure calculations. Hartke has found that the two empirical potentials produced global minimum structures that are surprisingly similar up to  $n = 11$  and differ only slightly in the cluster size regime  $n = 12-16$ . For  $n = 17$  and 21 the two empirical potentials produced very different results. The TIP4P potential exhibited all-surface structures as the lowest energy configuration, whereas the TTM2-F yielded an interior structure as the most stable one. However, both potentials agree in the predicted structures for  $n = 18, 19$  and 20 being all-surface, internally solvated, and all-surface, respectively. In summary, the TIP4P potential predicted all-surface global energy minima except for  $n = 19$ , whereas the TTM2-F potential suggested an alternation between internally solvated ( $n = 17, 19, 21$ ) and all-surface ( $n = 18, 20$ ) configurations for the global minimum (cf. Fig. 3.1).

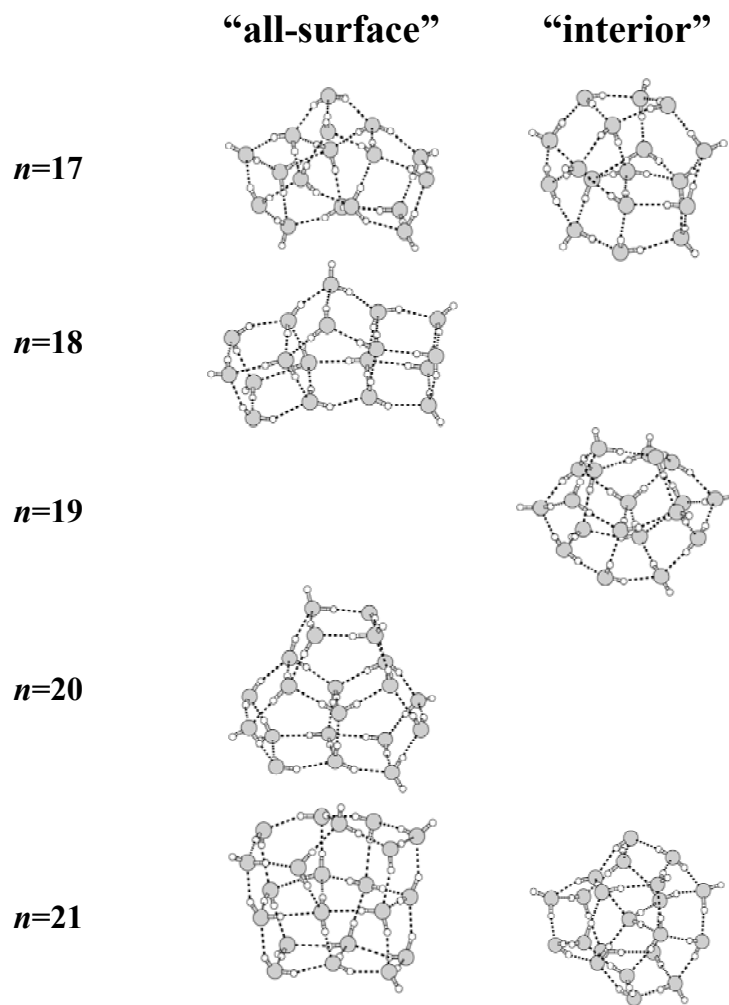


**Figure 3.1:** Minima structures for "all-surface" and "interior" configurations for the  $n = 17-21$  water clusters.



This chapter provides a summary of the major results of the examination of n = 17–21 water clusters with high level ab initio electronic structure calculations. The relative stability of the interior versus all-surface configurations predicted by the empirical potentials will be compared to new ab initio data. Furthermore, the vibrational spectra for the lowest energy structures reveal structure specific features of all-surface and interior type clusters. The results will be presented as an aid for future experimental studies. All results can be found in full detail in Ref. 5.

### 3.2 Summary of the Results

The structures of the global and local minima for the n = 17–21 clusters obtained by Hartke with the TIP4P and TTM2-F potentials were re-optimized at the second order Møller-Plesset perturbation theory (MP2) level with Dunning's augmented correlation-consistent basis sets of double- (aug-cc-pVDZ) and triple- $\zeta$  (aug-cc-pVTZ) quality.<sup>6</sup> Additional geometry optimizations and harmonic frequency calculations were performed at the density functional (DFT) level of theory using the B3LYP functional and Ahlrichs' polarized triple- $\zeta$  basis set.<sup>7</sup> The DFT calculations were performed with the TURBOMOLE program suite,<sup>8</sup> while the MP2 calculations were performed with the NWCHEM suite of codes.<sup>9</sup> A Lorentzian lineshape with a uniform 10 cm<sup>-1</sup> Half-Width at Half-Maximum (HWHM) was used to convolute the stick spectrum to the plotted B3LYP/TZVP frequencies.

#### Relative Stabilities

The calculated energy differences (in kJ mol<sup>-1</sup>) between the all-surface and interior structures,  $\Delta(\Delta E)$ , with the two empirical potentials as well as at the different levels of electronic structure theory (DFT and MP2) for the n = 17 and 21 clusters are listed in Table 3.1. The energy difference is computed with respect to the most stable configuration between the two, which is taken as the zero reference. For n = 17 both MP2 and DFT predict the interior structure to be more stable, which is in agreement with the predictions of the TTM2-F potential. The MP2 energy difference between the two configurations,  $\Delta(\Delta E)$ , is very well reproduced by the TTM2-F potential. At the MP2 level of theory this energy difference decreases with increasing basis set towards the value predicted by the TTM2-F potential. Inclusion of differential zero point energy corrections (1.88 kJ mol<sup>-1</sup> at the B3LYP/TZVP level of theory) furthermore tends to increase the energy difference between the two isomers

in favor of the interior configuration. The best estimate for the energy difference between the two isomers of  $n = 17$  is  $5.99 \text{ kJ mol}^{-1}$  ( $7.87 \text{ kJ mol}^{-1}$  including zero point energy corrections) at the MP2/aug-cc-pVTZ level of theory.

For the  $n = 21$  cluster, a similar behavior was found between the all-surface and the most stable interior isomers. The basis set effect at the MP2 level of theory also results in decreasing the energy difference whereas the inclusion of zero point energy corrections tends to stabilize the interior configuration over the all-surface one. For this case, however, the B3LYP/TZVP result, although predicting the correct ordering of the two isomers, yields an energy difference that is almost twice the one obtained at the MP2/aug-cc-pVTZ level. The TTM2-F potential again predicts the correct ordering by an energy difference that is almost half of the most accurate estimate (MP2/aug-cc-pVTZ). The interior configuration is stabilized by  $15.53 \text{ kJ mol}^{-1}$  ( $17.21 \text{ kJ mol}^{-1}$  including zero point energy corrections) with respect to the all-surface isomer for  $n = 21$ . Zero point corrections for the TIP4P potential are not considered since this potential should somehow implicitly contain those corrections. This is because this potential has been parametrized to produce the experimentally measured enthalpy of vaporization of the liquid at 298 K from classical molecular dynamics simulations (which do not explicitly account for zero point effects).

**Table 3.1:** Energy difference ( $\text{kJ mol}^{-1}$ ) between "all-surface" and "interior" local minima for  $n = 17$  and 21 with empirical potentials and several levels of electronic structure methods. Numbers in parentheses correspond to zero point energy corrected values.

Cluster size		$\Delta(\Delta E) / \text{kJ mol}^{-1}$				
$n$	Configuration	TIP4P	TTM2-F	B3LYP/ TZVP	MP2/aug- cc-pVDZ	MP2/aug- cc-pVTZ
17	all-surface	0	4.69 (6.28)	7.37 (9.25)	7.24 (9.13) <sup>a</sup>	5.99 (7.87) <sup>a</sup>
	interior	2.05	0	0	0	0
21	all-surface	0	7.58 (11.18)	28.97 (30.65)	17.88 (19.55) <sup>a</sup>	15.53 (17.21) <sup>a</sup>
	interior	1.47	0	0	0	0

<sup>a</sup>Using the B3LYP/TZVP zero point energy corrections.

The alternation between all-surface and interior minima at the  $n = 17-21$  cluster size regime predicted by the TTM2-F potential is therefore verified from high level electronic structure calculations. The onset of the first interior configuration occurs at cluster size  $n = 17$ .

### Vibrational Frequencies

In this section the harmonic vibrational spectra of the global minima for the  $n = 17-21$  clusters from electronic structure calculations are presented in order to investigate the spectral features associated with interior vs. all-surface structures. Previous studies<sup>10</sup> of the spectral features of the four major families of minima of  $(\text{H}_2\text{O})_{20}$  have suggested that these dissimilar hydrogen bonding networks are associated with different features in the O–H stretching region of the spectra ( $3000 - 4000 \text{ cm}^{-1}$ ). It is therefore of interest to investigate whether the observed structural alternation between all-surface and interior configurations between  $n = 17-21$  has a corresponding spectral signature.

The three distinct regions corresponding to the intermolecular (with cut-offs around  $1100 \text{ cm}^{-1}$ ), bending ( $\sim 1600 - 1750 \text{ cm}^{-1}$ ) and intramolecular O–H stretching vibrations ( $\sim 2900 - 3900 \text{ cm}^{-1}$ ) are found in the spectra. As noted earlier, this last region corresponding to the intramolecular O–H stretching vibrations is a signature of the underlying hydrogen bonding network and for that reason it will be analyzed further (cf. Fig. 3.2). The complete range of B3LYP/TZVP harmonic frequencies and their IR intensities for  $n = 17-21$  can be found in Ref. 5. It is readily seen that the observed alternation in the structural motif between interior and all-surface configurations in the  $n = 17-21$  clusters is associated with an alternation in the position of the most red-shifted O–H stretching vibrations. Interior configurations exhibit more red-shifted O–H stretching vibrations than all-surface ones. Thus the observed structural alternation between interior and all-surface global minima in this cluster regime has a corresponding spectral signature, namely the undulation in the position of the most red-shifted O–H stretching vibrations. Given this finding it would be of interest to further characterize these most red-shifted vibrations.

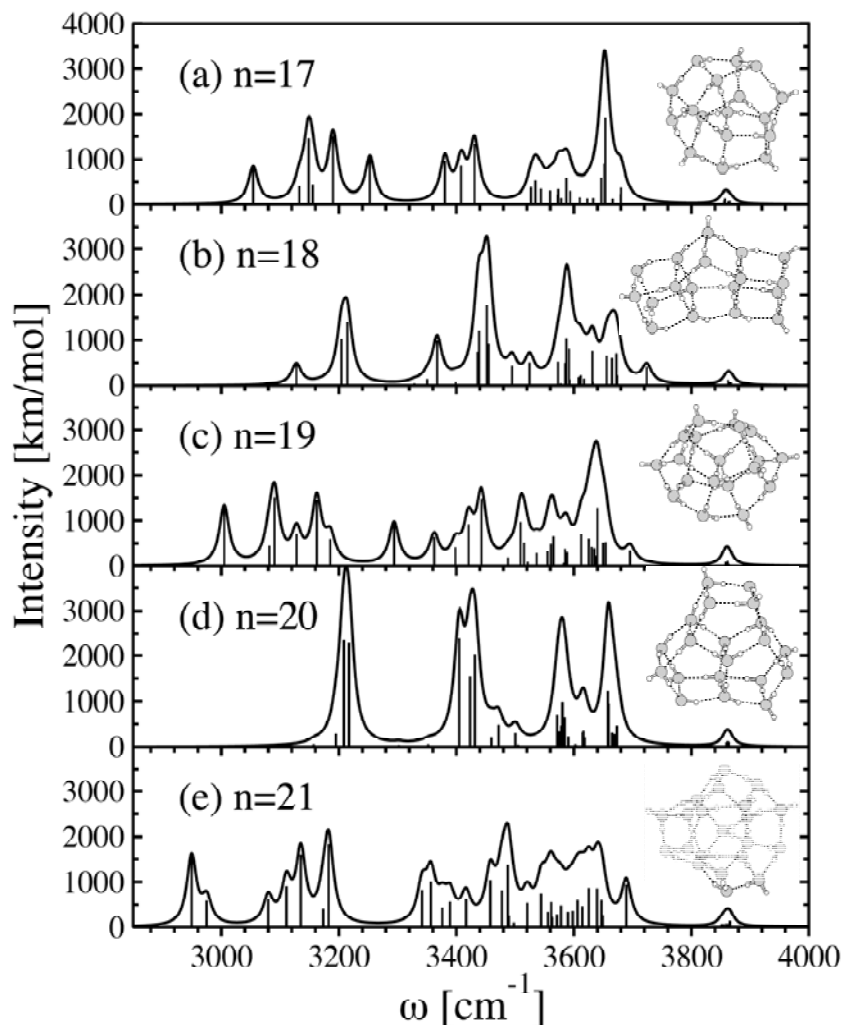


**Figure 3.2:** Calculated harmonic vibrational frequencies of the lowest energy structures for  $n = 17$ – $21$  at the B3LYP/TZVP level of theory.

### Origin of the Most Red-Shifted IR-Active O–H Stretching Vibrations

In a previous study<sup>10</sup> the origin of the most red-shifted IR-active O–H stretching vibrations has been characterized for the four major families of minima of  $(\text{H}_2\text{O})_{20}$ . These families of minima (edge-sharing pentagonal prisms, face-sharing pentagonal prisms, fused cubes and dodecahedron) are associated with very different hydrogen bonding networks which all correspond to all-surface configurations. The most red-shifted IR (hydrogen bonded) O–H vibrations have the following two characteristics which are common for all four different hydrogen bonding networks of  $(\text{H}_2\text{O})_{20}$ . They belong to a water molecule which has a "free", non hydrogen bonded O–H stretch and they act as donors to a neighboring water molecule via a "strong", water dimer-like, hydrogen bond. In the above notation a "strong" hydrogen bond is defined<sup>10</sup> as the one in which the two participating water molecules assume an arrangement reminiscent of the water dimer minimum in which the donor "free" O–H is in

a *trans* conformation with respect to the bisector of the acceptor H–O–H angle. Correspondingly, a "weak" hydrogen bond corresponds to a *cis* conformation. The most red-shifted IR-active O–H stretching vibrations for the  $n = 17-21$  clusters form a distinct group in the 2950 – 3260  $\text{cm}^{-1}$  region of the spectra (cf. Figure 3.2). Since in the context of the previous discussion these groups of the most red-shifted IR-active vibrations are associated with water molecules that have a free O–H stretch, they contain a number of IR-active frequencies that are at most equal to the number of free O–H stretches in each cluster. For a full list of all frequencies and corresponding intensities see Ref. 5.

Exemplarily, in cluster size  $n = 17$  (interior), the normal mode displacements for the six most red-shifted IR-active O–H stretching vibrations of the global minimum of  $n = 17$  are located in the range of 3054 – 3253  $\text{cm}^{-1}$ . Their number is equal to the number of "free" O–H stretches for this structure. In accordance with the findings of an earlier study<sup>11</sup> on the vibrational spectra of the various isomers of  $(\text{H}_2\text{O})_{20}$ , all these 6 vibrations have the two common characteristics that were found before, namely that they are part of a water molecule that has a free O–H stretch and acts as a donor to a neighboring molecule via a strong hydrogen bond. They are all mainly localized on the donor O–H stretch.

### 3.3 Conclusions

A transitional size regime where a structural stabilization between all-surface and interior configurations alternates with the addition or removal of a single water molecule occurs for water clusters at the  $n = 17-21$  size regime. This behavior has been previously suggested based on the results with the TTM2-F interaction potential and it is qualitatively different from the picture that the simpler TIP4P potential suggested. This result has been confirmed from high level electronic structure calculations, which suggest that for  $n = 17$  and 19 the interior configuration is energetically more stable than the all-surface one.

The analysis of the IR spectra in the intramolecular O–H stretching region (3000 – 4000  $\text{cm}^{-1}$ ) reveals that the spectroscopic signature of the favorable structures in the  $n = 17-21$  cluster size regime is accompanied by an undulation in the position of the most red-shifted O–H stretching vibrations. This result is clearly illustrated in Figure 3.3, which depicts the O–H stretching vibrational spectra for the (most stable) interior and (less stable) all-surface minima of  $n = 17$ . For this cluster the range of the O–H stretching vibrations for the interior

configuration extends approximately  $150\text{ cm}^{-1}$  to the red with respect to the ones for the all-surface minimum.

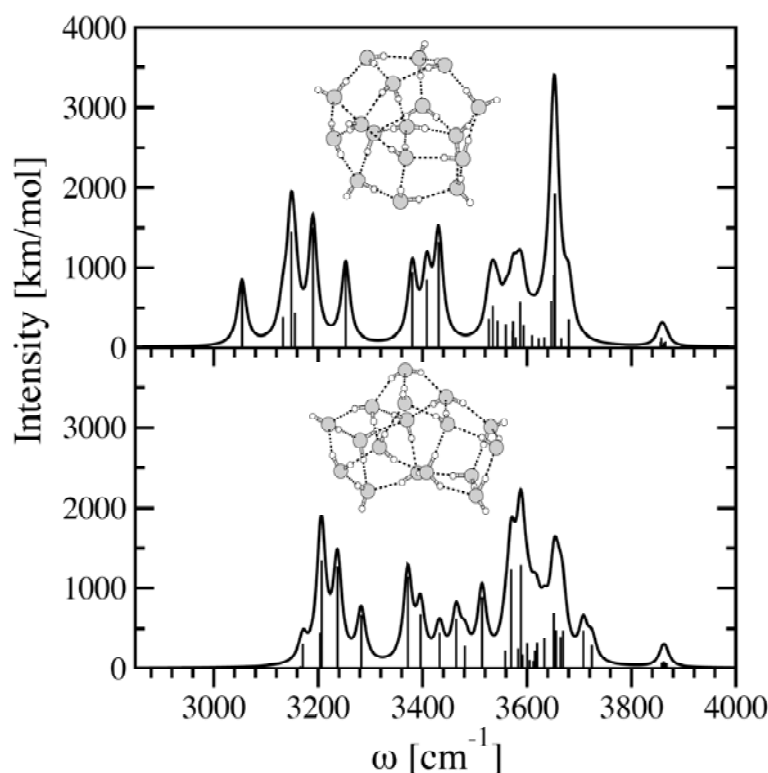


**Figure 3.3:** Comparison between the intramolecular O–H stretching vibrations for the two lowest energy isomers of  $n = 17$  at the B3LYP/TZVP level of theory. Upper panel: Interior global minimum, lower panel: All-surface local minimum.

Further characterization of the group of the most red-shifted vibrations for all clusters confirms previous findings<sup>10</sup> regarding their origin. They are localized vibrations of the hydrogen bonded O–H stretch of a water molecule which acts as a donor to a neighbor via a strong hydrogen bond and which has a “free” O–H stretch.

Recent experimental spectroscopic studies of the IR spectra of the  $\text{H}^+(\text{H}_2\text{O})_n$ ,  $n = 6\text{--}27$  clusters have identified sharp features of the spectra which have been assigned to excitation of the dangling O–H groups.<sup>12</sup> Furthermore it has been observed that this spectral pattern is simplified to a doublet in the  $n = 11\text{--}22$  cluster range, collapses to a single line for  $n = 21$  and  $22$  and reemerges at  $n = 23$ . It is therefore hoped that the results and spectral analysis of this present study can assist in the future experimental (spectroscopic) confirmation of this structural transition between all-surface and interior configurations in neutral water clusters.

### 3.4 References

- <sup>1</sup> B. Hartke, *European Physical Journal D* **24** (1-3), 57 (2003).
- <sup>2</sup> B. Hartke, *Phys. Chem. Chem. Phys.* **5** (2), 275 (2003).
- <sup>3</sup> W. L. Jorgensen, J. Chandrasekhar, J. D. Madura, R. W. Impey, and M. L. Klein, *J. Chem. Phys.* **79** (2), 926 (1983).
- <sup>4</sup> B. T. Thole, *Chem. Phys.* **59** (3), 341 (1981).
- <sup>5</sup> A. Lagutschenkov, G. S. Fanourgakis, G. Niedner-Schatteburg, and S. S. Xantheas, *J. Chem. Phys.* **122** (19), 194310 (2005).
- <sup>6</sup> T. H. Dunning, *J. Chem. Phys.* **90** (2), 1007 (1989).
- <sup>7</sup> A. Schafer, C. Huber, and R. Ahlrichs, *J. Chem. Phys.* **100** (8), 5829 (1994).
- <sup>8</sup> R. Ahlrichs, M. Bar, M. Haser, H. Horn, and C. Kolmel, *Chem. Phys. Lett.* **162** (3), 165 (1989).
- <sup>9</sup> R. A. Kendall, E. Apra, D. E. Bernholdt, E. J. Bylaska, M. Dupuis, G. I. Fann, R. J. Harrison, J. L. Ju, J. A. Nichols, J. Nieplocha, T. P. Straatsma, T. L. Windus, and A. T. Wong, *Comput. Phys. Commun.* **128** (1-2), 260 (2000).
- <sup>10</sup> G. S. Fanourgakis, E. Apra, W. A. de Jong, and S. S. Xantheas, *J. Chem. Phys.* **122** (13) (2005).
- <sup>11</sup> G. S. Fanourgakis, G. K. Schenter, and S. S. Xantheas, *Abstracts of Papers of the American Chemical Society* **229**, U747 (2005).
- <sup>12</sup> J. W. Shin, N. I. Hammer, E. G. Diken, M. A. Johnson, R. S. Walters, T. D. Jaeger, M. A. Duncan, R. A. Christie, and K. D. Jordan, *Science* **304** (5674), 1137 (2004).





#### 4. Infrared Spectrum of $\text{NH}_4^+(\text{H}_2\text{O})$ : Evidence for Mode Specific Fragmentation

The gas phase infrared spectrum ( $3250$  to  $3810\text{ cm}^{-1}$ ) of the singly hydrated ammonium ion,  $\text{NH}_4^+(\text{H}_2\text{O})$ , has been recorded by action spectroscopy of mass selected and isolated ions. The four bands obtained are assigned to N–H stretching modes and to O–H stretching modes, respectively. The N–H stretching modes observed are blueshifted with respect to the corresponding modes of the free  $\text{NH}_4^+$  ion, whereas a redshift is observed with respect to the modes of the free  $\text{NH}_3$  molecule. The O–H stretching modes observed are redshifted when compared to the free  $\text{H}_2\text{O}$  molecule. The asymmetric stretching modes give rise to rotationally resolved perpendicular transitions. The K-type equidistant rotational spacings of  $11.1(2)\text{ cm}^{-1}$  ( $\text{NH}_4^+$ ) and  $29(3)\text{ cm}^{-1}$  ( $\text{H}_2\text{O}$ ) deviate systematically from the corresponding values of the free molecules, a fact which is rationalized in terms of a symmetric top analysis. The relative band intensities recorded compare favorably with predictions of high level *ab initio* calculations – except on the  $\nu_3(\text{H}_2\text{O})$  band for which the observed value is about 20 times weaker than the calculated one. The  $\nu_3(\text{H}_2\text{O})/\nu_1(\text{H}_2\text{O})$  intensity ratios from other published action spectra in other cationic complexes vary such that the  $\nu_3(\text{H}_2\text{O})$  intensities become smaller, the stronger the complexes are bound. The recorded ratios vary, in particular among the data collected from action spectra that were recorded with and without rare gas tagging. The calculated anharmonic coupling constants in  $\text{NH}_4^+(\text{H}_2\text{O})$  further suggest that the coupling of the  $\nu_3(\text{H}_2\text{O})$  and  $\nu_1(\text{H}_2\text{O})$  modes to other cluster modes indeed varies by orders of magnitude. These findings together render a picture of a mode specific fragmentation dynamic that modulates band intensities in action spectra with respect to absorption spectra. Additional high-level electronic structure calculations at the coupled-cluster single and double, with perturbative treatment of triple excitations [CCSD(T)] level of theory with large basis sets, allow for the determination of an accurate binding energy and enthalpy of the  $\text{NH}_4^+(\text{H}_2\text{O})$  cluster. Our extrapolated values at the CCSD(T) complete basis set (CBS) limit are  $\Delta H^{(0\text{ K})}(\text{NH}_4^+-(\text{H}_2\text{O})) = -85.40(\pm 0.24)\text{ kJ/mol}$  and  $\Delta H^{(298\text{ K})}(\text{NH}_4^+-(\text{H}_2\text{O})) = -78.1(\pm 0.3)\text{ kJ/mol}$ , in which double standard deviations are indicated in parentheses.

## 4.1 Introduction

The development of experimental vibrational spectroscopy techniques such as IRPD and IRMPD (infrared photodissociation and infrared multiphoton dissociation) facilitates the study of molecules in the gas phase which would otherwise not be possible due to low number densities. Photodissociation spectra are realized by the combination of two classical methods, namely IR laser spectroscopy and mass spectrometry (cf. Chapter 2).

In recent years, a large number of experimental IRPD and IRMPD studies – as well as calculated absorption spectra based on ab initio methods – of cationic ion-molecule-clusters has been published (Refs. 1-26). It is noticeable that oftentimes a discrepancy appears between the relative band intensities of the experimental and the calculated spectra. For example in  $\text{NH}_4^+(\text{H}_2\text{O})$  the experimental intensity ratio of  $\nu_3(\text{H}_2\text{O})/\nu_1(\text{H}_2\text{O})$  of the O–H stretching bands is significantly lower as compared to both the calculated ratios and to the free water molecule (which was not expected in the first place and will be discussed in more detail below).

In the early 1990s, the ionic hydrogen bonded system  $\text{NH}_4^+(\text{H}_2\text{O})$  has been measured by G. Niedner-Schatteburg in the group of Y.- T. Lee. Due to non-sufficient compute performance at that time a complete interpretation backed up by high level quantum chemical calculations on a sufficient level of theory was not feasible. In 2005, we continued with the interpretation of the measurements of  $\text{NH}_4^+(\text{H}_2\text{O})$ . The first part of the quantum chemical calculations (geometry optimization, evaluation of the strength of the hydrogen bond at the complete basis set limit (CBS limit) on CC2 level of theory, rotational spacings within the vibrational bands and relative intensities of the vibrational bands) can be found in full detail in the diploma thesis of T. Pankewitz.<sup>27</sup> The calculation of the CBS limit of the binding energy on CCSD(T) level of theory and anharmonic frequencies based on the VPT2 approach were provided by S. S. Xantheas.<sup>1</sup>

In this thesis the main results of the joint work on  $\text{NH}_4^+(\text{H}_2\text{O})$  will be briefly summarized. In addition to the already published data (see Ref. 1), this work will present the potential energy curve of the main dissociation coordinate, the N–H stretching mode in  $\text{NH}_4^+(\text{H}_2\text{O})$ , which points out the anharmonic character of the N–H stretching mode within the hydrogen bond. Furthermore, a visualization of the collected data on ion-molecule-clusters from the literature will be provided and discussed with respect to the phenomenon of the mode specific fragmentation yields.

## 4.2 Summary of the Results

### Assignment

As presented in the preceding abstract, the photofragmentation (photodissociation) spectrum of  $\text{NH}_4^+(\text{H}_2\text{O})$  has been recorded in the region of 3250 to 3810  $\text{cm}^{-1}$ . Within this frequency range, four vibrational bands have been obtained which are pairwise assigned to the symmetric ( $\nu_1$ ) and asymmetric ( $\nu_3$ ) stretching bands of N–H and O–H (cf. Fig. 4.1). The bands show decreasing intensities towards higher energies. The widths of all four bands vary considerably. The bands centered at 3278 ( $\nu_1(\text{NH}_4^+)$ ) and 3610  $\text{cm}^{-1}$  ( $\nu_1(\text{H}_2\text{O})$ ) are about 50  $\text{cm}^{-1}$  wide. The second band at about 3370  $\text{cm}^{-1}$  ( $\nu_3(\text{NH}_4^+)$ ) is spread out over more than 100  $\text{cm}^{-1}$ . It partly overlaps with the neighboring band. The total width of the low intensity structure around 3700  $\text{cm}^{-1}$  ( $\nu_3(\text{H}_2\text{O})$ ) is uncertain due to its poor statistics. Nevertheless, resolvable features are more than 100  $\text{cm}^{-1}$  apart.

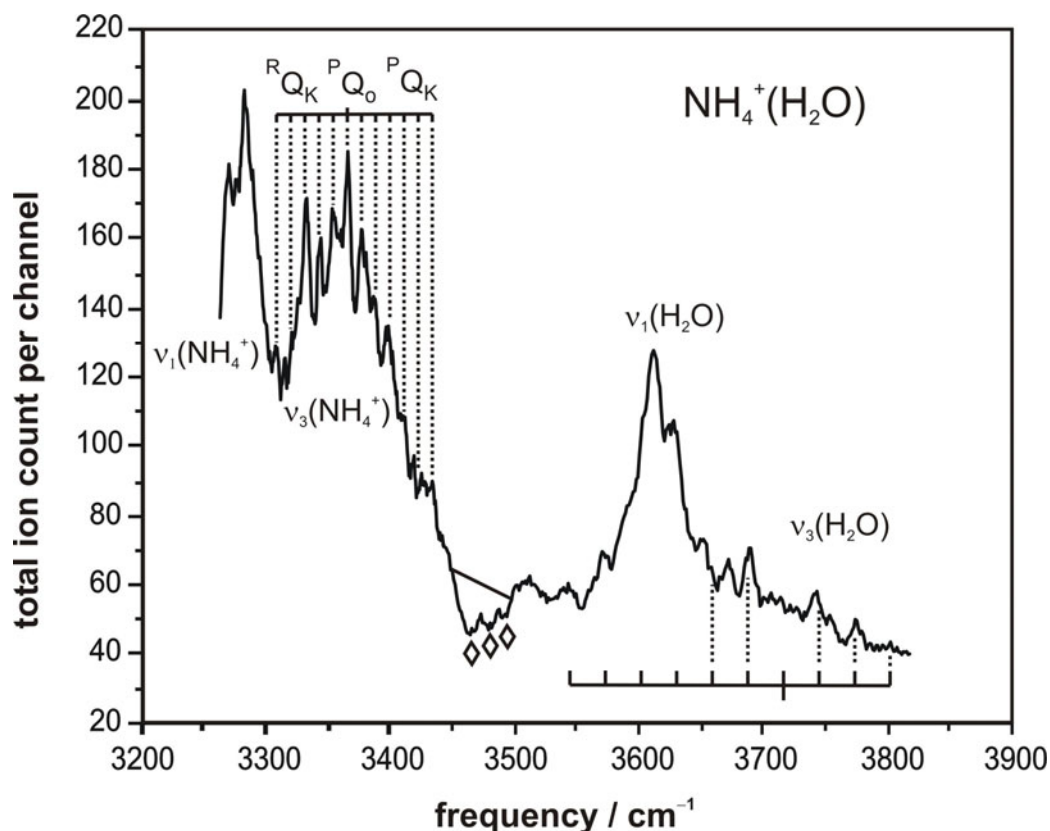


**Figure 4.1:** Experimental photodissociation spectrum of  $\text{NH}_4^+(\text{H}_2\text{O})$  in the spectral range of 3250 to 3810  $\text{cm}^{-1}$ . Diamonds  $\diamond$  label known impurities in the  $\text{LiNbO}_3$  crystal which were used for calibration of the spectrum.

### Geometry and Dissociation Enthalpy

The calculation of the structure of  $\text{NH}_4^+(\text{H}_2\text{O})$  has been performed on different levels of theory, MP2, CC2 and CCSD(T) and B3LYP, each with various basis sets. The notation  $\text{NH}_4^+(\text{H}_2\text{O})$  already implies the main geometrical feature, namely that the cluster consists of two subunits,  $\text{NH}_4^+$  and  $\text{H}_2\text{O}$ . These subunits are connected via a single hydrogen bond (cf. left inset in Fig. 4.2). The equilibrium structure of the  $\text{NH}_4^+(\text{H}_2\text{O})$  complex has two hydrogen atoms arranged eclipsically towards each other defining an angle of torsion  $\text{H}-\text{N}\cdots\text{O}-\text{H}$  of zero degrees. There is practically no rotational barrier when changing this angle to another value. Due to energetic reasons, a bisectonal structure containing two hydrogen atoms of the  $\text{NH}_4^+$  pointing towards the oxygen atom can be ruled out. The same holds true for another conceivable structure with the same stoichiometry which would be the  $\text{NH}_3(\text{H}_3\text{O})^+$  molecule. Bond lengths within the cluster are found to be more dependent on method and basis set than the binding energy of the hydrogen bond is. For all details see Refs. 1,27. Here, it is important to note that the usage of basis sets with diffuse functions is necessary for the correct description of the hydrogen bonded system.

The best values of the binding energies are determined on CCSD(T) level of theory yielding extrapolated values at the CBS limit of  $\Delta H^{(0\text{ K})}(\text{NH}_4^+-\text{H}_2\text{O}) = -85.40(\pm 0.24)$  kJ/mol and  $\Delta H^{(298\text{ K})}(\text{NH}_4^+-\text{H}_2\text{O}) = -78.1(\pm 0.3)$  kJ/mol. Double standard deviations are indicated in parantheses.

### Band Shifts, Band Positions and Anharmonic Frequencies

The comparison of the experimental spectrum of  $\text{NH}_4^+(\text{H}_2\text{O})$  with spectra of the free ammonium ion show a blueshift of the N–H stretch modes in the cluster. In contrast, the intramolecular  $\text{H}_2\text{O}$  modes shift to the red upon complexation with  $\text{NH}_4^+$  compared to the free  $\text{H}_2\text{O}$  molecule. The same behaviour is observed in the calculated spectra.

Calculation of the harmonic frequencies of  $\text{NH}_4^+(\text{H}_2\text{O})$  on RI-MP2/aug-cc-pVTZ level of theory (scaled with a factor  $f = 0.953$ ) provide blueshifts of  $56\text{ cm}^{-1}$  and  $24\text{ cm}^{-1}$  for the symmetric and asymmetric N–H stretching modes, respectively, compared to the calculated values of  $\text{NH}_4^+$ . The calculated redshifts of the O–H bands in  $\text{NH}_4^+(\text{H}_2\text{O})$  are  $-23\text{ cm}^{-1}$  and  $-58\text{ cm}^{-1}$  for the symmetric and asymmetric stretching modes with respect to the calculated ones of the water molecule.

At RI-MP2/aug-cc-pVTZ level of theory, we observe a very good agreement between the experimental and the calculated band positions when scaling the calculated frequencies with a standard factor of  $f = 0.953$ . Using the VPT2 approach for the calculation of

anharmonically corrected band positions on MP2-FC/aug-cc-pVDZ level of theory yields an even better agreement. The most significant deviation between both approaches lies in the calculation of the bound N–H stretch. Here the VPT2 approach is believed to yield significantly better results due to the anharmonic character of the potential energy curve of the N–H stretching mode within the hydrogen bond (displayed in Fig. 4.2). Unfortunately, the spectral range of the experiment does not reach down to  $2500\text{ cm}^{-1}$  where the bound N–H stretch is predicted to appear in the spectrum. This has to be verified in future experiments.

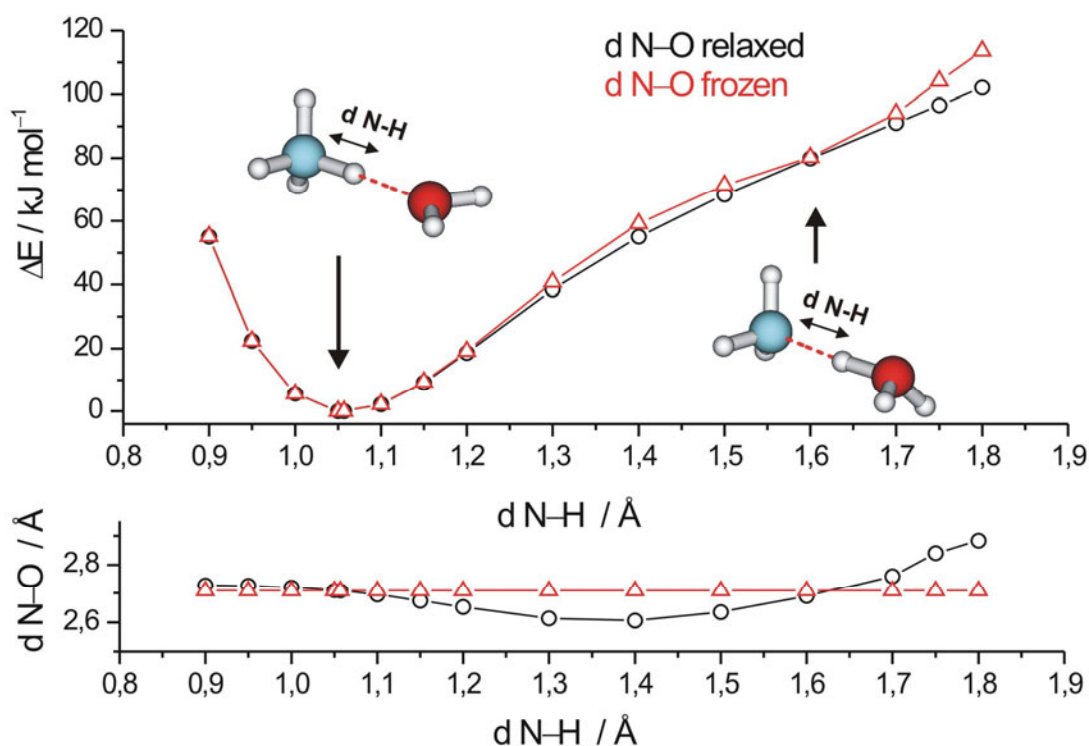


**Figure 4.2:** Potential energy curve of  $\text{NH}_4^+(\text{H}_2\text{O})$  along the N–H distance on MP2/aug-cc-pVDZ level of theory. Black curve: The N–H distance is frozen, while all other coordinates are allowed to relax in the course of the geometry optimization. Red curve: The N–H and the N–O distance are frozen.

### Rotational Spacings

Based on ab initio calculations, the rotational spacings within the  $\nu_3$  vibrational bands of  $\text{NH}_4^+(\text{H}_2\text{O})$  have been evaluated in terms of a symmetric top analysis.<sup>1,27</sup> The experimentally evaluated  $K$ -type equidistant rotational spacings are  $11.1(2)\text{ cm}^{-1}$  ( $\text{NH}_4^+$ ) and  $29(3)\text{ cm}^{-1}$  ( $\text{H}_2\text{O}$ ).<sup>1</sup> The values calculated on the RI-CC2/aug-cc-pVQZ level of theory are  $11.72\text{ cm}^{-1}$  and  $27.97\text{ cm}^{-1}$ . Those calculated with DFT on B3LYP/aug-cc-pVQZ level are  $11.67\text{ cm}^{-1}$  and  $27.57\text{ cm}^{-1}$ . Both quantum chemical methods underestimate the rotational spacings compared to the experimental values. Taking into account that both the experimental

and theoretical values are afflicted with a certain error (e.g. up to 10 % in case of the experimental value of  $\text{H}_2\text{O}$  within  $\text{NH}_4^+(\text{H}_2\text{O})$ ) the agreement justifies the interpretation in terms of a symmetric top analysis.

### Vibrations and their Relative Intensities

As mentioned in the introduction, a series of photofragmentation spectra of singly hydrated cations have revealed an small or inverse intensity ratio of  $I(\nu_3)$  to  $I(\nu_1)$  of  $\text{H}_2\text{O}$  within the clusters as compared to the intensity ratio of sole  $\text{H}_2\text{O}$ . It is only through argon or  $\text{N}_2$  tagging that the asymmetric stretch mode  $\nu_3$  regains an equal or even higher intensity than the symmetric stretch mode  $\nu_1$ . The ratio  $I(\nu_3)/I(\nu_1)$  in the experimental photofragmentation spectrum of  $\text{NH}_4^+(\text{H}_2\text{O})$  is 1:9, which means that the  $\nu_1(\text{H}_2\text{O})$  band is nine times as strong as the  $\nu_3(\text{H}_2\text{O})$  band. This is anything but obvious, as the  $\nu_3(\text{H}_2\text{O})$  is expected to be strongly infrared active and the intensity ratio in gaseous water is 14.5-18 in favor of the  $\nu_3(\text{H}_2\text{O})$  band.

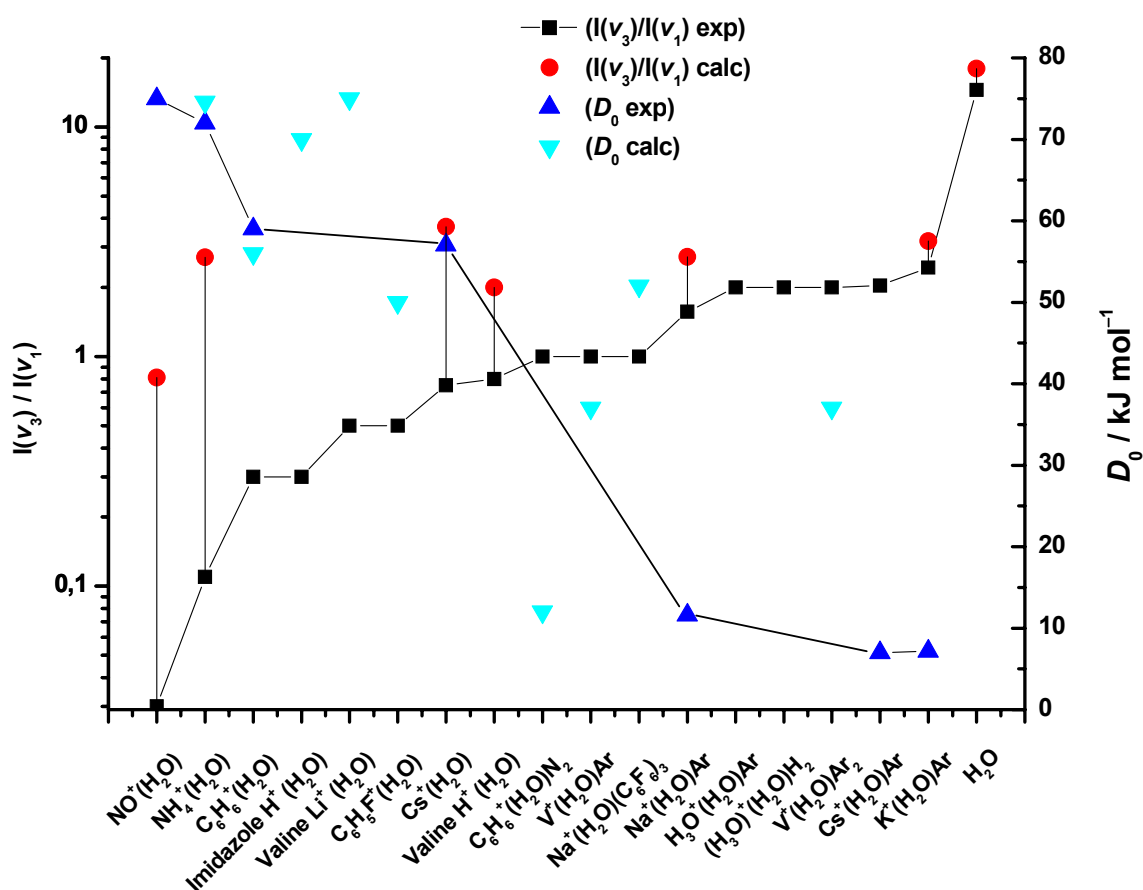


**Figure 4.3:** The ratio of  $\nu_3(\text{H}_2\text{O})$  to  $\nu_1(\text{H}_2\text{O})$  intensities from action spectra as compared to the enthalpy change along the lowest dissociation path – taken as the corresponding cluster binding energy – within various cation water complexes. The infrared absorption intensity ratio of isolated water molecules is included for comparison. A list of the used values and references can be found in Table 4.1.

**Table 4.1:** Ratio of  $\nu_3(\text{H}_2\text{O})$  to  $\nu_1(\text{H}_2\text{O})$  intensities from action spectra as compared to the enthalpy change along the lowest dissociation path – taken as the corresponding cluster binding energy – within various cation water complexes.

Species	$I(\nu_3) / I(\nu_1)$		Binding energies (kJ/mol)	
	Expt.	Calc.	Expt. $D_0$ (300 K)	Calc. $D_0$ (0 K)
$\text{NO}^+(\text{H}_2\text{O})$	$\sim 0^a$	0.81 <sup>a</sup>	75 <sup>b</sup> 81 <sup>c</sup>	
$\text{NH}_4^+(\text{H}_2\text{O})$	0.11 <sup>d</sup>	2.71 <sup>d</sup>	72.0 <sup>e</sup> 72.4 <sup>g</sup> 83.3, 86.2 <sup>i</sup>	74.6 <sup>f</sup> 78.2(1) <sup>h</sup>
$\text{H}_3\text{O}^+(\text{H}_2\text{O})(\text{H}_2)_{1,2}$	$\sim 2^j$			
$\text{H}_3\text{O}^+(\text{H}_2\text{O})\text{Ar}$	$\sim 2^k$			
$\text{Na}^+(\text{H}_2\text{O})\text{Ar}$	1.57 <sup>l</sup>	2.72 <sup>m</sup>	11.6 <sup>l</sup>	
$\text{Na}^+(\text{H}_2\text{O})(\text{C}_6\text{F}_6)_3$	$\sim 1^n$			52(8) <sup>n</sup>
$\text{K}^+(\text{H}_2\text{O})\text{Ar}$	2.44 <sup>l</sup>	3.19 <sup>m</sup>	7.2 <sup>l</sup>	
$\text{Cs}^+(\text{H}_2\text{O})$	$\sim 0.5 - 1^o$	3.68 <sup>m</sup>	57 <sup>p</sup>	
$\text{Cs}^+(\text{H}_2\text{O})\text{Ar}$	2.04 <sup>l</sup>		7 <sup>l</sup>	
$\text{V}^+(\text{H}_2\text{O})\text{Ar}$	$\sim 1^q$			37 <sup>r</sup>
$\text{V}^+(\text{H}_2\text{O})\text{Ar}_2$	$\sim 2^q$			37 <sup>r</sup>
$\text{C}_6\text{H}_6^+(\text{H}_2\text{O})$	$\sim 0.3^s$		59(12) <sup>s</sup>	36 – 56 <sup>s</sup>
$\text{C}_6\text{H}_6^+(\text{H}_2\text{O})\text{N}_2$	$\sim 1^s$			$< 12^s$
$\text{C}_6\text{H}_5\text{F}^+(\text{H}_2\text{O})$	$\sim 0.5^t$			50 <sup>t</sup>
Imidazole $\text{H}^+(\text{H}_2\text{O})$	$\sim 0.3^u$			70(3) <sup>u</sup>
Valine $\text{H}^+(\text{H}_2\text{O})$	$\sim 0.8^v$	$\geq 2^v$		
Valine $\text{Li}^+(\text{H}_2\text{O})$	$< 0.5^v$			75 <sup>v</sup>
$\text{H}_2\text{O}$	$\sim 14.53^w$	13.86 <sup>d</sup> 18 <sup>x</sup>	n.a.	n.a.

<sup>a</sup>No  $\nu_3$  band observed in action spectrum, reference 6.<sup>b</sup>Reference 4.<sup>c</sup>Reference 5.<sup>d</sup>This work.<sup>e</sup>Reference 7.<sup>f</sup>Reference 8.<sup>g</sup>Reference 9 and references therein.<sup>h</sup>CC2/CBS-limit, this work.<sup>i</sup>Reference 52.<sup>j</sup>Ratio estimated from Refs. 11 and 12.

<sup>k</sup>Ratio estimated from Refs. 13,14.

<sup>l</sup>Reference 15.

<sup>m</sup>Reference 16.

<sup>n</sup>References 17,18.

<sup>o</sup>Reference 19.

<sup>p</sup>Reference 20.

<sup>q</sup>Reference 21.

<sup>r</sup>Reference 18.

<sup>s</sup>Reference 28 and references therein.

<sup>t</sup>Reference 23 and references therein.

<sup>u</sup>Ratio estimated from Ref. 3 and references therein.

<sup>v</sup>Ratio estimated from Ref. 24 and references therein.

<sup>w</sup>Reference 25.

<sup>x</sup>Reference 26.

Figure 4.3 nicely shows the anti-correlation of the cluster binding energy and the fragmentation yields in various singly hydrated cations (the data visualized in Fig. 4.3 are taken from Table 4.1). Systems with higher binding energies only show small intensity ratios  $I(\nu_3)/I(\nu_1)$ . This is partly due to an increase in intensity of the symmetric  $\nu_1$  mode, but it cannot be the sole explanation. In the extreme case of  $\text{NO}^+(\text{H}_2\text{O})$  the  $\nu_3$  band is completely missing. Intensity ratios  $I(\nu_3)/I(\nu_1)$  closer to the one in the sole  $\text{H}_2\text{O}$  molecule are only observed in systems with very low binding energies in the dissociation coordinate. Thus it is no surprise to observe an increase of the  $I(\nu_3)/I(\nu_1)$  ratio in rare gas (mostly argon) tagged systems. Nevertheless, the intensity ratios of those systems are still about one order of magnitude smaller compared to those of  $\text{H}_2\text{O}$ .

To explain this mode specific fragmentation, two main reasons are under discussion. The first effect may be due to large anharmonicities in the  $\nu_3$  mode. Anharmonicities may reduce multiphoton absorption as overtone absorption is out of resonance. It is pointed out that this effect is stronger for the  $\nu_3(\text{H}_2\text{O})$  than for the  $\nu_1(\text{H}_2\text{O})$  mode. Nevertheless, our computed anharmonic overtone and absorption levels in  $\text{NH}_4^+(\text{H}_2\text{O})$  provide comparable magnitudes for the 'anharmonic walk-off' in both the  $\nu_3(\text{H}_2\text{O})$  and the  $\nu_1(\text{H}_2\text{O})$  band. Thus it is questionable if this phenomenon really explains the darkness (or decrease of intensity) of the  $\nu_3(\text{H}_2\text{O})$  band. The second reason may lie in different time scales for the intramolecular vibrational relaxation (IVR) when exciting the  $\nu_3(\text{H}_2\text{O})$  or  $\nu_1(\text{H}_2\text{O})$  modes. The motion of the oxygen atom is quite different when exciting the symmetric or the asymmetric stretching mode. Excitation of the symmetric stretching involves a motion of the oxygen atom parallel to the dissociation coordinate, while in case of excitation of the asymmetric stretch the oxygen atom moves perpendicular to the hydrogen bond (which is the most probable dissociation coordinate except for rare gas tagged systems). The coupling to other cluster modes therefore is considered to be more effective for  $\nu_1$  excitations. At the same time this may result in the  $\nu_3$



excitation failing to induce fast fragmentation due to the limited time scale of typical experiments.

To fully explain these findings, further studies of the dynamical couplings of single water molecules to atomic or molecular ions and determination of the IVR mechanisms would be needed.

### 4.3 References

- <sup>1</sup> T. Pankewitz, A. Lagutschenkov, G. Niedner-Schatteburg, S. S. Xantheas, and Y. T. Lee, *J. Chem. Phys.* **126** (7), 074307/1 (2007).
- <sup>2</sup> A. A. Adesokan, G. M. Chaban, O. Dopfer, and R. B. Gerber, *J. Phys. Chem. A* **111** (31), 7374 (2007).
- <sup>3</sup> H. S. Andrei, N. Solca, and O. Dopfer, *ChemPhysChem* **7** (1), 107 (2006).
- <sup>4</sup> M. A. French, L. P. Hills, and P. Kebarle, *Canadian Journal of Chemistry-Revue Canadienne De Chimie* **51** (3), 456 (1973).
- <sup>5</sup> N. A. Burdett and A. N. Hayhurst, *Journal of the Chemical Society-Faraday Transactions I* **78**, 2997 (1982).
- <sup>6</sup> J. H. Choi, K. T. Kuwata, B. M. Haas, Y. B. Cao, M. S. Johnson, and M. Okumura, *J. Chem. Phys.* **100** (10), 7153 (1994).
- <sup>7</sup> J. D. Payzant, Cunningham, A. J., and P. Kebarle, *Canadian Journal of Chemistry-Revue Canadienne De Chimie* **51** (19), 3242 (1973).
- <sup>8</sup> J. C. Jiang, H. C. Chang, Y. T. Lee, and S. H. Lin, *J. Phys. Chem. A* **103** (16), 3123 (1999).
- <sup>9</sup> P. Kebarle, *Annu. Rev. Phys. Chem.* **28**, 445 (1977).
- <sup>10</sup> M. Meotner, *J. Am. Chem. Soc.* **106** (5), 1265 (1984).
- <sup>11</sup> M. Okumura, L. I. Yeh, J. D. Myers, and Y. T. Lee, *J. Phys. Chem.* **94** (9), 3416 (1990).
- <sup>12</sup> L. I. Yeh, M. Okumura, J. D. Myers, J. M. Price, and Y. T. Lee, *J. Chem. Phys.* **91** (12), 7319 (1989).
- <sup>13</sup> J. M. Headrick, E. G. Diken, R. S. Walters, N. I. Hammer, R. A. Christie, J. Cui, E. M. Myshakin, M. A. Duncan, M. A. Johnson, and K. D. Jordan, *Science* **308** (5729), 1765 (2005).

- <sup>14</sup> E. G. Diken, J. M. Headrick, J. R. Roscioli, J. C. Bopp, M. A. Johnson, and A. B. McCoy, *J. Phys. Chem. A* **109** (8), 1487 (2005).
- <sup>15</sup> D. Lessen and P. J. Brucat, *J. Chem. Phys.* **91** (8), 4522 (1989).
- <sup>16</sup> D. Feller, E. D. Glendening, D. E. Woon, and M. W. Feyereisen, *J. Chem. Phys.* **103** (9), 3526 (1995).
- <sup>17</sup> G. N. Patwari and J. M. Lisy, *J. Phys. Chem. A* **107** (45), 9495 (2003).
- <sup>18</sup> G. N. Patwari and J. M. Lisy, *J. Chem. Phys.* **118** (19), 8555 (2003).
- <sup>19</sup> C. J. Weinheimer and J. M. Lisy, *J. Chem. Phys.* **105** (7), 2938 (1996).
- <sup>20</sup> I. Dzidic and P. Kebarle, *J. Phys. Chem.* **74** (7), 1466 (1970).
- <sup>21</sup> N. R. Walker, R. S. Walters, E. D. Pillai, and M. A. Duncan, *J. Chem. Phys.* **119** (20), 10471 (2003).
- <sup>22</sup> M. Polak, M. Gruebele, B. W. Dekock, and R. J. Saykally, *Mol. Phys.* **66** (6), 1193 (1989).
- <sup>23</sup> U. Lorenz, N. Solca, and O. Dopfer, *Chem. Phys. Lett.* **406** (4-6), 321 (2005).
- <sup>24</sup> A. Kamariotis, O. V. Boyarkin, S. R. Mercier, R. D. Beck, M. F. Bush, E. R. Williams, and T. R. Rizzo, *J. Am. Chem. Soc.* **128** (3), 905 (2006).
- <sup>25</sup> L. S. Rothman, R. R. Gamache, R. H. Tipping, C. P. Rinsland, M. A. H. Smith, D. C. Benner, V. M. Devi, J. M. Flaud, C. Camypeyret, A. Perrin, A. Goldman, S. T. Massie, L. R. Brown, and R. A. Toth, *J. Quant. Spectrosc. Radiat. Transfer* **48** (5-6), 469 (1992).
- <sup>26</sup> B. Galabov, Y. Yamaguchi, R. B. Remington, and H. F. Schaefer, *J. Phys. Chem. A* **106** (5), 819 (2002).
- <sup>27</sup> T. Pankewitz, Ab initio Studie des Systems  $\text{NH}_4^+\text{H}_2\text{O}$ : Interpretation des Photodissoziationsspektrums, Diplomarbeit, Technische Universität Kaiserslautern, 2005.
- <sup>28</sup> N. Solca and O. Dopfer, *J. Phys. Chem. A* **107** (20), 4046 (2003).

## 5. Beyond the Harmonic Approach: Calculation of Anharmonic Frequencies of Protonated and Deprotonated Dicarboxylic Acid Homologues, from Oxalic Acid to Adipic Acid

### 5.1 Introduction

Saturated dicarboxylic acids are described by the general structure  $\text{HOOC}-(\text{CH}_2)_n-\text{COOH}$ . Dicarboxylic acids are key precursors in industrial manufacturing of polymeric substances. Adipic acid is an important precursor in the production of polyamides, e.g. nylon, and other polyesters and polyurethanes. The smallest dicarboxylic acid, the oxalic acid, is amongst others used as a bleaching agent for wood.

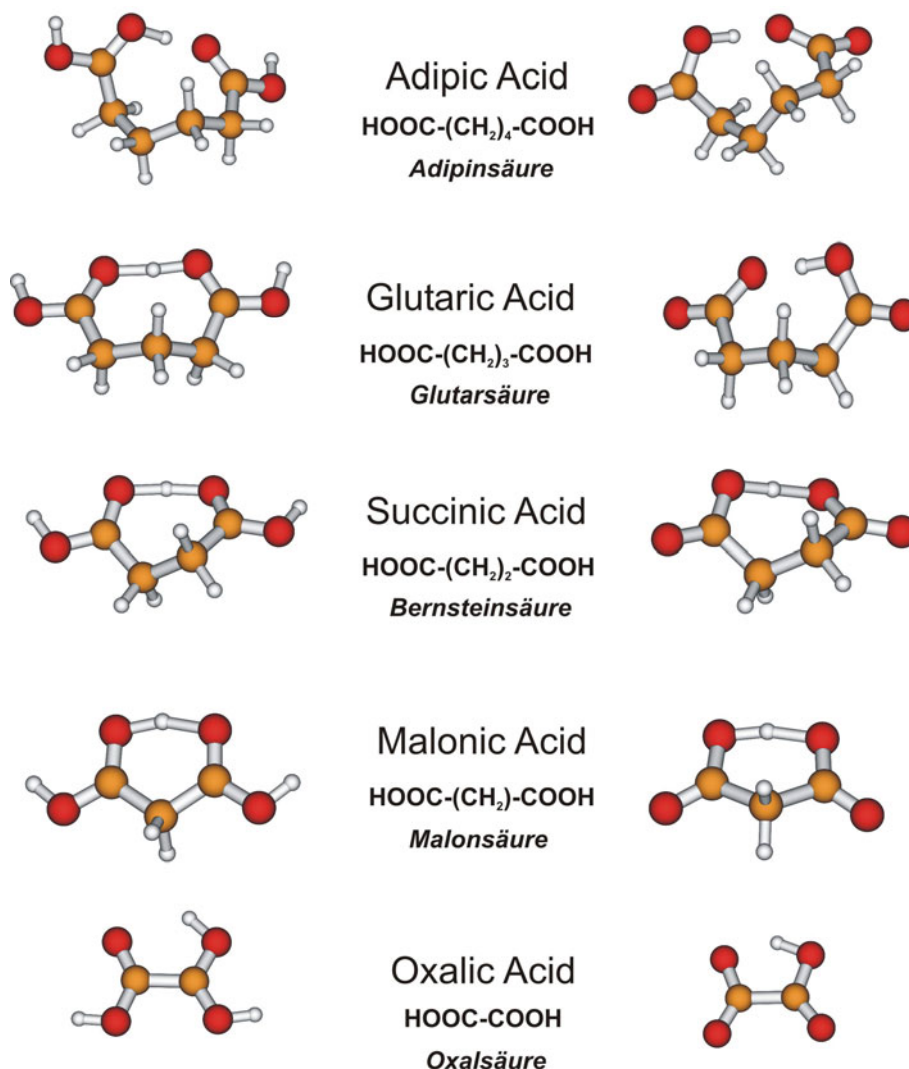


**Figure 5.1:** General structural motif of the energetically most favored protonated (left column) and deprotonated (right column) dicarboxylic acids. All protonated structures share the common feature of O–H groups, in which the hydrogen atoms point towards the direction of the intramolecular proton bridge.

Dicarboxylic acids are abundant species in aerosols, although the acids themselves are solids with mostly high boiling points and low vapor pressures. In turn, aerosols, together with greenhouse gases, crucially determine our global climate and are therefore worth being investigated. Zellner and coworkers found saturated (glutaric) and unsaturated (maleic) dicarboxylic acids in aerosols and studied their deliquescence behavior in ternary systems of acids, ammonium salts and water.<sup>1</sup> In their electrodynamic balance experiments they found the deliquescence relative humidity and the temperature of the systems to be strongly dependent on the nature of the acids.

However, dicarboxylic acids are relevant systems not only in climate and aerosol research. Due to their intrinsic structural properties, they are suitable model systems. It is known that polar carboxylic and dicarboxylic acids can form hydrogen bonds with each other in the liquid phase. At high temperatures, in vapor phase, carboxylic acids usually exist as doubly hydrogen bonded dimeric pairs. In the gas phase, neutral carboxylic acids are predominantly found as dimeric species. Whereas ionic dicarboxylic acids (protonated or deprotonated) form monomeric cyclic structures in the gas phase with an intramolecular proton bridge (cf. Fig. 5.1).

As we have already seen in the previous chapters (structures of  $(\text{H}_2\text{O})_{17-21}$  and  $\text{NH}_4^+(\text{H}_2\text{O})$ ), hydrogen bonds are crucial for the structure and thus for the effects of many chemical systems.<sup>2</sup> Investigation of hydrogen bonds, especially the ones of the protonated type  $[\text{A}-\text{H}^+\cdots\text{B}]$  (with A and B being electronegative atoms, sometimes with A being the same kind of atom as B), e.g. in positively charged  $\text{H}_5\text{O}_2^+$ , are of academic interest.<sup>3-6</sup> There also exist negatively charged systems, like  $[(\text{NH}_4)^+(\text{Cl}^-)]^-$ , which is formed after proton transfer through impact of an excess electron on the neutral species  $[(\text{NH}_3)(\text{HCl})]$ .<sup>7</sup> Due to their role in e.g. ion channels and membrane pump mechanisms, the ionic hydrogen bonds are of biological relevance. Another example of the importance of hydrogen bonds is protein folding, in which the 3-dimensional structure relies mainly on hydrogen bonds.<sup>8</sup>

In general, we differentiate between strong and weak hydrogen bonds. On the one hand, the strength depends on the nature of the participating donor and acceptor atom, on the other hand there is also a difference in strength between neutral  $(\text{A}-\text{H}\cdots\text{B})$  and ionic hydrogen bonds  $(\text{A}-\text{H}^+\cdots\text{B})$ . The bond strength therefore may vary from about  $12 \text{ kJ mol}^{-1}$  to about  $40 \text{ kJ mol}^{-1}$ . Moreover, the bond angle  $\text{A}-\text{H}-\text{B}$  plays an important role for the strength of the hydrogen bond. In strong hydrogen bonds the angle is close to  $180^\circ$ , which is called a strongly directional bond. In weak hydrogen bonds the angle is smaller and oftentimes angles of about  $165^\circ$  are observed. This type of hydrogen bond is then called weakly directional.<sup>8</sup> This finding

is due to the fact that hydrogen bonds are not only influenced by the nature of the donor and acceptor atom (not exclusively atom-pair effects) but the influence of whole groups of atoms is visible (group effects). For example if there are several electronegative atoms close by, of course all of them influence the position of the H atom. Sometimes we find hydrogen bonds, which are best described as three- or four-center bonds rather than the typical two-center bonds.<sup>8</sup>

Directly connected to the strength of the hydrogen bonds is the appearance of red shifts of O–H (in general A–H in an A–H···B system) frequencies in IR spectra. The stronger the hydrogen bond, the more does the O–H frequency shift to lower wave numbers.<sup>8</sup> By definition, strong hydrogen bonds usually shift A–H modes to the red down to less than 1600  $\text{cm}^{-1}$ . A–H bonds in weak hydrogen bonds in turn are found to be located in the region between 2000 and 3000  $\text{cm}^{-1}$ . Free A–H vibrational modes are above 3000  $\text{cm}^{-1}$ .

Detailed investigation of proton bound systems is not always straight forward. Depending on the size of the systems, it is far from trivial. Even in the relatively small system  $\text{H}_5\text{O}_2^+$  (sometimes also written as  $\text{H}_2\text{O}\cdots\text{H}^+\cdots\text{OH}_2$ ) the calculation of a complete 15-dimensional potential energy surface of both the mechanical and the electronic hyper surface of the dipole moment are necessary in order to explain the observed experimental results.<sup>3-6</sup> Based on these extensive calculations, the question whether the  $\text{H}_5\text{O}_2^+$  is rather an Eigen- or a Zundel-cation,<sup>9,10</sup> can be answered to be both at the same time, leading to an assignment as 'Eigen-Zundel-cation'.<sup>6</sup>

Experimentally, the investigation of proton bound systems is easier to handle, at least in case of ionic systems, in which spectroscopic and mass spectrometric methods can easily be combined. Johnson and coworkers observed a huge red shift in ionic proton bound dimers of various molecules by applying photofragmentation techniques.<sup>11</sup> Depending on the difference in proton affinity ( $\Delta\text{PA}$ ) of A and B in  $(\text{A}-\text{H}^+\cdots\text{B})$ , they found the red shift to be largest when  $\Delta\text{PA}$  is zero. With decreasing  $\Delta\text{PA}$  they found the shape of the potential energy curve of the A–H of the hydrogen bond to become wider. An example of such a system is the proton bound dimethylether dimer with a quartic potential energy curve, which is chosen as known reference system and will be presented in Sec. 5.3 later on.

Gas phase infrared multiphoton dissociation (IRMPD) experiments on various dicarboxylic acids with intramolecular hydrogen bonds were performed in our group. Protonated and deprotonated adipic acid were measured with two different experimental mass

spectrometric installations. First results were achieved using an Esquire 3000 Paul trap (Bruker, equipped with an ESI source) coupled to the Free Electron Laser CLIO. In this first experimental run, the resolution of the IRMPD spectra was not sufficient for an unambiguous interpretation. Repetition of the IRMPD measurements was carried out with a newly installed FT-ICR-MS (Apex-Q, 7 Tesla superconducting magnet, Apollo II ESI source, Bruker). Further IRMPD spectra of protonated glutaric acid have been measured with the FT-ICR-MS setup. Experimental details and in-depth discussion of these experimental spectra are documented elsewhere.<sup>12-14</sup>

For this work the relevant result from the experimental measurements of the dicarboxylic acid homologues glutaric, adipic and pimelic acid is the absence of the O–H stretch vibrations that are predicted by harmonic frequency calculations to locate in the region of 2000–2450  $\text{cm}^{-1}$ .

This chapter presents potential energy curves of the proton movement within the intramolecular hydrogen bond. Anharmonic frequencies of protonated and deprotonated dicarboxylic acids (from oxalic to adipic acid) are determined by ab initio calculations. Anharmonic frequencies are compared to standard harmonic frequencies and the results are discussed with regard to the experimentally derived data.

## 5.2 Computational Details

All calculations were performed at the second order Moller-Plesset<sup>15</sup> perturbation theory (MP2) level with Dunning's<sup>16</sup> correlation-consistent basis sets of double- $\zeta$  (cc-pVDZ) quality. A Lorentzian lineshape with a uniform 10  $\text{cm}^{-1}$  Half-Width at Half-Maximum (HWHM) was used to represent the stick diagram corresponding to the MP2/cc-pVDZ frequencies. All MP2 calculations were performed using the G03 program package.<sup>17</sup> Coordinate files were generated and visualized with MOLDEN version 4.5.<sup>18</sup>

Anharmonic frequencies<sup>19-23</sup> followed the approach of Barone,<sup>22-24</sup> which is based on second order perturbation theory and provides closed expressions for most of the spectroscopic constants needed to obtain anharmonic frequencies (cf. Chapter 2).

In contrast to the previously studied  $\text{NH}_4^+(\text{H}_2\text{O})$  system (cf. Chapter 4), the size of the dicarboxylic acid systems was too large to use augmented basis sets. Therefore two experimentally and quantum mechanically known reference systems,  $\text{NH}_4^+(\text{H}_2\text{O})$ <sup>25</sup> and the

proton bridged dimer of dimethylether,<sup>11</sup> were included into this study to ensure that the results do not differ significantly from those with the larger augmented basis sets.

Calculation of the anharmonic frequencies does not provide values for the IR intensities. Therefore diagrams with anharmonic frequencies are given in form of stick spectra with uniform arbitrary units on the ordinate.

Based on the calculated equilibrium structure of the respective dicarboxylic acid at zero Kelvin, potential energy curves are obtained by parametrical variation of the initially shortest O–H distance in the equilibrium structure. All other coordinates are free to relax in the course of the geometry optimization. The energy of the equilibrium structure is arbitrarily set to zero and all other values are given relative to it. With the exception of the equilibrium structures and some local minima, all other structures are not stationary points. Therefore the relative  $\Delta E$  values are not corrected by zero point energy (ZPE).

### 5.3 Results and Discussion of the Computational Results

Firstly, it was necessary to find out whether MP2 together with the cc-pVDZ basis set is appropriate for a sufficient description of the prior experimental results of  $\text{NH}_4^+(\text{H}_2\text{O})$  and proton bridged dimethylether dimer. These two systems have already been calculated on MP2/aug-cc-pVDZ level of theory<sup>11,25</sup> and, in case of  $\text{NH}_4^+(\text{H}_2\text{O})$ , anharmonic frequencies have been compared to the experimental results. A larger basis set is not applicable for the larger dicarboxylic acids, therefore it is important to know whether the smaller basis set yields approximately the same results.

In case of  $\text{NH}_4^+(\text{H}_2\text{O})$ , the harmonic approach yields  $2863\text{ cm}^{-1}$  and the anharmonic VPT2 approach gives  $2494\text{ cm}^{-1}$  for the N–H vibrational mode of the hydrogen bond when calculated on MP2/cc-pVDZ level of theory. When using MP2/aug-cc-pVDZ, the harmonic frequency is determined to be at  $2940\text{ cm}^{-1}$ , while the anharmonic VPT2 yields  $2574\text{ cm}^{-1}$ . Both times we observe a strong shift to lower wave numbers of the anharmonically calculated values with respect to the values derived by the harmonic approach. The smaller cc-pVDZ basis set gives values which are systematically lower than those of the larger basis set by approximately  $80\text{ cm}^{-1}$  in both the harmonic and anharmonic approach. We have to keep this result in mind for the calculation of the dicarboxylic acids, as it is most likely that all frequencies will be shifted too far to the red due to the small basis set. In Figure 5.2 the potential energy curve of the N–H mode of the hydrogen bond is displayed, nicely showing

the anharmonicity of this mode. Frequency calculations based on the VPT2 approach are therefore required to describe the experimental findings.

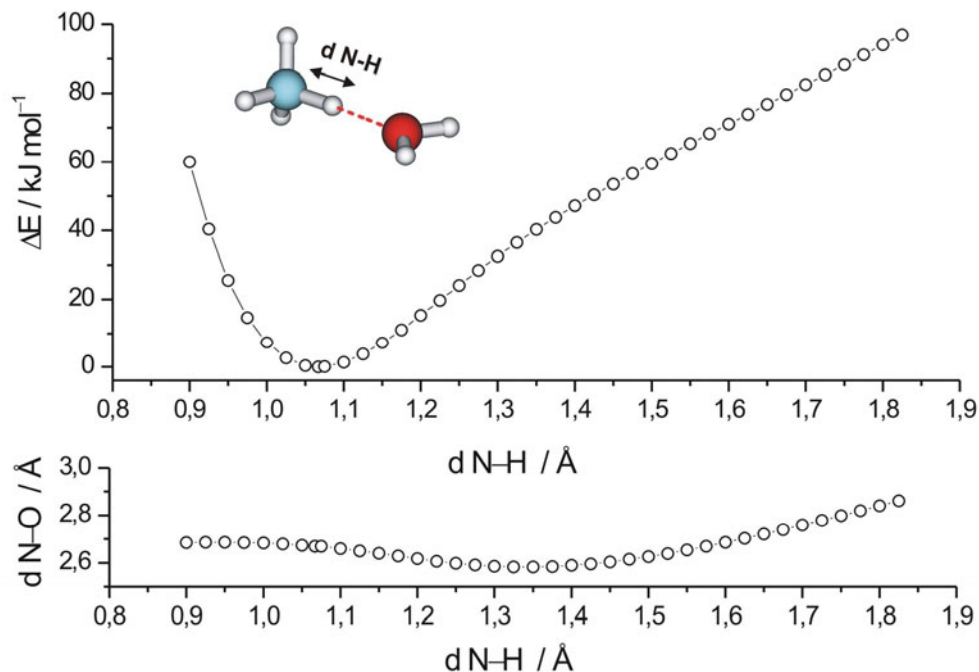


**Figure 5.2:** Potential energy curve of  $\text{NH}_4^+(\text{H}_2\text{O})$  (MP2/cc-pVDZ). Under stepwise variation of the N–H distance the N–O distance and all other coordinates relax to minimize the total energy.

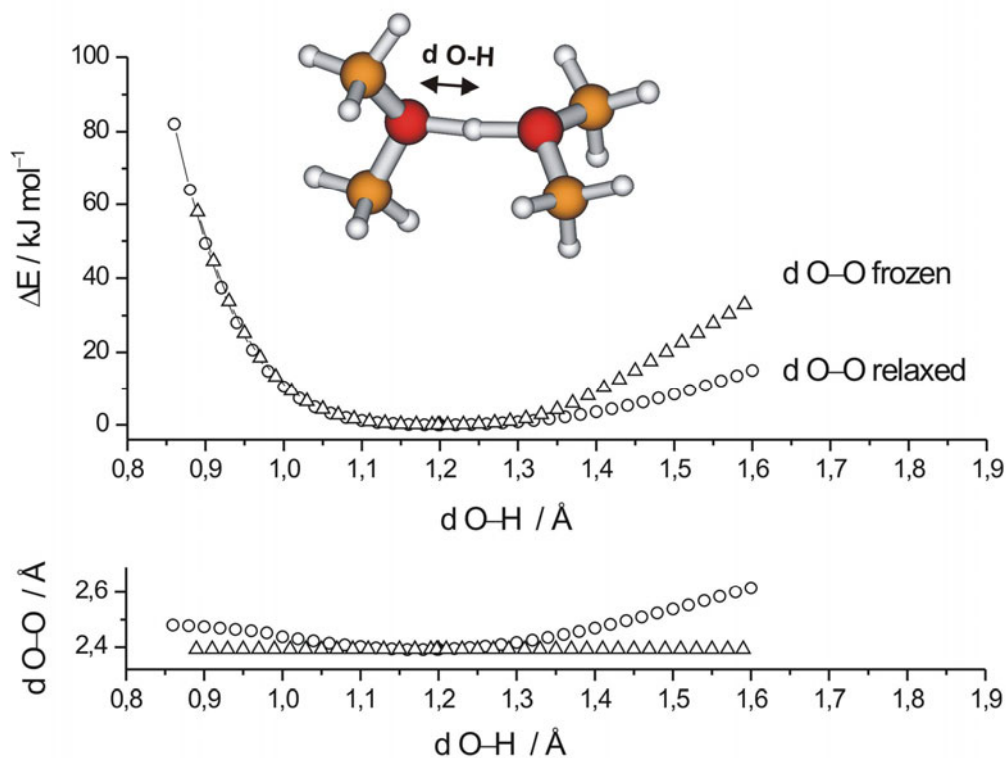


**Figure 5.3:** Potential energy curve of  $(\text{CH}_3)_2\text{O}-\text{H}^+-\text{O}-(\text{CH}_3)_2$ . One O–H distance is frozen, while the O–O distance is variable (MP2/cc-pVDZ).



The second reference system was chosen from a study of Mark Johnson and coworkers.<sup>11</sup> This is an example where the anharmonic perturbative approach is known to fail due to the quartic potential energy curve of the system. The proton bridged dimer of the dimethylether experimentally yields  $952\text{ cm}^{-1}$  for the  $\nu_{\parallel}$  mode of the shared proton. Here the result of the harmonic unscaled frequency calculations is  $991\text{ cm}^{-1}$ , while the anharmonic calculation erratically shifts the  $\nu_{\parallel}$  band to  $1255\text{ cm}^{-1}$ . Due to the shape of the potential energy curve this failure was foreseeable. Nevertheless, the potential energy curve was calculated in order to determine if there was a significant difference in shape to the one calculated by Johnson and coworkers with an augmented basis set. This is not the case. There are some differences, which are caused by keeping the O–O distance fixed in the course of the calculation of the potential energy curve, while in this study it is variable (cf. Fig. 5.4).

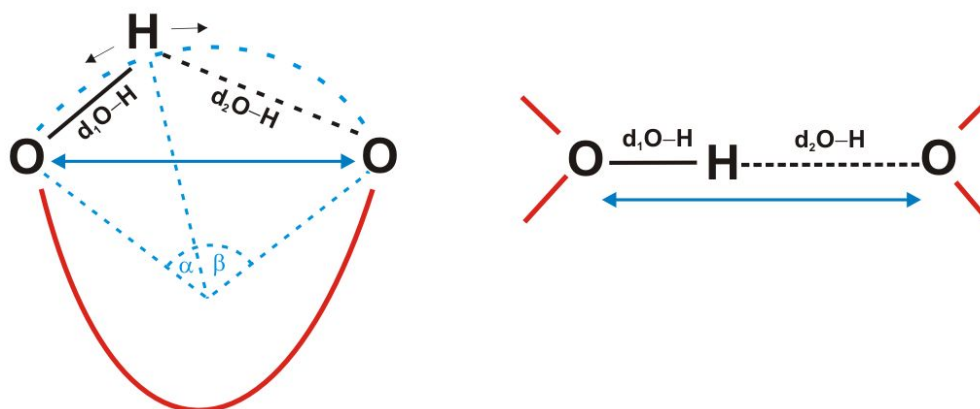


**Figure 5.4:** Scheme of the proton movement between the oxygen atoms in covalently linked dicarboxylic acids (left) and in proton bridged dimers with free side chains (right). The blue double headed arrows indicate the variable distance between the two electronegative atoms that constitute the proton bridge.

In proton bridged dimers there is no restriction or hindrance other than the hydrogen bond itself. Therefore it is only the proton movement along the hydrogen bond and the O–O distance relaxation that couple in the first place. Further relaxations are minor. In considerable contrast, the linking of the nucleophilic acceptor sites (O-atoms) through a single side chain leads to a conceptually altered situation. Ring strain and steric hindrance may in principle dictate whether (or not) an O–O distance relaxation is feasible and at which energetic expense. In consequence the potential energy curve along the proton displacement coordinate may become largely asymmetric. Moreover, the proton displacement itself does not follow a linear 1D-movement anymore. Instead, it is appropriately described by a two-dimensional (or higher) picture. The minimum energy path becomes curved (cf. Fig. 5.4) as much as ring

strain through the side chain prevails. At least three internal coordinates couple: O–O stretching, proton migration along the hydrogen bond and proton motion perpendicular to it.

This highly coupled situation certainly requires a quantum chemical description in terms of coupled eigenstates, maybe even time dependent multi-dimensional wave packet dynamics. Nevertheless, it might be challenging to try more approximate classical pictures (such as VPT2) and to check for the limits of their validity.

The covalent link (or loop) between the involved donor and acceptor molecule leads to differences in the resulting shape of the potential energy curves, which are no longer negligible (cf. Fig. 5.5). If the O–O distance is fixed, the shape of the potential energy curve of deprotonated glutaric acid is narrower than if the O–O distance is allowed to relax, and the form of a double-well potential is more pronounced. Keeping the O–O distance frozen also leads to an artificial increase of calculated barrier heights within double-well potentials.

For all these reasons the O–O distance is chosen to be variable. Only this allows for the best possible description of the potential energy curves of the dicarboxylic acid homologues.

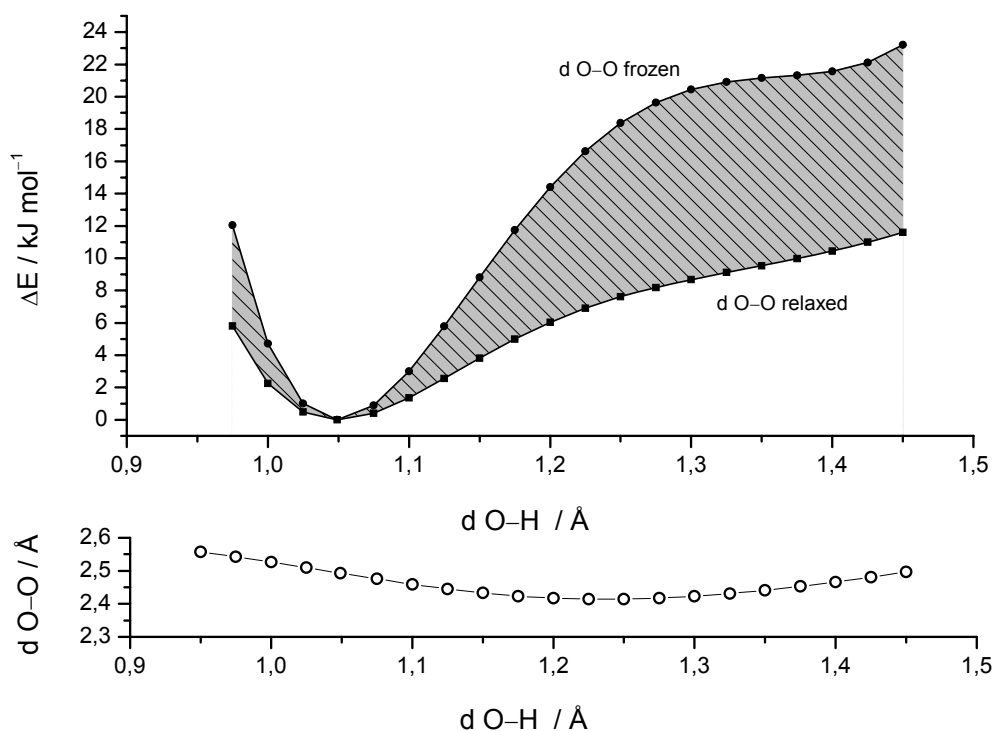


**Figure 5.5:** Potential energy curve of deprotonated glutaric acid calculated on MP2/cc-pVDZ level of theory. Comparison between frozen O–H distance only and the same system with additional freezing of the O–O distance. The grey area corresponds to the relaxation energy.

Potential energy curves for all protonated and deprotonated dicarboxylic acids from oxalic to adipic acid are plotted in Fig. 5.6. Diagrams are all scaled equally, except for oxalic acid. In the latter case the scale of the ordinate is expanded by a factor of two in order to make the barrier height of the protonated oxalic acid visible.

The potential energy curves of both protonated and deprotonated oxalic acids (gas phase geometries are displayed in Fig. 5.1) exhibit a well defined double minimum structure. Thereby the shape of the potential of protonated oxalic acid is closer to the shape of a harmonic parabolic potential than in case of the deprotonated oxalic acid. Also the barrier between the two minima in each potential is higher for the protonated acid ( $25.5 \text{ kJ mol}^{-1}$ ) than for the deprotonated acid ( $6.3 \text{ kJ mol}^{-1}$ ). This corresponds to the geometrical features of the oxalic acid. As described in Sec. 5.1, the strength of an  $A-H\cdots B$  bond is affected by the properties (e.g. electronegativity) of not only A and B, but also of whole groups of atoms. In oxalic acids this effect is nicely visible. Upon twofold protonation of the deprotonated oxalic acid, electron density is transferred to the free O–H groups, the C–C bond becomes shorter and the O–H–O angle in the potential hydrogen bond decreases from  $140^\circ$  to  $117^\circ$ . The short O–H bond contracts further from 1.027 to 0.997 Å, which is a typical value of strong O–H bonds (all O–H distances of the hydrogen bond, the angle and barrier heights are listed in Table 5.1 and the trend is visualized in Fig. 5.8). The O–H bond in deprotonated oxalic acid is best described to be a strong bond, too. Due to the large  $O\cdots H$  distance, we can speak of a very weak hydrogen bond in case of the oxalic acid systems. This in turn goes along with the almost harmonic double minimum potential. Due to the high barriers, tunnelling or an oscillation of the proton between the potential minima is not expected, especially in case of protonated oxalic acid. Therefore calculation of IR frequencies by a conventional harmonic approach should yield reasonable results that compare favourably with IRMPD spectra of oxalic acid systems, provided that the ions have a low temperature.

The shape of the potential energy curves of protonated and deprotonated malonic acid differ significantly from those of their oxalic acids analogues. Due to the decreased ring strain in the six membered cyclic structures of the malonic systems, the angles open up to  $158.3^\circ$  and  $165.7^\circ$  in protonated and deprotonated malonic acid, respectively. These systems are almost symmetrical with respect to the distances of O1–H and O2–H bonds. In consequence, the potential energy curves can no longer be described with a harmonic potential. Instead they show a quartic form with a very flat double minimum structure. Here the proton of the intramolecular hydrogen bond can easily oscillate between the minima. The barrier heights amount to negligible  $0.06 \text{ kJ mol}^{-1}$  in both cases. Due to the quartic character the calculation

of both harmonic and anharmonic frequencies will not provide reliable results for the intramolecular hydrogen bond, which was already shown before in case of the quartic potential of the proton bound dimethylether dimer.

Deprotonated succinic acid shows the same potential energy curve as the malonic acid congeners. Due to the minimized ring strain in this symmetric seven membered cyclic system, the O–H–O angle enlarges to  $179.2^\circ$ . This in turn leads to a quartic double minimum structure with a calculated barrier of only  $0.03 \text{ kJ mol}^{-1}$ .

In the protonated succinic acid, the symmetry is even higher leading to a wide quartic potential with a single minimum, although the O–H–O angle of the intramolecular hydrogen bond decreases to  $173.8^\circ$  under the influence of the additional free hydroxyl groups. In such a case calculation of IR frequencies of the hydrogen bond will not provide reliable results neither in the harmonic nor in the anharmonic approach.

As soon as the cyclic hydrogen bonded system contains eight atoms, the ring strain increases again. This leads to a loss of symmetry in the systems, as can be seen in the glutaric acids. In consequence, the shape of the potential energy curves becomes narrower. The deprotonated glutaric acid can be described by an anharmonic potential, while the protonated acid still shows a wide distinct double minimum potential.

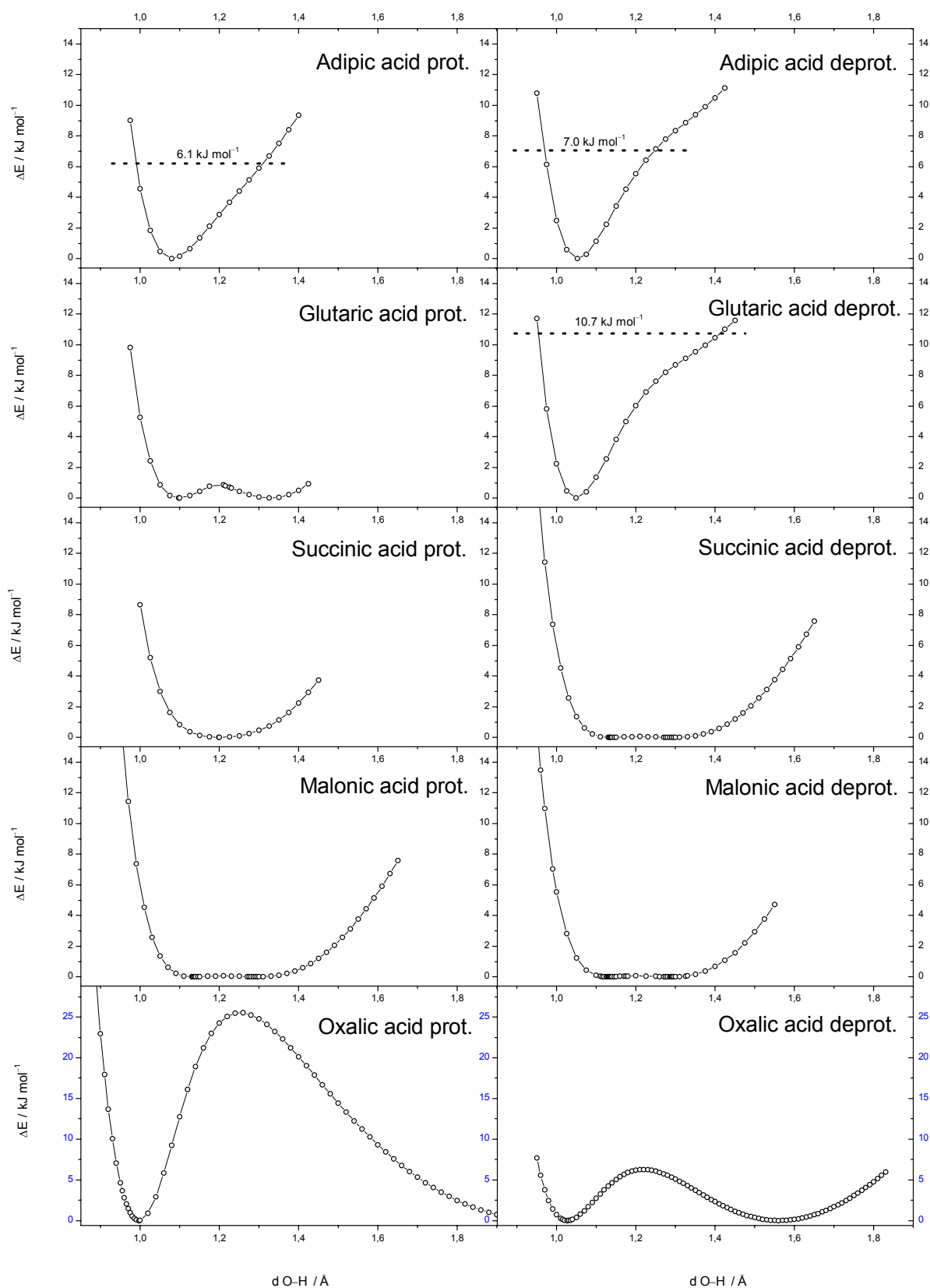


**Figure 5.6:** Calculated potential energy curves (MP2/cc-pVDZ) of protonated and deprotonated dicarboxylic acids from oxalic acid to adipic acid. The O–H distance is frozen, while all other coordinates are freely optimized. Please note that in the diagrams of oxalic acid the ordinates are enlarged by a factor of two relative to all other diagrams.

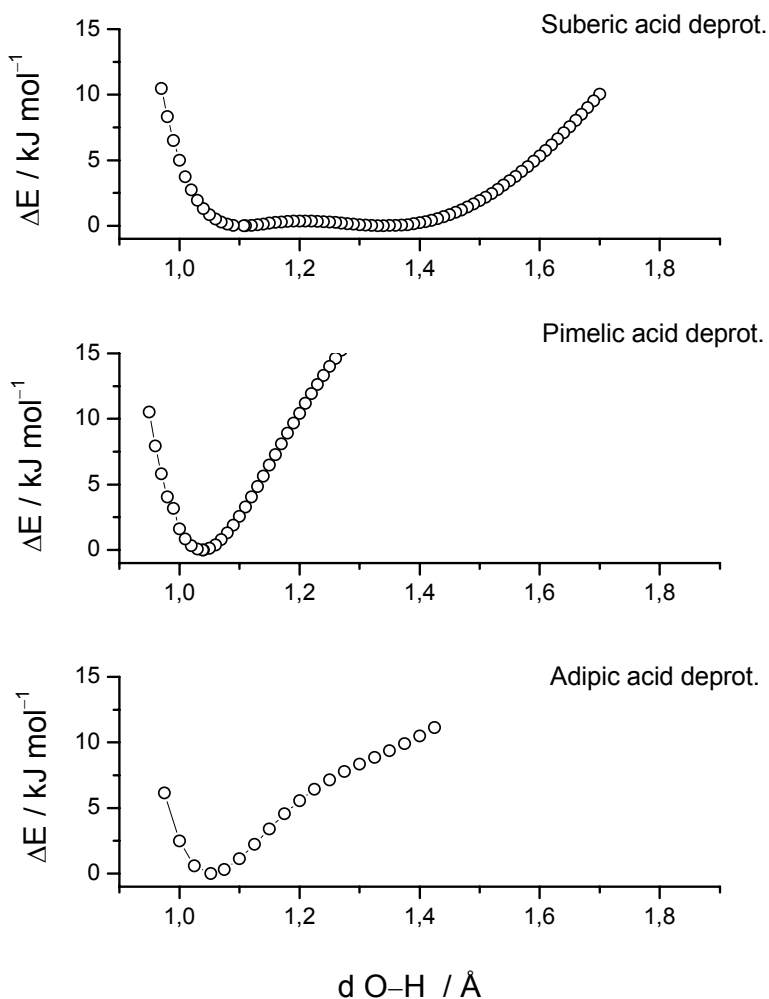


**Figure 5.7:** Calculated potential energy curves (MP2/cc-pVDZ) of deprotonated adipic, pimelic and suberic acid (curves of deprotonated pimelic and suberic acid from Ref. 26). The O–H distance is frozen, while all other coordinates are freely optimized.

In correlation to the increased ring strain, protonated and deprotonated adipic acids show narrower potential energy curves, which conforms to the slightly asymmetric hydrogen bond. According to the anharmonic shape of the potential, IR frequencies calculated with the VPT2 approach should in principle be close to the experimentally observed ones.

Considering the trends in the longer dicarboxylic acid homologues pimelic and suberic acid, as plotted for the deprotonated acids in comparison to adipic acid in Fig. 5.7, the shape of the potentials is clearly connected to the ring strain. Up to pimelic acid the ring strain is unfavorable in the cyclic systems, leading to narrower potentials. Not until a ring size of eleven atoms is reached, the behaviour changes, due to the now flexible system where only transannular interactions have a certain influence on the geometry of the systems.

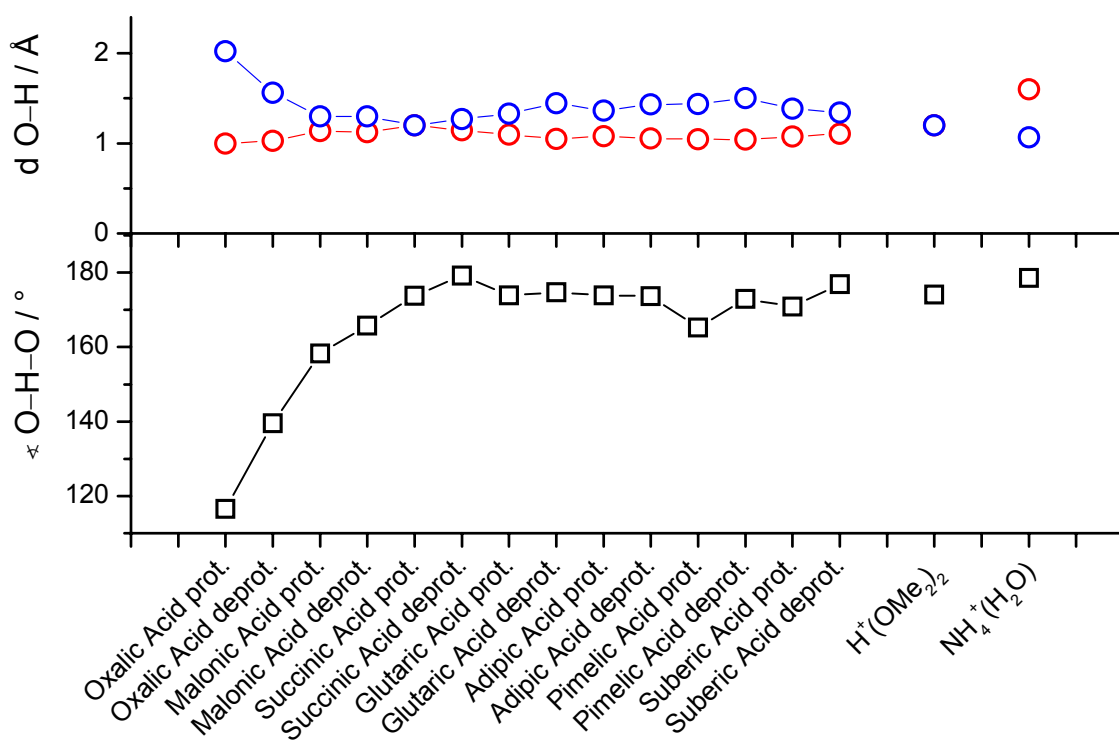


**Figure 5.8:** Angles  $\angle \text{O-H-O}$  and distances  $\text{O-H}$  within the hydrogen bond of various protonated and deprotonated dicarboxylic acids and two proton bridged reference systems.

**Table 5.1:** Data on the geometry of the hydrogen bond within the equilibrium structure and on the shape of the potential curves.

Compound	$\sphericalangle$ O–H–O / °	d O(1)–H / Å	d O(2)–H / Å	$\Delta$ d / Å	shape of potential curve	barrier height / kJ mol <sup>-1</sup>	# ring-atoms
Oxalic acid prot.	116.51	0.997	2.021	1.024	harmonic double min.	25.51	5
Oxalic acid deprot.	139.50	1.027	1.562	0.535	harmonic double min.	6.26	5
Malonic acid prot.	158.25	1.134	1.297	0.163	quartic double min.	0.06	6
Malonic acid deprot.	165.74	1.123	1.298	0.175	quartic double min.	0.06	6
Succinic acid prot.	173.76	1.199	1.202	0.003	quartic, wide	–	7
Succinic acid deprot.	179.17	1.144	1.270	0.126	quartic double min.	0.03	7
Glutaric acid prot.	173.87	1.098	1.327	0.229	quartic double min.	0.87	8
Glutaric acid deprot.	174.72	1.049	1.446	0.397	anharmonic, medium	–	8
Adipic acid prot.	173.92	1.080	1.363	0.283	anharmonic, medium	–	9
Adipic acid deprot.	173.62	1.052	1.431	0.379	anharmonic, medium	–	9
Pimelic acid prot.	165.25	1.436	1.047	0.389	anharmonic double min.	7.36	10
Pimelic acid deprot.	172.91	1.039	1.499	0.460	harmonic, narrow	–	10
Suberic acid prot.	170.87	1.076	1.384	0.308	–	–	11
Suberic acid deprot.	176.89	1.104	1.342	0.238	quartic double min.	–	11
H <sup>+</sup> (OMe <sub>2</sub> ) <sub>2</sub>	174.06	1.198	1.198	0	quartic, wide	–	–
NH <sub>4</sub> <sup>+</sup> *H <sub>2</sub> O	178.59	1.602	N: 1.067	0.535	anharmonic, wide	–	–



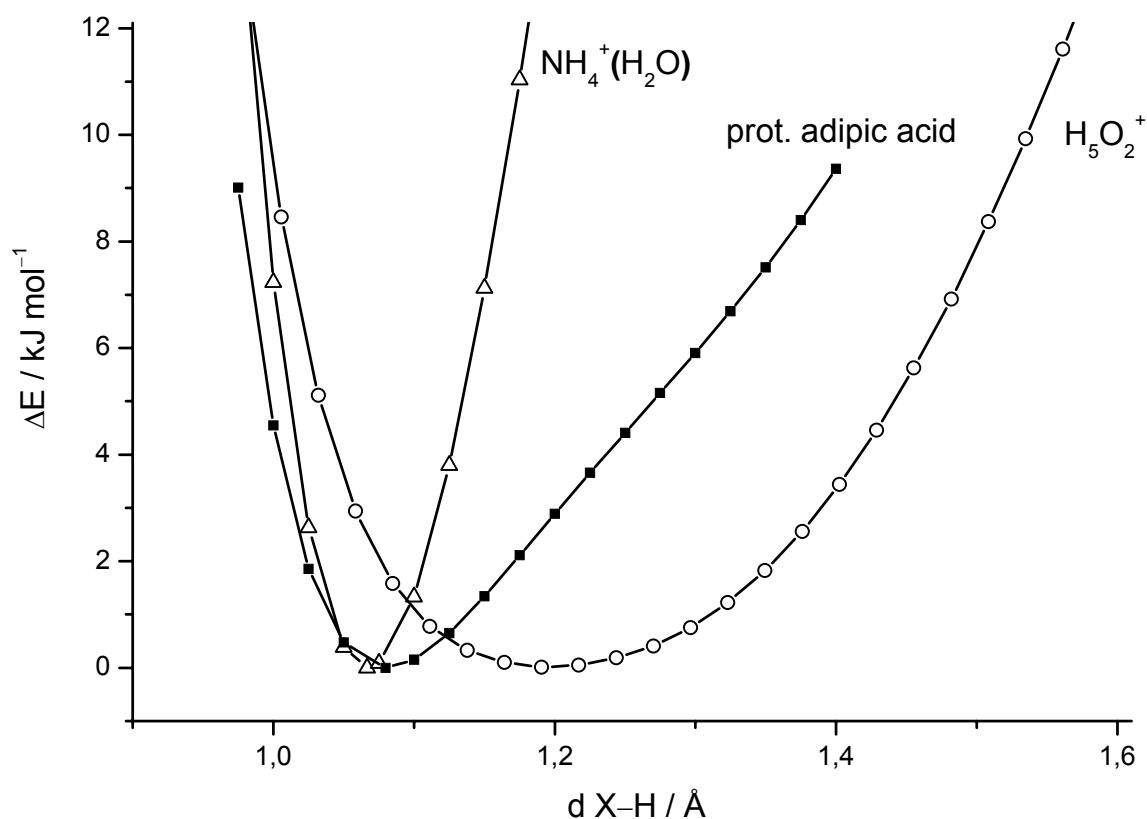


**Figure 5.9:** Comparison of the potential energy curves of  $\text{NH}_4^+(\text{H}_2\text{O})$ , protonated adipic acid (both MP2/cc-pVDZ level of theory) and the protonated water dimer  $\text{H}_5\text{O}_2^+$ , kindly provided by H.D. Meyer<sup>3,4</sup> (from the potential energy surface<sup>27,28</sup> based on CCSD(T)/aug-cc-pVTZ calculations). In case of  $\text{NH}_4^+(\text{H}_2\text{O})$  the N–H distance is frozen, while in adipic acid and  $\text{H}_5\text{O}_2^+$  one O–H distance is frozen. In each case all other coordinates are relaxed in the course of the geometry optimization. The anharmonic character of the X–H stretching mode within the hydrogen bond increases from  $\text{NH}_4^+(\text{H}_2\text{O})$  over adipic acid to the extreme case of  $\text{H}_5\text{O}_2^+$  where the potential shape is almost quartic.

Typically, IR spectra of compounds with weak hydrogen bonds provide signals of the bound O–H stretch in the region of  $2000 \text{ cm}^{-1}$  and  $3000 \text{ cm}^{-1}$ . If the potential of the proton movement is harmonic, standard harmonic frequency calculations may be scaled by a standard factor of 0.92 to 0.96. They then are in good agreement with experimental spectra. Figures 5.10 and 5.11 present an overview of all calculated frequencies of the dicarboxylic acids in harmonic approximation and when calculated by the VPT2 approach. In close correlation to the shapes of the potential energy curves, the red shift in the bound O–H stretching is the more pronounced the more the potential deviates from an ideal harmonic potential. In the protonated oxalic acid the red shift of  $260 \text{ cm}^{-1}$  is smallest (cf. Table 5.2), which correlates with its potential and the strength (or rather weakness) of the hydrogen bond. The order of the frequency shift is the same as if a scaling factor of 0.924 was applied. In

deprotonated oxalic acid, the red shift as calculated by VPT2 is already more distinctive. This is due to the slightly stronger intramolecular hydrogen bond.

Due to the quartic potentials in case of the malonic and succinic acids and in protonated glutaric acid, not only the harmonic approach is doomed to fail but also the VPT2 approach. Here the frequencies of the  $\nu_{\parallel}$  of the shared proton within the intramolecular hydrogen bond and those of some modes which couple to the motions of this proton, are either strongly shifted both to the red or to the blue. Thereby some modes are even shifted into negative wave numbers, which makes no physical sense. Due to strong vibrational couplings, a shift to low wave numbers in this systems is not only observed in the  $\nu_{\parallel}$  mode of the hydrogen bond, but also in both  $\nu_{\perp}$  modes and some other C=O modes in deprotonated and C–O–H modes in protonated acids (cf. Table 5.2). Due to their collective character, it is sometimes difficult to assign these modes correctly.

In contrast to protonated glutaric acid, deprotonated glutaric acid seems to be well described by the anharmonic approach. Due to the asymmetric intramolecular hydrogen bond, the shape of the potential is narrow, although the O–H–O angle is wider than in protonated glutaric acid. Here the anharmonic value of the  $\nu_{\parallel}$  mode is located at  $1783\text{ cm}^{-1}$ , which means a shift to lower wave numbers of  $616\text{ cm}^{-1}$  with respect to the unscaled harmonic value of  $2399\text{ cm}^{-1}$ .

Protonated and deprotonated adipic acid show a similar behavior as the deprotonated glutaric acid. Both possess slightly wider potentials than deprotonated glutaric acid, but can still be described anharmonically. Compared to the harmonic frequencies of the  $\nu_{\parallel}$  of the proton bridge, the anharmonic frequencies of protonated and deprotonated adipic acid are shifted from  $2060\text{ cm}^{-1}$  to  $1025\text{ cm}^{-1}$  and from  $2348\text{ cm}^{-1}$  to  $1172\text{ cm}^{-1}$ , respectively.

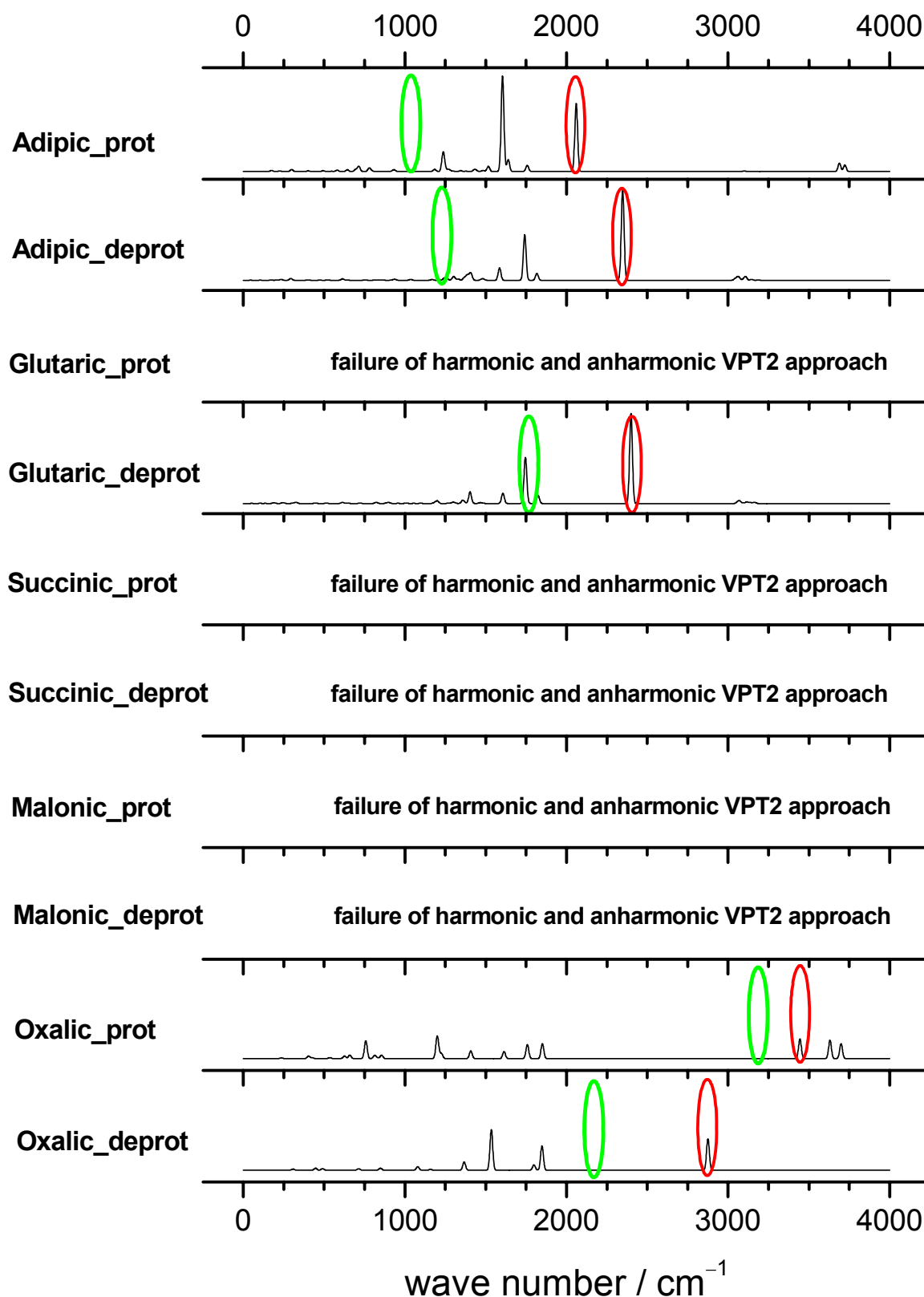


**Figure 5.10:** Calculated harmonic frequencies (MP2/cc-pVDZ, unscaled) of protonated and deprotonated dicarboxylic acids from oxalic acid to adipic acid. Red ellipses indicate the position of the  $\nu_{||}$  of the hydrogen bond, when calculated in harmonic approximation without scaling factors; green ellipses give the frequency of  $\nu_{||}$  within the anharmonic VPT2 approach.

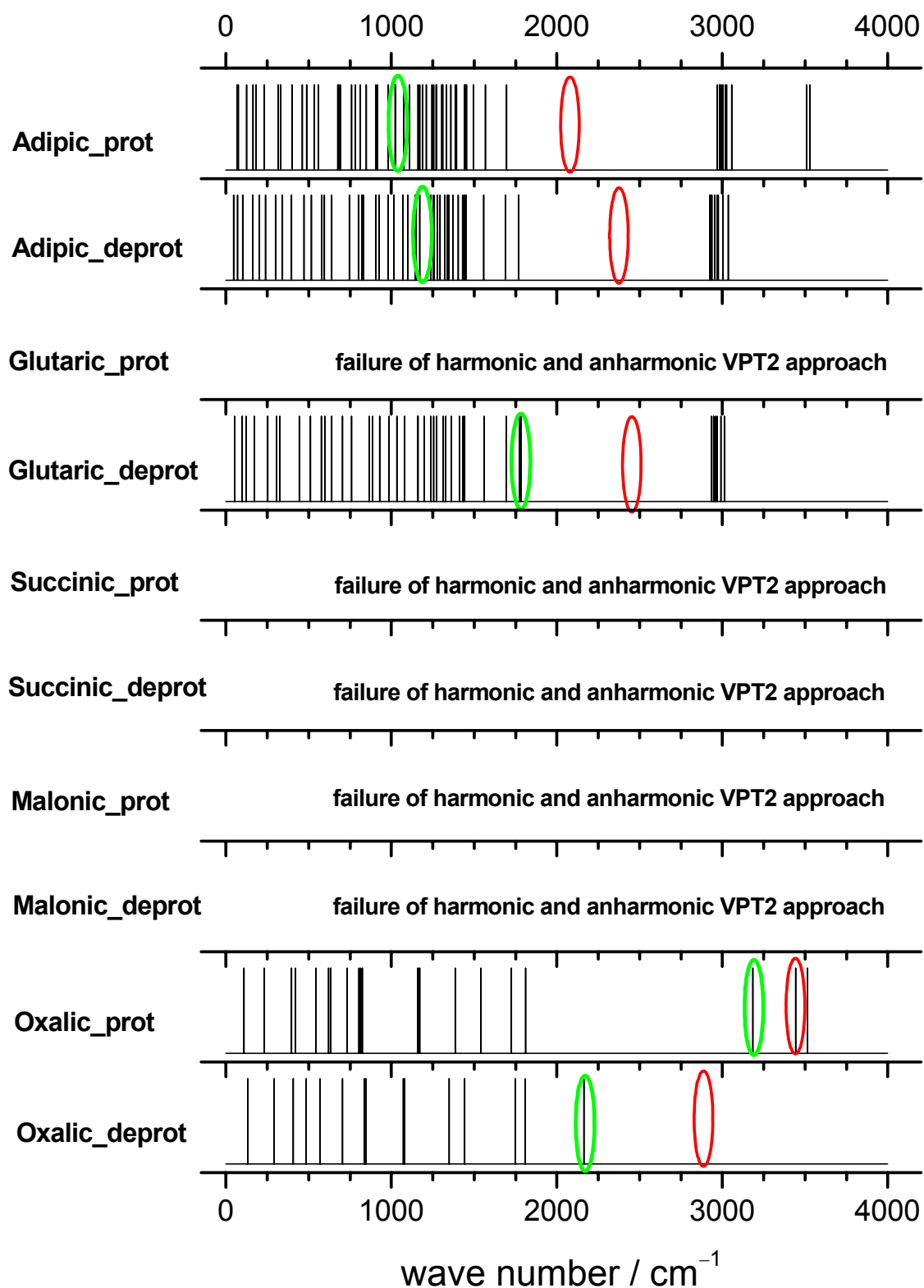


**Figure 5.11:** Calculated anharmonic frequencies (VPT2 with MP2/cc-pVDZ) of protonated and deprotonated dicarboxylic acids from oxalic acid to adipic acid. Red ellipses indicate the position of the  $\nu_{||}$  of the hydrogen bond, when calculated in harmonic approximation without scaling factors; green ellipses give the frequency of  $\nu_{||}$  within the anharmonic VPT2 approach.

**Table 5.2:** Shifts of vibration modes of protonated and deprotonated cyclic dicarboxylic acids due to anharmonicities calculated by VPT2 on MP2/cc-pVDZ level of theory. Only numbers of those frequencies are listed, which shift significantly farther than anticipated on the basis of linear standard scaling factors. Bold numbers denote frequencies due to the  $\nu_{||}$  of the shared proton within the intramolecular hydrogen bond.

	Protonated		Deprotonated	
	Harmonic $\rightarrow$ Anharmonic / $\text{cm}^{-1}$		Harmonic $\rightarrow$ Anharmonic / $\text{cm}^{-1}$	
Adipic acid	<b>2060</b> 1604	<b>1025</b> 1245	<b>2348</b>	<b>1172</b>
Glutaric acid	<b>1937</b> 1537 1516	<b>1063</b> 1171 1045	<b>2399</b>	<b>1783</b>
Succinic acid	<b>1811</b> 917 867 742 412	<b>1933</b> 1108 888 424 1057	<b>1826</b> 1807 1715 1508 1458 1036	<b>1545</b> 1550 1856 436 3114 -1629 (and more)
Malonic acid	<b>1906</b> 1750 1306 1040 387 254	<b>508</b> 2075 1620 -2225 -389 -1356	<b>1929</b> 1524 1054 295	<b>1399</b> 636 -968 -603
Oxalic acid	<b>3445</b>	<b>3184</b>	<b>2875</b>	<b>2162</b>
$\text{NH}_4^+ \cdot \text{H}_2\text{O}$	<b>2863</b>	<b>2495</b>		
$\text{H}^+(\text{OMe}_2)_2$	1629 1594 <b>991</b> 821	1405 1643 <b>1255</b> 1029		

In protonated adipic acid also the  $\nu_{\perp}$  mode perpendicular to the carbon-oxygen ring system is strongly shifted to lower wave numbers from  $1604 \text{ cm}^{-1}$  to  $1245 \text{ cm}^{-1}$ , which is significantly more than anticipated by the application of standard scaling factors.

As both the harmonic and the anharmonic approach fail to describe the O–H vibrational modes in malonic, succinic and protonated glutaric acid, the frequency shifts in their spectra are not discussed in more detail. If neither of the calculated frequencies (cf. Table 2.1) is trustworthy, their difference will not be as well.

The obtained calculated results of the adipic acid systems are expected to represent the experimental IRMPD spectra. The IRMPD spectra of deprotonated adipic acid can be interpreted in large parts, if the IRMPD spectra are compared to the calculated harmonic spectra – except for the O–H mode of the intramolecular hydrogen bond.<sup>12</sup> However, taking the results of the anharmonic frequency calculation into account, the large shift from 2348  $\text{cm}^{-1}$  to 1172  $\text{cm}^{-1}$  fully explains the absence of the O–H mode in the spectral region between 2200  $\text{cm}^{-1}$  and 2300  $\text{cm}^{-1}$  and at the same time explains the broadening of the bands observed in the region between 1100  $\text{cm}^{-1}$  and 1200  $\text{cm}^{-1}$ . It is known, that a broadening of the vibrational band is correlated to such large red shifts.<sup>6,11</sup> The intensities of the measured and the calculated modes are not always in perfect agreement. There are two explanations for this fact. First, the IRMPD spectra do not necessarily reflect the calculated absorption due to various fragmentation probabilities, and second the experimental spectra most likely represent combinations of spectra of the two lowest geometrical isomers. The energy difference between the lowest and the second lowest isomer is only 0.68  $\text{kJ mol}^{-1}$ . Due to the temperature of the ions, we can not exclude parallel existence of several isomers.

In protonated adipic acid, the calculated harmonic spectra do not fully resemble the experimental IRMPD spectra as well as in case of deprotonated adipic acid. Instead, a combination of the two or maybe even the three lowest energy isomers together with the explanation of the strongly shifted  $\nu_{\parallel}$  and  $\nu_{\perp}$  O–H modes of the hydrogen bridge yields a conclusive interpretation. One of these low energy isomers of protonated adipic acid is a Zundel-like structure in which the proton of the hydrogen bond is almost symmetrically located between the two oxygen atoms (see inset Fig. 5.12). This Zundel-like isomer is 10.4  $\text{kJ mol}^{-1}$  higher in energy than the minimum structure. After ZPE correction the energy gap between both isomers is reduced to only 6.9  $\text{kJ mol}^{-1}$ . Still these values include some systematic errors. Due to the anharmonic respectively quartic character of the potential energy curves of these protonated adipic acid isomers (see Fig. 5.12), standard ZPE correction based on the harmonic frequencies is only approximate. Each of the frequencies that contribute to

the evaluation of the ZPEs would need to be corrected with respect to their anharmonic shifts by an appropriate factor.

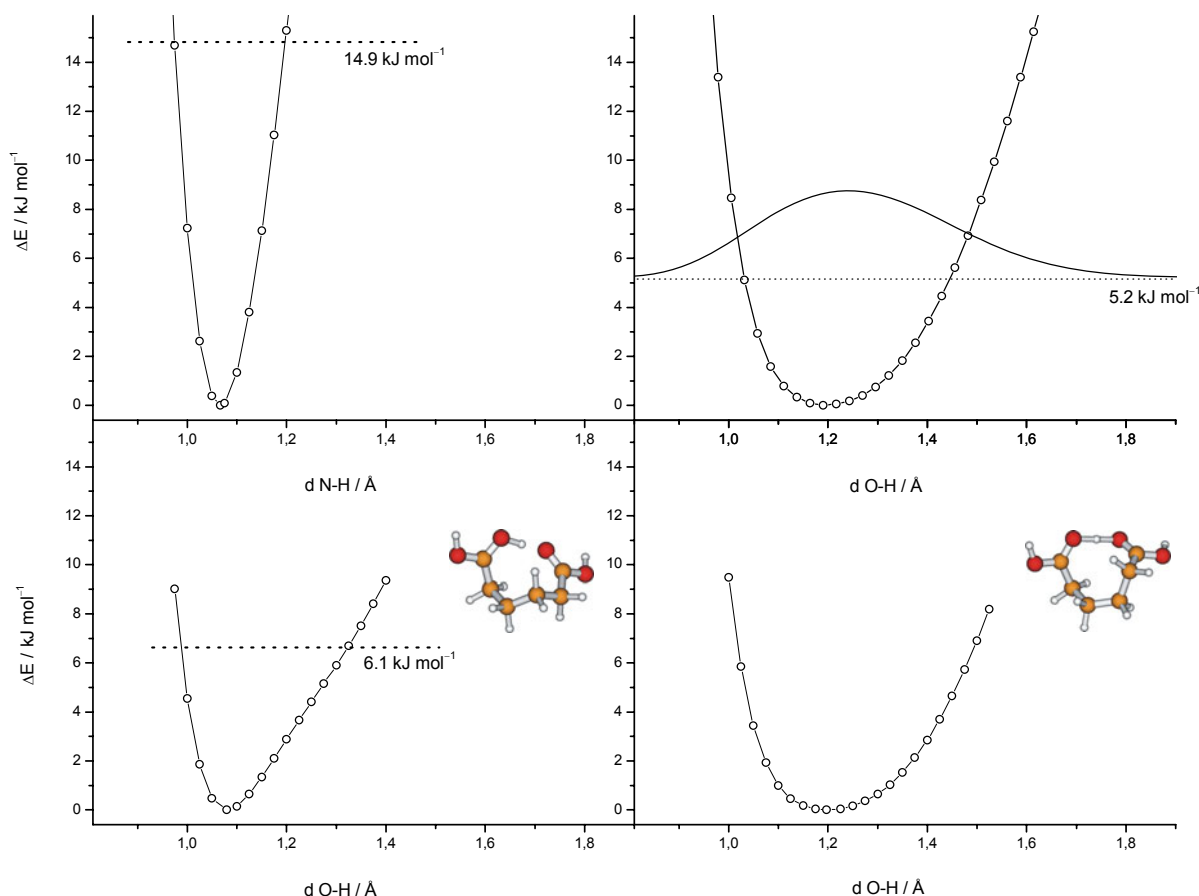


**Figure 5.12:** Comparison of the potential energy curves of  $\text{NH}_4^+(\text{H}_2\text{O})$ , top left, protonated adipic acid "Eigen-like" isomer, bottom left, protonated adipic acid "Zundel-like" isomer, bottom right (all MP2/cc-pVDZ level of theory) and the protonated water dimer  $\text{H}_5\text{O}_2^+$ , kindly provided by H.D. Meyer<sup>3,4</sup> (from the potential energy surface<sup>27,28</sup> based on CCSD(T)/aug-cc-pVTZ calculations), top right. In case of  $\text{NH}_4^+(\text{H}_2\text{O})$  the N–H distance is frozen, while in adipic acid and  $\text{H}_5\text{O}_2^+$  one O–H distance is frozen. In each case all other coordinates are relaxed in the course of the geometry optimization. The anharmonic character of the X–H stretching mode within the hydrogen bond increases from  $\text{NH}_4^+(\text{H}_2\text{O})$  over adipic acid "Eigen-like" isomer to the extreme cases of  $\text{H}_5\text{O}_2^+$  where the potential shape is almost quartic. In case of the energetically second lowest protonated adipic acid isomer, the shape of the potential energy curve is very similar to the one of  $\text{H}_5\text{O}_2^+$ , so it is justified to call this isomer a "Zundel-like" structure.

So far it remains unclear how large the contribution of this Zundel-like isomer is to the observed IRMPD spectra. Due to its quartic potential, the harmonic and the VPT2 approach fail to provide reliable IR frequencies of this structure.

#### 5.4 Summary and Conclusions

Calculation of potential energy curves of the O–H mode of the intramolecular hydrogen bond of various dicarboxylic acids revealed that the shapes of the potentials directly correlate to the size of the system and the resulting ring strain. The potentials are wide or even quartic in systems with strongly directional hydrogen bonds. The more the ring strain decreases, the wider the potential becomes. The shape of the potential is also influenced by the charge of the system and the resulting group effects. An oscillation of the strength of the hydrogen bond is observed between protonated and deprotonated dicarboxylic acids, with the protonated ones being weaker than the deprotonated ones.

Calculation of anharmonic frequencies based on the VPT2 approach leads to reasonable results in all systems with narrow potentials. However this approach fails in case of dicarboxylic systems with small ring strains and thus broad potentials like malonic and succinic acid. In case of adipic acid a good agreement with the experimental results is found in case of calculations of deprotonated adipic acid and still a reasonable agreement with protonated adipic acid. Due to the strongly harmonic character of the oxalic acid potentials predictions of the spectra are expected to be quite reasonable as well.

Further calculations on the basis of molecular dynamics (first principles Car-Parrinello molecular dynamics simulations (CPMD)<sup>29</sup>) are appreciated and are currently made in the group of Kwang Kim in order to take into account the temperature of the ions and the switching between energetically low lying isomers.<sup>13</sup>

Furthermore, a change of the experimental setup is under way, which will allow to cool down the ions as soon as they are stored in the analyzer cell. This will enhance the quality of the experimental IRMPD spectra, which makes it easier to compare them to ab initio spectra, which are calculated for ions at zero Kelvin.



## 5.5 References

- 1 L. Treuel, S. Schulze, T. Leisner, and R. Zellner, *Faraday Discuss.* **137**, 265 (2008).
- 2 D. Marx, *ChemPhysChem* **7** (9), 1848 (2006).
- 3 O. Vendrell, F. Gatti, D. Lauvergnat, and H. D. Meyer, *J. Chem. Phys.* **127** (18) (2007).
- 4 O. Vendrell, F. Gatti, and H. D. Meyer, *J. Chem. Phys.* **127** (18) (2007).
- 5 O. Vendrell, F. Gatti, and H. D. Meyer, *Angewandte Chemie-International Edition* **46** (36), 6918 (2007).
- 6 G. Niedner-Schatteburg, *Angew. Chem.* **120** (6), 1024 (2008).
- 7 S. N. Eustis, D. Radisic, K. H. Bowen, R. A. Bachorz, M. Haranczyk, G. K. Schenter, and M. Gutowski, *Science* **319** (5865), 936 (2008).
- 8 G. A. Jeffrey and W. Saenger, *Hydrogen Bonding in Biological Structures*. (Springer-Verlag, 1994).
- 9 M. Eigen, *Angew. Chem., Int. Ed.* **3** (1), 1 (1964).
- 10 G. Zundel and H. Metzger, *Zeitschrift Fur Physikalische Chemie-Frankfurt* **58** (5-6), 225 (1968).
- 11 J. R. Roscioli, L. R. McCunn, and M. A. Johnson, *Science* **316** (5822), 249 (2007).
- 12 S. Jaberg, *Reaktivitätsstudien von Übergangsmetallclustern in der Gasphase mittels Fourier-Transformation-Ionen-Zyklotron-Resonanz-Massenspektrometrie und Infrarot-Multiphotonen-Dissoziations-Spektren von Adipinsäure*, Dissertation, Technische Universität Kaiserslautern, 2008.
- 13 K. Kim, G. Niedner-Schatteburg, and coworkers, to be published (2008).
- 14 S. Jaberg, B. Pfeffer, G. Niedner-Schatteburg, and coworkers, to be published (2008).
- 15 C. Møller and M. S. Plesset, *Phys. Rev.* **46**, 618 (1934).
- 16 T. H. Dunning, *J. Chem. Phys.* **90** (2), 1007 (1989).
- 17 M. J. Frisch, G. W. Trucks, and H. B. Schlegel *et al.*, *Gaussian 03*, Revision C.02, Inc., Wallingford, CT (2004).
- 18 G. Schaftenaar and J. H. Noordik, *J. Comput.-Aided Mol. Des.* **14** (2), 123 (2000).
- 19 D. A. Clabo, W. D. Allen, R. B. Remington, Y. Yamaguchi, and H. F. Schaefer, *Chem. Phys.* **123** (2), 187 (1988).
- 20 W. D. Allen, Y. Yamaguchi, A. G. Csaszar, D. A. Clabo, R. B. Remington, and H. F. Schaefer, *Chem. Phys.* **145** (3), 427 (1990).
- 21 W. H. Miller, R. Hernandez, N. C. Handy, D. Jayatilaka, and A. Willetts, *Chem. Phys. Lett.* **172** (1), 62 (1990).

- 22 V. Barone, *J. Chem. Phys.* **120** (7), 3059 (2004).
- 23 V. Barone, *J. Chem. Phys.* **122** (1), 014108 (2005).
- 24 V. Barone, *J. Chem. Phys.* **101** (12), 10666 (1994).
- 25 T. Pankewitz, A. Lagutschenkov, G. Niedner-Schatteburg, S. S. Xantheas, and Y. T. Lee, *J. Chem. Phys.* **126** (7), 074307/1 (2007).
- 26 C. Merkert, Messungen und Rechnungen der Infrarotspektren der deprotonierten Pimelin- und Korksäure, Diplomarbeit, Technische Universität Kaiserslautern, 2007.
- 27 N. I. Hammer, E. G. Diken, J. R. Roscioli, M. A. Johnson, E. M. Myshakin, K. D. Jordan, A. B. McCoy, X. Huang, J. M. Bowman, and S. Carter, *J. Chem. Phys.* **122** (24), 244301 (2005).
- 28 X. C. Huang, B. J. Braams, and J. M. Bowman, *J. Chem. Phys.* **122** (4) (2005).
- 29 R. Car and M. Parrinello, *Phys. Rev. Lett.* **55** (22), 2471 (1985).

## 6. Preliminary Experimental and Quantum Chemical Studies for IRMPD and IR Matrix Isolation Spectroscopy of Dioxygen Containing Nonheme Iron(III) Catecholate Complexes

### 6.1 Introduction

Within the class of mononuclear nonheme enzymes the catechol dioxygenases play an important role in the degradation of aromatic compounds in the biosphere through soil bacteria under aerobic conditions.<sup>1-4</sup> Catechol dioxygenases are subclassified into intradiol and extradiol catechol dioxygenases. Both kinds of dioxygenases catalyze the C–C bond cleavage of the catechol ring, but differ in the resulting products. The intradiol dioxygenases use nonheme Fe(III) for the cleavage of the C–C bond of the enediol, which leads to the *cis,cis*-muconic acids (Fig. 6.1).

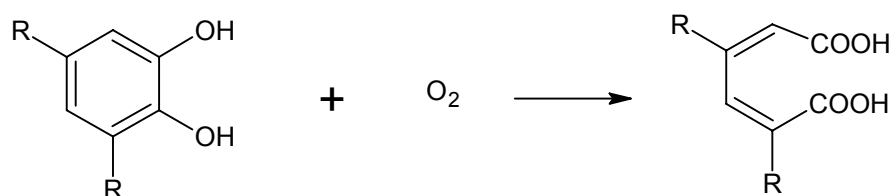


**Figure 6.1:** Oxidative cleavage of the intradiol-C–C bond of catechol derivatives yields the corresponding muconic acids (catechol (**cat**): R=H; 3,5-di-tert-butyl-catechol (**dbc**): R =tert-butyl).

In general, the extradiol dioxygenases use nonheme Fe(II) (or rarely a Mn(II) ion) and cleave the bond adjacent to the enediol, resulting, after hydrolysis, in the 2-hydroxy-muconic-aldehyde. In intradiol oxygenases, the Fe(III) ion is ligated by two tyrosine and two histidine residues and either a  $(\text{OH})^-$  or a water molecule in a distorted trigonal bipyramidal geometry.<sup>5-10</sup> When catechol coordinates to the Fe(III) ion in a chelating way, one tyrosine residue is released to form a distorted octahedral geometry with one vacant site. Essential for the catalytic activity of these enzymes is the activation and incorporation of molecular oxygen. Although a lot of effort has been put into the characterization of the assumed structure of the postulated intermediate peroxo-complex, up to date there is no unambiguous evidence for any of the proposed structures and resulting reaction mechanisms.

Functional model complexes for catechol dioxygenases have been developed for the evaluation of the reaction mechanisms and as catalytic systems for the oxidation of catecholes, with respect to a possible application in the amelioration of waters. Que et al. presented a

possible scheme for the reaction mechanism of the intradiol catechol dioxygenase (cf. Fig. 6.2).<sup>3</sup>

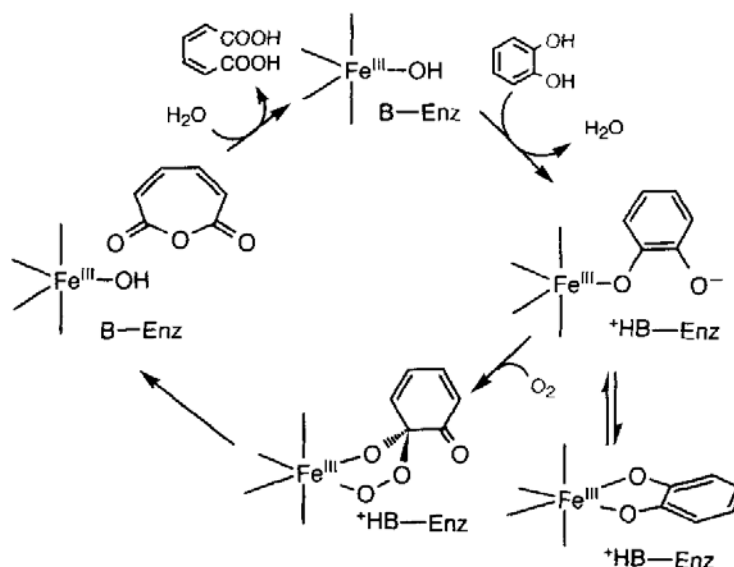


**Figure 6.2:** Assumed reaction mechanism of the intradiol-cleaving catechol dioxygenase.<sup>3</sup>

The model complexes of interest for this work were first synthesized in the group of H.- J. Krüger.<sup>11</sup> They contain the tetraazamacrocyclic ligand *N,N'*-Dimethyl-2,11-diaza[3.3](2,6)-pyridinophan (**1**), also named L-N<sub>4</sub>Me<sub>2</sub> (Fig. 6.3). Reaction of iron(III) chloride with the ligand in alcoholic solution, followed by the addition of catecholate anions yields the intense purple-colored ionic complexes [(L-N<sub>4</sub>Me<sub>2</sub>)Fe(cat)]<sup>+</sup> (**2a**) and [(L-N<sub>4</sub>Me<sub>2</sub>)Fe(dbc)]<sup>+</sup> (**3a**). The abbreviations *cat* and *dbc* stand for catecholate and 3,5-di-*tert*-butylcatecholate, respectively.

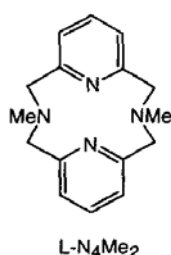


**Figure 6.3:** *N,N'*-Dimethyl-2,11-diaza[3.3](2,6)pyridinophan, L-N<sub>4</sub>Me<sub>2</sub> (**1**)

The experimental aim of this work is to perform a mass spectrometric analysis with an electrospray ion source coupled to a FT-ICR mass spectrometer (cf. Ch. 2). The first step is the representation of the catalytically active complex by means of ESI-MS. Tracking of the reaction of the complex with molecular oxygen out of the condensed phase will follow with

the aim of isolation of an intermediate structure which contains both the complex and the dioxygen. If the isolation of the complex-O<sub>2</sub>-adduct is ensured with sufficient intensity in the MS experiment, the necessary preliminary steps for further spectroscopic studies are provided. Possible spectroscopic experiments for an unambiguous determination of the structure of the intermediate complex-O<sub>2</sub>-adduct are infrared multiphoton dissociation (IRMPD) and infrared matrix isolation spectroscopy.

The results of the performed ESI-MS experiments can be found in full detail in the diploma thesis of Anna Bytzek.<sup>12</sup> In this chapter only the most crucial results and instructions for the future spectroscopic experiments will be described. The emphasis of this work is placed on the ab initio calculation of the complexes **2a** and **3a** and some of their possible O<sub>2</sub>-adducts **2b** and **3b** of the formal composition [(L-N<sub>4</sub>Me<sub>2</sub>)Fe(cat)O<sub>2</sub>]<sup>+</sup> (**2b**) and [(L-N<sub>4</sub>Me<sub>2</sub>)Fe(dbc)O<sub>2</sub>]<sup>+</sup> (**3b**), and their corresponding IR frequencies, together with a summary of the ESI-MS experiments.

## 6.2 Measurements with ESI-FT-ICR-MS

Dark blue crystals of the biomimetic model complex [(L-N<sub>4</sub>Me<sub>2</sub>)Fe(cat)](BPh<sub>4</sub>) were dissolved in dried and degassed acetonitrile. Careful handling of the solution under inert gas conditions enables the measurement of the ESI-FT-ICR-MS spectrum of [(L-N<sub>4</sub>Me<sub>2</sub>)Fe(cat)]<sup>+</sup> (**2a**) in the positive ion mode at a concentration of 10<sup>-6</sup> M (Fig. 6.4). The dominant signal at 432.121 m/z is assigned to the complex **2a**.

A very weak signal at 394.033 m/z belongs to [(L-N<sub>4</sub>Me<sub>2</sub>)FeCl<sub>2</sub>]<sup>+</sup> which is a byproduct originating from the synthesis of the model complex. Under inert gas conditions no signal corresponding to the O<sub>2</sub>-adducts **2b** is observed.

In the next step, the complex acetonitrile solution was allowed to get into contact with dioxygen (air) in an open flask. Every ten minutes mass spectra of the solution were recorded. Due to the extremely slow reaction of **2a** with dioxygen, the O<sub>2</sub>-adduct **2b** was not observed in the mass spectra. [(L-N<sub>4</sub>Me<sub>2</sub>)Fe(cat)](BPh<sub>4</sub>) was the first model complex which showed a ring cleavage of the coordinatively bound catecholate ligand although with much slower reaction constants (2.77×10<sup>-3</sup> M<sup>-1</sup> s<sup>-1</sup>) compared to the enzyme (2.5×10<sup>5</sup> M<sup>-1</sup> s<sup>-1</sup>). Nevertheless, the composition of the mass spectra changes with increasing reaction time. Further signals arise at lower masses (lower than the model complex **2a**). The assignment of those species shows that

they arise from the byproduct, as they contain chloride. No unambiguous products of the assumed main reaction are observed within a reasonable reaction time.

Sample solutions of  $10^{-6}$  M  $[(L-N_4Me_2)Fe(dbc)](BPh_4)$  in dried and degassed acetonitrile for the measurement of the ESI-FT-ICR-MS spectra were prepared in the same way as the corresponding solutions of the model complex **2a**.

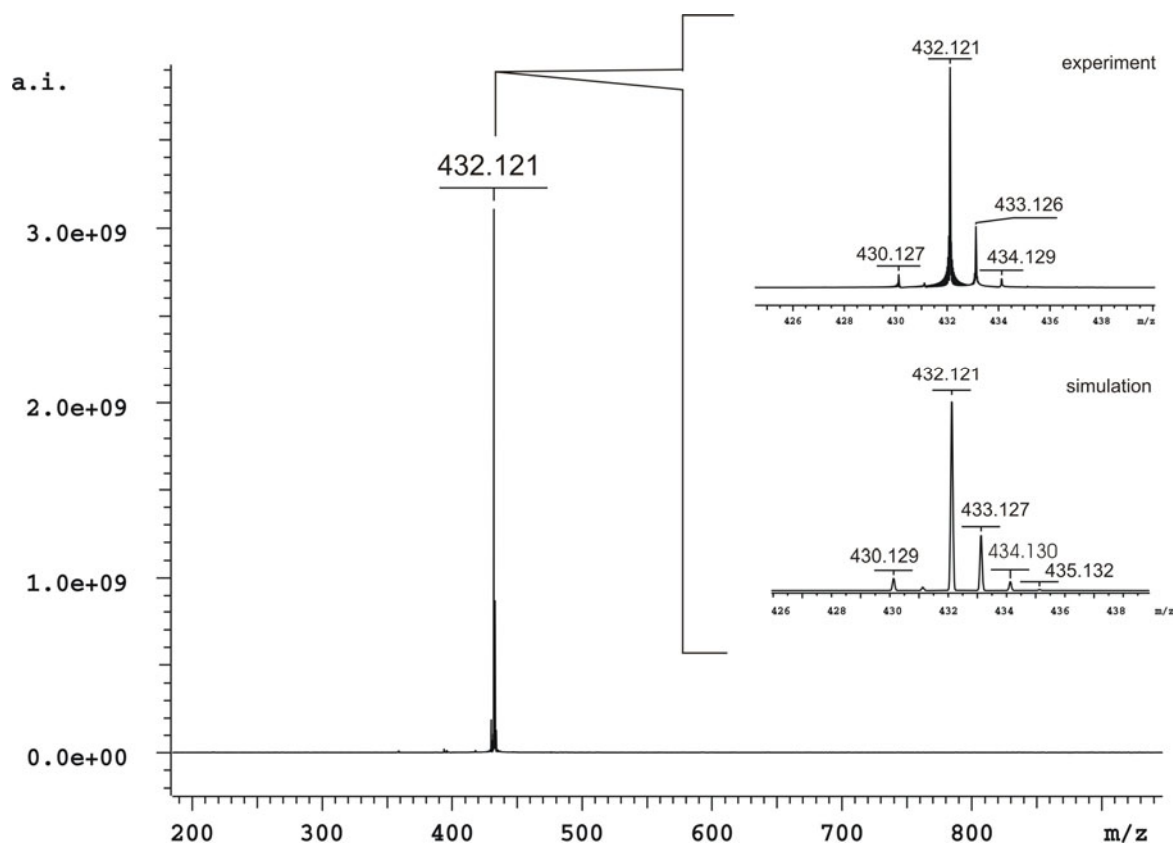


**Figure 6.4:** Positive ion mode ESI-FT-ICR-MS spectrum of  $[(L-N_4Me_2)Fe(cat)]^+$  (**2a**) in dried acetonitrile. The inset shows the isotopic pattern of the complex as found in the experiment and simulated by XMASS.

In contrast to the acetonitrile solution of  $(L-N_4Me_2)Fe(cat)]^+$ , the  $O_2$ -adduct **3b** is visible in the mass spectrum in case of  $(L-N_4Me_2)Fe(dbc)]^+$  (544.238 m/z) (Fig. 6.5). Nevertheless, the intensity of **3b** at 576.231 m/z is too small to perform an effective isolation close to the signal of the complex **3b** with its high intensity. Whether the  $O_2$ -adduct **3b** is formed during the ESI process in which the solution can get into contact with traces of  $O_2$  within the spraying chamber, or whether the small amount of the dioxygen adduct is already present in solution remains open. However, the observation of the  $O_2$ -adduct **3b** correlates with the increased reactivity of **3a** ( $3.77 \times 10^{-1} M^{-1} s^{-1}$ ) in solution compared to the reactivity of **2a**. Additional dioxygen, provided in form of compressed air (instead of pure dinitrogen) as

nebulizing and drying gas, did not increase the intensity of **3b** in the mass spectrum. The only visible effect is a slight increase in the intensity of signals of lower mass which are assigned to  $[(L-N_4Me_2)FeCl]^+$  ( $m/z = 359.072$ ) and  $[(L-N_4Me_2)Fe_2Cl_2O]^+$  ( $m/z = 367.073$ ) (for a complete list of all low intensity peaks in the spectrum refer to Ref. 12).

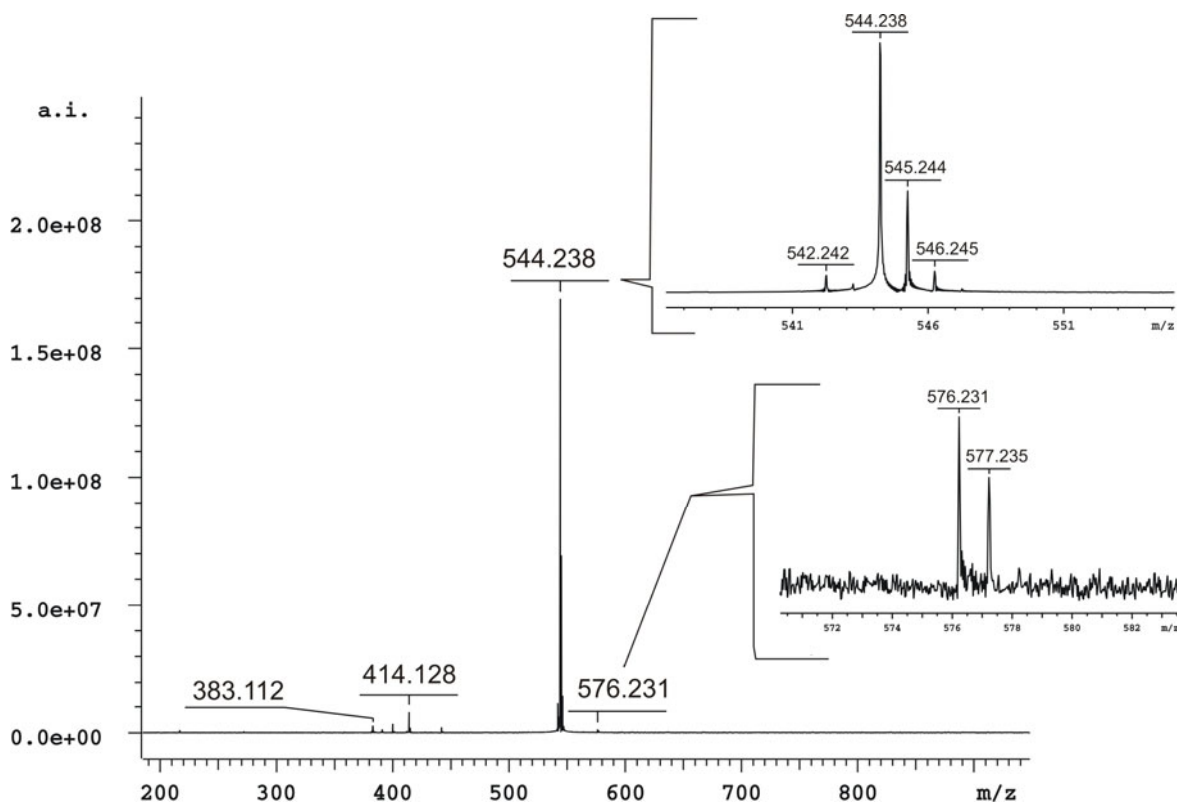


**Figure 6.5:** Positive ion mode ESI-FT-ICR-MS spectrum of  $[(L-N_4Me_2)Fe(dbc)]^+$  (**3a**) in dried acetonitrile. The inset shows the isotopic pattern of the pure complex and of the complex- $O_2$  (**3b**) adduct.

In the next step, the originally dried and degassed sample solution was allowed to react with ambient air in an open flask. Mass spectra were recorded every ten minutes. The model complex **3a** reacts with the dioxygen under formation of **3b**, which then further reacts into various products. The result of this mass spectrometric reaction control is that the intensity of **3b** is highest after 30 minutes.

In order to improve the poor intensity of the  $O_2$ -adduct **3b** and to make this species available for IRMPD and IR spectroscopic matrix isolation experiments with a temporally stable high concentration, a mixing scheme was developed as schematically presented in Figure 6.6. A  $10^{-5}$  M dried and degassed sample solution and a sample of acetonitrile of natural  $O_2$  content are injected separately at  $100\mu\text{l/h}$  into two tubes that connect to a T-fitting and from there via a 0.6 m capillary to the ESI spray chamber. This leads to a constant

reaction time of 30 minutes within the capillary before spraying the mixed sample and recording the mass spectra.

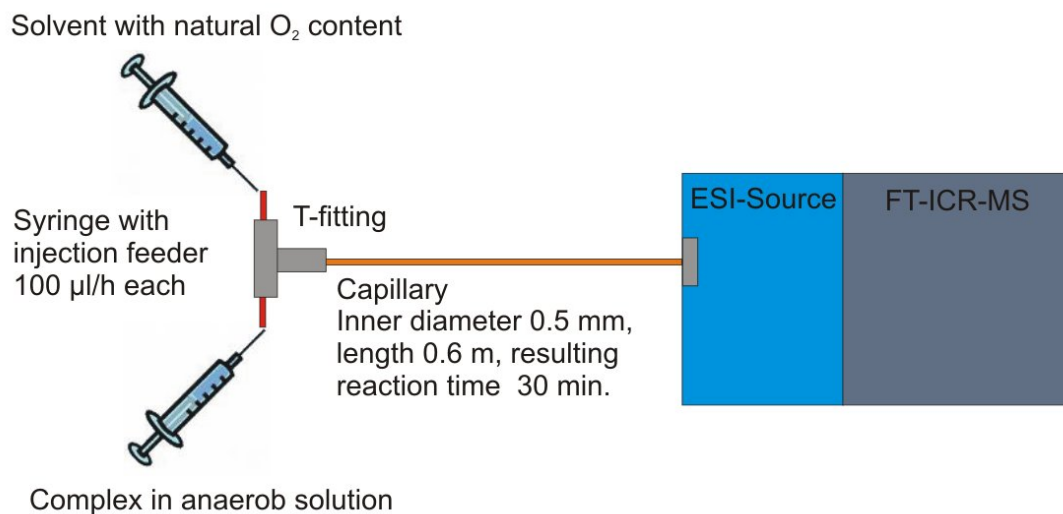


**Figure 6.6:** Scheme of the online mixing experiment for the temporal stabilization of the O<sub>2</sub>-adduct **3b** of the [(L-N<sub>4</sub>Me<sub>2</sub>)Fe(dbc)]<sup>+</sup> complex.

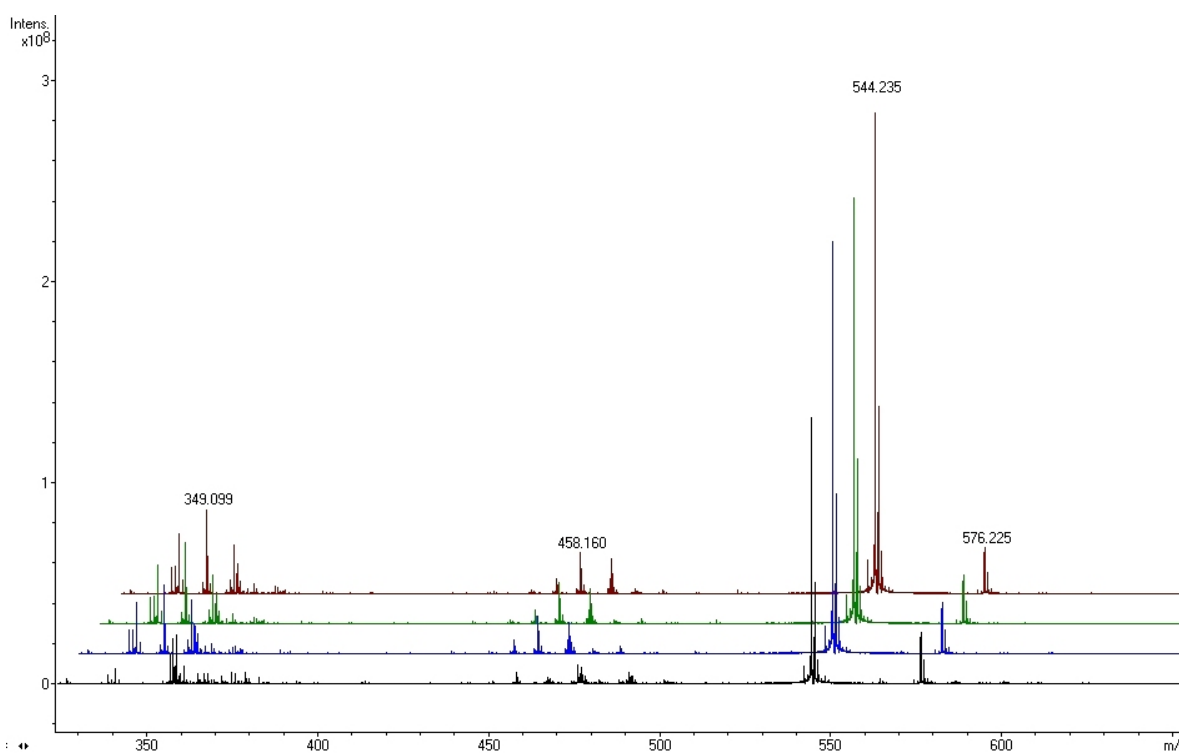


**Figure 6.7:** Positive ion mode ESI-FT-ICR-MS spectra of the temporal reproducibility of the O<sub>2</sub>-adduct of the [(L-N<sub>4</sub>Me<sub>2</sub>)Fe(dbc)]<sup>+</sup> complex (m/z = 576.225). The reaction time after mixing the O<sub>2</sub> containing acetonitrile with the solution of dried acetonitrile and the complex is always 30 minutes. The first spectrum after mixing (black, t = 0 min) slightly differs from the others. After some minutes an equilibrium within the mixing capillary is reached and the resulting spectra show the same peaks with constant intensities over two hours (blue t = 5 min.; green t = 60 min.; red t = 120 min).



The temporal evolution of the recorded mass spectra after mixing is presented in Fig. 6.7. The first spectrum, which was taken directly after a reaction time of 30 minutes, slightly differs from those that were recorded at later times. After an equilibration time of five minutes, all following spectra show the same signals which are of comparable intensities. Over a period of two hours we observed comparable spectra.

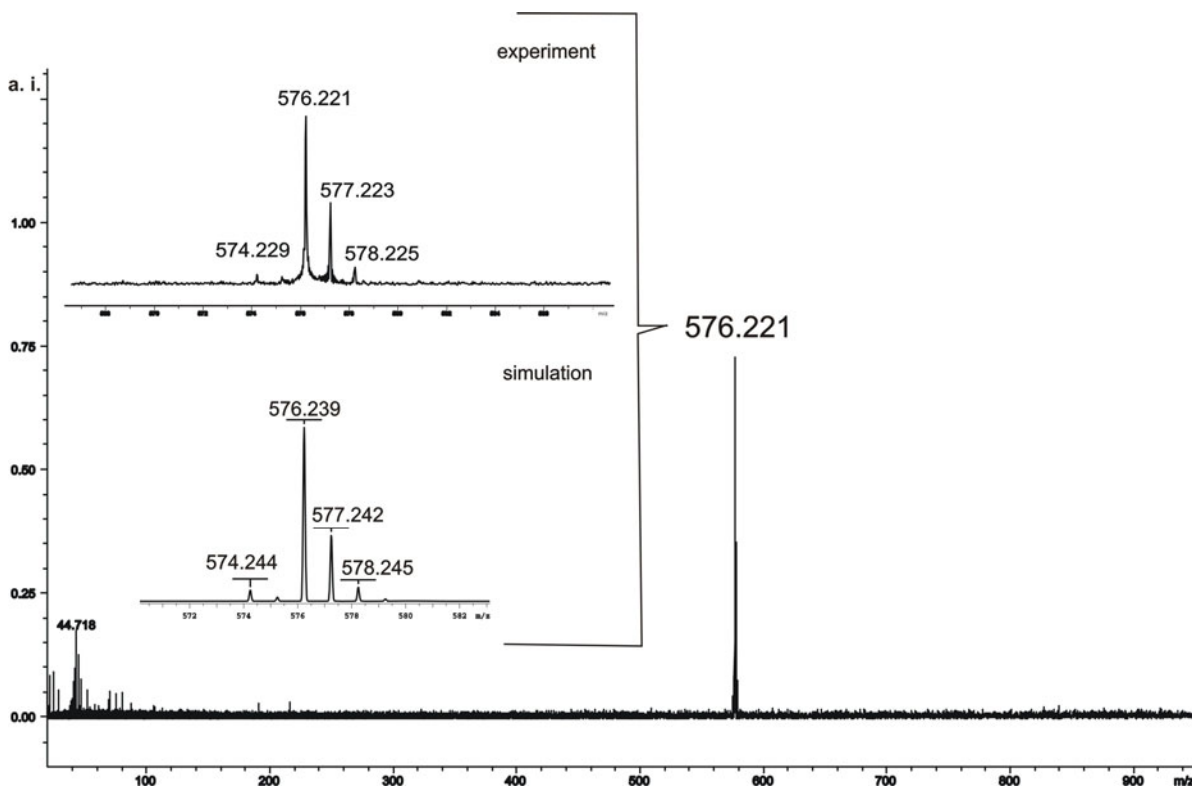


**Figure 6.8:** Positive ion mode ESI-FT-ICR-MS spectrum of the broadband isolation of the  $O_2$ -adduct (**3b**) of  $[(L-N_4Me_2)Fe(dbc)]^+$ . The inset shows the isotopic pattern of **3b** as observed in the experiment and as simulated by XMASS.

By means of the applied mixing scheme it was then possible to perform an effective broadband isolation of the  $O_2$ -adduct of interest (cf. Fig. 6.8). Although the model complex **3a** is still of high intensity compared to the  $O_2$ -adduct, the isolation of **3b** is successful under conservation of the natural isotopic pattern (see inset of Fig. 6.8).

These preliminary mass spectrometric experiments provide access to further IRMPD and matrix isolation studies of the  $O_2$ -adduct of the  $(L-N_4Me_2)Fe(dbc)]^+$  model complex in order to determine the particular structure of this complex.

### 6.3 Density Functional Calculations

Density functional calculations of  $[(L-N_4Me_2)Fe(cat)]^+$  **2a** and  $[(L-N_4Me_2)Fe(dbc)]^+$  **3a** as well as of several of their possible dioxygen containing constitutional congeners **2b** and **3b** (e.g. peroxo complexes) were carried out using the Gaussian03 program package.<sup>13</sup> Results are visualized with Gaussview.<sup>14</sup> The hybrid density functional B3LYP was used within all geometry and frequency calculations. Starting from a small basis set (3-21G) the resulting geometries were further optimized using the 6-31G basis set on all atoms. Due to the lack of polarization functions the results are regarded as approximate, preliminary results. A broad screening of potential structures was not possible with a larger basis set so far. However, first trials with larger basis sets (up to TZVP) showed the same energetic order of the various spin states of **2a**, which justifies the use of the smaller basis sets for a first screening.

Geometry optimizations of the model complexes **2a** and **3a** were carried out as described above. According to the DFT calculations of the gas phase structures, both model complexes prefer an electronic high spin configuration ( $S = 5/2$ ) which is in agreement with the observation of electron spin resonance (ESR) measurements of the complexes in solution. However, in the solid state these complexes also show a partial low spin character.<sup>15</sup> Recently, it has been shown that the spin state of catecholato-iron(III) complexes changes from high to low spin in the solid state when lowering temperatures<sup>10,16-18</sup> and that the substituents of the catecholate ligand affect the spin-crossover transition.<sup>18</sup> Therefore calculations of low spin structures are also included in this study. Nevertheless, doublet and quartet spin states of the complexes **2a** and **3a** are energetically disfavoured (cf. Table 6.1). The relative energy difference between sextet and quartet spin state in complex **2a** amounts to  $11.5 \text{ kJ mol}^{-1}$ , and the difference between sextet and doublet spin state is  $20.5 \text{ kJ mol}^{-1}$ . In case of the model complex **3a** the difference between sextet and quartet spin state is  $11.9 \text{ kJ mol}^{-1}$ . The doublet spin state is again more unfavored by  $18.8 \text{ kJ mol}^{-1}$  with respect to the sextet state. The calculated structures of the energetically favored sextet spin states of **2a** and **3a** are depicted in Figure 6.9.

Even with a comparably small basis set, the comparison of the calculated structures of the model complexes **2a** and **3a** and their corresponding crystal structures shows good agreement of the structural parameters like bond lengths and angles (cf. Table 6.2). However, small deviations between the experimental X-ray data and the calculated ones are expected, as the X-ray data refers to the complexes in the solid phase in which the complex exists together

with its counterion and incorporated solvent molecules. The calculated structures, on the other hand, represent the bare cationic complexes in the gas phase.

**Table 6.1:** B3LYP/6-31G calculated relative energy differences  $\Delta E$  between different spin states for  $[(L-N_4Me_2)Fe(cat)]^+$  (**2a**) and  $[(L-N_4Me_2)Fe(dbc)]^+$  (**3a**). The respective minimum isomer of **2a** and **3a** are arbitrarily set to zero, all other values are given relative to them in  $\text{kJ mol}^{-1}$ .

	S = 1/2	S = 3/2	S = 5/2
<b>2a</b>	20.5	11.5	0
<b>3a</b>	18.8	11.9	0

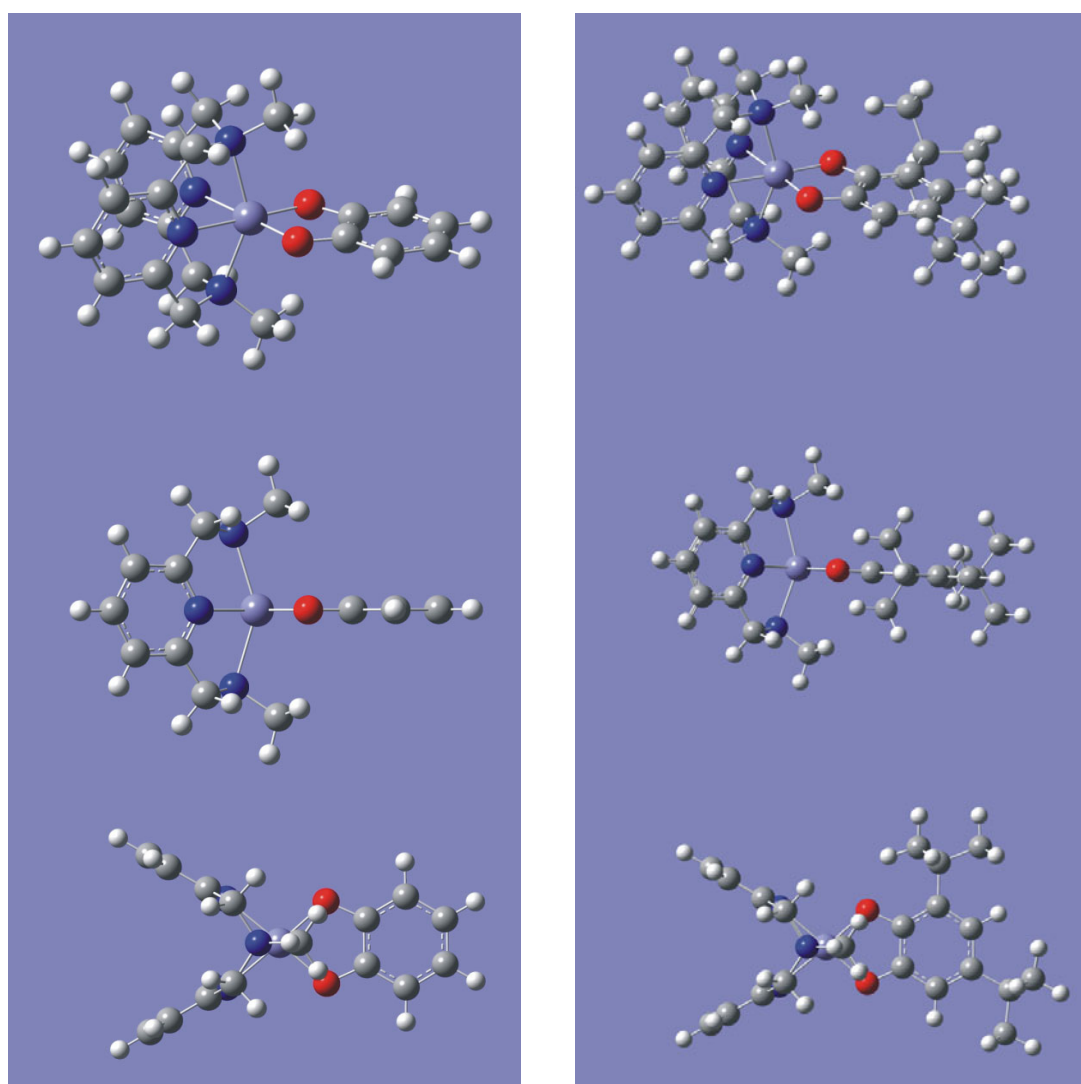


**Figure 6.9:** B3LYP/6-31G geometry optimized structures of high spin ( $S = 5/2$ )  $[(L-N_4Me_2)Fe(cat)]^+$  (**2a**, left) and high spin ( $S = 5/2$ )  $[(L-N_4Me_2)Fe(dbc)]^+$  (**3a**, right) (from top to bottom: tilted, side and top view). Grey = C, white = H, light blue = Fe, blue = N, red = O.

**Table 6.2:** Comparison of selected bond lengths (Å) and angles (degrees) in [(L-N<sub>4</sub>Me<sub>2</sub>)Fe(cat)]<sup>+</sup> (**2a**) and [(L-N<sub>4</sub>Me<sub>2</sub>)Fe(dbc)]<sup>+</sup> (**3a**) derived from crystal structure analysis and DFT calculations (B3LYP/6-31G, S=5/2).

	[(L-N <sub>4</sub> Me <sub>2</sub> )Fe(cat)] <sup>+</sup> (x 2.5 CH <sub>3</sub> CN)			[(L-N <sub>4</sub> Me <sub>2</sub> )Fe(dbc)] <sup>+</sup> (x 0.5 CHCl <sub>3</sub> )		
	X-ray	B3LYP	Δ	X-ray	B3LYP	Δ
Fe(1)–O(1)	1.903(3)	1.929	+0.026	1.895(5)	1.932	+0.037
Fe(1)–O(2)	1.915(3)	1.929	+0.014	1.911(5)	1.936	+0.025
Fe(1)–N(1)	2.222(3)	2.286	+0.064	2.241(6)	2.295	+0.054
Fe(1)–N(2)	2.105(3)	2.138	+0.033	2.121(6)	2.139	+0.018
Fe(1)–N(3)	2.223(3)	2.286	+0.063	2.235(6)	2.295	+0.06
Fe(1)–N(4)	2.106(3)	2.138	+0.032	2.115(6)	2.141	+0.026
O(1)–C(17)	1.353(5)	1.367	+0.014	1.344(8)	1.365	+0.021
O(2)–C(18)	1.329(5)	1.367	+0.038	1.368(8)	1.367	-0.001
C(17)–C(18)	1.415(7)	1.428	+0.013	1.411(10)	1.427	+0.016
C(17)–C(22)	1.385(7)	1.400	+0.015	1.380(10)	1.400	+0.020
C(18)–C(19)	1.394(6)	1.400	+0.006	1.409(10)	1.418	+0.009
C(19)–C(20)	1.369(8)	1.398	+0.029	1.396(10)	1.400	+0.004
C(20)–C(21)	1.369(9)	1.409	+0.040	1.399(10)	1.422	+0.023
C(21)–C(22)	1.427(8)	1.398	-0.029	1.393(10)	1.397	+0.004
O(1)–Fe(1)–O(2)	85.6(1)	83.5	-2.1	85.1(2)	82.8	-2.9
O(1)–Fe(1)–N(1)	97.7(1)	102.1	+4.4	105.1(2)	102.3	-2.8
O(1)–Fe(1)–N(2)	100.4(1)	97.9	-2.5	95.4(2)	98.4	+3.0
O(1)–Fe(1)–N(3)	107.3(1)	102.1	-5.2	98.3(2)	102.2	+3.9
O(1)–Fe(1)–N(4)	174.7(1)	178.6	+3.9	174.1(2)	179.0	+4.9
O(2)–Fe(1)–N(1)	103.7(1)	102.1	-1.6	104.4(2)	102.1	-2.3
O(2)–Fe(1)–N(2)	173.7(1)	178.6	+4.9	178.2(2)	178.8	+0.6
O(2)–Fe(1)–N(3)	99.0(1)	102.1	+3.1	100.8(2)	102.2	+1.4
O(2)–Fe(1)–N(4)	93.0(1)	97.9	+4.9	99.5(2)	98.2	-1.3
N(1)–Fe(1)–N(2)	77.4(1)	77.7	+0.3	77.2(2)	77.6	+0.4
N(1)–Fe(1)–N(3)	147.3(1)	147.4	+0.1	146.8(2)	147.3	+0.5
N(1)–Fe(1)–N(4)	77.6(1)	77.7	+0.1	77.7(2)	77.6	-0.1
N(2)–Fe(1)–N(3)	77.6(1)	77.7	+0.1	77.4(2)	77.6	+0.2
N(2)–Fe(1)–N(4)	81.1(1)	80.7	-0.4	79.9(2)	80.6	+0.7
N(3)–Fe(1)–N(4)	77.9(1)	77.7	-0.2	77.3(2)	77.6	+0.3

Atom numbering scheme of Fig. 1 in Ref. 11. Values taken from H.- J. Krüger, habilitation thesis,<sup>15</sup> complexes 7.6 and 7.7 p. 208.

The calculated bond lengths of the complexes **2a** and **3a** tend to be longer by 1 – 6 pm than the ones derived from the crystal structures. The only exception is the bond length between the catecholates' C-3- and C-4-atom (labels C(21) and C(22) according to the labels in Ref.11). This calculated bond is about 3 pm shorter than observed in the crystal structure. Generally, the differences of the bond lengths within the C–C bonds of the catecholate moiety are less pronounced than in the crystal structure. Thus the catecholate moiety exhibits a stronger aromatic character in the calculated gas phase data than in the solid state data. Comparison of the bond angles does not provide a clear trend. Overall, the calculated angles are in good agreement with the experimental ones and do not differ more than a few degrees from each other (max. 4.9°).

In the next step, possible intermediary peroxo isomers of the formal stoichiometry  $[(L-N_4Me_2)Fe(cat)O_2]^+$  (**2b**) and  $[(L-N_4Me_2)Fe(dbc)O_2]^+$  (**3b**) are calculated on B3LYP/6-31G level of theory, each in different spin states. The postulated intermediate peroxo structures favor a spin state  $S=3/2$  for both model complexes (cf. Figure 6.10 and Table 6.3) in the calculated gas phase structures. However, this finding does not correspond to EPR measurements in solution where no change of spin during the reaction (incorporation of  $O_2$  and formation of the muconic anhydride product) was observable.<sup>12</sup> More accurate calculations may take a multiconfigurational approach in the future.

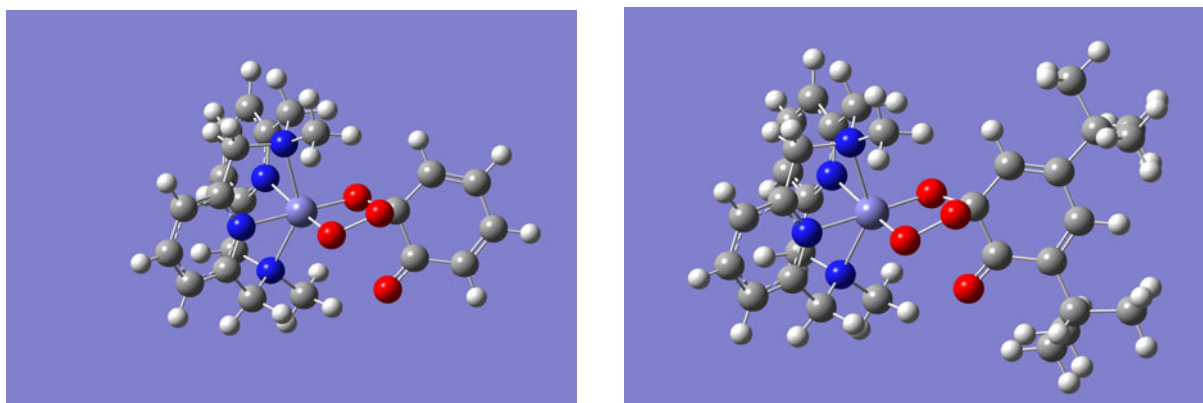


**Figure 6.10:** B3LYP/6-31G geometry optimized structures of isomers of the formal stoichiometries  $[(L-N_4Me_2)Fe(cat)O_2]^+$  (left) and  $[(L-N_4Me_2)Fe(dbc)O_2]^+$  (right) which incorporate the  $O_2$  ligand as a peroxo unit between the catecholate and the iron center. Grey = C, white = H, light blue = Fe, blue = N, red = O.

Other possible structures with the same formal elemental compositions which refer to **2b** or **3b** are found as association complexes with  $S = 7/2$ , where the  $O_2$  molecule is placed above or next to the ring-system of the catecholate moiety (see Fig. 6.11) in both kinds of model complexes.

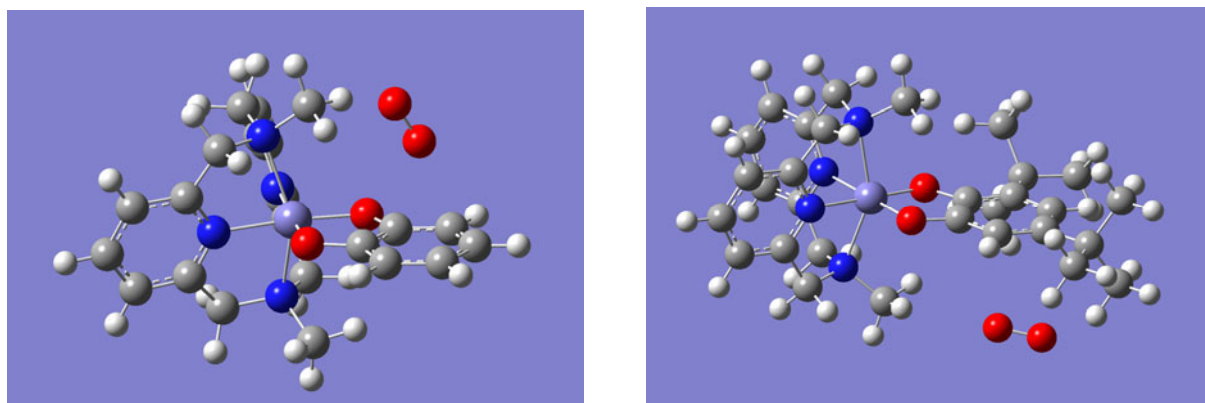


**Figure 6.11:** B3LYP/6-31G geometry optimized structures of isomers with the formal stoichiometries  $[(L-N_4Me_2)Fe(cat)O_2]^+$  (left) and  $[(L-N_4Me_2)Fe(dbc)O_2]^+$  (right) which loosely associate  $O_2$  next to the catechol unit. Grey = C, white = H, light blue = Fe, blue = N, red = O.

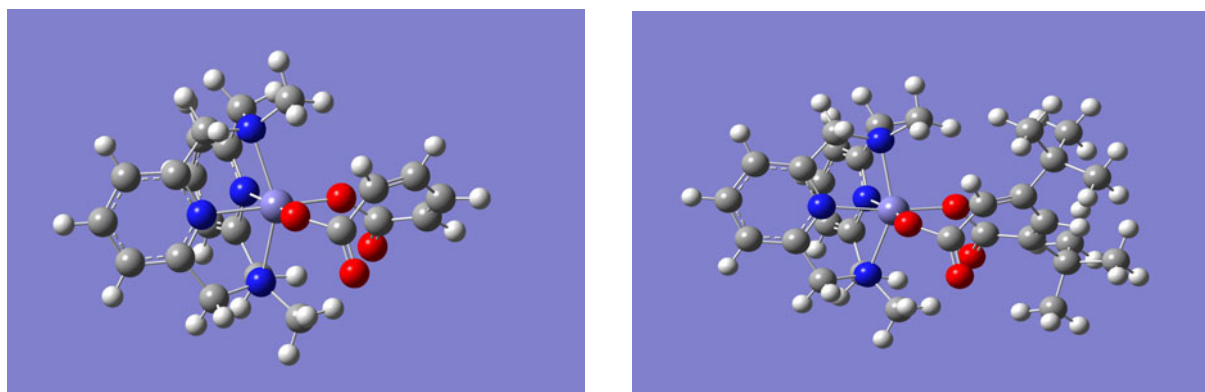


**Figure 6.12:** B3LYP/6-31G geometry optimized structures of isomers with the formal stoichiometries  $[(L-N_4Me_2)Fe(cat)O_2]^+$  (left) and  $[(L-N_4Me_2)Fe(dbc)O_2]^+$  (right) which contain a muconic acid unit, which corresponds to the preformed end product of the catalytic cycle. Grey = C, white = H, light blue = Fe, blue = N, red = O.

Nevertheless, our CID experiments (for a detailed description refer to Ref. 12) did not give rise to the assumption of either a peroxo or an association structure as no loss of molecular oxygen was observed in these experiments.<sup>12</sup> However, the peroxo complex structure has the elemental composition (the same mass) as the deprotonated muconic acid product, when coordinated to the iron(III) complex. Therefore, other possible structures than the peroxo and the association structure have to be considered, too.

**Table 6.3:** B3LYP/6-31G calculated relative energy differences  $\Delta E$  between different structures and spin states for complexes of the formal stoichiometry  $[(L-N_4Me_2)Fe(cat)O_2]^+$  (**2b**) and  $[(L-N_4Me_2)Fe(dbc)O_2]^+$  (**3b**) together with the asymptotic value of the sum of the separated triplet  $O_2$  and the complex **2a** resp. **3a**. The respective minimum isomers are arbitrarily set to zero, all other values are given relative to them in  $\text{kJ mol}^{-1}$ .

	S = 1/2	S = 3/2	S = 5/2	S = 7/2
<b>2b peroxo</b>	n.c.*	296.8	n.c.	-
<b>2b association</b>	n.c.	n.c.	273.3	263.6
<b>2b muconic</b>	41.7	37.6	0	-
<b>2a + O<sub>2</sub></b>	293.2	283.1	271.7	-
<b>3b peroxo</b>	n.c.	275.0	290.3	-
<b>3b association</b>	n.c.	n.c.	265.6	252.7
<b>3b muconic</b>	44.8	n.c.	0	-
<b>3a + O<sub>2</sub></b>	276.9	270.0	258.1	-

\*n.c. denotes calculations in which no convergence was achieved.

The energetically most favored isomers of the formal stoichiometry of **2b** and **3b** are isomers that already contain the structural motif of the endproduct, the muconic acid moiety. While the molecular oxygen is only weakly bound in the association complex (few  $\text{kJ mol}^{-1}$  in both cases), the respective isomers containing the peroxo motif are energetically even higher than the asymptotic values of the sum of the separated molecular oxygen and the complexes **2a** or **3a**. In contrast, the muconic isomers are significantly stabilized with respect to the sum of the educts by  $263.6 \text{ kJ mol}^{-1}$  (**2b**) and  $252.7 \text{ kJ mol}^{-1}$  (**3b**). The energy profile of the stabilization (or destabilization) is depicted in Figure 6.13.

As our CID experiments did not reveal loss of molecular oxygen within the structure of **3b** (the intensity of the  $O_2$ -adduct of **2b** was too low to perform CID studies), these findings together with the rate constants of the reaction in solution render the picture of the complexes **2b** and **3b** being muconic acid isomers. Absolute certainty about the structure of the complexes can only be obtained by means of further optical spectroscopy.

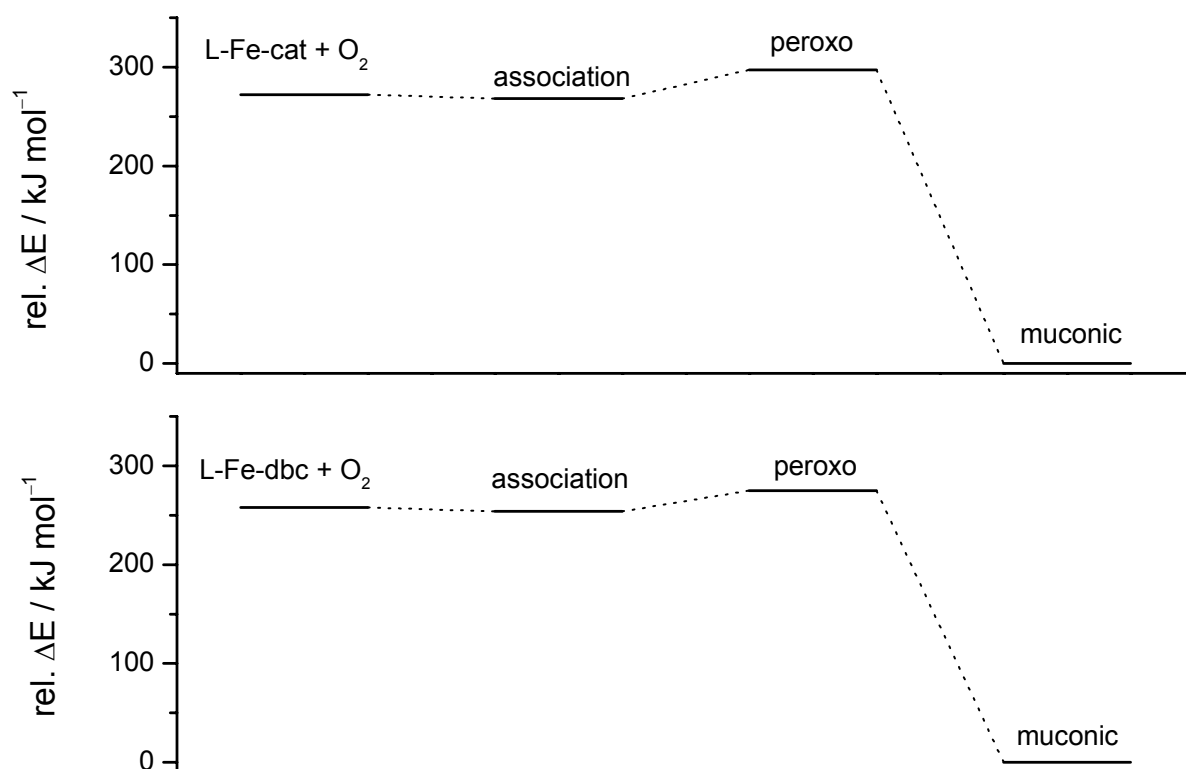


**Figure 6.13** Energy profile of several calculated isomers of **2b** (upper panel) and **3b** (lower panel). The asymptotic value of the separated complex and triplet O<sub>2</sub> are included for comparison. Barrier heights between the isomers are not known so far. The substituents at the catechol moiety show only small effects on the relative energetic position of the various isomers.

Next the IR absorption spectra of the three isomer types of **2b** and **3b** were calculated (cf. Figures 6.14 and 6.15). The comparison of the IR spectra of association and peroxo isomers predominantly reveals differences in the wavenumber region below 1100 cm<sup>-1</sup> independent of the model complex under study. These differences are due to the low frequency modes of the iron-peroxo unit, which appear around 550 cm<sup>-1</sup> to 640 cm<sup>-1</sup>. If the intermediate structure was either an association structure or a peroxo structure, then the initially planned IRMPD measurements at the Free Electron Laser CLIO most likely would not be successful. IRMPD spectra are based on the measurement of photon induced fragmentation of the complexes. However, to efficiently induce fragmentation, a certain amount of energy must be provided. In case of the low frequency region this is more difficult than in higher frequency regions due to the lower energy per photon (at constant binding energy). Thus unwarranted side effects like so called dark modes, where no fragmentation occurs due to an internal vibrational energy redistribution process (IVR) or broadening of the modes' profile (typically 10–20 cm<sup>-1</sup>, in the worst case up to 50 cm<sup>-1</sup>), may cause unambiguous



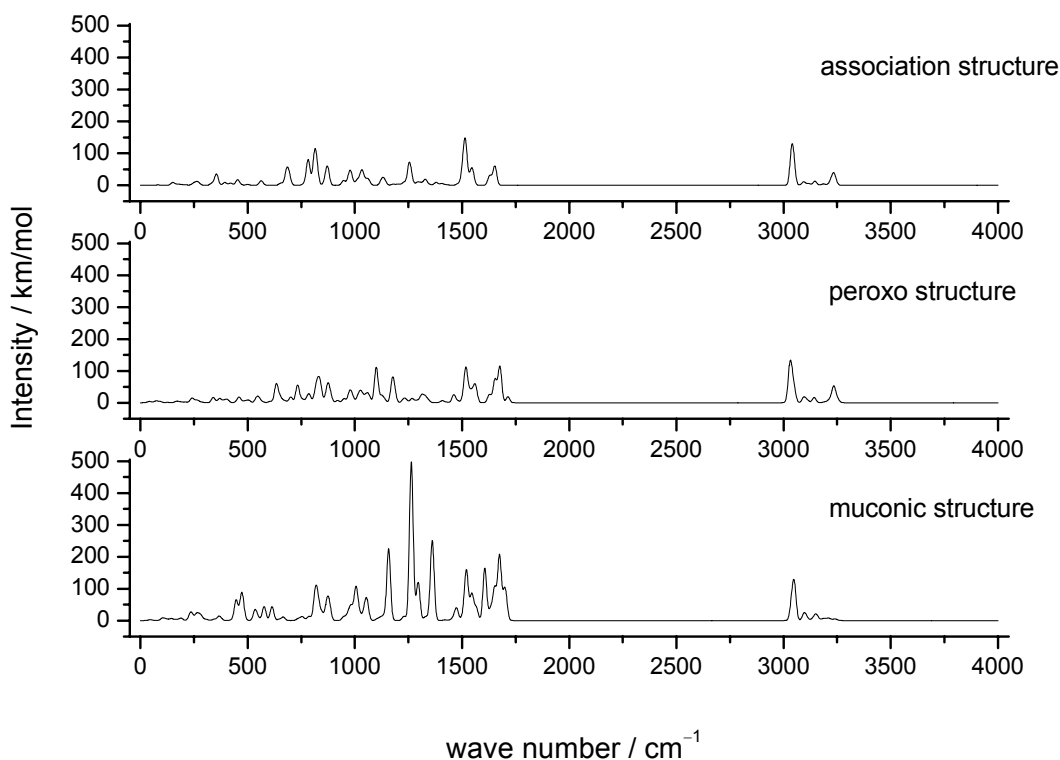


**Figure 6.14:** Unscaled frequencies of the most stable association, peroxy and muconic acid isomers of  $[(L-N_4Me_2)Fe(cat)O_2]^+$  calculated on B3LYP/6-31G level of theory, plotted with HWHM of  $10\text{ cm}^{-1}$ .

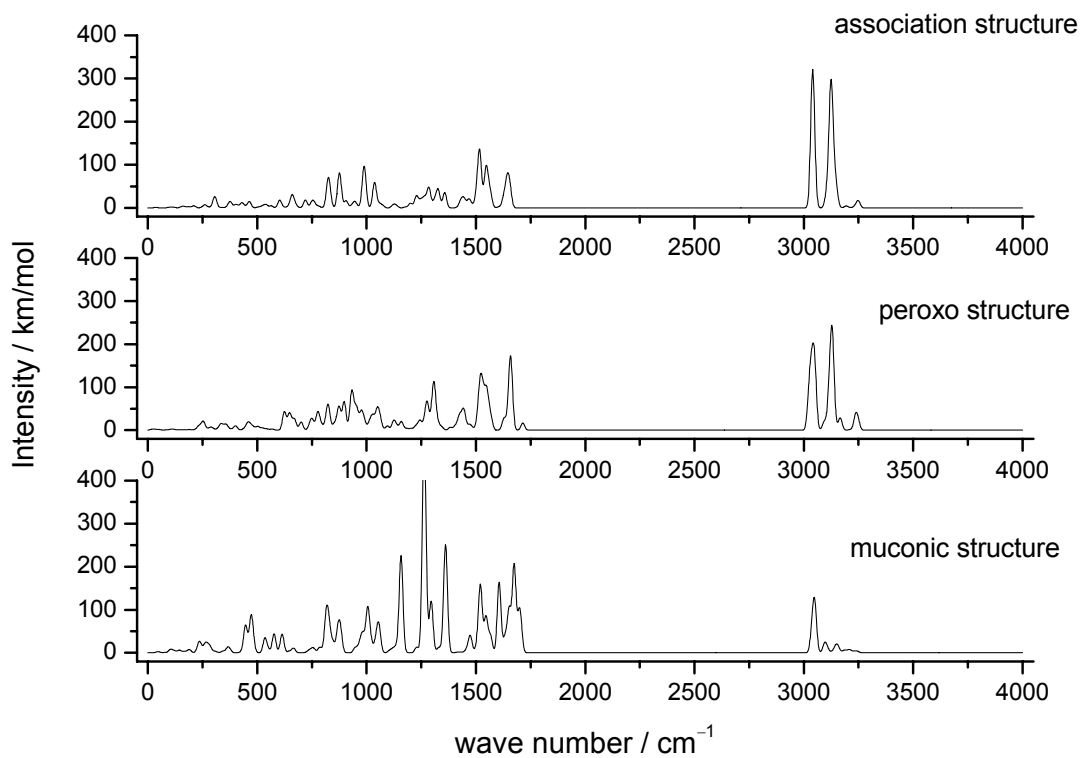


**Figure 6.15:** Unscaled frequencies of the most stable association, peroxy and muconic acid isomers of  $[(L-N_4Me_2)Fe(dbc)O_2]^+$  calculated on B3LYP/6-31G level of theory, plotted with HWHM of  $10\text{ cm}^{-1}$ .

spectra. In contrast, in case of the muconic isomer, the calculated spectrum clearly differs from those of the other two possible isomers in mode positions and intensity. This specific pattern in the region of 1100 to 1400  $\text{cm}^{-1}$  will most likely be measurable with CLIO, which provides high laser power in this wave number region. Furthermore the involved modes are predominately those that are located within the catecholate moiety close to the possible fragmentation sides, which are most likely the iron-carboxylate bonds, leading to the deprotonated muconic acid fragment and the  $(\text{L-N}_4\text{Me}_4)\text{Fe}^+$  fragment.

One further possibility to elucidate the structures of **2b** and **3b** is the application of IR (cryo) matrix isolation spectroscopy. This technique uses mass selected, isolated ions, which are deposited onto a (cryo) matrix.<sup>19,20</sup> This matrix usually consists of cooled rare gas atoms. The number density of the deposited ions is larger than the number of ions in the gas phase, which then makes the ions available to standard spectroscopy methods like IR or UV/VIS spectroscopy. The advantage of the conventional spectroscopy methods thereby lies in the applicability of narrow band lasers, in contrast to e.g. CLIO with its comparably broad laser profile. By means of the matrix isolation technique it would be possible to resolve spectral features in the region below 1100  $\text{cm}^{-1}$ . In addition, the generation of difference spectra between the  $^{16}\text{O}$  and  $^{18}\text{O}$  labelled  $\text{O}_2$ -adducts would be possible, which would provide additional information of the structures of the complexes **2b** and **3b**. Density functional calculations of the labelled and unlabelled difference spectra of the peroxo isomer **2b** are shown in Figure 6.16. The main difference appears in the low energy region from 550  $\text{cm}^{-1}$  to 750  $\text{cm}^{-1}$ . The peak to peak difference of the O–Fe–O mode at 633  $\text{cm}^{-1}$  (all O atoms  $^{16}\text{O}$ ) to the mode at 601  $\text{cm}^{-1}$  ( $^{18}\text{O}_2$  molecule added to the  $^{16}\text{O}$  containing complex) is only 32  $\text{cm}^{-1}$ , which would most probably not be clearly resolvable in IRMPD experiments with CLIO (if the available CLIO wave length actually goes down to this energy region which was not always the case – in the last few campaigns measurements below 650  $\text{cm}^{-1}$  were not feasible). If we further take into account that the presented spectra are unscaled, the possible usage of CLIO would be even more unlikely, as the relevant modes would shift to smaller numbers upon scaling. Due to the mode specific scaling factors this was not done here so far. Nevertheless, the main conclusion remains unaffected thereof.

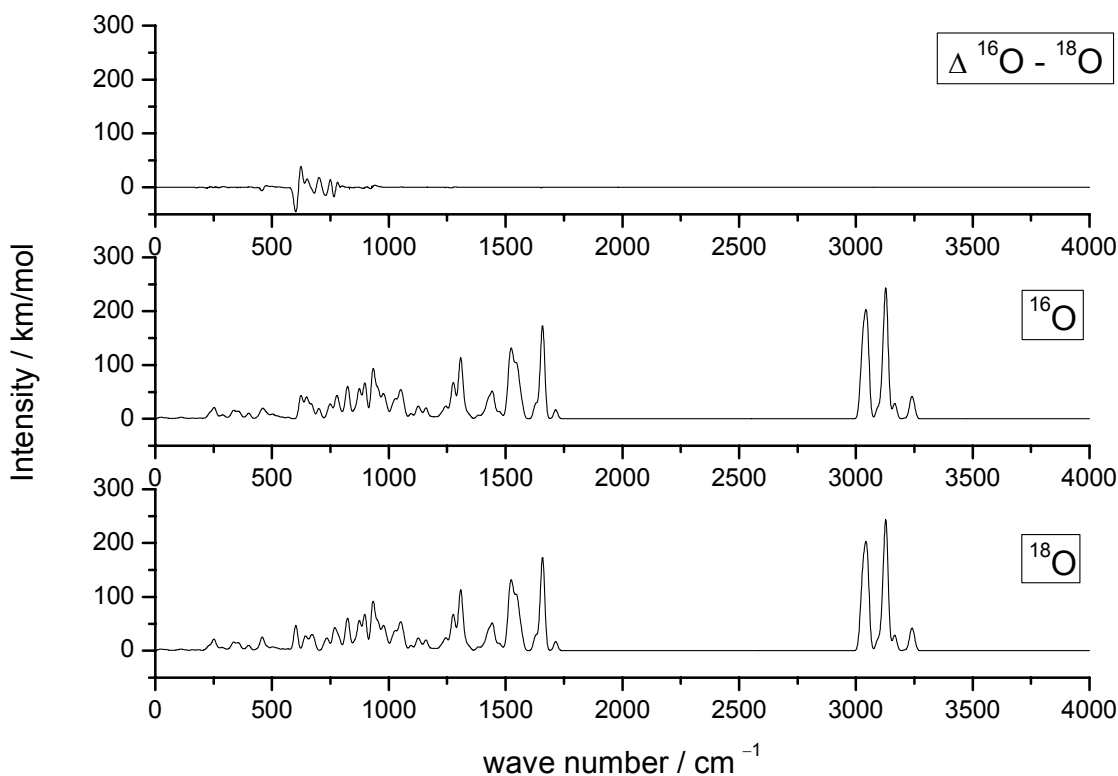


**Figure 6.16:** Calculated difference spectrum of the  $^{16}\text{O}$  and the  $^{18}\text{O}$  labelled peroxy structure of  $[(\text{L-N}_4\text{Me}_2)\text{Fe}(\text{dbc})\text{O}_2]^+$  (unscaled B3LYP/6-31G frequencies). The largest isotope shift is observed in the symmetric  $^{16}\text{O}\text{-Fe-}^{16}\text{O}$  mode to the  $^{18}\text{O}\text{-Fe-}^{16}\text{O}$  mode. The peak to peak difference of the respective modes is approximately  $32\text{ cm}^{-1}$ .

## 6.4 Summary and Outlook

ESI-FT-ICR-MS spectra unambiguously determined the model complexes  $[(\text{L-N}_4\text{Me}_2)\text{Fe}(\text{cat})]^+$  (**2a**) and  $[(\text{L-N}_4\text{Me}_2)\text{Fe}(\text{dbc})]^+$  (**3a**) after measurement of the complexes dissolved in acetonitrile under inert gas conditions. In case of the  $\text{O}_2$ -adduct of  $[(\text{L-N}_4\text{Me}_2)\text{Fe}(\text{dbc})]^+$ , the complex  $[(\text{L-N}_4\text{Me}_2)\text{Fe}(\text{dbc})\text{O}_2]^+$  (**3b**) has been successfully isolated in the ICR ion trap. The intensity of **3b** is sufficient for further spectroscopic studies. The necessary temporal stability of the intensity of **3b** is provided by means of a special online mixing scheme of the complex in dried and degassed solvent and additional solvent with natural  $\text{O}_2$  content.

The structures of the intermediate O<sub>2</sub>-adducts **2b** and **3b** remain unknown. Mass spectrometry experiments did not yield unambiguous evidence for the exclusive existence of any of the possible isomers. Due to the non-observation of O<sub>2</sub> loss within the CID experiment, it is unlikely that the O<sub>2</sub>-adducts are weakly bound association complexes. Furthermore, usually only energetically very stable species survive the transfer into the gas phase and the following long transfer from the ion source into the ion trap. The probability of observing unstable or meta-stable species in the ESI-MS spectra is low.

Preliminary quantum chemical calculations provide geometries and frequencies of the model complexes **2a** and **3a** as well as an energy profile and calculated IR spectra of various possible isomers of their O<sub>2</sub>-adducts **2b** and **3b**.

The MS experiments along with the calculated energetics and the rate constants of the catalytic reaction observed in solution together render the picture of the muconic isomer to be the most probable structure of the O<sub>2</sub>-adducts **2b** and **3b** in the MS spectra.

To gain final certainty of the structure of the complexes further spectroscopic data are needed. Due to its capability of high resolution over a broad spectral range, the spectroscopic method of choice would be IR (cryo) matrix isolation spectroscopy at sufficiently high resolution. IRMPD measurements at the Free Electron Laser CLIO could provide good results, if the O<sub>2</sub>-adducts **2b** and **3b** are of muconic-type, yet they are believed to yield unambiguous results in case of the existence of other isomer types.

Further quantum chemical calculations should be extended towards a postulated semi-quinone-like intermediate structure of the model complexes. This semi-quinone structures might act as contact points for the incorporation of the O<sub>2</sub> molecule. However, in our experiments no reproducible signals referring to this semi-quinone structures could be determined so far. The calculation of the reaction dynamics and barrier heights along the way from the model complex to the final products is of high interest. Furthermore, the effect of solvent influences on the energy profile of the various O<sub>2</sub>-adduct isomers should be considered in future studies.

## 6.5 References

- 1 L. Que, *Adv. Inorg. Biochem.* **5**, 167 (1983).
- 2 L. Que, *J. Chem. Educ.* **62** (11), 938 (1985).
- 3 L. Q. Jr., *Iron Carriers and Iron Proteins*, T. M. Loehr. (VCH, New York, 1989).
- 4 G. P. Horsman, A. Jirasek, F. H. Vaillancourt, C. J. Barbosa, A. A. Jarzecki, C. L. Xu, Y. Mekmouche, T. G. Spiro, J. D. Lipscomb, M. W. Blades, R. F. B. Turner, and L. D. Eltis, *J. Am. Chem. Soc.* **127** (48), 16882 (2005).
- 5 D. H. Ohlendorf, J. D. Lipscomb, and P. C. Weber, *Nature* **336** (6197), 403 (1988).
- 6 D. H. Ohlendorf, A. M. Orville, and J. D. Lipscomb, *J. Mol. Biol.* **244** (5), 586 (1994).
- 7 M. Ferraroni, I. P. Solyanikova, M. P. Kolomytseva, A. Scozzafava, L. Golovleva, and F. Briganti, *J. Biol. Chem.* **279** (26), 27646 (2004).
- 8 M. W. Vetting, D. A. D'Argenio, L. N. Ornston, and D. H. Ohlendorf, *Biochemistry* **39** (27), 7943 (2000).
- 9 M. W. Vetting and D. H. Ohlendorf, *Structure* **8** (4), 429 (2000).
- 10 M. Higuchi, Y. Hitomi, H. Minami, T. Tanaka, and T. Funabiki, *Inorg. Chem.* **44** (24), 8810 (2005).
- 11 W. O. Koch and H. J. Krüger, *Angewandte Chemie-International Edition in English* **34** (23-24), 2671 (1996).
- 12 A. Bytzek, *Untersuchung der elektronischen und strukturellen Eigenschaften sowie der Reaktivität von Catecholat-, Semichinonat- und Benzochinonat-Komplexen*, Diplomarbeit, Technische Universität Kaiserslautern, 2007.
- 13 M. J. T. Frisch, G. W.; Schlegel, H. B.; Scuseria, G. E.; Robb, M. A.; Cheeseman, J. R.; Montgomery, Jr., J. A.; Vreven, T.; Kudin, K. N.; Burant, J. C.; Millam, J. M.; Iyengar, S. S.; Tomasi, J.; Barone, V.; Mennucci, B.; Cossi, M.; Scalmani, G.; Rega, N.; Petersson, G. A.; Nakatsuji, H.; Hada, M.; Ehara, M.; Toyota, K.; Fukuda, R.; Hasegawa, J.; Ishida, M.; Nakajima, T.; Honda, Y.; Kitao, O.; Nakai, H.; Klene, M.; Li, X.; Knox, J. E.; Hratchian, H. P.; Cross, J. B.; Bakken, V.; Adamo, C.; Jaramillo, J.; Gomperts, R.; Stratmann, R. E.; Yazyev, O.; Austin, A. J.; Cammi, R.; Pomelli, C.; Ochterski, J. W.; Ayala, P. Y.; Morokuma, K.; Voth, G. A.; Salvador, P.; Dannenberg, J. J.; Zakrzewski, V. G.; Dapprich, S.; Daniels, A. D.; Strain, M. C.; Farkas, O.; Malick, D. K.; Rabuck, A. D.; Raghavachari, K.; Foresman, J. B.; Ortiz, J. V.; Cui, Q.; Baboul, A. G.; Clifford, S.; Cioslowski, J.; Stefanov, B. B.; Liu, G.; Liashenko, A.; Piskorz, P.; Komaromi, I.; Martin, R. L.; Fox, D. J.; Keith, T.; Al-Laham, M. A.; Peng,

C. Y.; Nanayakkara, A.; Challacombe, M.; Gill, P. M. W.; Johnson, B.; Chen, W.; Wong, M. W.; Gonzalez, C.; and Pople, J. A, Gaussian 03 Rev. C.02 (Gaussian, Inc., Wallingford CT, 2004).

<sup>14</sup> R. K. Dennington II, Todd; Millam, John; Eppinnett, Ken; Hovell, W. Lee; and Gilliland, Ray, GaussView, Version 3.09 (Semichem, Inc., Shawnee Mission, KS, 2003).

<sup>15</sup> H.-J. Krüger, Habilitation.

<sup>16</sup> S. Floquet, A. J. Simaan, E. Riviere, M. Nierlich, P. Thuery, J. Ensling, P. Gutlich, J. J. Girerd, and M. L. Boillot, Dalton Trans. (9), 1734 (2005).

<sup>17</sup> A. J. Simaan, M. L. Boillot, R. Carrasco, J. Cano, J. J. Girerd, T. A. Mattioli, J. Ensling, H. Spiering, and P. Gutlich, Chemistry-A European Journal **11** (6), 1779 (2005).

<sup>18</sup> T. Funabiki, A. Fukui, Y. Hitomi, M. Higuchi, T. Yamamoto, T. Tanaka, F. Tani, and Y. Naruta, J. Inorg. Biochem. **91** (1), 151 (2002).

<sup>19</sup> E. Whittle, D. A. Dows, and G. C. Pimentel, J. Chem. Phys. **22** (11), 1943 (1954).

<sup>20</sup> V. E. Bondybey, A. M. Smith, and J. Agreiter, Chem. Rev. **96** (6), 2113 (1996).

## 7. Complexes of Vanadium and Vanadium Oxides with Organic Solvents: FT-ICR-MS Study and IRMPD Spectra Compared to Ab Initio Calculations

### 7.1 Introduction

Transition metal oxides are known to be important in various industrial reactions as effective catalysts. In particular vanadium oxides are subject to intensive investigations as they can be found in heterogeneous catalysis, in semiconductor applications or coating materials.<sup>1</sup> Vanadium oxides are known to be oxidation catalysts.<sup>2</sup> The most important application in this field is the catalytic oxidation of SO<sub>2</sub> to SO<sub>3</sub> for the production of sulfuric acid. Further applications of vanadium oxide as catalysts can be found in the synthesis of maleic anhydride, phthalic anhydride and in the oxidative dehydrogenation of propane and butane.<sup>1-7</sup> Gas phase studies, mostly of mass spectrometric nature, are concerned with vanadium oxide clusters which have been suggested to be suitable model systems for the study of catalytically active sites. A whole series of studies has been published about the vanadium oxide clusters,<sup>8-13</sup> as well as about the clusters' reactivities towards organic molecules.<sup>8,14-26</sup> Together with ab initio calculations<sup>27-29</sup> all these experiments aim at elucidating not only structures of vanadium oxide clusters and their reaction products with organic molecules but also at revealing insight into the mechanistic details of catalytic reactions.

This work presents the first free electron laser (FEL) IR multiphoton dissociation (IRMPD) vibrational spectra of vanadium and vanadium oxide monocations when reacted with acetonitrile, methanol and ethanol. It has been shown before that a FEL is well suitable for IRMPD over a wide frequency range, yielding data that closely mimic IR absorption spectra.<sup>30-32</sup> The performed IRMPD experiments are supplemented by ab initio calculations which assist to give an interpretation of the gas phase IR spectra of the mass selected complexes and as such provide a powerful tool for structural elucidation.

FT-ICR-MS data recorded at the Kaiserslautern ICR will be presented in comparison with the data from the Orsay ICR setup MICRA (the mobile ICR analyzer). Due to the low mass resolution at MICRA, these additional will help to reensure the correct assignment of the mass peaks.

## 7.2 Experimental Details

IRMPD spectra were recorded at the "Centre Laser Infrarouge d'Orsay" (CLIO) free electron laser (FEL) facility. The experimental setup at CLIO is based on a 10 to 50 MeV electron accelerator with a gap tunable undulator. It provides for a large wavelength range in the infrared (3 to 90  $\mu\text{m}$ ) and it is continuously tuneable. The FEL temporal structure is composed of sequences of macropulses with duration of 8  $\mu\text{s}$  at a repetition rate of 25 Hz. Each of these macropulses comprises of 500 micropulses, each of which is only a few picoseconds long. The FEL laser light was focused into the center of a 1.24 T Fourier transform ion cyclotron resonance (FT-ICR) ion trap<sup>33</sup> by a spherical mirror of 1 m focal length. The ICR cell in use provides good optical access to its center, facilitating spectroscopic studies of ions stored within. Atomic  $\text{V}^1$  monocations were generated by a 1 Hz Quantel laser. It drives the ablation off a vanadium target adjacent to the ICR cell. The gaseous reactant (acetonitrile, methanol or ethanol) was admitted into the cell through a pulsed valve. Subsequently,  $\text{V}^1$  ions were allowed to form complexes with the reactant, and the most prominent complexes were mass selected by resonant frequency ejection techniques. Exposure to FEL IR radiation led to multiphoton absorption and fragmentation of complexes when resonant with a fundamental vibration. Fragment ion intensities and parent ion dips were recorded via mass spectrometry in dependence of the FEL wavelength in order to obtain the experimental IRMPD spectra. IRMPD spectra of the vanadium oxide alcohol complexes are computed as

$$\text{efficiency} = P_{\text{frag}} = -\ln \left( \frac{I_{\text{parent}}}{I_{\text{parent}} + \sum_i I_{\text{fragment}(i)}} \right) \quad (7.1)$$

while the some older apply spectra of vanadium oxide acetonitrile complexes are created by plotting the non-logarithmic  $\text{Frag}_{\text{norm}}$  values for reasons of convenience. The advantage of the logarithmic scale is the less pronounced noise level. However, in most cases differences in the spectra are small.

As long as the definite structure of a complex is uncertain, we utilize its formal composition in squared brackets, e.g.  $[\text{VC}_2\text{H}_3\text{NO}]^+$ . As soon as a reliable structure is determined, the composition of the complex will be given – where possible – in a (condensed) structure formula without squared brackets, e.g.  $\text{OV}(\text{NCCH}_3)^+$ . This is meant to mimic the proposed structure. For the sake of simplicity, the overall charge is given at the end, although



presumably located at the metal atom. Brackets are omitted wherever possible for the same reason.

### 7.3 Computational Details

Ab initio IR absorption spectra were calculated at the B3LYP level of theory for various electronic states of the complexes. Ahlrichs polarized triple- $\zeta$  basis sets<sup>34</sup> were applied for N, C, H, O and V. The calculated spectra are scaled appropriately and then compared to the experimental IRMPD spectra.

In an earlier work we used a uniform scaling factor of 0.98 for the niobium acetonitrile complexes.<sup>32</sup> This factor was derived by comparing the known modes of free acetonitrile with the experimental spectrum of the complexes. However, this scaling factor is not always the best, especially if the complexes of interest contain vanadyl moieties. Asmis et al. reported a best fit when applying a scaling factor of 0.91 in their B3LYP study of vanadyl modes, whereas V–O–V modes were best matched when scaling by a factor of 0.98.<sup>10</sup> In consequence, they applied an averaged scaling factor of 0.94 in their study. Fielicke<sup>21</sup> et al. used a uniform scaling factor of 0.95 in their study of vanadium oxide ethene complexes for the same reason. In this chapter an average scaling factor of 0.95 will be applied unless otherwise stated.

Zero point energy corrected relative energy differences are given with respect to the energetically lowest isomer and are denoted as  $\Delta E_0$ . For all determined structures vibrational frequencies were computed at the same level of theory in order to confirm that these structures correspond to local minima and thus do not possess imaginary frequencies. All calculations were performed with the TURBOMOLE program package<sup>35</sup> unless otherwise stated.

Molecule pictures are generated with MOLDEN<sup>36</sup>. The color code is for all pictures as follows: Yellow–vanadium, red–oxygen, blue–nitrogen, brown–carbon and grey–hydrogen.

## 7.4 Results and Discussion

### 7.4.1 IRMPD Spectra and DFT Calculations of Vanadium Oxide Acetonitrile Complexes

Vanadium oxide acetonitrile complexes of various stoichiometries have been prepared by laser vaporization within an ICR as described in the experimental section. Six complexes were mass selected and irradiated with the FEL IR beam. Table 7.1 provides the formal stoichiometries together with the most crucial parameters for the preparation of the complexes.

**Table 7.1.** Vanadium oxide acetonitrile complexes and experimental parameters for their preparation at MICRA, the mobile FT-ICR-MS analyzer at Orsay, by laser vaporization.

Formula	$m/z$ <sup>*</sup>	$p_{\text{acetonitrile}} / \text{mbar}$	$t_{\text{pulse}} / \text{ms}$	$t_{\text{react}} / \text{ms}$
$[\text{VC}_2\text{H}_3\text{NO}]^+$	108.0	$1 \times 10^{-7}$	40	700
$[\text{VC}_4\text{H}_6\text{N}_2\text{O}]^+$	149.0	$1 \times 10^{-6}$	45	700
$[\text{VC}_4\text{H}_6\text{N}_2\text{O}_2]^+$	165.0	$1 \times 10^{-6}$	40	700
$[\text{VC}_4\text{H}_6\text{N}_2\text{O}_3]^+$	181.0	$3 \times 10^{-6}$	45	700
$[\text{VC}_6\text{H}_9\text{N}_3\text{O}_2]^+$	206.0	$1 \times 10^{-6}$	35	6000
$[\text{VC}_6\text{H}_{10}\text{N}_3\text{O}_2]^+$	207.0	$1 \times 10^{-6}$	35	6000

<sup>\*</sup> Due to low mass resolution at MICRA, only values rounded to one decimal place are given here.

The original aim of this study was to prepare vanadium acetonitrile complexes. The mass spectrum of pure ablated vanadium (without pulsing in acetonitrile) showed only a very low intensity of vanadium oxide and even less vanadium dioxide. Therefore the resulting oxides must be due to a small leak in the inlet system of the acetonitrile or stem from the acetonitrile itself, despite repeated pump and freeze of the acetonitrile. As we were not able to resolve this problem in due time during our official CLIO beam time, we decided to measure the vanadium oxides instead.

For comparison and assurance of the right assignment of the obtained species, FT-ICR mass spectra were recorded at the Kaiserslautern ICR which provides a much better mass resolution. Due to the different types of laser vaporization sources, parameters for the preparation of the complexes vary significantly. Nevertheless, all vanadium oxide acetonitrile species of which IRMPD spectra will be shown in the present chapter were reproduced with the setup in Kaiserslautern (cf. Figure 7.1, blue stars).

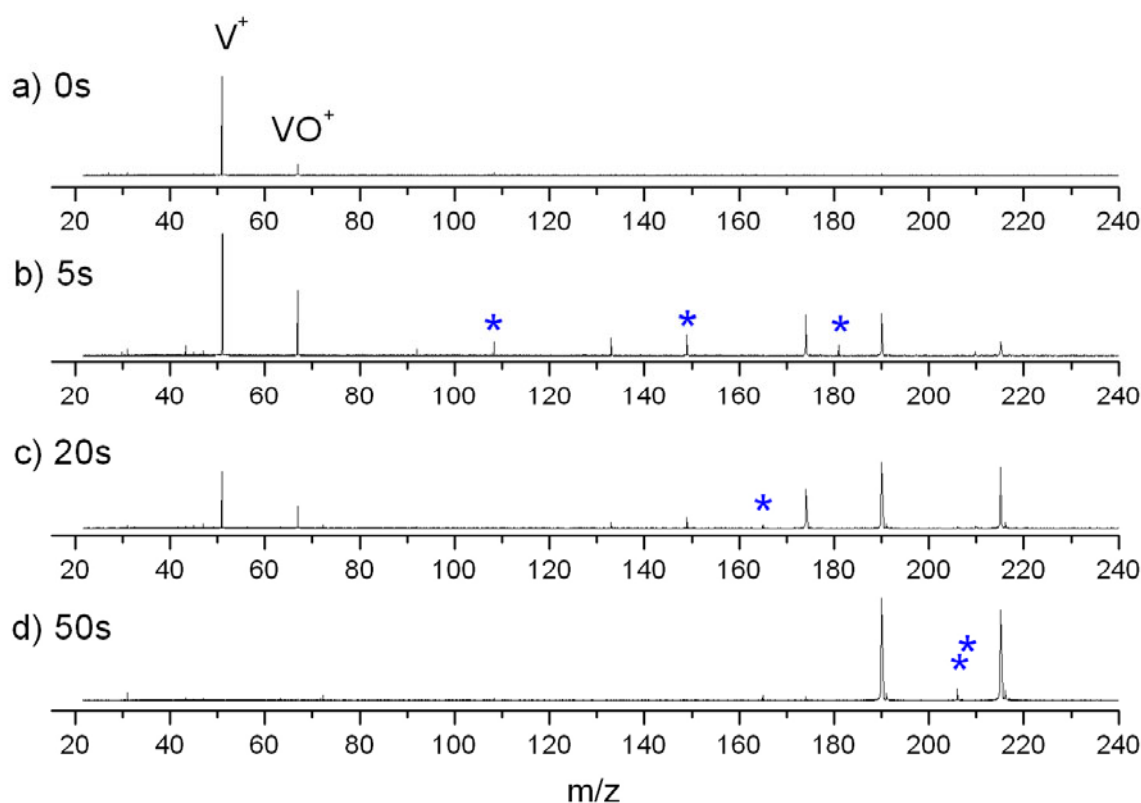


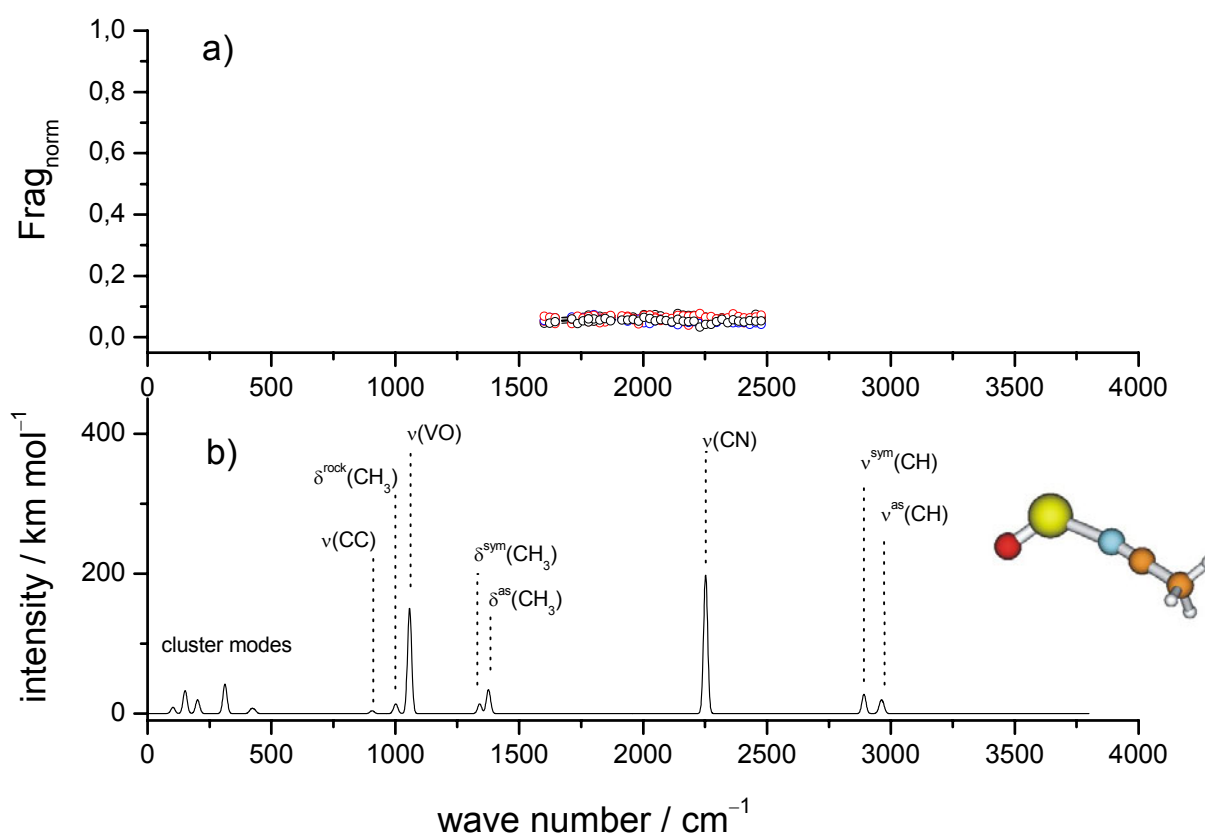
**Figure 7.1:** Laser vaporization FT-ICR mass spectra of vanadium oxide acetonitrile complexes as produced with the setup in Kaiserslautern. Panels a) to d) show spectra derived at different reaction times. By a cw inlet system, the acetonitrile background pressure was raised to  $3 \times 10^{-8}$  mbar. Blue stars denote the vanadium oxide acetonitrile species of which IRMPD spectra were recorded at CLIO.

### IRMPD Spectrum of $[\text{VC}_2\text{H}_3\text{NO}]^+$

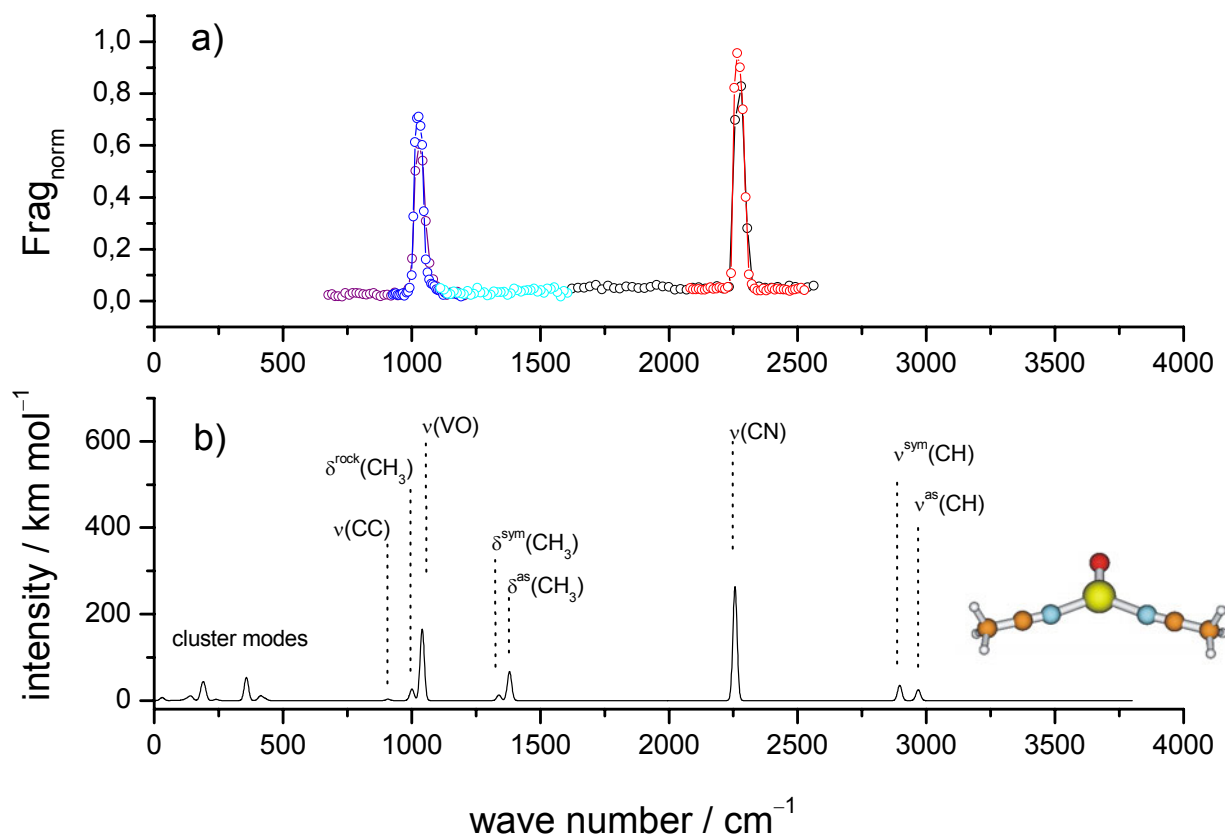
Irradiation of the mass selected complex with formal composition  $[\text{VC}_2\text{H}_3\text{NO}]^+$  does not lead to a fragmentation of the complex in the spectral range from  $1600 \text{ cm}^{-1}$  to  $2500 \text{ cm}^{-1}$  (cf. Figure 7.2. a)). Based on the B3LYP/TZVP calculations the most reasonable structural isomer of this composition is a structure which is best described as the coordination compound  $\text{OV}(\text{NCCH}_3)^+$  in an electronic triplet state (cf. Figure 7.2. b)). The calculated absorption spectrum of this complex predicts a  $\nu(\text{CN})$  mode at  $2250 \text{ cm}^{-1}$ . This would be well within the spectral range of the experiment. Nevertheless, IR induced dissociation of the complex is not observed. Fragmentation of the complex is expected to yield  $\text{VO}^+$  and a neutral acetonitrile molecule. The calculated binding energy of  $239 \text{ kJ mol}^{-1}$  between the acetonitrile ligand and  $\text{VO}^+$  seems to be too high to induce fragmentation by the FEL. Despite

high FEL power and long radiation times the absorption of energy by a single  $\nu(\text{CN})$  mode is not sufficient to lead to fragmentation.

Further conceivable structural isomers which could explain the absence of any fragmentation in case of  $[\text{VC}_2\text{H}_3\text{NO}]^+$  in the spectral range from  $1600\text{ cm}^{-1}$  to  $2500\text{ cm}^{-1}$  could be C–H or C–C activated complexes, e.g.  $(\text{HO})\text{V}(\text{NCCH}_2)^+$ ,  $\text{O}(\text{H})\text{V}(\text{NCCH}_2)^+$  or  $(\text{CN})\text{V}(\text{OCH}_3)^+$ . However, the calculated relative energies are in favor of the coordination complex  $\text{OV}(\text{NCCH}_3)^+$  by at least  $\Delta E_0 = +114\text{ kJ mol}^{-1}$ . Their calculated absorption spectra would yield a  $\nu(\text{CN})$  mode as well. We therefore discard the hypothesis of their formation for multiple reasons.



**Figure 7.2:** IRMPD spectrum of the complex with the formal stoichiometry  $[\text{VC}_2\text{H}_3\text{NO}]^+$  ( $m/z = 108.0$ ) in the spectral range of  $1600$  to  $2500\text{ cm}^{-1}$ . The different colors indicate five independent measurements. Despite a FEL power of up to  $570\text{ mW}$  and a radiation time of up to  $5800\text{ ms}$ , no fragmentation of the parent ion is observed, which is indicative of large binding energies within the complex. The inset shows the most stable calculated structure ( $S = 1$ ) on B3LYP/TZVP level of theory,  $\text{OV}(\text{NCCH}_3)^+$ .

IRMPD Spectrum of  $[\text{VC}_4\text{H}_6\text{N}_2\text{O}]^+$ 

**Figure 7.3:** a) IRMPD spectrum of the complex with the formal stoichiometry  $[\text{VC}_4\text{H}_6\text{N}_2\text{O}]^+$  ( $m/z = 149.0$ ) in the spectral range of  $700 \text{ cm}^{-1}$  to  $2550 \text{ cm}^{-1}$ . Different colors indicate independent measurements in which the FEL power varied between 270 mW and 730 mW and radiation times varied between 3800 ms and 5000 ms. Resonant IR radiation leads to the fragment  $m/z = 108.0$ , which emerges from the complex through elimination of an intact acetonitrile molecule. b) B3LYP/TZVP frequencies (scaled by 0.95) of the most stable calculated structure  $\text{OV}(\text{NCCH}_3)_2^+$  ( $S = 1$ ).

The IRMPD spectrum of the vanadium oxide acetonitrile complex of the formal composition  $[\text{VC}_4\text{H}_6\text{N}_2\text{O}]^+$  shows effective dissociation in the spectral regions around the two maxima at  $1023 \text{ cm}^{-1}$  and  $2268 \text{ cm}^{-1}$ . The only observed fragment is found at  $m/z = 108.0$ . This implies a formal loss of one acetonitrile molecule. The resulting bands in the IRMPD spectrum can be assigned to a  $\nu(\text{VO})$  stretching mode at  $1023 \text{ cm}^{-1}$  and a  $\nu(\text{CN})$  stretching vibration at  $2268 \text{ cm}^{-1}$  (cf. Figure 7.3 a)). The absorption spectrum of the energetically most favored structure calculated on B3LYP/TZVP level of theory (cf. Figure 7.3 b)) is in good agreement with the experimental spectrum except for the calculated bands in the spectral range between  $1350 \text{ cm}^{-1}$  and  $1400 \text{ cm}^{-1}$ . These are not visible in the experimental IRMPD

spectrum. The fact that the  $\text{CH}_3$  deformation bands are not observed in the experiment may be attributed to ineffective energy redistribution from the  $\text{CH}_3$  groups to the N–V bonds. Furthermore the calculations predict these bands to be of lower intensity than the stretching vibrations and therefore they are expected to provide significantly weaker IRMPD intensity. To explain their absence one has to take into account that the IRMPD technique yields only indirectly recorded spectra. After resonant absorption of (approximately 16 photons) photons by a given ion, the energy must be redistributed in such a way that dissociation of the weakest bond (in this example the N–V bond) can occur. Breaking this bond leads to the loss of one acetonitrile molecule which conforms to the observed fragmentation pattern. In case of the complex  $\text{OV}(\text{NCCH}_3)^+$  shown above no fragmentation occurred. Due to the decreased binding energy of  $208 \text{ kJ mol}^{-1}$ , it is easier to break a N–V bond in  $\text{OV}(\text{NCCH}_3)_2^+$ , assuming that the experimentally measured structure corresponds to the calculated lowest energy structure. Although the binding energy is still high, we now have twice the number of modes available for absorption of energy. Therefore fragmentation is observed in  $\text{OV}(\text{NCCH}_3)_2^+$  when resonant with the IR wavelength, leading to the two bands at  $1023 \text{ cm}^{-1}$  and  $2268 \text{ cm}^{-1}$  discussed above. Therefore it is reasonable that the  $\delta(\text{CH}_3)$  bands are not recorded in the IRMPD spectrum.

Based on these arguments and the otherwise good agreement between experiment and ab initio calculations the complex  $[\text{VC}_4\text{H}_6\text{N}_2\text{O}]^+$  is best described as  $\text{OV}(\text{NCCH}_3)_2^+$ .

### IRMPD Spectrum of $[\text{VC}_4\text{H}_6\text{N}_2\text{O}_2]^+$

Before conducting the experiments presented in this chapter, IRMPD spectra of niobium acetonitrile complexes had been recorded. In the course of these measurements also the IRMPD spectrum of the niobium oxide acetonitrile complex  $[\text{NbC}_4\text{H}_6\text{N}_2\text{O}_2]^+$  in the spectral range from  $800 \text{ cm}^{-1}$  to  $1600 \text{ cm}^{-1}$  has been recorded. Fragmentation occurred strongly around  $1000 \text{ cm}^{-1}$ , whereas close to  $1500 \text{ cm}^{-1}$  only some minor bands appeared. Unfortunately the spectral region of the nitrile band has not been scanned at that time. While repeating the measurement of the spectrum of pure niobium acetonitrile complex  $\text{Nb}(\text{NCCH}_3)_5^+$  at higher photon fluxes, the niobium oxide acetonitrile complexes were obtained only as a byproduct. Nevertheless, the complex of the formal composition  $[\text{NbC}_4\text{H}_6\text{N}_2\text{O}_2]^+$  is believed to possess a structure similar to the analogous vanadium complex and is best described as tetrahedral  $\text{NbO}_2(\text{NCCH}_3)_2^+$ .

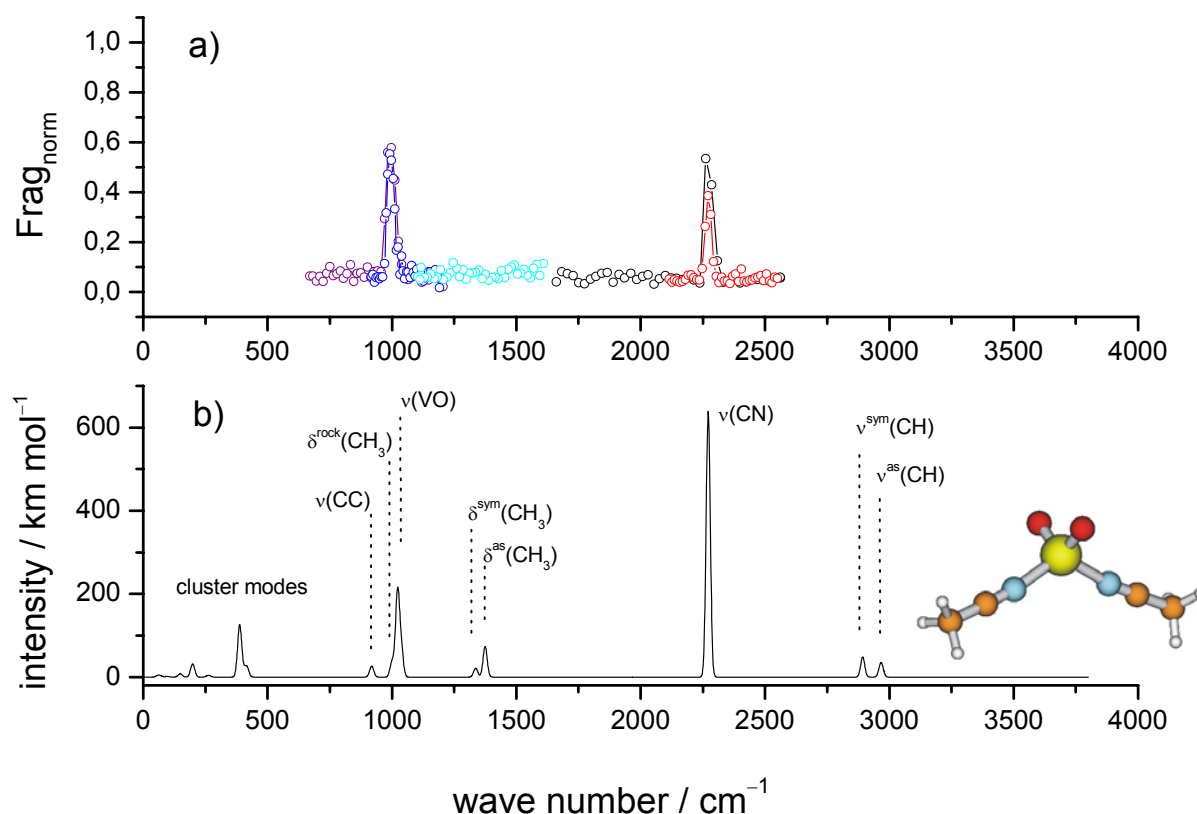


**Figure 7.4:** a) IRMPD spectrum of the complex with the formal stoichiometry  $[\text{VC}_4\text{H}_6\text{N}_2\text{O}_2]^+$  ( $m/z = 165.0$ ) in the spectral range of  $700 \text{ cm}^{-1}$  to  $2550 \text{ cm}^{-1}$ . Different colors indicate independent measurements in which the FEL power varied between 280 mW and 530 mW and radiation times varied between 4000 ms and 5000 ms. Resonant IR radiation leads to the fragment  $m/z = 124.0$ , which emerges from the complex through elimination of an intact acetonitrile molecule. b) B3LYP/TZVP frequencies (scaled by 0.95) of the most stable calculated structure  $\text{VO}_2(\text{NCCCH}_3)_2^+$  ( $S = 0$ ).

Irradiation of the vanadium oxide acetonitrile complex of the formal composition  $[\text{VC}_4\text{H}_6\text{N}_2\text{O}_2]^+$  leads to detectable dissociation in the spectral regions around the maxima at  $998 \text{ cm}^{-1}$  and  $2269 \text{ cm}^{-1}$ . Thereby, the only observed fragment is found in the mass spectrum at  $m/z = 124.0$  which implies a formal loss of one acetonitrile molecule. The resulting bands in the IRMPD spectrum can be assigned to a  $\nu(\text{VO})$  stretching vibration at  $998 \text{ cm}^{-1}$  and a  $\nu(\text{CN})$  stretching vibration at  $2269 \text{ cm}^{-1}$  (cf. Figure 7.4 a)). The absorption spectrum of the energetically most favored structure calculated on B3LYP/TZVP level of theory (cf. Figure 7.4 b)) is again in good agreement with the experimental spectrum except for the calculated bands in the spectral range between  $1350 \text{ cm}^{-1}$  and  $1400 \text{ cm}^{-1}$ . For the same reasons as discussed in the case of the previous complex  $[\text{VC}_4\text{H}_6\text{N}_2\text{O}]^+$  the  $\text{CH}_3$  deformation vibrations are not present in the experimental spectrum. A small decrease in intensity of the  $\nu(\text{CN})$

relative to the  $\nu(\text{VO})$  band is observed in the experiment when compared to the calculated spectrum. Due to the higher formal oxidation state of  $\text{VO}_2^+$  (V) compared to  $\text{VO}^+$  (III) the binding energy of the second acetonitrile ligand is again increased ( $246 \text{ kJ mol}^{-1}$  compared to  $208 \text{ kJ mol}^{-1}$  in  $[\text{VC}_4\text{H}_6\text{N}_2\text{O}]^+$ ). This may lead to the variation in the experimentally observed intensities. In total there is strong evidence for a structure which is best described as tetrahedral  $\text{VO}_2(\text{NCCH}_3)_2^+$  without evidence for any other structural isomer.

### IRMPD Spectrum of $[\text{VC}_4\text{H}_6\text{N}_2\text{O}_3]^+$

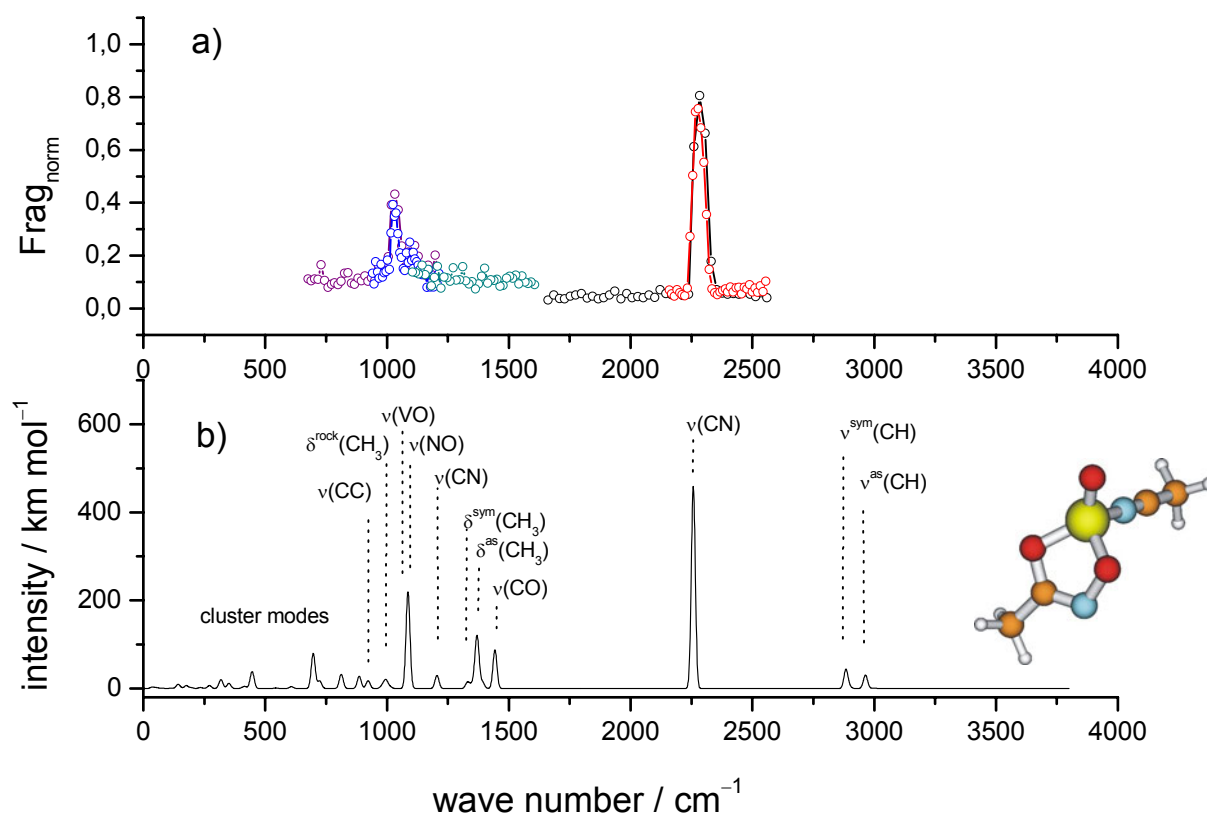


**Figure 7.5:** a) IRMPD spectrum of the complex with the formal stoichiometry  $[\text{VC}_4\text{H}_6\text{N}_2\text{O}_3]^+$  ( $m/z = 181.0$ ) in the spectral range of  $700 \text{ cm}^{-1}$  to  $2550 \text{ cm}^{-1}$ . Different colors indicate independent measurements in which the FEL power varied between 250 mW and 650 mW and radiation times varied between 4000 ms and 5000 ms. Resonant IR radiation leads to the fragments  $m/z = 140.0$  and to a smaller extend to  $m/z = 108.0$ . The fragments emerge from the complex through elimination of one intact acetonitrile molecule in the former case and loss of (formal) nitrosoacetaldehyde in the latter case. b) B3LYP/TZVP frequencies (scaled by 0.95) of the most favored calculated structure.



In case of the complex of the formal stoichiometry  $[\text{VC}_4\text{H}_6\text{N}_2\text{O}_3]^+$ , again loss of one molecule of acetonitrile was observed when the parent ion was irradiated by the IR beam of the FEL leading to the cationic fragment that is found in the mass spectrum at  $m/z = 140.0$ . This is the first case in which also a second fragment appears in the mass spectrum, namely the fragment at  $m/z = 108.0$  which is observed to a smaller extent. This fragment formally conforms to a loss of  $\text{O}_2$  along with an acetonitrile molecule. However, no mode specific fragmentation occurred.

Irradiation of  $[\text{VC}_4\text{H}_6\text{N}_2\text{O}_3]^+$  leads to effective dissociation in the spectral regions around the maxima at  $1023\text{ cm}^{-1}$  and  $2277\text{ cm}^{-1}$ . The resulting bands in the IRMPD spectrum can be assigned to a  $\nu(\text{VO})$  stretching vibration at  $1023\text{ cm}^{-1}$  and a  $\nu(\text{CN})$  stretching vibration at  $2277\text{ cm}^{-1}$  (cf. Figure 7.5 a)). The absorption spectrum of the energetically most favored structure calculated on B3LYP/TZVP level of theory (cf. Figure 7.5 b)) agrees with the experimental spectrum. Here for the first time, the bands of lower intensity in the spectral range between  $700\text{ cm}^{-1}$  and  $1450\text{ cm}^{-1}$  are noticeable in the experimental spectrum where they seem to provide for a broad and unstructured background in the IRMPD signal. A slightly asymmetric shape of the  $\nu(\text{CN})$  band may be interpreted in terms of a Fermi-like resonance with the  $\delta(\text{CH}_3) + \nu(\text{CC})$  combination band, which is known from free acetonitrile to appear at  $2300\text{ cm}^{-1}$  (see Ref 37) and has also been present in our previously studied niobium acetonitrile complexes.<sup>32</sup>

The calculated structure not only agrees with the IRMPD spectrum but also explains the fragmentation pattern. It is conceivable that a loss of acetonitrile occurs. Moreover, it is possible that upon irradiation a part of the metallacyclic moiety is lost, splitting the complex into  $\text{OV}(\text{NCCH}_3)^+$  and formal nitrosoacetaldehyde.

### IRMPD Spectrum of $[\text{VC}_6\text{H}_9\text{N}_3\text{O}_2]^+$

Irradiation of the vanadium oxide acetonitrile complex of the formal composition  $[\text{VC}_6\text{H}_9\text{N}_3\text{O}_2]^+$  leads to dissociation in the spectral regions around the observed peak maxima at  $1017\text{ cm}^{-1}$ ,  $1491\text{ cm}^{-1}$  and  $1636\text{ cm}^{-1}$ . Only one fragment is observed which is found in the mass spectrum at  $m/z = 165.0$ . This implies a formal loss of one acetonitrile molecule. Most significantly, no nitrile band is observed around  $2300\text{ cm}^{-1}$ . Instead, two new bands, as compared to the complexes discussed before, appear in the spectral range between  $1500\text{ cm}^{-1}$  and  $1650\text{ cm}^{-1}$ , which is interpreted as an indicator for an intramolecular reaction (cf. Figure 7.6 a)). Calculated absorption spectra on B3LYP/TZVP level of theory of the global minimum

structure (three acetonitriles coordinated to a  $\text{VO}_2^+$ , c)) and of a high energy isomer ( $\Delta E_0 = +180 \text{ kJ mol}^{-1}$ ) which best matches the experimental spectrum b) are plotted in comparison with the experiment a) in Figure 7.6.

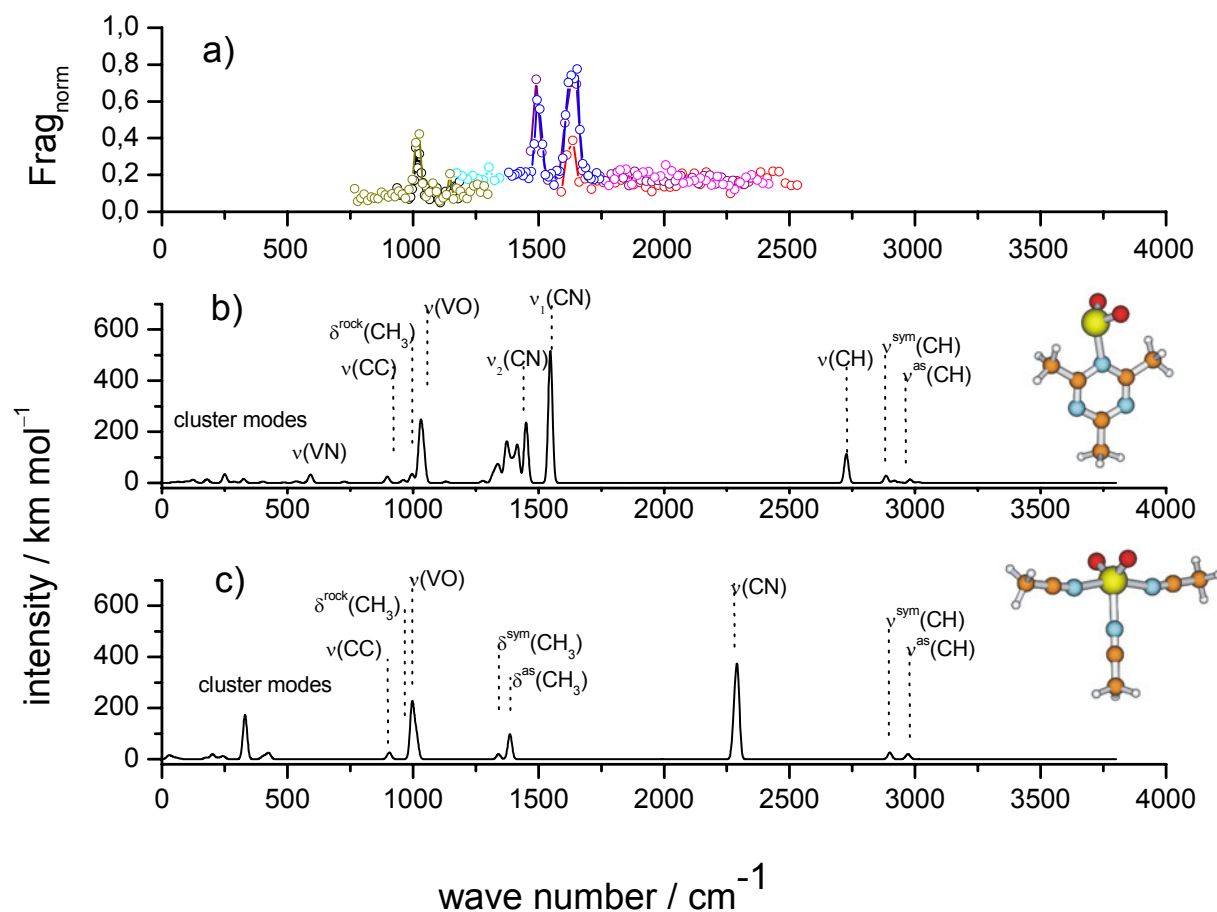


**Figure 7.6:** a) IRMPD spectrum of the complex with the formal stoichiometry  $[\text{VC}_6\text{H}_9\text{N}_3\text{O}_2]^+$  ( $m/z = 206.0$ ) in the spectral range of  $750 \text{ cm}^{-1}$  to  $2550 \text{ cm}^{-1}$ . Different colors indicate independent measurements in which the FEL power varied between 130 mW and 730 mW and the radiation time was 3000 ms. Resonant IR radiation leads to the fragment  $m/z = 165.0$ . The fragment emerges from the complex through elimination of one acetonitrile molecule. b) and c) represents the B3LYP/TZVP frequencies (scaled by 0.95) of two calculated structures (both  $S = 0$ ).

It is noticeable that the new bands in the range between  $1500 \text{ cm}^{-1}$  and  $1650 \text{ cm}^{-1}$  can not be assigned to deformation vibrations of the  $\text{CH}_3$  groups which would appear below  $1500 \text{ cm}^{-1}$ . The new bands are clearly shifted to the blue with respect to the calculated  $\delta(\text{CH}_3)$  bands and to the  $\delta(\text{CH}_3)$  bands in IRMPD spectra of similar complexes. Taking into account that the applied scaling factor is averaged to match both the VO bands and bands from the organic ligands, and therefore scales the organic molecules' bands too much, the calculated spectrum of the high energy triazine-like structure (cf. Figure 7.6 b)) agrees well with the

experimental spectrum. Despite its relatively high energy of  $\Delta E_0 = +180 \text{ kJ mol}^{-1}$  compared to the more stable coordination structure, the triazine-like structure  $\text{VO}_2(2,4,6\text{-trimethyl-1,3,5-triazine})^+$  is the only conceivable one that explains the simultaneous disappearance of the nitrile band, the occurrence of new bands in the region of CN double bands and the loss of a formal acetonitrile unit upon irradiation. This statement will gain in importance through the following spectrum of  $[\text{VC}_6\text{H}_{10}\text{N}_3\text{O}_2]^+$  in the next section. Note, that the triazine ring formation seems reversible since IRMPD yields loss of intact acetonitrile.

However, to ensure that the calculations are reliable and consistent, the two relevant different structures for  $[\text{VC}_6\text{H}_9\text{N}_3\text{O}_2]^+$  were double-checked on MP2/TZVP level of theory and additionally with the Gaussian03 program package<sup>38</sup> on B3LYP/6-311+G(d,p) level. Each method and program package yielded the same energetic order as before. Nevertheless, it is known that the quantum chemical description of vanadium oxides is problematic due to the multireference character of the VO and VO<sub>2</sub> groups.<sup>27,28</sup>

### IRMPD Spectrum of $[\text{VC}_6\text{H}_{10}\text{N}_3\text{O}_2]^+$

Once more, in case of the complex of the formal stoichiometry  $[\text{VC}_6\text{H}_{10}\text{N}_3\text{O}_2]^+$  loss of a single molecule of acetonitrile is observed when the parent ion was irradiated by the IR beam of the FEL. Loss of acetonitrile then leads to the cationic fragment detected at  $m/z = 166.0$ . Dissociation is observed in the spectral regions around the maxima at  $1002 \text{ cm}^{-1}$ ,  $1499 \text{ cm}^{-1}$  and  $1646 \text{ cm}^{-1}$ . Despite of multiply repeated measurements no nitrile band appears in the relevant spectral region around  $2300 \text{ cm}^{-1}$ . Instead, new bands arise between  $1500 \text{ cm}^{-1}$  and  $1650 \text{ cm}^{-1}$  (cf. Figure 7.7 a)). As discussed in the previous case of  $[\text{VC}_6\text{H}_9\text{N}_3\text{O}_2]^+$ , the best match of calculated and experimental spectrum is found in case of the high energy isomer b) the triazine-like structure  $(\text{HO})\text{OV}(2,4,6\text{-trimethyl-1,3,5-triazine})^+$  ( $\Delta E_0 = +130 \text{ kJ mol}^{-1}$ ). The most stable calculated isomer  $(\text{HO})\text{OV}(\text{NCCH}_3)_3^+$  fails to reproduce the experimental IRMPD spectrum.

Due to the large similarity of the IRMPD spectra of  $[\text{VC}_6\text{H}_9\text{N}_3\text{O}_2]^+$  and  $[\text{VC}_6\text{H}_{10}\text{N}_3\text{O}_2]^+$  the additional H-atom in the latter case does not observably influence the spectra in the measured spectral range from  $750 \text{ cm}^{-1}$  to  $2250 \text{ cm}^{-1}$ . Furthermore, it must be possible to eliminate a fragment of the formal mass of acetonitrile from each of these complexes upon irradiation by the FEL. For these reasons, the most probable structure is the one shown in Figure 7.7. b), in which a 2,4,6-trimethyl-1,3,5-triazine is coordinated via one of its nitrogen lone-pairs to the  $(\text{HO})\text{VO}^+$  ion forming  $(\text{HO})\text{OV}(2,4,6\text{-trimethyl-1,3,5-triazine})^+$ .

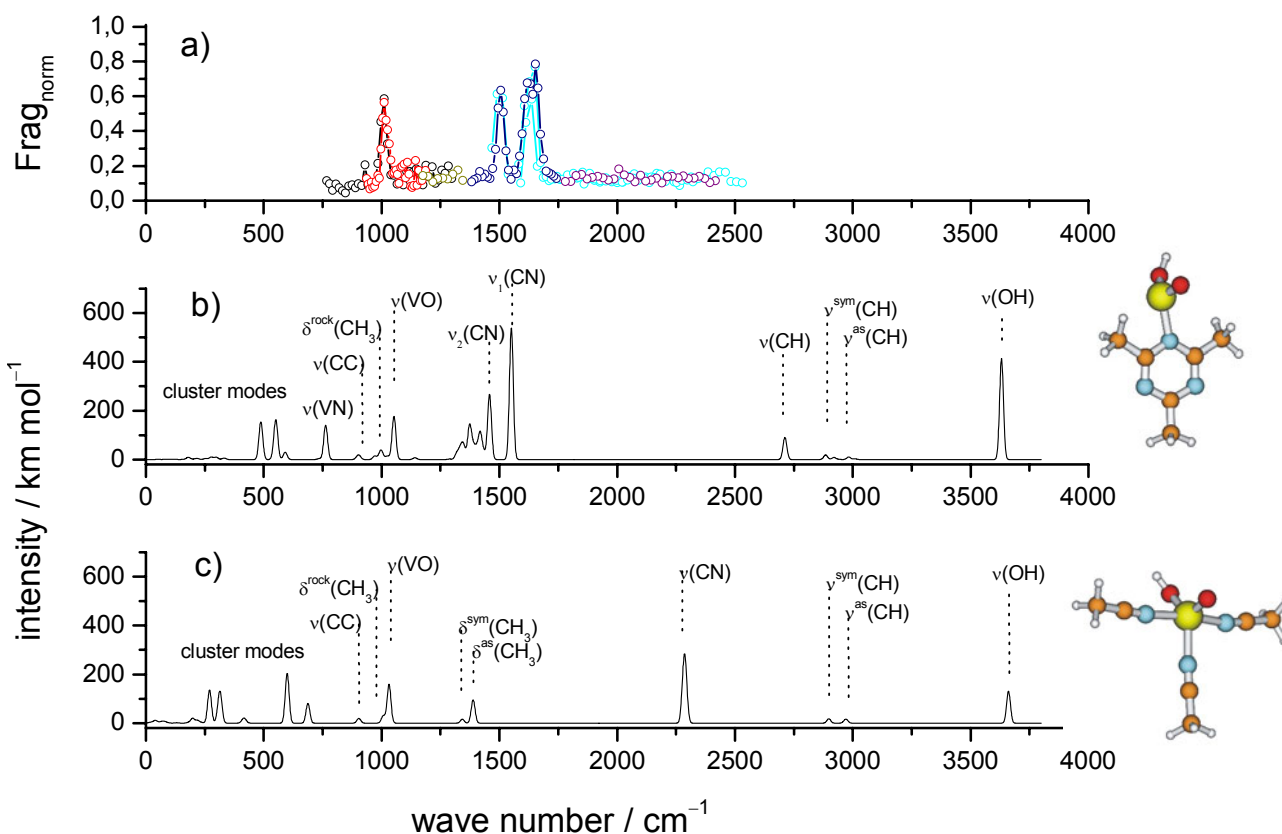


**Figure 7.7:** a) IRMPD spectrum of the complex with the formal stoichiometry  $[\text{VC}_6\text{H}_{10}\text{N}_3\text{O}_2]^+$  ( $m/z = 207.0$ ) in the spectral range from  $750\text{ cm}^{-1}$  to  $2550\text{ cm}^{-1}$ . Different colors indicate independent measurements in which the FEL power varied between 130 mW and 730 mW and the radiation time was 3000 ms. Resonant IR radiation leads to the fragment  $m/z = 166.0$ . The fragment emerges from the complex through elimination of one acetonitrile molecule. b) and c) represent the B3LYP/TZVP frequencies (scaled by 0.95) of two calculated structures (both  $S = 1/2$ ).

However, the calculated total energy of the vanadium oxide triazine structures  $\text{VO}_2(2,4,6\text{-trimethyl-1,3,5-triazine})^+$  and  $(\text{HO})\text{OV}(2,4,6\text{-trimethyl-1,3,5-triazine})^+$  is significantly higher than that of the non-reacted coordination structures  $\text{VO}_2(\text{NCCH}_3)_3^+$  and  $(\text{HO})\text{OV}(\text{NCCH}_3)_3^+$  ( $\Delta E_0 = +180\text{ kJ mol}^{-1}$  and  $+130\text{ kJ mol}^{-1}$ , respectively). This disagreement could not be solved so far. Intensive systematic search for alternative structures failed to provide any conceivable alternative structure of isomers, which would be low in energy and at the same time would explain the experimental spectrum. Other possible triazine structures would be 1,2,4- or 1,2,3-triazines, but they are higher in energy than the 1,3,5-isomer. This implies a likely assignment of the experimental  $[\text{VC}_6\text{H}_9\text{N}_3\text{O}_2]^+$  and  $[\text{VC}_6\text{H}_{10}\text{N}_3\text{O}_2]^+$  IRMPD spectra to the theoretically identified heterocyclic coordination compounds, which include the 2,4,6-trimethyl-1,3,5-triazine moiety. This assignment bears its

justification from a one to one correspondence between experimental and theoretical vibration bands. It is in question, however, through the computed high total energy.

Other examples which document high energy isomers to be the most reasonable candidates in similar IRMPD experiments exist. Von Helden and coworkers found a high energy isomer of the vanadium oxide ethene system  $[\text{V}_2\text{O}_5\text{C}_2\text{H}_4]^+$  in their IRMPD study when preparing these ions with a molecular beam setup that generates ions near thermal energy.<sup>21</sup> In this case, the calculated high energy isomer appears to be  $191 \text{ kJ mol}^{-1}$  above the lowest isomer on B3LYP/TZVP level of theory. Nevertheless, they find it to best match the experimental spectrum and at the same time to explain the observed fragmentation pattern.

Another explanation might be that the nitrile bands vanish because of a failure of IRMPD recording. However, this possibility can also be ruled out. It is not conceivable that the free electron laser itself failed while scanning the CN stretch band region. This measurement was repeated three times at different days. All recorded spectra provide IRMPD signal at the bands in the fingerprint region while none of them reveals any indication of the nitrile bands. In contrast the corresponding complex with two acetonitrile ligands does provide very strong nitrile bands. It thus seems unlikely that any experimental deficiency leads to the absence of the nitrile bands. The above conclusion is further supported by the following argument. Should there be an experimental problem with the nitrile bands then we may well assume  $[\text{VC}_6\text{H}_9\text{N}_3\text{O}_2]^+$  to be a simple coordination complex of  $\text{VO}_2^+$  with three acetonitrile ligands attached ( $\text{VO}_2(\text{NCCH}_3)_3^+$ ). Then we may expect to see spectral structure in the fingerprint region which would be indicative of these ligands and therefore similar to the recorded  $\text{VO}_2(\text{NCCH}_3)_2^+$  spectrum which is not the case.

Triazines are also known to be formed out of acetonitrile under high pressure.<sup>39</sup> Although we do not have high pressure conditions in our experiment, for a short period of time we provide a pulse of acetonitrile gas in which more than only one collision per second occurs. If we further assume that the precursor ions contain a relatively high amount of internal energy out of the laser vaporization this might be enough to enable a formation of high energy isomers. This holds especially in case of  $[\text{VC}_6\text{H}_9\text{N}_3\text{O}_2]^+$  and  $[\text{VC}_6\text{H}_{10}\text{N}_3\text{O}_2]^+$  where the necessary reaction time of up to six seconds allowed for multiple collisions within the ICR cell and thus for rearrangements on the given timescale. Together with the possibly

catalytical influence of the vanadium oxide containing precursors, this may explain why we find the triazine-like structures as the ones formed in the experiment. There is no evidence so far that the vanadium oxides would directly activate a C–H or C–C bond of the acetonitrile to form e.g. vanadium hydroxides or methoxides. Thus the catalytic effect might well be restricted to induce reaction between the acetonitrile ligands.

If indeed high energy isomers of  $[\text{VC}_6\text{H}_9\text{N}_3\text{O}_2]^+$  and  $[\text{VC}_6\text{H}_{10}\text{N}_3\text{O}_2]^+$  have formed the building process would have to be highly non-ergodic. Formation is expected to occur through attachment of a single  $\text{CH}_3\text{CN}$  molecule to pre-formed  $\text{VO}_2(\text{NCCH}_3)_2^+$  resp.  $(\text{HO})\text{OV}(\text{NCCH}_3)_2^+$ . IR spectra of  $\text{VO}_2(\text{NCCH}_3)_2^+$  indicate with certainty a purely non-reactive attachment structure. Thus the question arises whether it is conceivable that the third acetonitrile ligand attaches and reacts to a high energy isomer while the non-reacted structure is a much more stable isomer. No steric hindrance and no significant activation barrier towards non-reactive association were found in B3LYP/TZVP calculations for the coordination of the third acetonitrile. However, due to the catalytic influence of the  $\text{VO}_2^+$  unit and the increased steric demand when going from complexes with two to complexes with three acetonitrile ligands the formation of a triazine structure might happen nevertheless. In conclusion there is no final justification for the triazine-like structures except that their calculated spectra are the only ones that match the experiment at all. No other structure could be thought of by chemical intuition to explain all the observed bands in the IRMPD spectrum and at the same time to explain the fragmentation pattern.

### 7.4.2 IRMPD Spectra of Vanadium Oxide Methanol Complexes

Vanadium oxide methanol complexes of various stoichiometries have been prepared by laser vaporization at MICRA as described in the experimental section. Five complexes were mass selected and irradiated with the FEL IR beam. Table 7.2 provides the formal stoichiometries together with the most crucial parameters for the preparation of the complexes.

**Table 7.2.** Vanadium oxide methanol complexes and experimental parameters for their preparation at MICRA by laser vaporization.

Formula	m/z <sup>*</sup>	p <sub>methanol</sub> / mbar	t <sub>pulse</sub> / ms	t <sub>react</sub> / ms
[VCH <sub>6</sub> O <sub>2</sub> ] <sup>+</sup>	101.0	2x10 <sup>-6</sup>	140	1700
[VCH <sub>5</sub> O <sub>3</sub> ] <sup>+</sup>	116.0	1x10 <sup>-6</sup>	80	1200
[VCH <sub>7</sub> O <sub>3</sub> ] <sup>+</sup>	118.0	2x10 <sup>-6</sup>	100	1500
[VC <sub>2</sub> H <sub>9</sub> O <sub>3</sub> ] <sup>+</sup>	132.0	3x10 <sup>-6</sup>	140	1700
[VC <sub>2</sub> H <sub>12</sub> O <sub>4</sub> ] <sup>+</sup>	151.0	4x10 <sup>-6</sup>	140	1700

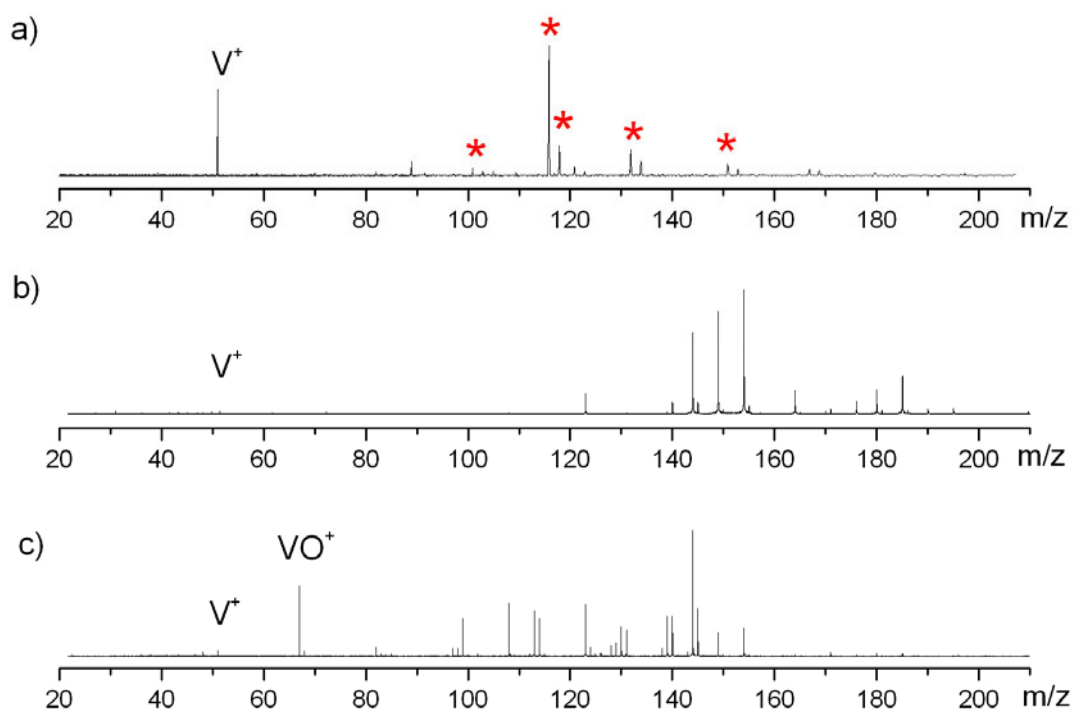
<sup>\*</sup>Due to low mass resolution at MICRA, only values rounded to one decimal place are given here.

In addition, FT-ICR mass spectra were recorded at the Kaiserslautern ICR which provides a much better mass resolution. Due to the different types of laser vaporization sources parameters for the preparation of the complexes vary significantly (cf. Figure 7.8). In contrast to the vanadium oxide acetonitrile complexes, the vanadium oxide methanol species studied at MICRA (marked by red stars) could not be reproduced with the experimental setup at Kaiserslautern.

However, in their FT-ICR-MS study<sup>40</sup> on reactions of vanadium oxides with methanol, Schwarz and co-workers reported about differences in the observed products compared to an earlier guided ion beam study by Castleman and co-workers.<sup>41</sup> The final product pattern strongly depends on the initial ratio between VO<sup>+</sup> and VOH<sup>+</sup>. Both precursor ions are found to be generated in the reaction of vanadium with methanol.<sup>40</sup> The reactivity of these precursor ions towards methanol differs by an order of magnitude, where the VOH<sup>+</sup> reacts faster than the VO<sup>+</sup>.<sup>40</sup> Therefore the techniques used for ion preparation and ion selection in case of vanadium oxide methanol complexes are crucial as they determine the initial ratio of the precursor ions and thus the formation of further products.

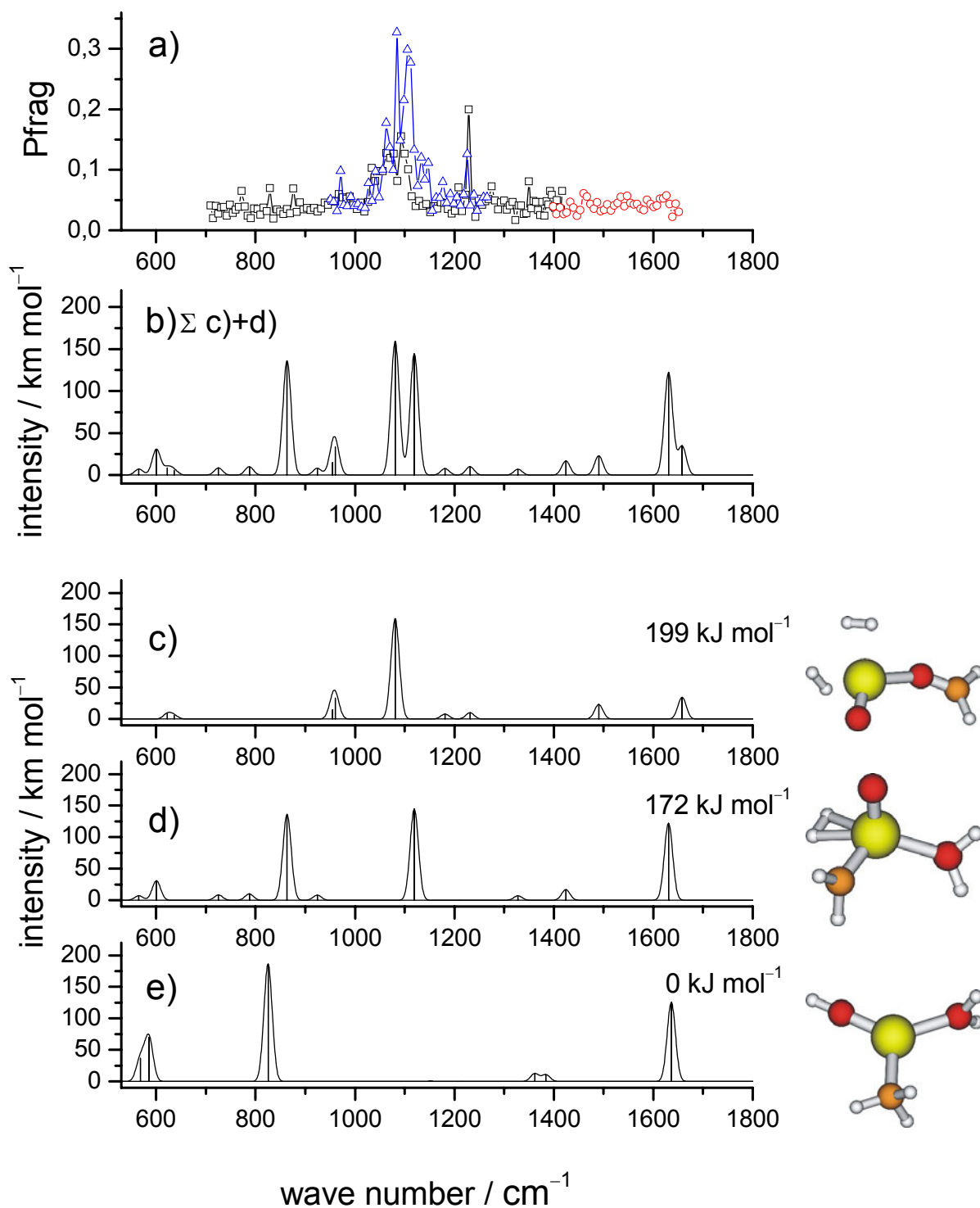
Furthermore, different pressures of methanol as reactant seem to have a stronger influence on the resulting products than it was the case for acetonitrile. For the latter the same products were observed with both experimental setups, although the products showed different intensities.

Please note that for the ease of comparison, the vanadium oxide methanol complexes are presented and discussed in order of similarity of the IRMPD spectra and not in ascending order of their mass to charge ratio.



**Figure 7.8:** a) FT-ICR-MS spectra of vanadium oxide methanol species recorded at MICRA ( $1 \times 10^{-6}$  mbar, reaction time 1.7 s) and at the Kaiserslautern setup, b)  $3 \times 10^{-8}$  mbar reaction time 2 s and c)  $1 \times 10^{-8}$  mbar, reaction time 2 s. Red stars denote the species of which IRMPD spectra were recorded. The red marked species found at MICRA were not present in the spectra recorded at the Kaiserslautern setup.



IRMPD Spectrum of  $[\text{VCH}_6\text{O}_2]^+$ 

**Figure 7.9:** a) IRMPD spectrum of the complex with the formal stoichiometry  $[\text{VCH}_6\text{O}_2]^+$  ( $m/z = 101.0$ ) in the spectral range of  $700 \text{ cm}^{-1}$  to  $1650 \text{ cm}^{-1}$ . Different colors indicate independent measurements in which the FEL power varied between 730 mW and 1500 mW and the radiation time was 1000 ms. Resonant IR radiation leads to the fragment  $m/z = 31.0$ . c), d) and e) represent the B3LYP/TZVP frequencies (scaled by 0.98) of three calculated structures (c) and e)  $S = 1$ ; d)  $S = 0$ ). b) shows the sum of the frequencies of c) and d).

The IRMPD spectrum of the vanadium oxide methanol complex of the formal composition  $[\text{VCH}_6\text{O}_2]^+$  ( $m/z = 101.0$ ) shows effective dissociation in the spectral regions around the maxima at  $970\text{ cm}^{-1}$ ,  $1083\text{ cm}^{-1}$ ,  $1111\text{ cm}^{-1}$  and  $1218\text{ cm}^{-1}$ . Some bands of smaller intensity are observed at  $771\text{ cm}^{-1}$ ,  $826\text{ cm}^{-1}$ ,  $875\text{ cm}^{-1}$ ,  $1349\text{ cm}^{-1}$ ,  $1417\text{ cm}^{-1}$  and  $1459\text{ cm}^{-1}$  (see Figure 7.9 a)).

Noteworthy, the only ionic fragment present in the mass spectrum after irradiation of the complex is  $m/z = 31$ . This mass corresponds to either a methoxy cation or to a protonated formaldehyde ion, with the latter being more stable by  $180.4\text{ kJ mol}^{-1}$  (according to Ref. 42 and 43). The complex  $[\text{VCH}_6\text{O}_2]^+$  is the only species in which loss of a neutral vanadium containing fragment was observed throughout this study of vanadium oxide complexes when reacted with organic molecules up to this point.

So far ab initio calculations of potential structures of the complex  $[\text{VCH}_6\text{O}_2]^+$  did not provide an unambiguous interpretation of the recorded IRMPD spectrum. Due to the absence of bands at  $1300\text{ cm}^{-1}$  and  $1500\text{ cm}^{-1}$  an association complex  $(\text{H}_2\text{O})\text{V}(\text{HOCH}_3)^+$  can be ruled out. Furthermore, the band observed at  $1218\text{ cm}^{-1}$  indicates the presence of a  $\text{V}-\text{O}-\text{CH}_2$  group, which is only present in complexes in which the methanol is dehydrogenated, and formaldehyde is formed. However, calculation shows that complexes containing the formaldehyde attached to vanadium and at the same time still possessing the  $\text{H}_2$  molecule in order to fulfill the stoichiometry related to the observed  $m/z$  value are high energy isomers. The calculated structure  $(\text{H}_2\text{O})\text{V}(\text{CH}_3)(\text{OH})^+$ , which refers to the most stable (cf. Figure 7.9.e)), does not explain neither the observed bands between  $1000\text{ cm}^{-1}$  and  $1100\text{ cm}^{-1}$  nor the band at  $1218\text{ cm}^{-1}$  in the IRMPD spectrum. Neither does any of the other calculated structures alone explain the large number of observed vibrations. The closest resemblance of calculated frequencies with experimental band positions is achieved by summation of frequencies of two high energy isomers (see Figure 7.9. b) = sum of c) and d)). One exception is observed in the calculated deformation vibrations of the associated water molecule at  $1620\text{ cm}^{-1}$  which are not present in the IRMPD spectrum. In contrast to the band positions, the calculated intensities are not well reproduced. This might be attributed to the known deficiencies of the IRMPD technique.

Further problems in the comparison may arise through the choice of the appropriate scaling factor. Vibrations without direct involvement of  $\text{V}-\text{O}$  units are scaled too strongly when applying an average factor of 0.95 while the  $\text{V}-\text{O}$  groups themselves are still not scaled enough. This has to be considered, too, when comparing the calculated spectra.

This mixture of isomers does not provide an unambiguous evidence for the observed fragmentation behaviour. However, it is the most likely explanation for the occurrence of the large number of vibrations so far.

### IRMPD Spectrum of $[\text{VC}_2\text{H}_{12}\text{O}_4]^+$

The IRMPD spectrum of the vanadium oxide methanol complex of the formal composition  $[\text{VC}_2\text{H}_{12}\text{O}_4]^+$  ( $m/z = 151.0$ ) yields prominent bands in the spectral regions around the maxima at  $972\text{ cm}^{-1}$ ,  $1099\text{ cm}^{-1}$ ,  $1116\text{ cm}^{-1}$ ,  $1207\text{ cm}^{-1}$  and  $1247\text{ cm}^{-1}$ . Bands of smaller intensity are observed at  $748\text{ cm}^{-1}$ ,  $777\text{ cm}^{-1}$ ,  $835\text{ cm}^{-1}$ ,  $1367\text{ cm}^{-1}$ ,  $1389\text{ cm}^{-1}$  and  $1438\text{ cm}^{-1}$  (cf. Figure 7.10 a)). Most remarkably, the comparison of the observed spectroscopic signatures of  $[\text{VCH}_6\text{O}_2]^+$  ( $m/z = 101.0$ ) and  $[\text{VC}_2\text{H}_{12}\text{O}_4]^+$  ( $m/z = 151.0$ ) reveals high similarity between both complexes. Moreover, the  $m/z = 151.0$  complex yields the sole IRMPD fragment at  $m/z = 101.0$  discussed before. The mass difference between the two complexes is best described in terms of a water molecule and a methanol molecule.

The spectrum of  $[\text{VC}_2\text{H}_{12}\text{O}_4]^+$  clearly shows the dependence of the IRMPD spectrum on the FEL power. Due to high fragmentation yields, the spectrum recorded with 1.2 W to 1.3 W FEL power (blue curve in Figure 7.10 a) poorly resolves spectral features in the region between  $1070\text{ cm}^{-1}$  and  $1330\text{ cm}^{-1}$ . Therefore a threefold attenuator grid was used to record an attenuated spectrum (plotted in black). Due to the decreased FEL power a better resolution could be achieved. However, this is accompanied by the non-observance of the band at  $972\text{ cm}^{-1}$ .

Calculated absorption spectra of low and high energy isomers of  $[\text{VC}_2\text{H}_{12}\text{O}_4]^+$  (Figure 7.10 b) and c)) agree well with the experimental spectrum. The most stable calculated isomer (depicted in c)) can be described as  $(\text{HO})\text{V}(\text{OH}_2)_2(\text{CH}_3)(\text{HOCH}_3)^+$ . The high energy isomer (shown in b)) can be written as  $(\text{HO})\text{V}(\text{H}_2)(\text{OH}_2)_2(\text{CH}_3)(\text{OCH}_2)^+$  ( $\Delta E_0 = +221\text{ kJ mol}^{-1}$ ). Both structures would allow for a simultaneous loss of a methanol and water upon irradiation by the FEL and thus for the formation of the observed fragment at  $m/z = 101.0$ . This finding supports the assumption that the complex at  $m/z = 101.0$  does not contain an intact methanol group. Otherwise loss of two methanol molecules should be observed as well. It seems unlikely, however, that strongly bound molecules such as methanol or water desorb while weakly bound  $\text{H}_2$  sticks. It therefore seems certain to restrict further interpretation to the other, more stable isomer.

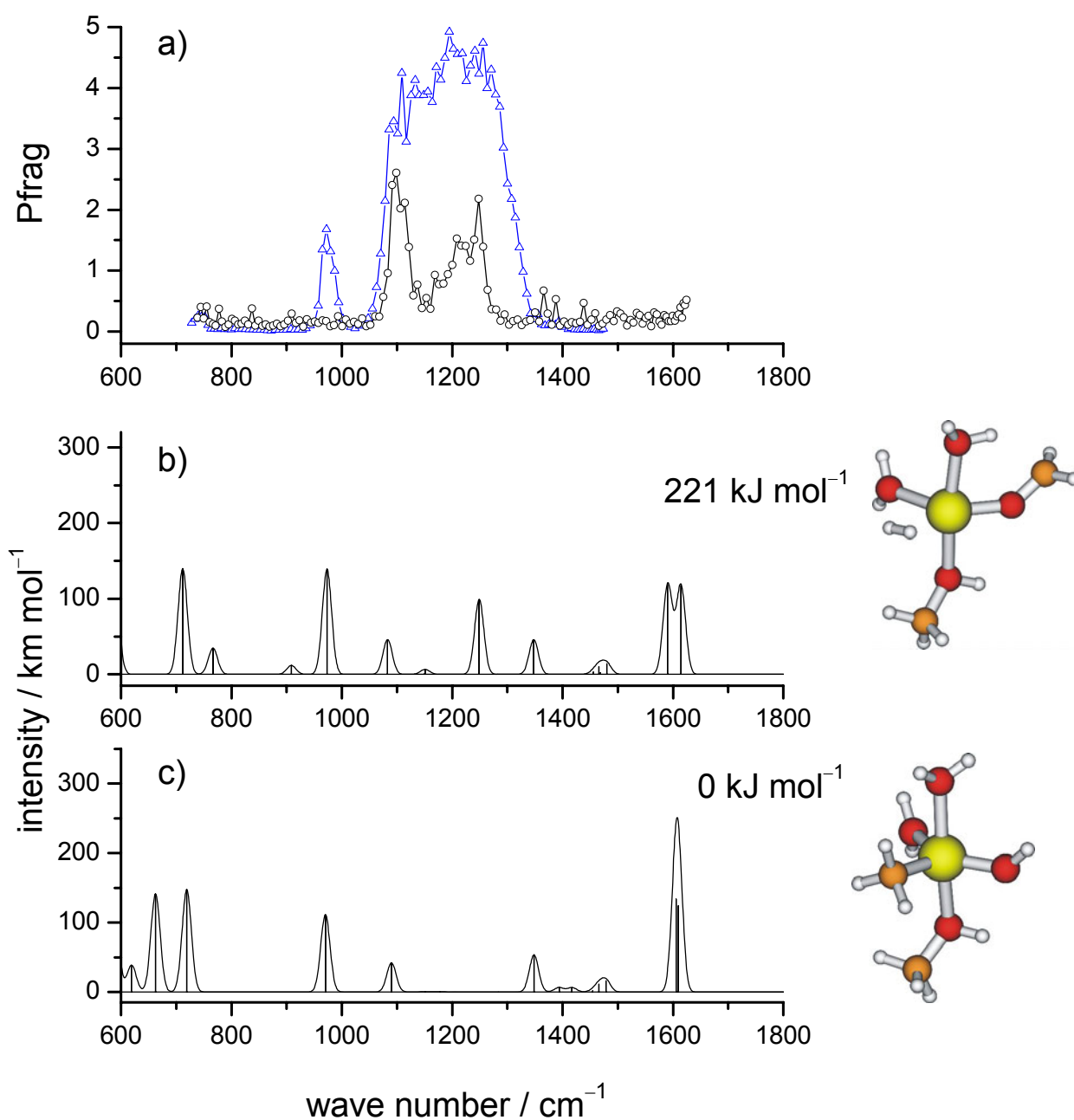


**Figure 7.10:** a) IRMPD spectrum of the complex with the formal stoichiometry  $[\text{VC}_2\text{H}_{12}\text{O}_4]^+$  ( $m/z = 150.0$ ) in the spectral range of  $730 \text{ cm}^{-1}$  to  $1620 \text{ cm}^{-1}$ . Different colors indicate independent measurements in which the FEL power varied between 1.2 W and 1.3 W. For the recording of the black spectrum a threefold attenuator grid was used. The radiation time was 1000 ms. Resonant IR radiation leads to the fragment  $m/z = 101.0$ . The fragment emerges from the complex through formal elimination of one methanol and one water molecule. c) and d) represent the B3LYP/TZVP frequencies (scaled by 0.98) of two calculated structures (both  $S = 1$ ).

Due to the high reactivity of the precursor ions  $\text{VO}^+$  and  $\text{VOH}^+$ , which are formed in the first step from vanadium and methanol under release of methane or methyl, respectively, the next collision with methanol almost certainly leads to an activation of the second

methanol molecule. This yields either formaldehyde by dehydrogenation or an insertion structure. Based on the high pressures achieved during the pulsed inlet of the reactant into the ICR cell, larger complexes might form association structures due to termolecular stabilization, which may explain why the expected loss of H<sub>2</sub> is not observed. Collisions with further methanol molecules then may lead to an association structure under the assumption that the catalytic activity of vanadium is limited to the activation of two methanol molecules when forming complexes with methanol.

### IRMPD Spectrum of [VC<sub>2</sub>H<sub>9</sub>O<sub>3</sub>]<sup>+</sup>

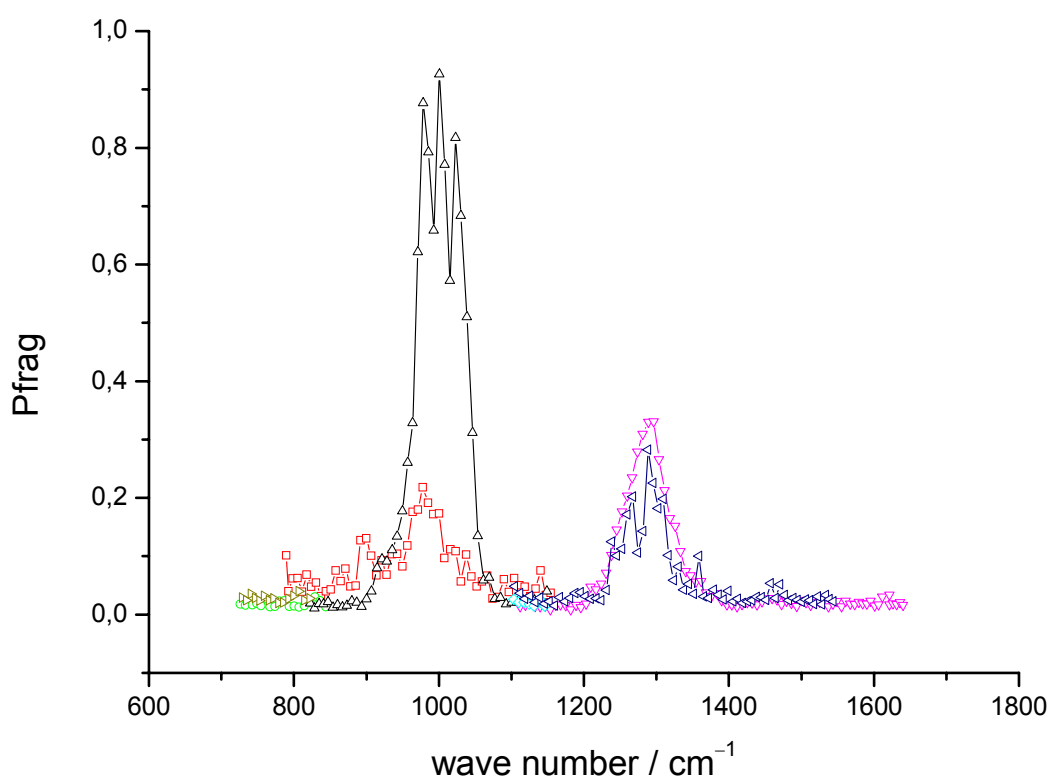


**Figure 7.11:** a) IRMPD spectrum of the complex with the formal stoichiometry [VC<sub>2</sub>H<sub>9</sub>O<sub>3</sub>]<sup>+</sup> ( $m/z = 132.0$ ) in the spectral range of 730 cm<sup>-1</sup> to 1620 cm<sup>-1</sup>. Different colors indicate independent measurements in which the FEL power varied between 830 mW and 1100 mW. The radiation time was 1000 ms. Resonant IR radiation leads to the fragment  $m/z = 82.0$ . The fragment emerges from the complex through formal elimination of water and methanol.

The IRMPD spectrum of the vanadium oxide methanol complex of the formal composition [VC<sub>2</sub>H<sub>9</sub>O<sub>3</sub>]<sup>+</sup> ( $m/z = 132.0$ ) differs from those of the two complexes discussed before (cf. Figure 7.11). The most dominant bands are observed around the maxima at 897 cm<sup>-1</sup>, 977 cm<sup>-1</sup>, 1004 cm<sup>-1</sup>, 1023 cm<sup>-1</sup>, 1262 cm<sup>-1</sup> and 1287 cm<sup>-1</sup>. Some bands of smaller intensity are observed at 1138 cm<sup>-1</sup>, 1464 cm<sup>-1</sup>, and 862 cm<sup>-1</sup>. The only ionic fragment

observed in the mass spectrum after irradiation of the complex is  $m/z = 88.0$ . This mass corresponds to either a  $\text{VOCH}_3^+$ ,  $\text{OVCH}_3^+$  or  $\text{V}(\text{HOCH}_2)^+$ . The most reasonable structure, however, is  $\text{VOCH}_3^+$ , which could have been formed by hydrogen abstraction from methanol and following hydrogen transfer to an oxygen containing unit. This oxygen unit might then form a water molecule, which in turn is formally lost as neutral fragment together with the loss of a formal methanol molecule.

Although several possible structural isomers of this formal composition have been calculated, so far no reasonable candidate could be found to explain the experimental spectrum.

### IRMPD Spectrum of $[\text{VCH}_5\text{O}_3]^+$

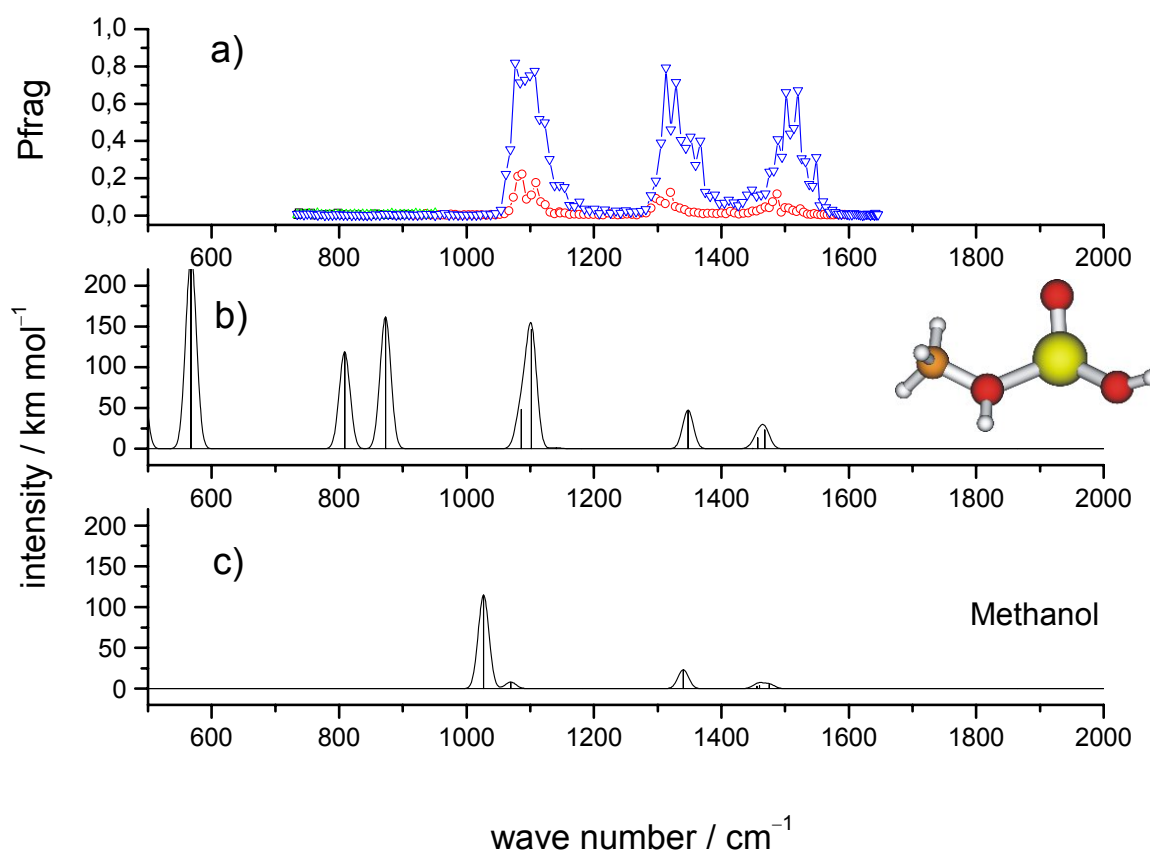


**Figure 7.12:** a) IRMPD spectrum of the complex with the formal stoichiometry  $[\text{VCH}_5\text{O}_3]^+$  ( $m/z = 116.0$ ) in the spectral range of  $730 \text{ cm}^{-1}$  to  $1630 \text{ cm}^{-1}$ . Different colors indicate independent measurements in which the FEL power varied between 1.1 W and 1.3 W. The radiation time was 500 ms for the red curve and 1200 ms for the blue curve. Resonant IR radiation leads to the cationic fragment  $m/z = 84.9$ . The fragment emerges from the complex through formal elimination of one methoxy radical. b) Calculated absorption spectrum of the best matching structure ( $S = 1/2$ ). c) Calculated spectrum of methanol. Spectra b) and c) are both calculated with B3LYP/TZVP and scaled by 0.98.

The IRMPD spectrum of the vanadium oxide methanol complex of the formal composition  $[\text{VCH}_5\text{O}_3]^+$  ( $m/z = 116.0$ ) shows effective dissociation in the spectral regions around the peaks at  $1087\text{ cm}^{-1}$ ,  $1108\text{ cm}^{-1}$ ,  $1123\text{ cm}^{-1}$  (weak shoulder),  $1310\text{ cm}^{-1}$ ,  $1355\text{ cm}^{-1}$  and  $1502\text{ cm}^{-1}$  (cf. Figure 7.12 a)). The bands close to  $1300\text{ cm}^{-1}$  and  $1500\text{ cm}^{-1}$  were not observed in the preceding spectra of  $[\text{VCH}_6\text{O}_2]^+$ ,  $[\text{VC}_2\text{H}_{12}\text{O}_4]^+$  and  $[\text{VC}_2\text{H}_9\text{O}_3]^+$ .

The broad band around  $1100\text{ cm}^{-1}$  is made up of three sub-bands (two strong bands and one weak shoulder) which can be assigned to combinations of  $\nu(\text{VO})$  and  $\delta(\text{CH}_3)$  modes according to the calculated structure shown in Figure 7.12 b). Feyel et al. reported about a similar structural pattern to appear in gas phase IR spectra of mass selected  $\text{V}_4\text{O}_9(\text{OCH}_3)^-$  in the spectral region between  $950\text{ cm}^{-1}$  and  $1150\text{ cm}^{-1}$ .<sup>8</sup> They assign the observed signals to  $\nu(\text{VO})$ ,  $\nu(\text{OC})$  and a H–C–H bending mode. However, this is not the case for  $[\text{VCH}_5\text{O}_3]^+$ . A calculated structure of  $[\text{VCH}_5\text{O}_3]^+$  which contains the methoxy group is slightly lower in energy than the isomer that includes an intact methanol molecule by approximately  $6\text{ kJ mol}^{-1}$ . Such a structure can be excluded for  $[\text{VCH}_5\text{O}_3]^+$ , nevertheless. If the methanol would have been transformed into a methoxy group, then the band located at  $1310\text{ cm}^{-1}$  had not been present in the experiment. This broad band arises from a combination of C–O–H and H–C–H bending modes, which is only possible when the methanol molecule does not transfer hydrogen to the vanadium or oxygen in the complex. The observed spectral feature at  $1502\text{ cm}^{-1}$  can be attributed to deformation modes of the  $\text{CH}_3$  group.

In comparison to the calculated spectrum of the free methanol molecule (cf. Figure 7.12 c)) a blue shift of the bands is observed upon complexation.

The two bands predicted by DFT calculations to be located at  $808\text{ cm}^{-1}$  and  $872\text{ cm}^{-1}$ , namely the  $\nu(\text{V–OH})$  and  $\nu(\text{OC})$  are not visible in the experiment. Most likely the quantum yield of fragmentation decreases steeply towards lower photon energies. Recordable IRMPD yields would require either higher FEL power or much longer radiation time.

In summary, the most reasonable structure of  $[\text{VCH}_5\text{O}_3]^+$  may be assumed as  $(\text{HO})\text{VO}(\text{HOCH}_3)^+$ .

### IRMPD Spectrum of $[\text{VCH}_7\text{O}_3]^+$

$[\text{VCH}_7\text{O}_3]^+$  exhibits an IRMPD spectrum which is very similar to the one of  $[\text{VCH}_5\text{O}_3]^+$ . Irradiation of the vanadium oxide methanol complex of the formal composition  $[\text{VCH}_5\text{O}_3]^+$  leads to dissociation in the spectral regions around the peaks at  $1077\text{ cm}^{-1}$ ,  $1301$

$\text{cm}^{-1}$  and  $1487 \text{ cm}^{-1}$ . However, in this case there is no fine resolution of the bands (cf. Figure 7.13 a)). Nevertheless, the assignment of the modes can be done in analogy to the modes of  $[\text{VCH}_5\text{O}_3]^+$  except for the  $\nu(\text{VO})$  mode which is no longer present.

The complexes  $[\text{VCH}_5\text{O}_3]^+$  and  $[\text{VCH}_7\text{O}_3]^+$  formally differ by two H atoms. The same holds true for their fragments  $[\text{VH}_2\text{O}_2]^+$  and  $[\text{VH}_4\text{O}_2]^+$ . The neutral fragment is identical, formally it is  $\bullet\text{OCH}_3$ .

The best matching calculated structure  $(\text{HO})\text{V}(\text{OH}_2)(\text{HOCH}_3)^+$  may also explain the observed fragment. It is assumed that an activated hydrogen transfer from the methanol to the VOH group would be possible (cf. Figure 7.13 b)). This would yield the ionic fragment  $[\text{VH}_4\text{O}_2]^+$  and the  $\bullet\text{OCH}_3$  radical.

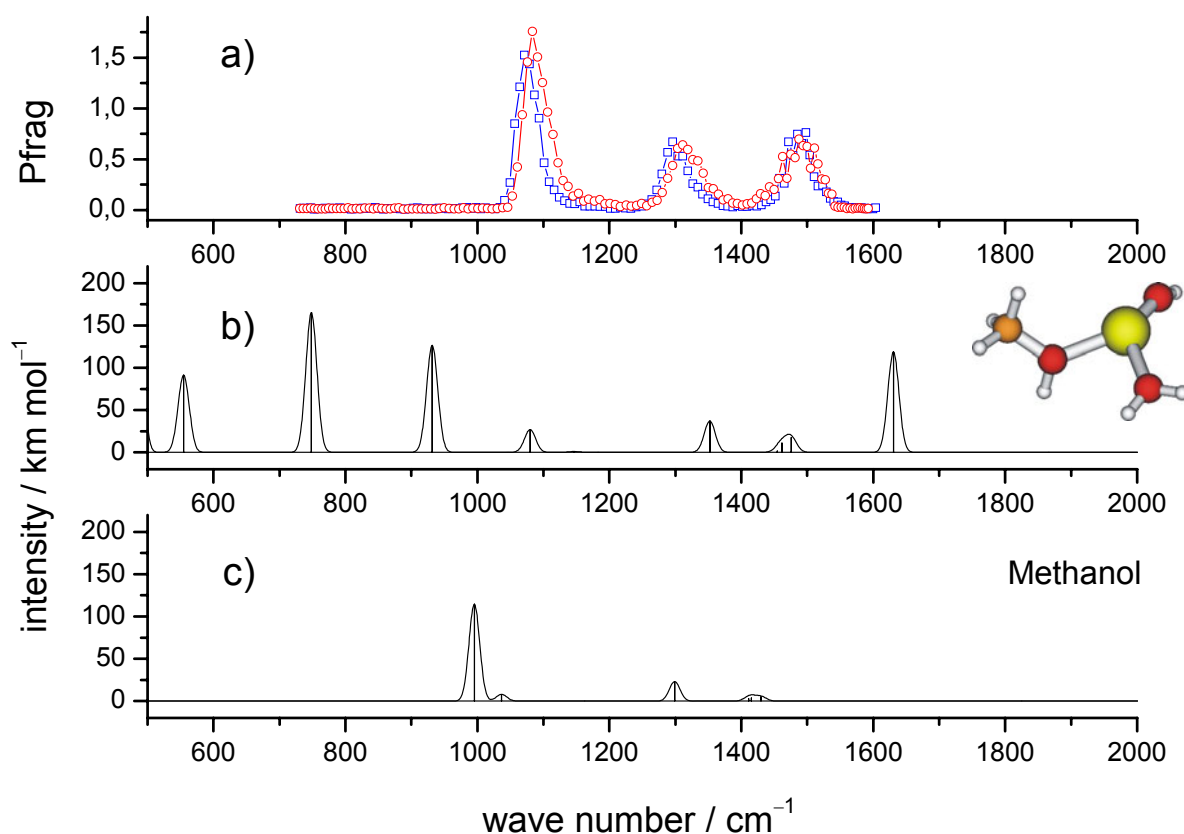


**Figure 7.13:** a) IRMPD spectrum of the complex with the formal stoichiometry  $[\text{VCH}_7\text{O}_3]^+$  ( $m/z = 118.0$ ) in the spectral range of  $730 \text{ cm}^{-1}$  to  $1610 \text{ cm}^{-1}$ . Different colors indicate independent measurements in which the FEL power varied between 600 mW and 1300 mW. The radiation time was 1200 ms. Resonant IR radiation leads to the fragment  $m/z = 87.0$ . The fragment emerges from the complex through formal elimination of one  $\bullet\text{OCH}_3$ . b) Calculated absorption spectrum of the best matching structure ( $S = 3/2$ ). c) Calculated spectrum of methanol. Spectra b) and c) are both calculated with B3LYP/TZVP and scaled by 0.98.



Most noticeable, the methoxy radical exclusively occurs as neutral fragment upon irradiation of the complexes  $[\text{VCH}_5\text{O}_3]^+$  and  $[\text{VCH}_7\text{O}_3]^+$ . In contrast, a  $\text{VOCH}_3^+$  fragment is formed out of the complex  $[\text{VC}_2\text{H}_9\text{O}_3]^+$  after irradiation by the FEL which also includes a methoxy group.

Schröder et al. found a similar behavior towards the types of fragment ions formed by ESI at elevated cone voltages.<sup>44</sup> Depending on the valence of the initial neutral vanadium compound, the observed fragments differ in the number of H atoms. Parent ions with the formal oxidation state (III) or (V) lead to cationic complexes with an even number of H atoms. Parent ions of formal oxidation state (II) or (IV) form cationic complexes with an odd number of H atoms, e.g.  $[\text{VCH}_5\text{O}_3]^+$  and  $[\text{VCH}_7\text{O}_3]^+$ . In turn, we observe that complexes with an odd number of H atoms appear to release or at least involve the methoxy group. This is not observed in the IRMPD spectra of complexes with even numbers of H atoms. Thus the formal oxidation state and therefore the spin state of the complexes have a strong influence on the fragmentation pattern.

Concluding, the vanadium oxide methanol complex  $[\text{VCH}_7\text{O}_3]^+$  can be assigned to  $(\text{HO})\text{V}(\text{OH}_2)(\text{HOCH}_3)^+$ .

**Table 7.3:** Frequencies of the most prominent bands of various vanadium oxide methanol complexes observed in the IRMPD spectra. Due to the position of the frequencies, three similar groups can be identified.

m/z	$[\text{VCH}_6\text{O}_2]^+$ 101.0	$[\text{VC}_2\text{H}_{12}\text{O}_4]^+$ 151.0	$[\text{VC}_2\text{H}_9\text{O}_3]^+$ 132.0	$[\text{VCH}_5\text{O}_3]^+$ 116.0	$[\text{VCH}_7\text{O}_3]^+$ 118.0
cm <sup>-1</sup>			897		
	970	972	977		
			1004		
			1023		
	1083	1099		1087	1077
	1111	1116		1108	
	1218	1207			
		1247			
			1262		
			1287		
				1310	1301
				1355	
				1502	1487

### 7.4.2 IRMPD Spectra of Vanadium Oxide Ethanol Complexes

Vanadium oxide monocations activate alcohols rapidly in gas phase experiments. Schwarz and co-workers reported in their FT-ICR-MS studies about different product channels depending on the nature of the alcohol, and especially on the alkyl chain length. While the dehydrogenation via a selective 1,2-elimination predominates the reaction of  $\text{VO}^+$  with methanol, alkene formation is observed as the main pathway in the reaction of  $\text{VO}^+$  with ethanol.<sup>45</sup>

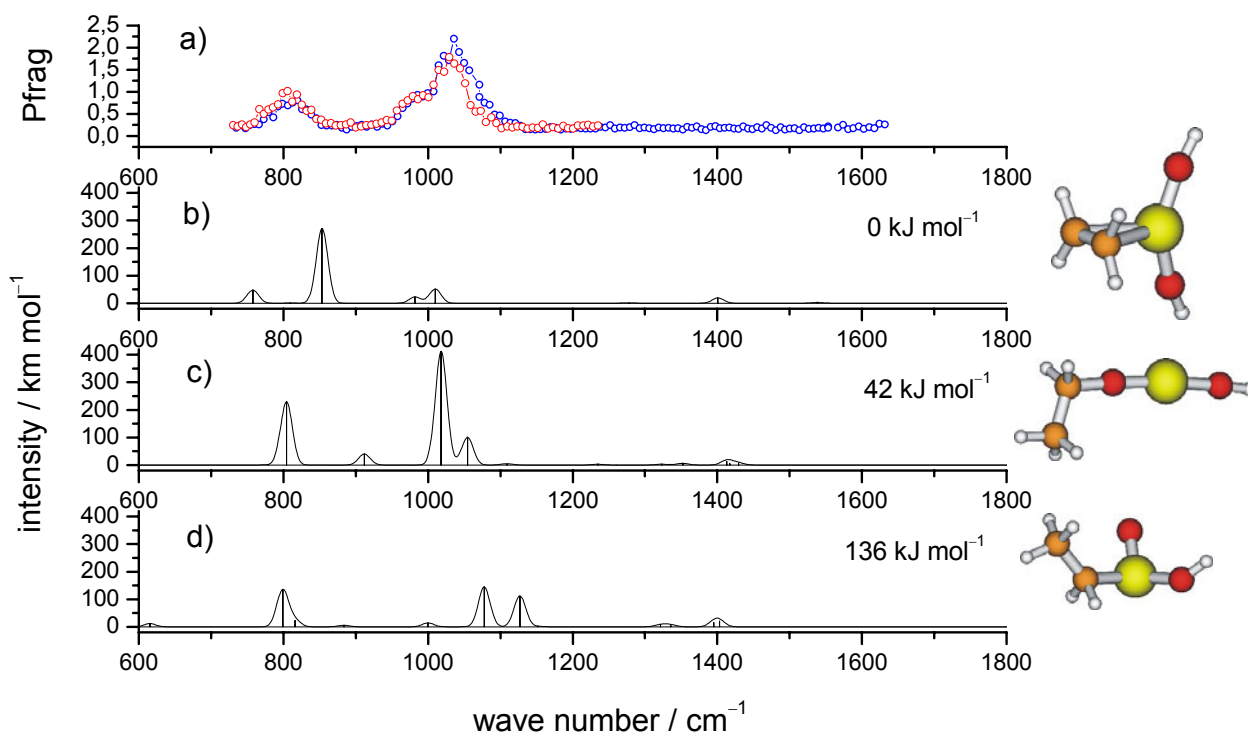
The following IRMPD spectra of vanadium oxide ethanol complexes will provide additional information about the fragmentation behaviour of some selected complexes when irradiated by the FEL CLIO.

Vanadium oxide ethanol complexes of various stoichiometries have been prepared by laser vaporization within MICRA as described in the experimental section. Three complexes were mass selected and irradiated by the FEL IR beam. Table 7.4 provides the formal composition together with the most crucial parameters for the preparation of the complexes.

**Table 7.4.** Vanadium oxide ethanol complexes and experimental parameters for their preparation at MICRA by laser vaporization.

Formula	$m/z$ <sup>*</sup>	$p_{\text{ethanol}}$ / mbar	$t_{\text{pulse}}$ / ms	$t_{\text{react}}$ / ms
$[\text{VC}_2\text{H}_6\text{O}_2]^+$	113.0	$1 \times 10^{-6}$	30	1200
$[\text{VC}_4\text{H}_{10}\text{O}_3]^+$	157.0	$2 \times 10^{-6}$	40	1200
$[\text{VC}_4\text{H}_{12}\text{O}_3]^+$	159.0	$2 \times 10^{-6}$	40	1200

<sup>\*</sup> Due to low mass resolution at MICRA, only values rounded to one decimal place are given here.

IRMPD Spectrum of  $[\text{VC}_2\text{H}_6\text{O}_2]^+$ 

**Figure 7.14:** a) IRMPD spectrum of the complex with the formal stoichiometry  $[\text{VC}_2\text{H}_6\text{O}_2]^+$  ( $m/z = 113.0$ ) in the spectral range of  $730\text{ cm}^{-1}$  to  $1610\text{ cm}^{-1}$ . Different colors indicate independent measurements in which the FEL power varied between  $1.4\text{ W}$  and  $1.7\text{ W}$ . The radiation time was  $500\text{ ms}$ . Resonant IR radiation leads to the ionic fragments  $m/z = 111.0$ ,  $m/z = 84.9$  and  $m/z = 66.9$ . b), c) and d) present calculated absorption spectra of some possible structural isomers (B3LYP/TZVP, scaled by  $0.95$ ;  $S = 1$  in b) and c),  $S = 0$  in d)).

The IRMPD spectrum of the vanadium oxide ethanol complex of the formal composition  $[\text{VC}_2\text{H}_6\text{O}_2]^+$  ( $m/z = 113.0$ ) shows prominent bands in the spectral regions of the maxima at  $805\text{ cm}^{-1}$ ,  $1025\text{ cm}^{-1}$ ,  $1032\text{ cm}^{-1}$  and some further less distinct shoulders at  $768\text{ cm}^{-1}$ ,  $979\text{ cm}^{-1}$  and  $1072\text{ cm}^{-1}$  (cf. Figure 7.14 a)).

The vibrational frequencies of the most stable calculated structural isomer (Figure 7.14 b)) explain all recorded bands qualitatively. Nevertheless, the positions of some bands do not agree exactly with each other. Especially the  $\nu_{\text{asym}}(\text{HO}-\text{V}-\text{OH})$ , calculated to appear around  $853\text{ cm}^{-1}$  (when applying a scaling factor of  $0.95$ ), does not match the experimental band at  $805\text{ cm}^{-1}$ . However, this might be due to the non-appropriate average scaling factor for this type of vibration. Another possible structural isomer is (Figure 7.14 c)) is  $42\text{ kJ mol}^{-1}$  less stable. This structure would account well for the experimental band at  $805\text{ cm}^{-1}$ . As the existence of high energy isomers is possible, it can not be excluded that this structure might contribute to the experimental spectrum as well. This structure would also help to explain the

weak shoulder at  $1072\text{ cm}^{-1}$  and to explain the observed intensity ratios, which are not well represented alone by the lowest isomer. Weak calculated bands are missing in the IRMPD spectrum around  $1400\text{ cm}^{-1}$ , possibly due to inefficient fragmentation yields. A plain association complex of an intact ethanol on  $\text{VO}^+$  can be ruled out due to the non existing bands in the spectrum around  $1280\text{ cm}^{-1}$  and due to further energetic reasons.

All of the three detected ionic fragments  $m/z = 111.0$ ,  $m/z = 84.9$  and  $m/z = 66.9$  are present whenever dissociation occurs, although at varying yields. The fragments correspond to formal loss of  $\text{H}_2$ , loss of  $\text{C}_2\text{H}_4$  and loss of  $\text{C}_2\text{H}_6\text{O}$ , respectively. A distinct mode selective fragmentation was not observed. In good approximation the fragment ratio is 25:50:25 as is graphically displayed in Figure 7.15.

In contrast to this result, Schwarz and co-workers found  $\text{H}_2$ ,  $\text{H}_2\text{O}$  and  $\text{C}_2\text{H}_4$  in a ratio of 20:2:77 to be the major neutral products in their FT-ICR-MS study of the reaction of  $\text{VO}^+$  and ethanol. Fragments due to the loss of  $\text{H}_2\text{O}$  are not observed in the IRMPD spectra.

On the basis of the calculated spectra the complex  $[\text{VC}_2\text{H}_6\text{O}_2]^+$  can be described as  $(\text{C}_2\text{H}_4)\text{V}(\text{OH})_2^+$ , which is the most likely isomer, and possibly coexisting with some  $(\text{CH}_3\text{CH}_2\text{O})\text{V}(\text{OH})^+$ .

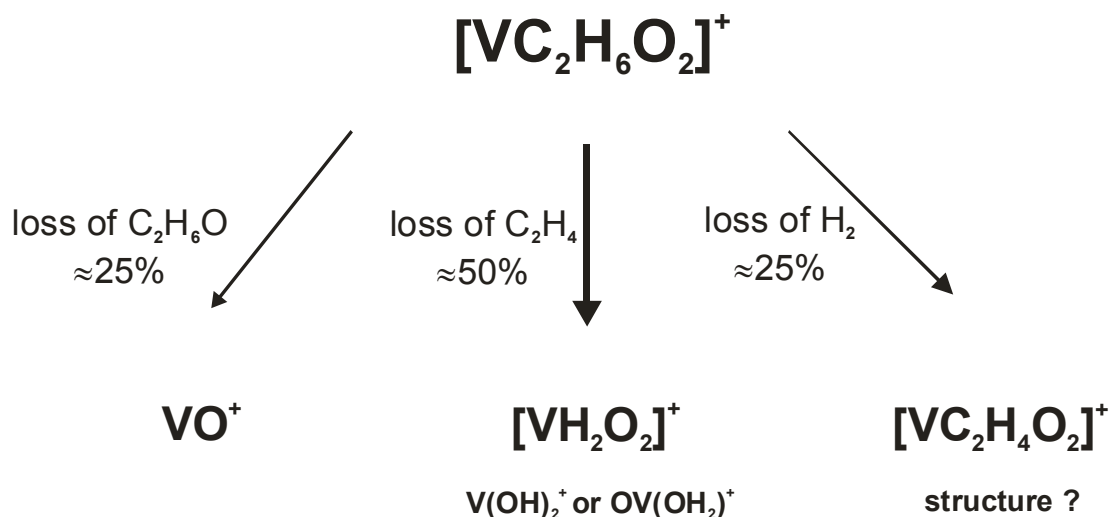


**Figure 7.15:** Observed fragmentation pattern of  $[\text{VC}_2\text{H}_6\text{O}_2]^+$  after resonant absorption of the FEL IR radiation in the spectral region of  $730\text{ cm}^{-1}$  to  $1610\text{ cm}^{-1}$ .

**IRMPD Spectra of  $[\text{VC}_4\text{H}_{10}\text{O}_3]^+$  and  $[\text{VC}_4\text{H}_{12}\text{O}_3]^+$** 

IRMPD spectra of  $[\text{VC}_4\text{H}_{10}\text{O}_3]^+$  and  $[\text{VC}_4\text{H}_{12}\text{O}_3]^+$  recorded at CLIO in the range of  $720\text{ cm}^{-1}$  to  $1650\text{ cm}^{-1}$  provide numerous bands in this spectral region (cf. Figures 7.16 and 7.17).  $[\text{VC}_4\text{H}_{12}\text{O}_3]^+$  loses  $\text{H}_2$  to form  $[\text{VC}_4\text{H}_{10}\text{O}_3]^+$  while applying mass selection within the icr cell. Therefore both complexes were recorded at the same time, with very wide isolation parameters applied. Due to the very broad bands in the IRMPD spectrum, an unambiguous assignment is difficult. Similar to the complex  $[\text{VC}_2\text{H}_6\text{O}_2]^+$ , discussed in the previous section, both spectra exhibit bands whose maxima are close to  $800\text{ cm}^{-1}$  and  $1000\text{ cm}^{-1}$ . Also a shoulder at approximately  $1072\text{ cm}^{-1}$  appears. An assured assignment without supplementing calculations remains difficult as both VOH and VO bands and various  $\text{CH}_2$  and  $\text{CH}_3$  modes may be obtained in these spectral regions. All the same, the rather sharp band observed in both spectra at  $1248\text{ cm}^{-1}$  is indicative of the presence of an intact ethanol molecule within the complexes. This band is due to a combined deformation vibration of C–O–H and H–C–H groups, which can only appear in intact ethanol that is not activated by vanadium or vanadium oxide yet. A comparable mode was observed in case of methanol attached to vanadium oxide, although the respective mode there appeared somewhat shifted (close to  $1300\text{ cm}^{-1}$ ).

Unfortunately, up to date, calculations which definitively explain all of the observed spectral features are not available yet.

Nevertheless, the fragmentation pattern of these two complexes yields in itself some implications for the possible connectivity within these complexes. According to the worked out fragmentation scheme (Figure 7.18), FEL activated  $[\text{VC}_4\text{H}_{12}\text{O}_3]^+$  loses a formal ethanol molecule, yielding the ionic fragment  $[\text{VC}_2\text{H}_6\text{O}_2]^+$  (main fragmentation path on the right side of Figure 7.18). The likewise studied complex  $[\text{VC}_4\text{H}_{10}\text{O}_3]^+$  forms the ionic fragment  $[\text{VC}_2\text{H}_4\text{O}_2]^+$ , which is also accompanied by the loss of a formal ethanol unit (see left side of Figure 7.18). The lost unit of ethanol might as well be one water molecule plus one molecule of  $\text{C}_2\text{H}_4$ . Anyhow, this would not explain the band at  $1248\text{ cm}^{-1}$  in the experimental spectra. The existence of an intact associated ethanol molecule further provides for a good leaving group, which is easily released from the complex upon irradiation. Thus through elimination of ethanol from the complexes  $[\text{VC}_4\text{H}_{10}\text{O}_3]^+$  and  $[\text{VC}_4\text{H}_{12}\text{O}_3]^+$  the ionic fragments detected at  $m/z = 111.0$  and  $m/z = 113.0$  are formed, respectively.

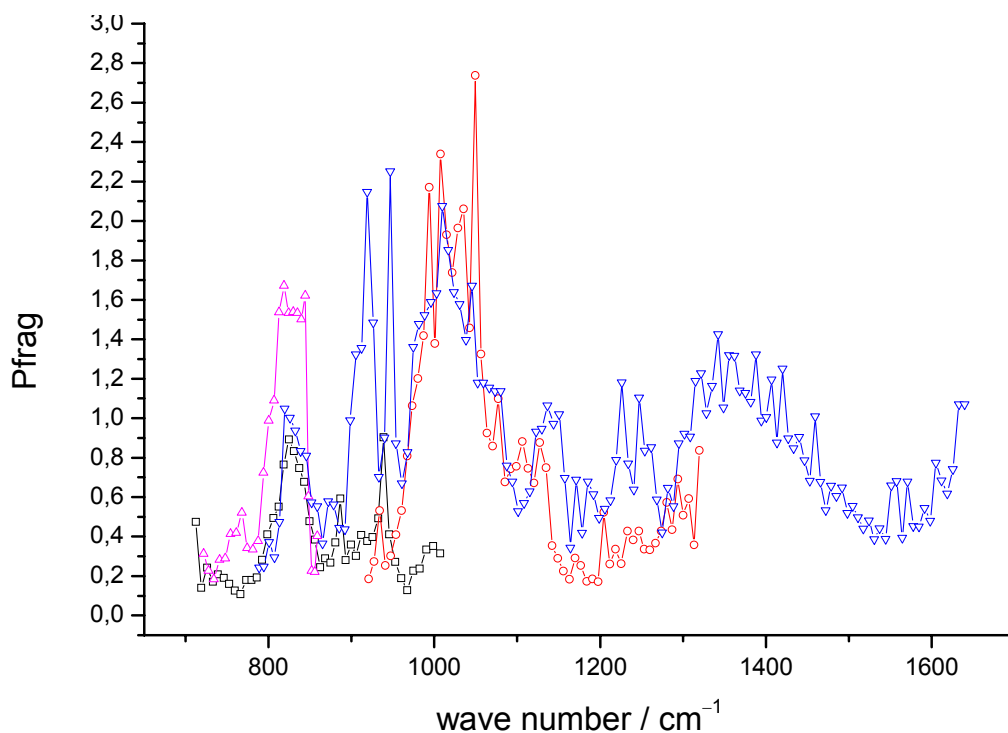


**Figure 7.16:** IRMPD spectrum of the complex with the formal stoichiometry  $[\text{VC}_4\text{H}_{10}\text{O}_3]^+$  ( $m/z = 157.0$ ) in the spectral range of  $720\text{ cm}^{-1}$  to  $1650\text{ cm}^{-1}$ . Different colors indicate independent measurements in which the FEL power varied between 1.0 W and 1.7 W. The radiation time was 500 ms. Resonant IR radiation leads to ionic fragments  $m/z = 111.0$  and  $m/z = 66.9$ .

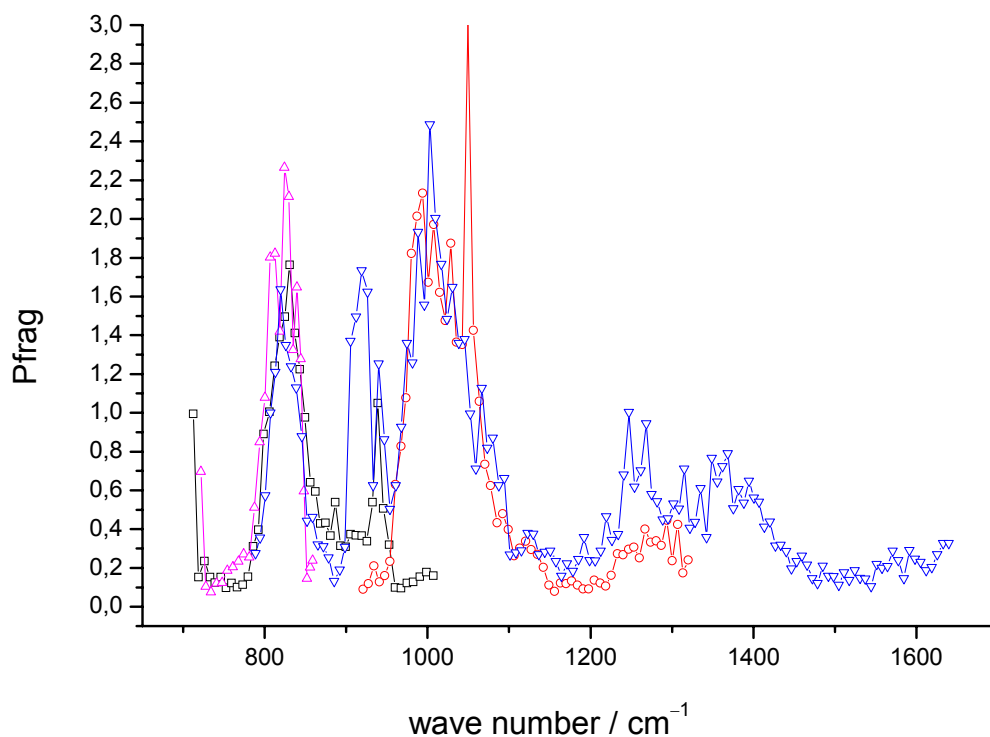


**Figure 7.17:** IRMPD spectrum of the complex with the formal stoichiometry  $[\text{VC}_4\text{H}_{12}\text{O}_3]^+$  ( $m/z = 159.0$ ) in the spectral range of  $720\text{ cm}^{-1}$  to  $1650\text{ cm}^{-1}$ . Different colors indicate independent measurements in which the FEL power varied between 0.8 W and 1.0 W. The radiation time was 500 ms. Resonant IR radiation leads to ionic fragments  $m/z = 113.0$  and  $m/z = 84.9$ .

It is also conceivable that in case of the complex  $[\text{VC}_4\text{H}_{12}\text{O}_3]^+$  a mixture of two or more isomers exists. Such a mixture may explain the observed loss of  $\text{H}_2$  in the course of the RF isolation, while no significant loss of  $\text{H}_2$  is found after irradiation by the FEL. Still, the complex would need to contain at least one intact ethanol moiety. Loss of  $\text{H}_2$  would then be most probable if two intact ethanol units were present in the complex. This however would not account for the band at  $800\text{ cm}^{-1}$ , which is believed to originate from VOH groups.

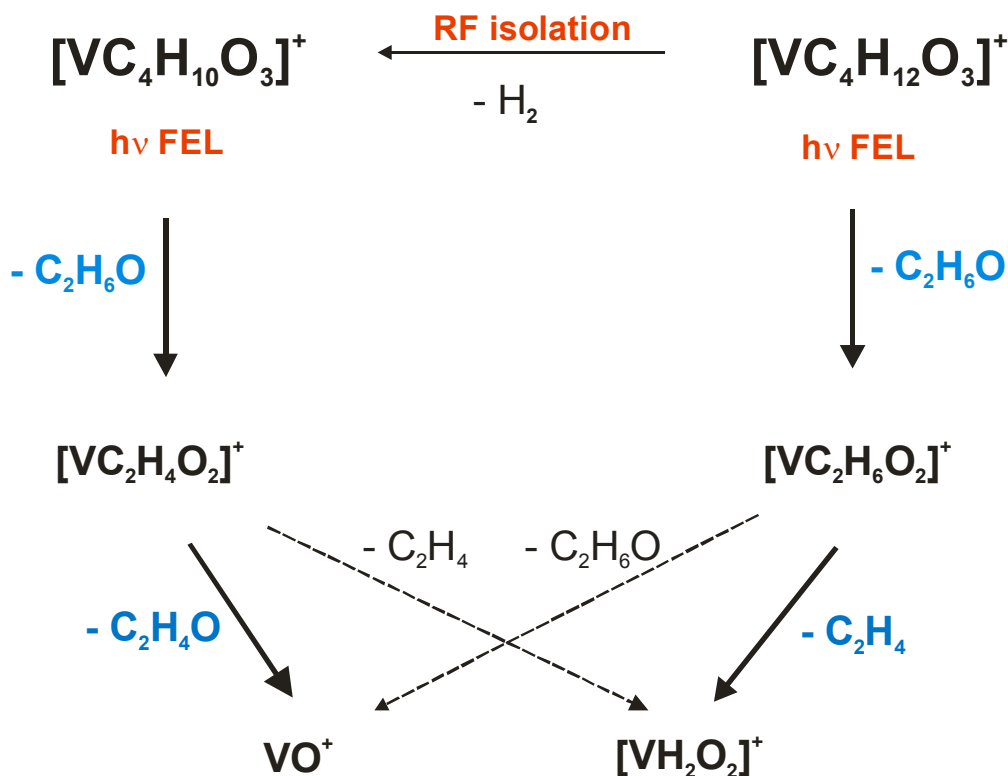


**Figure 7.18:** Observed fragmentation pathway of  $[\text{VC}_4\text{H}_{10}\text{O}_3]^+$  and  $[\text{VC}_4\text{H}_{12}\text{O}_3]^+$  after resonant absorption of the FEL IR radiation in the spectral region from  $730\text{ cm}^{-1}$  to  $1610\text{ cm}^{-1}$ .  $[\text{VC}_4\text{H}_{12}\text{O}_3]^+$  loses  $\text{H}_2$  forming  $[\text{VC}_4\text{H}_{10}\text{O}_3]^+$  when mass selection by radiofrequency is performed.

The second ionic fragment formed from  $[\text{VC}_4\text{H}_{10}\text{O}_3]^+$  upon irradiation is  $\text{VO}^+$  ( $m/z = 66.9$ ). Formally it stems from loss of ethanol and  $\text{C}_2\text{H}_4\text{O}$ . Whether the  $\text{VO}^+$  originates from parallel or from sequential loss of ethanol and  $\text{C}_2\text{H}_4\text{O}$ , can not be deduced from the IRMPD spectra. In case of the heavier complex  $[\text{VC}_4\text{H}_{12}\text{O}_3]^+$  the correlated second fragment  $[\text{VH}_2\text{O}_2]^+$  arises through elimination of ethanol and  $\text{C}_2\text{H}_4$ . The fragmentation pathways have been determined by correlation of the fragment ions to the respective parent ion. The conceivable crossing of the fragmentation pathways can not be entirely excluded.

Based on these considerations, the complex of the formal composition  $[\text{VC}_4\text{H}_{10}\text{O}_3]^+$  is likely to correspond to a structure that can be described as  $\text{OV}(\text{OCH}_2\text{CH}_2)(\text{HOCH}_2\text{CH}_3)^+$ . While the fragmentation pattern of  $[\text{VC}_4\text{H}_{12}\text{O}_3]^+$  would allow for the assignment of this complex to  $\text{HOV}(\text{OCH}_2\text{CH}_3)(\text{HOCH}_2\text{CH}_3)^+$ , a mixture of this complex with further isomers is conceivable. The assumption of a mixture of isomers could explain the observed loss of  $\text{H}_2$  through RF isolation in contrast to irradiation by the FEL where no loss of  $\text{H}_2$  is observed.



**Figure 7.19:** Assumed structures of  $[\text{VC}_4\text{H}_{10}\text{O}_3]^+$  (left) and  $[\text{VC}_4\text{H}_{12}\text{O}_3]^+$  (right).

## 7.5 Summary and Outlook

IRMPD spectroscopy of ionic complexes in the gas phase allow for structural elucidation where more conventional spectroscopic techniques would fail. The addition of DFT calculations is mandatory in order to interpret the recorded spectra that often comprise of high complexity. Together these methods provide a powerful tool for the elucidation of structures of complexes, clusters and molecular ions in the gas phase. In the present case of vanadium oxides, however, one has to be careful in applying standard quantum chemical methods. Problems may arise from the multireference character of electronic wavefunctions in VO containing species. This becomes especially obvious in the choice of the appropriate scaling factor for the calculated frequencies and in the sometimes questionable quality of predicted energetics. Nevertheless a whole series of complexes could be assigned to reasonable structures by combining experiment and theory to cancel their respective deficiencies.



The vanadium oxide acetonitrile complexes  $[\text{VC}_2\text{H}_3\text{NO}]^+$ ,  $[\text{VC}_4\text{H}_6\text{N}_2\text{O}]^+$  and  $[\text{VC}_4\text{H}_6\text{N}_2\text{O}_2]^+$  are assigned to coordination compounds in which the acetonitrile ligands are coordinated via the lone-pair of the nitrogen atom to  $\text{VO}^+$  or  $\text{VO}_2^+$ . The complexes can then be described as the energetically most favored structures  $\text{OV}(\text{NCCH}_3)^+$ ,  $\text{OV}(\text{NCCH}_3)_2^+$  and  $\text{VO}_2(\text{NCCH}_3)_3^+$ .

This work further provides strong evidence for the reaction of three acetonitrile ligands in  $[\text{VC}_6\text{H}_9\text{N}_3\text{O}_2]^+$  and  $[\text{VC}_6\text{H}_{10}\text{N}_3\text{O}_2]^+$  yielding most likely  $\text{VO}_2(2,4,6\text{-trimethyl-1,3,5-triazine})^+$  and  $(\text{HO})\text{OV}(2,4,6\text{-trimethyl-1,3,5-triazine})^+$ . Both the experimental IRMPD spectra and the ab initio computed IR absorption spectra of such structures agree well in this regard. The computed total energies of the predicted structures are  $+180 \text{ kJ mol}^{-1}$  and  $+130 \text{ kJ mol}^{-1}$  higher than those of the coordination isomers  $\text{VO}_2(\text{NCCH}_3)_3^+$  and  $(\text{HO})\text{OV}(\text{NCCH}_3)_3^+$ , respectively. Further more elaborate quantum mechanical calculations, based on multireference methods, would be appreciable.

IRMPD spectra of vanadium oxide methanol complexes have been assigned to a mixture of isomers in the case of  $[\text{VCH}_6\text{O}_2]^+$ . The recorded spectrum of  $[\text{VC}_2\text{H}_{12}\text{O}_4]^+$  resembles that of  $[\text{VCH}_6\text{O}_2]^+$  leading to the conclusion that these two species should be of similar structure.

The spectra of  $[\text{VCH}_5\text{O}_3]^+$  and  $[\text{VCH}_7\text{O}_3]^+$  differ significantly in number and position of bands from those of  $[\text{VCH}_6\text{O}_2]^+$  and  $[\text{VC}_2\text{H}_{12}\text{O}_4]^+$ . The observed spectral features are due to a strong dependence on the formal oxidation state respectively on the number of H atoms. Complexes with an odd number of H atoms appear to release either a formal methoxy cation or a neutral  $\text{CH}_3\text{O}$  radical or at least involve a methoxy group. This is not observed in the IRMPD spectra of complexes with even numbers of H atoms.

The most likely isomer of  $[\text{VCH}_5\text{O}_3]^+$  is predicted to be  $\text{OV}(\text{OH})(\text{HOCH}_3)^+$ , while  $[\text{VCH}_7\text{O}_3]^+$  can be assigned to  $(\text{HO})\text{V}(\text{OH}_2)(\text{HOCH}_3)^+$ . Both complexes lose a neutral  $\text{CH}_3\text{O}$  radical upon irradiation.

Ethanol is rapidly activated by vanadium and its oxides. The IRMPD spectrum of the vanadium oxide ethanol complex  $[\text{VC}_2\text{H}_6\text{O}_2]^+$  shows the expected loss of ethene as the main fragment. Based on the comparison of the experiment with the calculated spectra  $[\text{VC}_2\text{H}_6\text{O}_2]^+$  can be described as  $(\text{C}_2\text{H}_4)\text{V}(\text{OH})_2^+$ , which is the energetically most likely isomer.

**Table 7.5:** Overview of some figures of merit of vanadium oxide complexes with acetonitrile, methanol and ethanol.

Formula	ligands	oxid. State	# e <sup>-</sup> <sub>tot</sub>	spin state	# e <sup>-</sup> <sub>vanad.</sub>	rel. ΔE in kJ/mol	neutral fragments	ionic fragments	spectral evidence
<b>Acetonitrile</b>									
[VC <sub>2</sub> H <sub>3</sub> NO] <sup>+</sup>	O <sup>2-</sup> , CH <sub>3</sub> CN	V <sup>III</sup>	52	triplet	2	0	–	–	(+)
[VC <sub>4</sub> H <sub>6</sub> N <sub>2</sub> O] <sup>+</sup>	O <sup>2-</sup> , 2 CH <sub>3</sub> CN	V <sup>III</sup>	74	triplet	2	0	CH <sub>3</sub> CN	[VC <sub>2</sub> H <sub>3</sub> NO] <sup>+</sup>	+
	2 O <sup>2-</sup> , 2 CH <sub>3</sub> CN	V <sup>V</sup>	82	singlet	0	0	CH <sub>3</sub> CN	[VC <sub>4</sub> H <sub>6</sub> N <sub>2</sub> O <sub>2</sub> ] <sup>+</sup>	+
[VC <sub>4</sub> H <sub>6</sub> N <sub>2</sub> O <sub>3</sub> ] <sup>+</sup>	O <sup>2-</sup> , CH <sub>3</sub> CN, CH <sub>3</sub> C(O)NO <sup>2-</sup>	V <sup>V</sup>	90	singlet	0	0			+
	O <sup>2-</sup> , CH <sub>3</sub> CN, CH <sub>3</sub> C(O)NO <sup>2-</sup>	V <sup>III</sup>	90	triplet	2	deg.	two fragments CH <sub>3</sub> CN CH <sub>3</sub> C(O)NO	two fragments [VC <sub>3</sub> H <sub>3</sub> N <sub>1</sub> O <sub>3</sub> ] <sup>+</sup> [VC <sub>2</sub> H <sub>3</sub> NO] <sup>+</sup>	+
[VC <sub>6</sub> H <sub>9</sub> N <sub>3</sub> O <sub>2</sub> ] <sup>+</sup>	2 O <sup>2-</sup> , 3 CH <sub>3</sub> CN	V <sup>V</sup>	104	singlet	0	0	CH <sub>3</sub> CN	[VC <sub>4</sub> H <sub>6</sub> N <sub>2</sub> O <sub>2</sub> ] <sup>+</sup>	-
	2 O <sup>2-</sup> , triazine	V <sup>V</sup>	104	singlet	0	+180			+
[VC <sub>6</sub> H <sub>10</sub> N <sub>3</sub> O <sub>2</sub> ] <sup>+</sup>	2 O <sup>2-</sup> , 3 CH <sub>3</sub> CN	V <sup>IV</sup>	105	doublet	1	0	CH <sub>3</sub> CN	[VC <sub>4</sub> H <sub>7</sub> N <sub>2</sub> O <sub>2</sub> ] <sup>+</sup>	-
	2 O <sup>2-</sup> , triazine	V <sup>IV</sup>	105	doublet	1	+130			+
<b>Methanol</b>									
[VCH <sub>6</sub> O <sub>2</sub> ] <sup>+</sup>	OH <sup>-</sup> , CH <sub>3</sub> <sup>-</sup> , H <sub>2</sub> O	V <sup>III</sup>	50	triplet	2	0	[VOH <sub>3</sub> ]	CH <sub>2</sub> OH <sup>+</sup>	-
	O <sup>2-</sup> , CH <sub>2</sub> <sup>2-</sup> , H <sub>2</sub> O	V <sup>V</sup>	50	singlet	0	+172			+
		V <sup>III</sup>	50	triplet	2	+199			+
[VCH <sub>5</sub> O <sub>3</sub> ] <sup>+</sup>	2OH <sup>-</sup> , CH <sub>3</sub> O <sup>-</sup>	V <sup>IV</sup>	57	doublet	1	0	CH <sub>3</sub> O•	[VH <sub>2</sub> O <sub>2</sub> ] <sup>+</sup>	-
	O <sup>2-</sup> , OH <sup>-</sup> , CH <sub>3</sub> OH	V <sup>IV</sup>	57	doublet	1	+46			+

Formula	ligands	oxid. State	# e <sup>-</sup> <sub>tot</sub>	spin state	# e <sup>-</sup> <sub>vanad.</sub>	rel. ΔE in kJ/mol	neutral fragments	ionic fragments	spectral evidence
<b>Methanol</b>									
[VCH <sub>7</sub> O <sub>3</sub> ] <sup>+</sup>	2OH <sup>-</sup> , CH <sub>3</sub> <sup>-</sup> , H <sub>2</sub> O	V <sup>IV</sup>	59	doublet	1	0	CH <sub>3</sub> O•	[VH <sub>4</sub> O <sub>2</sub> ] <sup>+</sup>	-
	CH <sub>3</sub> O <sup>-</sup> , 2 H <sub>2</sub> O	V <sup>II</sup>	59	quartet	3	+26			-
	OH <sup>-</sup> , CH <sub>3</sub> OH, H <sub>2</sub> O	V <sup>II</sup>	59	quartet	3	+32			+
[VC <sub>2</sub> H <sub>9</sub> O <sub>3</sub> ] <sup>+</sup>	OH <sup>-</sup> , CH <sub>3</sub> <sup>-</sup> , CH <sub>3</sub> O <sup>-</sup> , H <sub>2</sub> O,	V <sup>IV</sup>	67	doublet	1	0	CH <sub>3</sub> OH + H <sub>2</sub> O	[VC <sub>1</sub> H <sub>3</sub> O] <sup>+</sup>	-
	2OH <sup>-</sup> , CH <sub>3</sub> <sup>-</sup> , CH <sub>3</sub> OH	V <sup>IV</sup>	67	doublet	1	+11			-
[VC <sub>2</sub> H <sub>12</sub> O <sub>4</sub> ] <sup>+</sup>	OH <sup>-</sup> , CH <sub>3</sub> <sup>-</sup> , 2 H <sub>2</sub> O, CH <sub>3</sub> OH	V <sup>III</sup>	78	triplet	2	0	CH <sub>3</sub> OH + H <sub>2</sub> O	[VC <sub>1</sub> H <sub>6</sub> O <sub>2</sub> ] <sup>+</sup>	+
	H <sub>2</sub> O, H <sub>2</sub> CO, CH <sub>3</sub> OH, H <sub>2</sub>	V <sup>III</sup>	78	triplet	2	+221			+
<b>Ethanol</b>									
[VC <sub>2</sub> H <sub>6</sub> O <sub>2</sub> ] <sup>+</sup>	2OH <sup>-</sup> , C <sub>2</sub> H <sub>4</sub> ,	V <sup>III</sup>	56	triplet	2	0			+
	OH <sup>-</sup> , CH <sub>3</sub> CH <sub>2</sub> O <sup>-</sup>	V <sup>III</sup>	56	triplet	2	+42			+
	O <sup>2-</sup> , OH <sup>-</sup> , CH <sub>3</sub> CH <sub>2</sub> <sup>-</sup>	V <sup>V</sup>	56	singlet	0	+136	three fragments H <sub>2</sub> C <sub>2</sub> H <sub>4</sub> C <sub>2</sub> H <sub>6</sub> O	three fragments [VC <sub>2</sub> H <sub>4</sub> O <sub>2</sub> ] <sup>+</sup> [VH <sub>2</sub> O <sub>2</sub> ] <sup>+</sup> [VO] <sup>+</sup>	-
[VC <sub>4</sub> H <sub>10</sub> O <sub>3</sub> ] <sup>+</sup>	O <sup>2-</sup> , CH <sub>2</sub> CH <sub>2</sub> O <sup>2-</sup> , CH <sub>3</sub> CH <sub>2</sub> OH	V <sup>V</sup>	80	?	?	-	two fragments C <sub>2</sub> H <sub>6</sub> O; C <sub>2</sub> H <sub>10</sub> O <sub>2</sub>	two fragments [VC <sub>2</sub> H <sub>4</sub> O <sub>2</sub> ] <sup>+</sup> [VO] <sup>+</sup>	-
[VC <sub>4</sub> H <sub>12</sub> O <sub>3</sub> ] <sup>+</sup>	O <sup>2-</sup> , CH <sub>3</sub> CH <sub>2</sub> O <sup>-</sup> , CH <sub>3</sub> CH <sub>2</sub> OH	V <sup>III</sup>	82	?	?	-	two fragments C <sub>2</sub> H <sub>6</sub> O; C <sub>4</sub> H <sub>10</sub> O	two fragments [VC <sub>2</sub> H <sub>6</sub> O <sub>2</sub> ] <sup>+</sup> [VH <sub>2</sub> O <sub>2</sub> ] <sup>+</sup>	-

Due to the broad spectral features observed in the spectra of  $[\text{VC}_4\text{H}_{10}\text{O}_3]^+$  and  $[\text{VC}_4\text{H}_{12}\text{O}_3]^+$  a definite assignment could not be made at this point. The best possible assignments are mainly based on some distinct features visible in the IRMPD spectra together with the observed fragmentation pattern. These are  $\text{OV}(\text{OCH}_2\text{CH}_2)(\text{HOCH}_2\text{CH}_3)^+$  and  $(\text{HO})\text{V}(\text{OCH}_2\text{CH}_3)(\text{HOCH}_2\text{CH}_3)^+$ , respectively.

Future calculations are expected to validate the suggested structural assignments. The availability of better resolved IRMPD spectra would also contribute to a more precise structural assignment of the studied complexes, where necessary.

## 7. 5 References

- 1 C. N. R. Rao, B. Raveau, and Editors, *Transition Metal Oxides*. (1995).
- 2 B. M. Weckhuysen and D. E. Keller, *Catal. Today* **78** (1-4), 25 (2003).
- 3 J. Hagen, *Technische Katalyse. Eine Einführung*. (VCH, Weinheim, 1996).
- 4 M. Kaczorowska, H. Schwarz, and D. Schroeder, *Eur. J. Inorg. Chem.* (21), 3335 (2007).
- 5 N. Song, Z. Xuan, J. K. Bartley, S. H. Taylor, D. Chadwick, and G. J. Hutchings, *Catal. Lett.* **106** (3-4), 127 (2006).
- 6 O. B. Lapina, B. S. Bal'zhinimaev, S. Boghosian, K. M. Eriksen, and R. Fehrmann, *Catal. Today* **51** (3-4), 469 (1999).
- 7 L. R. Makedonski and V. A. Nikolov, *Bulg. Chem. Commun.* **28** (1), 27 (1995).
- 8 S. Feyel, H. Schwarz, D. Schröder, C. Daniel, H. Hartl, J. Dobler, J. Sauer, G. Santambrogio, L. Woste, and K. R. Asmis, *ChemPhysChem* **8** (11), 1640 (2007).
- 9 K. R. Asmis, M. Brummer, C. Kaposta, G. Santambrogio, G. von Helden, G. Meijer, K. Rademann, and L. Woste, *Phys. Chem. Chem. Phys.* **4** (7), 1101 (2002).
- 10 K. R. Asmis, G. Meijer, M. Brummer, C. Kaposta, G. Santambrogio, L. Woste, and J. Sauer, *J. Chem. Phys.* **120** (14), 6461 (2004).
- 11 K. R. Asmis and J. Sauer, *Mass Spectrom. Rev.* **26** (4), 542 (2007).
- 12 R. C. Bell, K. A. Zemski, D. R. Justes, and A. W. Castleman, Jr., *J. Chem. Phys.* **114** (2), 798 (2001).
- 13 K. R. Asmis, G. Santambrogio, M. Brummer, and J. Sauer, *Angewandte Chemie-International Edition* **44** (20), 3122 (2005).
- 14 R. C. Bell and A. W. Castleman, Jr., *J. Phys. Chem. A* **106** (42), 9893 (2002).
- 15 R. C. Bell, K. A. Zemski, and A. W. Castleman, Jr., *J. Phys. Chem. A* **102** (43), 8293 (1998).
- 16 R. C. Bell, K. A. Zemski, and A. W. Castleman, Jr., *J. Phys. Chem. A* **103** (16), 2992 (1999).
- 17 R. C. Bell, K. A. Zemski, and A. W. Castleman, Jr., *J. Phys. Chem. A* **103** (11), 1585 (1999).
- 18 M. Engeser, T. Weiske, D. Schröder, and H. Schwarz, *J. Phys. Chem. A* **107** (16), 2855 (2003).
- 19 S. Feyel, L. Scharfenberg, C. Daniel, H. Hartl, D. Schröder, and H. Schwarz, *J. Phys. Chem. A* **111** (17), 3278 (2007).

- 20 S. Feyel, D. Schröder, and H. Schwarz, *J. Phys. Chem. A* **110** (8), 2647 (2006).
- 21 A. Fielicke, R. Mitric, G. Meijer, V. Bonacic-Koutecky, and G. von Helden, *Journal of the American Chemical Society* FIELD Publication Date:2003 **125** (51), 15716.
- 22 D. R. Justes, A. W. Castleman, Jr., R. Mitric, and V. Bonacic-Koutecky, *Eur. Phys. J. D* **24** (1-3), 331 (2003).
- 23 K. A. Zemski, R. C. Bell, and A. W. Castleman, Jr., *Clusters and Nanostructure Interfaces*, [Proceedings of the International Symposium on Clusters and Nanostructure Interfaces], Richmond, VA, United States, Oct. 25-28, 1999, 535 (2000).
- 24 K. A. Zemski, D. R. Justes, and A. W. Castleman, Jr., *J. Phys. Chem. A* **105** (45), 10237 (2001).
- 25 M. Engeser, M. Schlangen, D. Schröder, H. Schwarz, T. Yumura, and K. Yoshizawa, *Organometallics* **22** (19), 3933 (2003).
- 26 A. Fielicke and K. Rademann, *Phys. Chem. Chem. Phys.* **4** (12), 2621 (2002).
- 27 M. Pykavy and C. van Wullen, *J. Phys. Chem. A* **107** (29), 5566 (2003).
- 28 M. Pykavy, C. van Wullen, and J. Sauer, *J. Chem. Phys.* **120** (9), 4207 (2004).
- 29 J. Dobler, M. Pritzsche, and J. Sauer, *J. Am. Chem. Soc.* **127** (31), 10861 (2005).
- 30 J. Oomens, J. M. Bakker, B. G. Sartakov, G. Meijer, and G. von Helden, *Chem. Phys. Lett.* **367** (5-6), 576 (2003).
- 31 J. Lemaire, P. Boissel, M. Heninger, G. Mauclaire, G. Bellec, H. Mestdagh, A. Simon, S. Le Caer, J. M. Ortega, F. Glotin, and P. Maitre, *Phys. Rev. Lett.* **89** (27), 273002/1 (2002).
- 32 B. M. Reinhard, A. Lagutschenkov, J. Lemaire, P. Maitre, P. Boissel, and G. Niedner-Schatteburg, *J. Phys. Chem. A* **108** (16), 3350 (2004).
- 33 P. Maitre, S. Le Caer, A. Simon, W. Jones, J. Lemaire, H. Mestdagh, M. Heninger, G. Mauclaire, P. Boissel, R. Prazeres, F. Glotin, and J.-M. Ortega, *Nucl. Instrum. Methods Phys. Res., Sect. A* **507** (1-2), 541 (2003).
- 34 A. Schafer, C. Huber, and R. Ahlrichs, *Journal of Chemical Physics* **100** (8), 5829 (1994).
- 35 R. Ahlrichs, M. Bar, M. Haser, H. Horn, and C. Kolmel, *Chemical Physics Letters* **162** (3), 165 (1989).
- 36 G. Schaftenaar and J. H. Noordik, *J. Comput.-Aided Mol. Des.* **14** (2), 123 (2000).
- 37 Y. Koga, S. Kondo, S. Saeki, and W. B. Person, *J. Phys. Chem.* **88** (14), 3152 (1984).

- 38 M. J. T. Frisch, G. W.; Schlegel, H. B.; Scuseria, G. E.; Robb, M. A.; Cheeseman, J. R.; Montgomery, Jr., J. A.; Vreven, T.; Kudin, K. N.; Burant, J. C.; Millam, J. M.; Iyengar, S. S.; Tomasi, J.; Barone, V.; Mennucci, B.; Cossi, M.; Scalmani, G.; Rega, N.; Petersson, G. A.; Nakatsuji, H.; Hada, M.; Ehara, M.; Toyota, K.; Fukuda, R.; Hasegawa, J.; Ishida, M.; Nakajima, T.; Honda, Y.; Kitao, O.; Nakai, H.; Klene, M.; Li, X.; Knox, J. E.; Hratchian, H. P.; Cross, J. B.; Bakken, V.; Adamo, C.; Jaramillo, J.; Gomperts, R.; Stratmann, R. E.; Yazyev, O.; Austin, A. J.; Cammi, R.; Pomelli, C.; Ochterski, J. W.; Ayala, P. Y.; Morokuma, K.; Voth, G. A.; Salvador, P.; Dannenberg, J. J.; Zakrzewski, V. G.; Dapprich, S.; Daniels, A. D.; Strain, M. C.; Farkas, O.; Malick, D. K.; Rabuck, A. D.; Raghavachari, K.; Foresman, J. B.; Ortiz, J. V.; Cui, Q.; Baboul, A. G.; Clifford, S.; Cioslowski, J.; Stefanov, B. B.; Liu, G.; Liashenko, A.; Piskorz, P.; Komaromi, I.; Martin, R. L.; Fox, D. J.; Keith, T.; Al-Laham, M. A.; Peng, C. Y.; Nanayakkara, A.; Challacombe, M.; Gill, P. M. W.; Johnson, B.; Chen, W.; Wong, M. W.; Gonzalez, C.; and Pople, J. A, Gaussian 03 Rev. C.02 (Gaussian, Inc., Wallingford CT, 2004).
- 39 T. L. Cairns, A. W. Larchar, and B. C. McKusick, *J. Am. Chem. Soc.* **74** (22), 5633 (1952).
- 40 M. Engeser, D. Schröder, and H. Schwarz, *Chem.--Eur. J.* **11** (20), 5975 (2005).
- 41 D. R. Justes, N. A. Moore, and A. W. Castleman, Jr., *J. Phys. Chem. B* **108** (12), 3855 (2004).
- 42 D. F. McMillen and D. M. Golden, *Annu. Rev. Phys. Chem.* **33**, 493 (1982).
- 43 L. Batt, K. Christie, R. T. Milne, and A. J. Summers, *Int. J. Chem. Kinet.* **6** (6), 877 (1974).
- 44 D. Schröder, M. Engeser, H. Schwarz, E. C. E. Rosenthal, J. Dobler, and J. Sauer, *Inorg. Chem.* **45** (16), 6235 (2006).
- 45 M. Engeser, D. Schröder, and H. Schwarz, *Eur. J. Inorg. Chem.* (17), 2454 (2007).





## 8. Energetics and Reaction Pathways of Intramolecular Reductive Nitrile Coupling of Monocationic Group 3 through 7 Transition Metal Acetonitrile Complexes

*Infrared multiphoton dissociation spectra revealed the occurrence of an intramolecular reaction within cationic niobium acetonitrile complexes  $[\text{Nb}^I, n(\text{CH}_3\text{CN})]^+$  for  $n = 5$  in the gas phase. Generally, this reaction starts from the coordination compound  $[\text{Nb}^I(\text{NCCH}_3)_n]^+$ , primarily formed under our experimental conditions, and leads to the metallacyclic species  $[\text{Nb}^{III}(\text{N}=\text{C}(\text{CH}_3)\text{C}(\text{CH}_3)=\text{N})(\text{NCCH}_3)_{n-2}]^+$  after intramolecular reductive nitrile coupling.*

*This chapter presents a systematic density functional (B3LYP) study of the reaction enthalpies of  $[\text{M}^I, n(\text{CH}_3\text{CN})]^+$ ,  $n = 4, 5$ , coordination complexes and their corresponding metallacyclic isomers in various spin states, where  $M$  stands for any transition metal of group 3 to 7. We further calculated the minimum energy pathways for all group 5 metal acetonitrile complexes  $n = 4, 5$ , as well as for fivefold ligated titanium and tungsten complexes in various spin states.*

*A whole series of transition metals favors a metallacyclic structure over pure coordination of acetonitrile for enthalpic reasons. However, taking spin restrictions and/or kinetic hindrance into account, according to our DFT calculations the reductive nitrile coupling takes place readily only within three complexes,  $M = \text{Nb}, \text{Ta}, \text{W}$  with  $n = 5$ , out of the 30 complexes studied.*

### 8.1 Introduction

Characterization of transition metal complexes and clusters has been an active field of research for many years. Attention has focused not only on the catalytic properties of transition metal compounds in the liquid phase<sup>1-3</sup> but also in the gas phase.<sup>4-8</sup> Low valent niobium and tantalum complexes are able to activate  $\text{N}_2$ ,  $\text{CO}$ , acetylene,  $\text{H}_2$ , as well as to cleave  $\text{C-H}$  bonds.<sup>9-26</sup> Another prominent example is the  $\text{C-C}$  bond formation in the McMurry reaction,<sup>27,28</sup> which involves in situ generated low valent titanium species for the coupling of aldehydes and / or ketones to alkenes.

Transition metals are also known to catalyze reductive nitrile coupling.<sup>2,29,30</sup> Finn et al. found a dimerization of both niobium and tantalum acetonitrile complexes to dinuclear complexes, in which two nitrile groups reductively couple and form a bridging  $[\text{NC}(\text{CH}_3)]_2$

ligand.<sup>31</sup> Templeton and coworkers reported similar  $[\text{NC}(\text{CH}_3)]_2$  bridged dinuclear tungsten acetonitrile complexes  $[\text{Tp}'(\text{O})(\text{I})\text{W}(\text{NC}(\text{CH}_3)\text{C}(\text{CH}_3)\text{N})\text{W}(\text{I})(\text{O})\text{Tp}']$ .<sup>32</sup> Reductive nitrile coupling has also been observed in other transition metal complexes in the liquid phase.<sup>22,33-36</sup>

The generation of transition metal complexes and clusters in unusual, low valent oxidation states is well feasible in the gas phase. Thereby it becomes possible to investigate the intrinsic properties of species without the disturbing influence of additional solvent molecules.

An example for a reductive nitrile coupling in the gas phase induced by a single transition metal monocation has been found in our group by means of infrared spectroscopy and concomitant *ab initio* calculations.<sup>37</sup> Infrared multiphoton dissociation (IRMPD) spectra of cationic niobium acetonitrile complexes  $[\text{Nb}^{\text{I}},n(\text{CH}_3\text{CN})]^+$ ,  $n = 4, 5$ , revealed the size specific intramolecular reductive nitrile coupling. Comparison of geometry and energy calculations and their associated IR absorption spectra for different spin states with the experimental IRMPD spectra allowed for an unambiguous assignment of the structure. We have found a square planar coordination compound  $[\text{Nb}^{\text{I}}(\text{NCCH}_3)_n]^+$  for  $n = 4$  (quintet,  $S = 2$ ) and a metallacyclic species  $[\text{Nb}^{\text{III}}(\text{N}=\text{C}(\text{CH}_3)\text{C}(\text{CH}_3)=\text{N})(\text{NCCH}_3)_{n-2}]^+$  due to an intramolecular reductive nitrile coupling for  $n = 5$  (triplet,  $S = 1$ ).

Whether this coupling reaction (Fig. 8.1) takes place depends strongly on the experimental setup. In our experiment the atomic  $\text{Nb}^{\text{I}}$  cations were generated by laser ablation off a niobium target adjacent to the ion cyclotron resonance (ICR) cell, in which the ions were stored, mass selected and detected. A pulsed valve admits gaseous acetonitrile ( $\text{CH}_3\text{CN}$ ,  $p = 10^{-6}$  mbar for 200 ms) into the ICR cell, which cools down the metal ions by collisions. The final temperature is low enough to enable successive attachment of acetonitrile ligands to the metal ions.

Finally, the complexes may still contain enough energy to overcome the activation barrier for the intramolecular reductive nitrile coupling (Fig. 8.1):

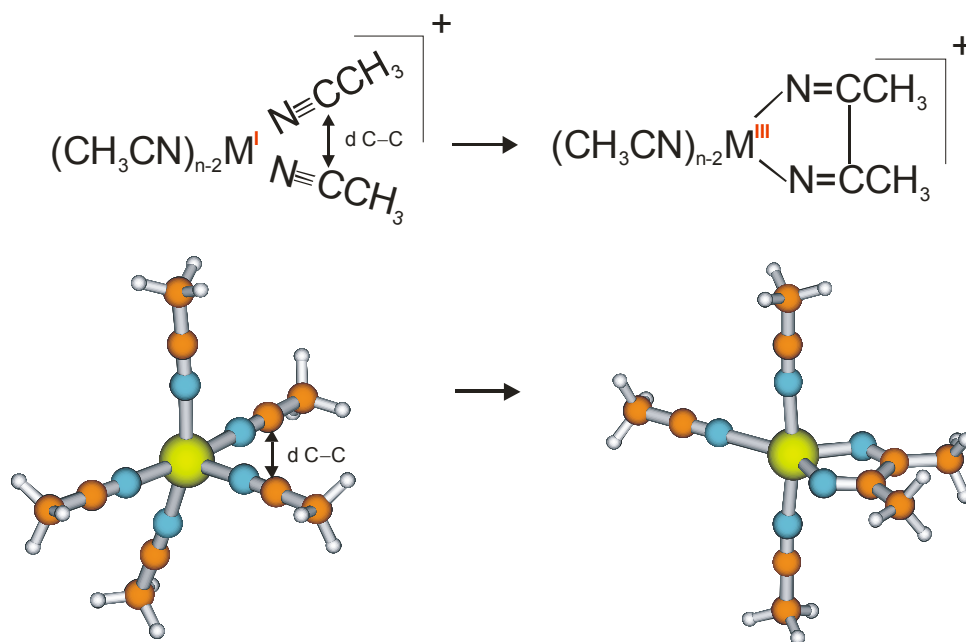


**Figure 8.1:** Scheme of the intramolecular reductive nitrile coupling in transition metal acetonitrile complexes  $[M^I, n(\text{CH}_3\text{CN})]^+$ .

The occurrence of intramolecular reductive nitrile coupling depends on the cluster size. Thus we have to consider steric effects caused by the number of ligands and the size of the metal ion. Furthermore, the electronic properties of the metal ion are crucial. The number of valence electrons and the polarizability of the metal ion could change its chemical behaviour. Taking into account specific electronic trends for transition metal ions within the periodic table, we expect to find an according change in their chemical behaviour when investigating complexes of the formal stoichiometry  $[M^I, n(\text{CH}_3\text{CN})]^+$ ,  $n = 4, 5$ .

This work presents a systematic *ab initio* study of the elements of group 3 through group 7 (nomenclature of the groups of elements within the periodic table is following the most recent IUPAC rules<sup>38</sup>). For those elements energies of different spin states and geometries (pure coordination compound versus metallacyclic structure) are calculated. Special emphasis is put on the calculation of the reaction coordinates and the activation barriers of niobium and its homologues, vanadium and tantalum when solvated by four or five acetonitrile molecules as well as titanium and tungsten acetonitrile complexes with  $n = 5$ .

## 8.2 Computational Details

All calculations were performed with the 5.7. version of the TURBOMOLE<sup>39</sup> program package. We used the B3LYP level of theory<sup>40</sup> together with Ahlrichs polarized triple- $\zeta$  basis sets for C, N, H, V and all of the other investigated first row transition metals.<sup>41</sup> Relativistic effective core potentials are used for all second and third row transition metals.<sup>42</sup> This method and basis sets were chosen for their accurate geometries and vibrational frequencies in transition metal compounds.<sup>43,44</sup> In contrast, pure density functional theory (DFT) methods tend to overrate low spin states in (transition) metal containing systems, while pure Hartree Fock (HF) based methods overrate the high spin states. B3LYP as a hybrid method combines elements of both approaches. Due to the important inclusion of the HF exchange, it often achieves favorable comparison with experiments. In B3LYP, there is a slight preference for high spin states, however.<sup>45-49</sup> In total, the B3LYP hybrid functional is best suited for the systems under investigation with respect to the accuracy/computational cost ratio. More advanced methods, like coupled cluster or even two component relativistic approaches, are out of reach for a detailed study of the present systems. These methods would allow for the calculation of spin-orbit couplings within the complexes. Such couplings are only of the order of e.g.  $150\text{ cm}^{-1}$  ( $1.8\text{ kJ mol}^{-1}$ ) in bare  $\text{Nb}^+$  ( $^5D_1$ - $^5D_0$ ) and  $516\text{ cm}^{-1}$  ( $6.2\text{ kJ mol}^{-1}$ ) in bare  $\text{Ta}^+$  ( $^5F_2$ - $^5F_1$ ).<sup>50</sup> Therefore we proceed without including spin-orbit effects explicitly.

In order to determine activation barriers for the reductive nitrile coupling reactions of mono cationic V, Nb and Ta on the singlet, triplet and quintet diabatic potential energy surfaces, the nitriles' C-C bond distance is parametrically varied between two adjacent acetonitrile ligands  $\text{CH}_3\text{CN}$ , while all other coordinates are optimized freely. In case of titanium ligated with five acetonitrile molecules the reaction coordinates on the doublet and quartet potential energy surfaces were computed stepwise. In this case the  $\Delta E$  and  $E_a$  values within these reaction coordinates are not corrected by zero point energy (ZPE).

ZPE corrections to all other cases were calculated using the NumForce/Aoforce option as implemented in TURBOMOLE. Coordinate files were generated and visualized with MOLDEN version 4.5.<sup>51</sup>

$\Delta E_{\text{ZPE}}^{(OK)}$  denotes the ZPE corrected relative energy difference at zero Kelvin between the isomers of one transition metal compound, either as coordination complex  $[\text{M}^{\text{I}}(\text{NCCH}_3)_n]^+$ , or as metallacyclic species  $[\text{M}^{\text{III}}(\text{N}=\text{C}(\text{CH}_3)\text{C}(\text{CH}_3)=\text{N})(\text{NCCH}_3)_{n-2}]^+$ , each within different spin states. The most stable isomer is arbitrarily set to zero. Therefore all values of  $\Delta E_{\text{ZPE}}^{(OK)}$  are positive.

In contrast,  $\Delta_r H_{ZPE}^{(0K)}$ , the ZPE corrected reaction enthalpy at zero Kelvin, is the reaction enthalpy between the initial coordination structure and the final cyclic structure and therefore may be positive or negative. This notation is used to emphasize enthalpies along the reaction coordinates in contrast to general energy differences between any other two electronic and / or geometric isomers.

Frequency calculations for all coordination and metallacyclic structures have been performed to ensure those structures to be stationary points. Small imaginary frequencies correlated to methyl-group rotations have been neglected. Lumo-Homo energies of all structures have been checked to ensure positive energy differences. Spin contamination was checked for exemplarily for the vanadium, niobium and tantalum complexes with  $n = 4$ .

### 8.3 Results and Discussion

#### 8.3.1 Energetics of Pure Coordination Versus Reactive Nitrile Coupling in Group 3 to Group 7 Transition Metal Acetonitrile Complexes $[M^I, n(CH_3CN)]^+$ , $n = 4, 5$

ZPE corrected energy differences  $\Delta E_{ZPE}^{(0K)}$  of complexes with the formal stoichiometry  $[M^I, n(CH_3CN)]^+$ ,  $n = 4$  were calculated for two constitutional isomers in three different electronic states each. These constitutional isomers are coordination complexes with coordination of the metal cation by the nitrogen lone pair of the acetonitrile ligand  $[M^I(NCCH_3)_n]^+$  and a five membered metal containing heterocyclic structure  $[M^{III}(N=C(CH_3)C(CH_3)=N)(NCCH_3)_{n-2}]^+$ . In principle, the cationic transition metal acetonitrile complexes of groups 3, 5 and 7 may occur in singlet, triplet and quintet states. In contrast, transition metal cations of group 4 and 6 form doublet, quartet and sextet spin states when ligated by  $CH_3CN$ .

Metal cations of the group 3 (Sc, Y, La) and 4 (Ti, Zr, Hf) are too short of valence electrons for sextet and quintet states, respectively. Such high spin complexes of group 3 and 4 require unpaired electrons of the  $CH_3CN$  ligands, which is energetically noncompetitive (cf.  $\Delta E_{ZPE}^{(0K)}$  values in Table 8.1). Some calculations of the high energy isomers did not converge in the course of the DFT optimization (see gaps in Table 8.1).

Complexes containing metals of groups 3 and 4 favor low spin states. Among those, scandium, yttrium and lanthanum prefer metallacyclic singlet structures. Zircon and hafnium complexes form metallacycles in a doublet state, whereas titanium privileges a tetrahedral coordination with  $S = 3/2$ .

In groups 5 through 7, the energetic preference for low spin states vanishes with increasing group number. Metals in the first transition row build up coordination compounds  $[M^I(\text{NCCH}_3)_4]^+$  for  $M^I = \text{V}^I, \text{Cr}^I, \text{Mn}^I$  with the highest accessible spin state when only the valence electrons of the metal cation are contributing. The vanadium monocation ( $[\text{Ar}] 3d^4 4s^0$ ) forms a square planar coordination compound (quintet,  $S = 2$ ), while the chromium ( $[\text{Ar}] 3d^5 4s^0$ ) and manganese ( $[\text{Ar}] 3d^5 4s^1$ ) monocations form tetrahedral complexes for  $n = 4$  of sextet ( $S = 5/2$ ) and quintet ( $S = 2$ ) states, respectively.

**Table 8.1:** Zero point energy corrected energy differences  $\Delta E_{ZPE}^{(0K)}$  (given in  $\text{kJ mol}^{-1}$ ) for various isomers of  $[M^I, n(\text{CH}_3\text{CN})]^+$ , with  $n = 4, 5$ . The respective most stable isomer of each transition metal compound is set to zero and written in bold face. Dashes indicate that no convergence was reached. Stars denote high energy structures (with negative Lumo-Homo energies).

Group	3 $S=0 / S=1 / S=2$			4 $S=1/2 / S=3/2 / S=5/2$			5 $S=0 / S=1 / S=2$			6 $S=1/2 / S=3/2 / S=5/2$			7 $S=0 / S=1 / S=2$		
<b><math>[M^I, 4(\text{CH}_3\text{CN})]^+</math></b>															
	<b>Sc</b>			<b>Ti</b>			<b>V</b>			<b>Cr</b>			<b>Mn</b>		
<b>coordinated</b>	86.7	/ 72.4	/*	50.8	/ <b>0.0</b>	/*	124.8	/ 72.7	/ <b>0.0</b>	122.1	/ 45.7	/ <b>0.0</b>	150.3	/ 68.2	/ <b>0.0</b>
<b>C-C coupled</b>	<b>0.0</b>	/ 162.2	/*	30.9	/ -	/*	171.2	/ 100.7	/ -	232.4	/ 147.6	/ 157.5	297.0	/ 210.9	/ 100.7
	<b>Y</b>			<b>Zr</b>			<b>Nb</b>			<b>Mo</b>			<b>Tc</b>		
<b>coordinated</b>	92.4	/ 89.0	/*	86.6	/ 78.7	/*	67.2	/ 58.0	/ <b>0.0</b>	114.6	/ <b>0.0</b>	/ 91.2	72.1	/ <b>0.0</b>	/ 99.9
<b>C-C coupled</b>	<b>0.0</b>	/ 166.7	/ -	<b>0.0</b>	/ 187.5	/*	14.2	/ 24.8	/ 183.9	80.2	/ 99.5	/ 259.2	119.3	/ 119.2	/ 142.1
	<b>La</b>			<b>Hf</b>			<b>Ta</b>			<b>W</b>			<b>Re</b>		
<b>coordinated</b>	96.8	/ 77.1	/*	105.6	/ 88.7	/*	98.5	/ 76.9	/ 35.6	52.1	/ <b>0.0</b>	/ 138.6	97.4	/ <b>0.0</b>	/ 145.8
<b>C-C coupled</b>	<b>0.0</b>	/ 175.6	/*	<b>0.0</b>	/ 208.8	/*	<b>0.0</b>	/ 31.7	/ 260.9	46.9	/ 90.5	/ 265.8	94.8	/ 98.5	/ 121.4
<b><math>[M^I, 5(\text{CH}_3\text{CN})]^+</math></b>															
	<b>Sc</b>			<b>Ti</b>			<b>V</b>			<b>Cr</b>			<b>Mn</b>		
<b>coordinated</b>	89.9	/ 50.1	/*	37.1	/ <b>0.0</b>	/*	109.8	/ 25.7	/ <b>0.0</b>	73.1	/ 14.9	/ <b>0.0</b>	64.6	/ 40.5	/ <b>0.0</b>
<b>C-C coupled</b>	<b>0.0</b>	/ 130.7	/ -	23.4	/ 140.1	/*	117.4	/ 38.5	/ 107.3	134.8	/ 57.1	/ -	209.3	/ 123.6	/ 47.2
	<b>Y</b>			<b>Zr</b>			<b>Nb</b>			<b>Mo</b>			<b>Tc</b>		
<b>coordinated</b>	-	/ 73.9	/*	60.0	/ 33.7	/*	62.2	/ 16.8	/ 26.6	<b>0.0</b>	/ 22.2	/ -	<b>0.0</b>	/ 68.3	/ -
<b>C-C coupled</b>	<b>0.0</b>	/ 143.3	/*	<b>0.0</b>	/ 137.1	/*	<b>0.0</b>	/ 0.5	/ 157.4	22.4	/ 47.0	/*	110.8	/ 112.0	/ 172.2
	<b>La</b>			<b>Hf</b>			<b>Ta</b>			<b>W</b>			<b>Re</b>		
<b>coordinated</b>	95.1	/ 64.7	/*	88.2	/ 66.2	/*	95.4	/ 73.6	/ 83.0	8.1	/ 39.6	/ -	<b>0.0</b>	/ 88.9	/ -
<b>C-C coupled</b>	<b>0.0</b>	/ 145.6	/*	<b>0.0</b>	/ 150.2	/*	<b>0.0</b>	/ 24.7	/ 191.7	<b>0.0</b>	/ 43.5	/*	88.6	/ 92.4	/*

Among the heavier homologues of groups 5 through 7 the highest possible spin state is observed only in the square planar niobium acetonitrile complex. In contrast, molybdenum, technetium, tungsten and rhenium prefer a medium spin state, quartet or triplet, in the

geometry of a square planar coordination compound  $[M^I(\text{NCCH}_3)_4]^+$ .  $\text{Ta}^I$  instead favors the propensity to perform an intramolecular reductive nitrile coupling.

The classification of the complexes into pure coordination compounds  $[M^I(\text{NCCH}_3)_n]^+$  or metallacycles  $[M^{III}(\text{N}=\text{C}(\text{CH}_3)\text{C}(\text{CH}_3)=\text{N})(\text{NCCH}_3)_{n-2}]^+$  according to their energetic preference yields a dividing line which runs through the periodic table from  $\text{Sc} \rightarrow \text{Zr} \rightarrow \text{Ta}$ . Complexes of these three elements plus all transition metal complexes to their left form metallacyclic structures, transition metals to their right are pure coordination compounds (Fig. 8.2 a)).

		$[M^I,4(\text{CH}_3\text{CN})]^+$				
Group		3	4	5	6	7
Energetic preference	a)	<b>Sc</b> singlet tetrahedral	<b>Ti</b> quartet tetrahedral	<b>V</b> quintet planar	<b>Cr</b> sextet tetrahedral	<b>Mn</b> quintet tetrahedral
		<b>Y</b> singlet tetrahedral	<b>Zr</b> doublet tetrahedral	<b>Nb</b> quintet planar	<b>Mo</b> quartet planar	<b>Tc</b> triplet planar
		<b>La</b> singlet tetrahedral	<b>Hf</b> doublet tetrahedral	<b>Ta</b> singlet tetrahedral	<b>W</b> quartet planar	<b>Re</b> triplet planar
Expected behavior including spin restrictions and reaction enthalpies along the reaction coordinate	b)	<b>Sc</b> triplet tetrahedral	<b>Ti</b> quartet tetrahedral	<b>V</b> quintet planar	<b>Cr</b> sextet tetrahedral	<b>Mn</b> quintet tetrahedral
		<b>Y</b> triplet planar	<b>Zr</b> quartet planar	<b>Nb</b> quintet planar	<b>Mo</b> quartet planar	<b>Tc</b> triplet planar
		<b>La</b> triplet tetrahedral	<b>Hf</b> quartet planar	<b>Ta</b> quintet planar	<b>W</b> quartet planar	<b>Re</b> triplet planar

**Figure 8.2:** Summary of the energetic preference and expected structures of group 3 to group 7 transition metal acetonitrile complexes  $[M^I,4(\text{CH}_3\text{CN})]^+$ . Grey: Coordination compound; Blue: Metallacyclic structure. Light-green highlights planar structures.

Moreover, the energy differences in compounds with the formal stoichiometry  $[M^I, n(CH_3CN)]^+$ ,  $n = 5$  were calculated on B3LYP level of theory for two constitutional isomers in three different electronic states each.

For  $n = 5$  the metal cation acetonitrile complexes of Sc, Y, La, Zr, Hf und Ta behave in the same manner as their analogous compounds with  $n = 4$ . All of them are in favor of the metallacyclic constitutional isomer in a low spin state (cf. Table 8.1).

The prior preference for high and medium spin in the cases of  $V^I$  and  $Ti^I$  complexes with  $n = 4$  persists upon addition of a further acetonitrile ligand. From an energetic point of view the pure coordination complex remains the likeliest geometry in both cases.

In contrast to the square planar coordination of niobium and tungsten complexes, with  $n = 4$ , the complexes with  $n = 5$  are most stable as low spin  $[M^{III}(N=C(CH_3)C(CH_3)=N)(NCCH_3)_3]^+$ . In these complexes the ringforming acetonitriles are coplanar with one further acetonitrile molecule. The remaining two acetonitrile ligands are perpendicular to this plane.

Molybdenum, technetium and rhenium reduce their spin state after addition of the fifth acetonitrile ligand from high to medium spin (sextet to quartet and quintet to triplet). The acetonitrile ligands then coordinate square pyramidally to the metal cation.

Chromium and manganese are listed in Table 8.1 as coordination compounds which are energetically privileged with respect to metallacyclic structures, although they are not the overall minimum structures. Due to steric hindrance (from left to the right the radius of the metal cation decreases within one period) positioning of one ligand into the second solvation sphere lowers the total energy in these systems by 20.9 and 8.9  $\text{kJmol}^{-1}$ , respectively. Thus none of the primarily calculated isomers should be of relevance for experimental studies.

In summary, the dividing line in the periodic table shifts by one group to the right when adding the fifth acetonitrile ligand – with the exception of titanium. Quartet  $[Ti^I(NCCH_3)_5]^+$  is significantly lower in energy than doublet  $[Ti^{III}(N=C(CH_3)C(CH_3)=N)(NCCH_3)_3]^+$ , with  $\Delta E_{ZPE}^{(OK)} = 23.4 \text{ kJmol}^{-1}$

The energetic trends for  $n = 4$  and  $n = 5$  are visualized in Figs. 8.2 a) and 8.3 a), respectively, including detailed information on spin states and geometries of the transition metal acetonitrile complexes.

Not only the energetics, but the whole process of the complex formation is crucial for the complexes' propensity to perform a reductive nitrile coupling. First, the complexes



assemble through successive attachment of  $\text{CH}_3\text{CN}$  ligands to the metal cation. There the most probable and reasonable structural development runs via the coordination of the nitrogen lone pair of the ligands. The formation of the metallacycle out of the coordination compound then follows in a second step. Whether the metallacycle is formed or not depends on the energetics and on the primarily formed electronic state. The previously investigated reaction in niobium acetonitrile complexes suggests the reaction to take place on one single potential energy surface.<sup>37</sup> There has been no evidence for a change in the electronic state. Thus the reaction enthalpy  $\Delta_r H_{ZPE}^{(OK)}$  between the most stable coordination compound and the metallacyclic structure in the same spin state is another decisive factor. Furthermore, the activation energy  $E_a$  must be low enough to make sure that the reaction is not kinetically delayed or completely hindered. Under the experimental conditions the originally formed coordination complexes  $[\text{M}^{\text{I}}(\text{NCCH}_3)_n]^+$  contain a limited amount of internal energy which can be used to overcome the activation barrier. Still, this energy has to be lower than the binding energy of the weakest ligand, otherwise dissociation would compete with the formation of the heterocyclic structure or any other internal reaction (activation barriers will be discussed in more detail in section 8.3.2).

After determination of the electronic state of the "entrance channel" (lowest coordination compound isomer) and evaluation of  $\Delta_r H_{ZPE}^{(OK)}$  on the way to the metallacyclic structure under the constraint of spin conservation, in case of  $n = 4$ , no candidates remain for the reductive nitrile coupling. Scandium, yttrium, lanthanum, zircon, hafnium and tantalum all prefer metallacyclic structures with respect to  $\Delta E_{ZPE}^{(OK)}$ . When including the experimental conditions, spin restrictions and  $\Delta_r H_{ZPE}^{(OK)}$  values altogether, all of the complexes with  $n = 4$  should remain in the geometry of the pure coordination compound. They all possess positive values for  $\Delta_r H_{ZPE}^{(OK)}$  and an intramolecular reductive nitrile coupling reaction would be considerably endothermic ( $\Delta_r H_{ZPE}^{(OK)}$ : Sc = +89.7; Y = +77.8; La = +98.5; Zr = +108.8; Hf = +120.1; Ta = +225.4, each value is given in  $\text{kJ mol}^{-1}$ ). Under the given experimental conditions these endothermic reactions are unlikely (summarized in Fig. 8.2 b)).

		$[M^I,5(CH_3CN)]^+$				
Group		3	4	5	6	7
a)	<b>Energetic preference</b>	<b>Sc</b> * singlet (ring+1) : 2	<b>Ti</b> quartet quadr.pyr.	<b>V</b> quintet quadr.pyr.	<b>Cr</b> ** sextet trig. pyr.	<b>Mn</b> ** quintet trig. bipy.
		<b>Y</b> singlet ring : 3	<b>Zr</b> doublet (ring+1) : 2	<b>Nb</b> singlet (ring+1) : 2	<b>Mo</b> doublet quadr. pyr.	<b>Tc</b> singlet quadr. pyr.
		<b>La</b> singlet (ring+1) : 2	<b>Hf</b> doublet (ring+1) : 2	<b>Ta</b> singlet (ring+1) : 2	<b>W</b> doublet (ring+1) : 2	<b>Re</b> singlet quadr. pyr.
b)	<b>Expected behavior including spin restrictions and reaction enthalpies along the reaction coordinate</b>	<b>Sc</b> <i>triplet</i> <i>trig. bipy.</i>	<b>Ti</b> quartet quadr.pyr.	<b>V</b> quintet quadr.pyr.	<b>Cr</b> ** sextet trig. pyr.	<b>Mn</b> ** quintet trig. bipy.
		<b>Y</b> <i>triplet</i> <i>trig. bipy.</i>	<b>Zr</b> <i>quartet</i> <i>quadr.pyr.</i>	<b>Nb</b> <i>triplet</i> <i>(ring+1) : 2</i>	<b>Mo</b> doublet quadr. pyr.	<b>Tc</b> singlet quadr. pyr.
		<b>La</b> <i>triplet</i> <i>trig. bipy.</i>	<b>Hf</b> <i>quartet</i> <i>quadr.pyr.</i>	<b>Ta</b> <i>triplet</i> <i>(ring+1) : 2</i>	<b>W</b> doublet (ring+1) : 2	<b>Re</b> singlet quadr. pyr.
c)	<b>Expected overall behavior including activation barrier</b>	<b>Sc</b> <i>triplet</i> <i>trig. bipy.</i>	<b>Ti</b> quartet quadr.pyr.	<b>V</b> quintet quadr.pyr.	<b>Cr</b> ** sextet trig. pyr.	<b>Mn</b> ** quintet trig. bipy.
		<b>Y</b> <i>triplet</i> <i>trig. bipy.</i>	<b>Zr</b> <i>quartet</i> <i>quadr.pyr.</i>	<b>Nb</b> <i>triplet</i> <i>(ring+1) : 2</i>	<b>Mo</b> doublet quadr. pyr.	<b>Tc</b> singlet quadr. pyr.
		<b>La</b> <i>triplet</i> <i>trig. bipy.</i>	<b>Hf</b> <i>quartet</i> <i>quadr.pyr.</i>	<b>Ta</b> <i>triplet</i> <i>(ring+1) : 2</i>	<b>W</b> doublet (ring+1) : 2	<b>Re</b> singlet quadr. pyr.

**Figure 8.3:** Summary of the energetic preference and expected structures of group 3 to group 7 transition metal acetonitrile complexes  $[M^I,5(CH_3CN)]^+$ .

Grey: Coordination compound; Blue: Metallacyclic structure. Plume: Metallacycle expected, but uncertain due to high activation barrier. \* (ring+1) : 2 denotes one ligand to share the same plane as the metallacycle. \*\* Overall energetic preference, when one ligand is located in the second sphere.

For complexes with  $n = 5$ , the reaction proceeds endothermically from  $[M^I(\text{NCCH}_3)_5]^+$  to  $[M^{III}(\text{N}=\text{C}(\text{CH}_3)\text{C}(\text{CH}_3)=\text{N})(\text{NCCH}_3)_3]^+$ , with  $M = \text{Sc}, \text{Y}, \text{La}, \text{Zr},$  and  $\text{Hf}$  ( $\Delta_r H_{ZPE}^{(OK)}$ :  $\text{Sc} = +80.7$ ;  $\text{Y} = +69.4$ ;  $\text{La} = +80.9$ ;  $\text{Zr} = +103.3$  and  $\text{Hf} = +84.0$ , each value is given in  $\text{kJ mol}^{-1}$ ). Here again we assumed the most competitive coordination compound as starting point for the reaction

At this point only three transition metal complexes with  $n = 5$  remain for which the spin allowed reaction is exothermic: Those of Nb, Ta and W. It is interesting to note that niobium and tantalum complexes do not end up in the energetically lowest metallacyclic structures (singlet) if the reaction proceeds under spin conservation starting from the lowest coordination structure (triplet). This fact has already been observed spectroscopically for niobium acetonitrile complexes.<sup>37</sup>  $\Delta E_{ZPE}^{(OK)}$  values of the triplet metallacyclic complexes amount to  $+0.5 \text{ kJ mol}^{-1}$  and  $+24.7 \text{ kJ mol}^{-1}$  for niobium and tantalum, respectively. Hence the triplet states are close in energy to the singlet states and the gain in energy is not high enough to enforce a change of the electronic state from  $S = 1$  to  $S = 0$ .

$[\text{W}^I,5(\text{CH}_3\text{CN})]^+$  exhibits a weakly exothermic reaction ( $\Delta_r H_{ZPE}^{(OK)} = -8.1 \text{ kJ mol}^{-1}$ ). The starting point of the reaction as well as the final metallacyclic isomer prefer a low spin configuration ( $S = 1/2$ ).

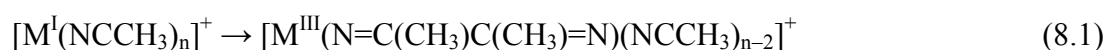
Due to the systematics described by the diagonal trend through the periodic table, titanium complexes of the formal stoichiometry  $[\text{Ti}^I,5(\text{CH}_3\text{CN})]^+$  could have been expected to form metallacyclic structures. The quartet entrance channel leads to an endothermic reaction. Nevertheless, when considering the doublet coordination structure ( $\Delta E_{ZPE}^{(OK)} = +37.1 \text{ kJ mol}^{-1}$ ) as an entrance channel, the reaction would end up in a cyclic structure, which is only  $+23.4 \text{ kJ mol}^{-1}$  higher in energy than the quartet coordination complex. On the doublet potential energy surface (PES) this reaction would be exothermic. Taking into account that the complexes contain an initial internal energy, the doublet state might be accessible in the experiment. The activation barrier for the reductive nitrile coupling in  $[\text{Ti}^I,5(\text{CH}_3\text{CN})]^+$  will be discussed in the following section.

Summarizing the results, the number of potential metallacycle-forming complexes with  $n = 4$  drops from initially six down to zero (Fig. 8.2 b)) and for  $n = 5$  from eight down to three: niobium, tantalum and tungsten (Fig. 8.3 b)). Titanium might be another candidate,

although the probability for the formation of a metallacycle is definitively lower than in the case of niobium, tantalum and tungsten.

### 8.3.2 Reaction Coordinates for the Reductive Nitrile Coupling in $[M^I, n(CH_3CN)]^+$

The occurrence of the reductive nitrile coupling reaction



depends not only on  $\Delta_r H_{ZPE}^{(OK)}$ , but also on the activation energies  $E_a$ . Activation barriers were calculated for cationic group 5 transition metal acetonitrile complexes with  $n = 4, 5$ , as well as for titanium and tungsten complexes with  $n = 5$ .

The graphical representations of the reaction coordinates display energy differences  $\Delta E$ , which are not corrected by ZPE. Among all of the constitutional and electronic isomers of each stoichiometry, the isomer which is lowest in energy is arbitrarily set to zero. This is the reference point for all other isomers of the same constitution. In the following, reading the subsequent diagrams from left to right, the curves start with the energy of the pure coordination compounds  $[M^I(NCCH_3)_n]^+$ . This corresponds to the large C–C distances which are given on the x-axis and chosen to act as the primary reaction coordinate. With proceeding reaction, the C–C distance decreases and the plotted energies approach those of the metallacyclic structures. Color coding depicts electronic states. It is important to note that a crossing of two PESs does not necessarily reflect a real spin cross-over point in this representation. At such a crossing point the total electronic energy and the length of one C–C bond of two isomers become equal. Equal geometry with respect to other coordinates is not mandatory. In fact, geometries might differ distinctively. Spontaneous spin flipping might occur in transition metal complexes, nevertheless, as has been shown before (for a detailed review see Ref. 52 and references therein) provided that the PESs of different spin states have an opportunity to interact. To fulfill this requirement, complexes of different multiplicity at least need to be similar in chemical nature and geometry. Similar geometries are essential for the vertical transition between two states and their Franck Condon factors. If these factors are large, the overlap between the involved states is large, which is crucial for the probability of a spin flip.

There is no experimental evidence for a spin flip in  $[\text{Nb}^{\text{I}},n(\text{CH}_3\text{CN})]^+$  with  $n = 4, 5$ . Nevertheless, in the present study,  $E_a$  is determined under the assumption that hopping from one diabatic PES to another can occur in the vicinity of the formal cross-over point, which then represents the potentially lowest value of the activation barrier.

Due to the observed diagonal trend in the periodic table, titanium could have been expected to show a tendency towards formation of a metallacycle for  $n = 5$ . However, calculation of  $\Delta E_{\text{ZPE}}^{(\text{OK})}$  reveals a quadratic pyramidal coordination compound ( $S = 3/2$ ) to be the energetically favored isomer.  $E_a$  is another factor that influences the (non-)reactivity. Thus, to substantiate this finding, the activation barrier for the reductive nitrile coupling in  $[\text{Ti}^{\text{I}},5(\text{CH}_3\text{CN})]^+$  is determined.

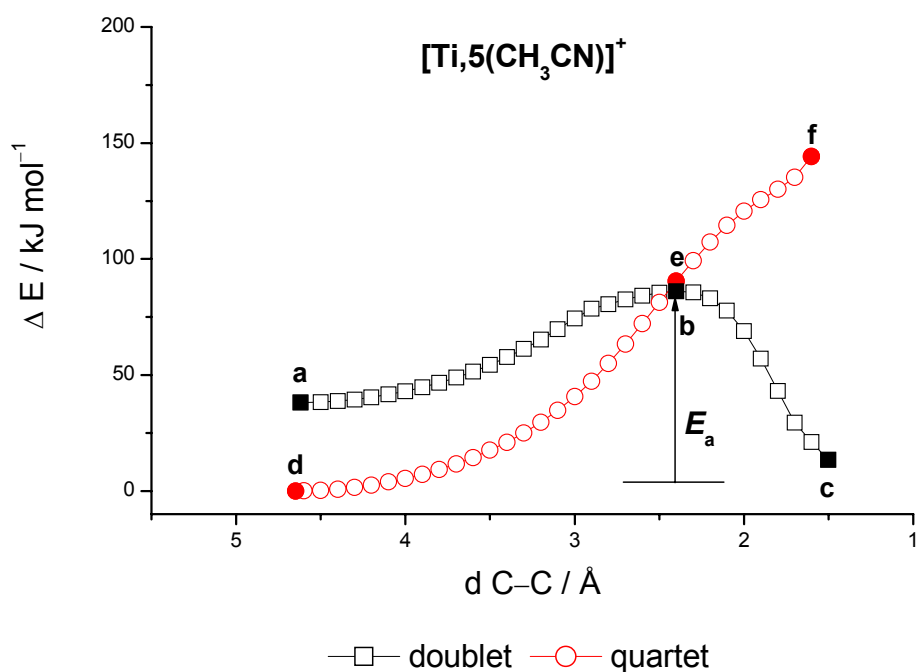


**Figure 8.4:** Calculated reaction coordinates of  $[\text{Ti}^{\text{I}},5(\text{CH}_3\text{CN})]^+$ . The respective most stable isomer is arbitrarily set to zero.

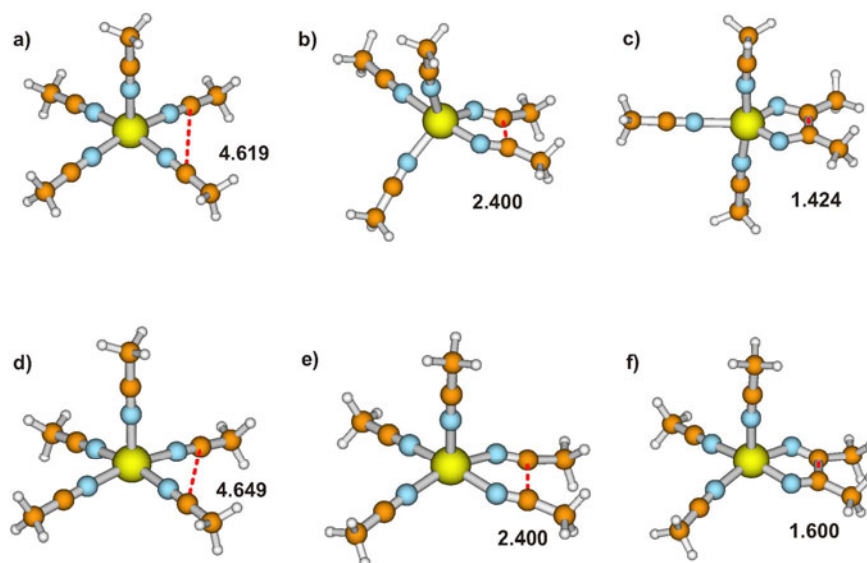


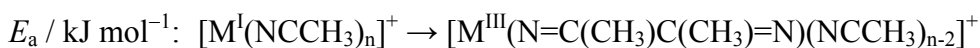
**Figure 8.5:** Calculated geometries of doublet and quartet structures along the reaction coordinates of  $[\text{Ti}^{\text{I}},5(\text{CH}_3\text{CN})]^+$  (a, b and c are structures with  $S = 1/2$ , d, e and f are structures with  $S = 3/2$ ; numbers denote the C–C distance in Ångström).

The plot in Fig. 8.4 shows the energies of the doublet and quartet states as functions of the C–C distance, which is the decisive coordinate for reductive nitrile coupling, in  $[\text{Ti}^{\text{I}},5(\text{CH}_3\text{CN})]^+$ . Structure **f** (Fig. 8.5) is a high energy isomer ( $S = 3/2$ ). Therefore a change from the initial quartet to the final doublet PES would be necessary to form a stable metallacyclic complex in  $[\text{Ti}^{\text{I}},5(\text{CH}_3\text{CN})]^+$ . The geometries **b** and **e** at the intersection of the doublet and quartet PES (C–C distance approx. 2.4 Ångström, Fig. 8.5) differ strongly in the tetrahedral angles between the acetonitrile ligands (distorted trigonal bipyramid versus quadratic pyramid). Thus the overlap for a vertical transition is not optimal, which is yet another example for the low probability of a spin forbidden reaction in these systems. Even if there was a spin flip from the quartet to the doublet PES, the activation energy of 86.1 kJ mol<sup>-1</sup> (Table 8.2) is nearly doubled in comparison to the analogous niobium complex (48.8 kJ mol<sup>-1</sup>). This makes the formation of the metallacycle unlikely to occur.

Considering the small energy difference of the initial coordination compounds **a** and **d** of 37.1 kJ mol<sup>-1</sup> and their initial internal energy, the possibility remains to start on the doublet PES. The activation energy  $E_a$  on the doublet PES then amounts to 49.0 kJ mol<sup>-1</sup>, which is of the order of the calculated  $E_a$  in  $[\text{Nb}^{\text{I}},5(\text{CH}_3\text{CN})]^+$ . The  $E_a$  of this niobium complex has been proven to be accessible in the experiment. Still, it is unlikely to have enough energy in the

complex for reaching the doublet state and overcoming the corresponding activation barrier on the doublet PES under typical experimental conditions.

**Table 8.2:** Values of the activation barrier of the reductive nitrile coupling in selected transition metal acetonitrile complexes  $[M^I, n(\text{CH}_3\text{CN})]^+$ .



	n = 4	n = 5
Ti	-	86.1 *
V	155.4 *	75.6 *
Nb	111.2 *	48.8
Ta	110.7 *	38.9
W	-	72.8

\*Lowest barrier, starting from the most stable coordination structure, if change of the total spin is possible.

The energy as a function of the C–C distance of the reaction coordinates of the reductive nitrile coupling in  $[M^I, n(\text{CH}_3\text{CN})]^+$ ,  $M = \text{V}, \text{Nb}$  and  $\text{Ta}$ ;  $n = 4, 5$ , is presented in Fig. 8.6. Here the involved electronic states are singlet, triplet and quintet states. This depiction allows for an evaluation of the activation barriers (Table 8.2).

The calculated activation energies decrease from V through Nb to Ta. Nevertheless, in case of niobium and tantalum complexes with  $n = 4$ , the difference in  $E_a$  is almost negligible ( $E_a$  in  $\text{kJ mol}^{-1}$ : V 155.4; Nb 111.2; Ta 110.7). It is important to keep in mind, that these values are evaluated using spin forbidden reactions for  $n = 4$ . If only activation energies from spin allowed intramolecular couplings were considered, the activation barriers would increase compared to the ones presented in Table 8.2. In group 5 transition metal acetonitrile complexes  $[M^I, n(\text{CH}_3\text{CN})]^+$  with  $n = 4$  the activation barriers are definitively too high to be overcome when using the internal energy of the complex. If such an amount of energy was available, the most competitive reaction channel would be the dissociation of one acetonitrile ligand off the complex, according to the reaction



with the reaction enthalpy  $\Delta_r H_{ZPE}^{(OK)} = +108.8 \text{ kJmol}^{-1}$ .

Activation energies for group 5 complexes with  $n = 5$  show the same decreasing tendency with increasing atomic number. Here a significant energetic difference exists both between vanadium and niobium, and niobium and tantalum complexes ( $E_a$  in  $\text{kJ mol}^{-1}$ : V 75.6, Nb 48.8 and Ta 38.9). The coupling reactions of niobium and tantalum complexes with  $n = 5$  each proceed under spin conservation on the triplet PES and in both cases the  $E_a$  values are low enough to be overcome. This has been proven experimentally for  $[\text{Nb}^{\text{I}}, 5(\text{CH}_3\text{CN})]^+$ . Starting from the triplet entrance channel, the evolving metallacyclic structure is not the global minimum isomer, which is instead a metallacyclic structures with  $S = 0$  and within a few  $\text{kJ mol}^{-1}$ . This explains the deviating annotations for the geometries in Figs. 8.3 a) and b).

Regarding the reverse reaction from the metallacyclic structure to the coordination compound in  $[\text{M}^{\text{I}}, 5(\text{CH}_3\text{CN})]^+$   $M = \text{Nb}$  and  $\text{Ta}$ , the values for  $E_a$  are considerably larger than those of the forward reaction. Therefore the complexes will remain in the stable metallacyclic structure.

A decrease of the activation barrier  $E_a$  with increasing atomic number is consistent with the metallic character, the larger polarizabilities and increasing size of the metal cations. Valence electrons of heavier homologues are in general less tightly bound. This facilitates the donation of two valence electrons to the ligands. A new bond results between two acetonitriles. Anyhow, not all of the investigated transition metal acetonitrile complexes follow this trend. They do, if only  $\Delta E_{\text{ZPE}}^{(0K)}$  is taken into account, which gives rise to the observed diagonal trend (compare Fig. 8.2 a) and Fig. 8.3 a)). As soon as the experimental conditions and spin restrictions are included, the metallic character is not the dominant factor any longer. If it was, all elements to the left of the dividing line would prefer metallacyclic structures.



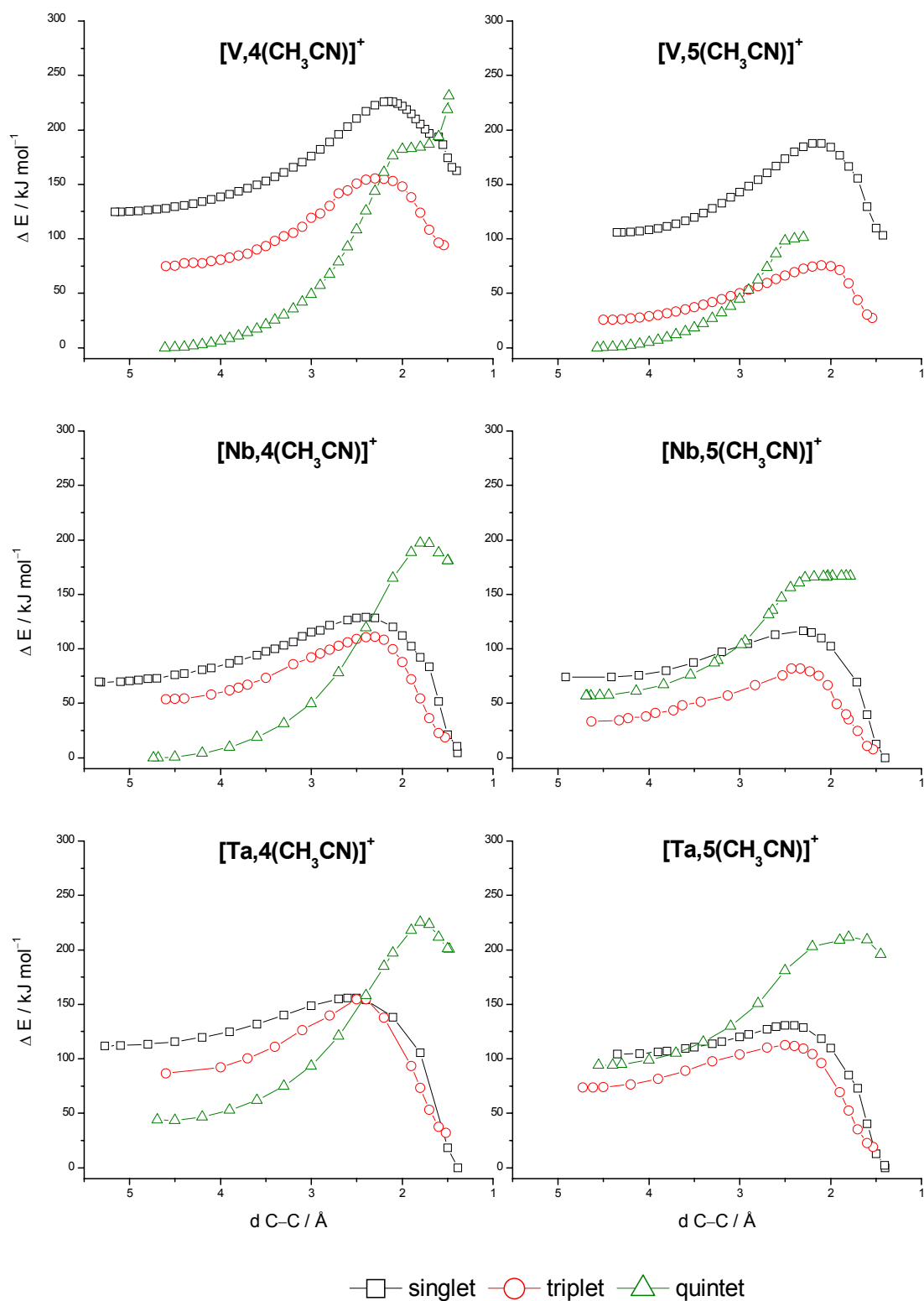


**Figure 8.6:** Calculated reaction coordinates of  $[M^I, n(\text{CH}_3\text{CN})]^+$ ,  $M = \text{V}, \text{Nb}, \text{Ta}$ ,  $n = 4, 5$ . The respective most stable isomer for each transition metal compound is arbitrarily set to zero.

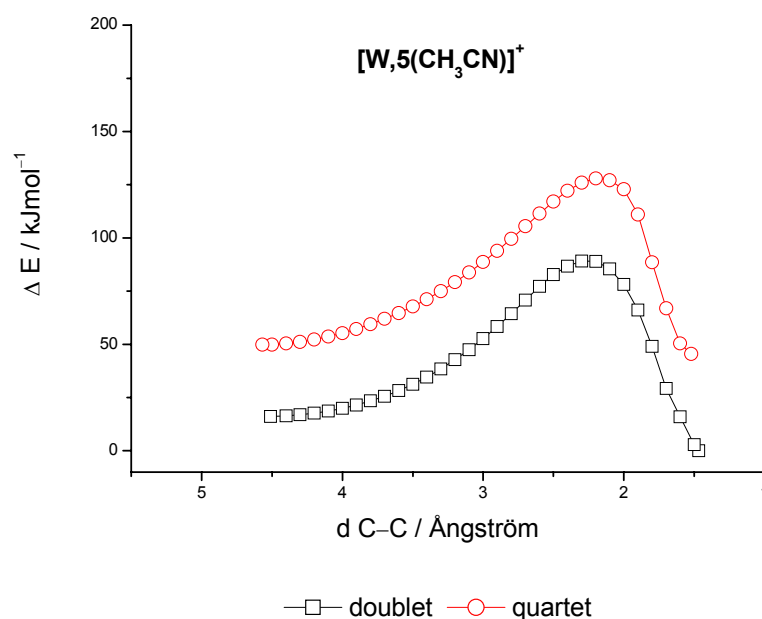


**Figure 8.7:** Calculated reaction coordinates of  $[\text{W}^{\text{I}},5(\text{CH}_3\text{CN})]^+$ . The respective most stable isomer is arbitrarily set to zero.

So far, the results from the previous sections have shown that two out of three candidate complexes may form metallacyclic structures. It remains to discuss the case of tungsten. Reaction coordinates of the tungsten complexes with  $n = 5$  reveal a preference for doublet electronic states, regardless of the complexes' geometries (Fig. 8.7). This allows for a reductive nitrile coupling reaction under spin conservation.  $E_a$  amounts to  $72.8 \text{ kJ mol}^{-1}$  on the doublet PES. Compared to niobium and tantalum complexes with  $n = 5$ , the activation barrier for tungsten is clearly higher in energy, which conforms to the general trend.

Due to the high activation barrier in case of  $[\text{W}^{\text{I}},5(\text{CH}_3\text{CN})]^+$ , these findings do not lead to an unambiguous assignment of either constitution. No clear prediction for the reaction of  $[\text{W}^{\text{I}},5(\text{CH}_3\text{CN})]^+$  under our experimental conditions can be made from the calculations alone.

Finally, the initial number of thirty potentially reactive complexes studied in this work is reduced to two, plus one borderline candidate (Fig. 8.3 c)).

## 8.4 Summary and Outlook

This systematic DFT study identified potential candidates for the reductive nitrile coupling in cationic transition metal acetonitrile complexes of the formal stoichiometry  $[M^I, n(\text{CH}_3\text{CN})]^+$ , with  $n = 4, 5$ . The single case  $[\text{Nb}^I, n(\text{CH}_3\text{CN})]^+$ ,  $n = 4, 5$ , had already been investigated by means of IRMPD spectroscopy and concomitant quantum mechanical calculations before. This has led to the assignment to the coordination structure  $[\text{Nb}^I(\text{NCCH}_3)_4]^+$  and to the metallacyclic structure  $[\text{Nb}^{\text{III}}(\text{N}=\text{C}(\text{CH}_3)\text{C}(\text{CH}_3)=\text{N})(\text{NCCH}_3)_3]^+$ , respectively.

On the basis of the calculated energetic preferences, of the reaction enthalpies, of the activation energies, and under the assumption of spin conservation for the coupling reaction, the formation of metallacyclic structures in group 3 through 7 complexes  $[M^I, 4(\text{CH}_3\text{CN})]^+$  can be ruled out.

Solvation of the transition metal cation by five acetonitrile ligands leads to a coupling reaction in two types of complexes, namely those containing either niobium or tantalum. Within the complexes of group 5 homologues activation barriers are observed to decrease with increasing atomic number. This is attributed to the increasing polarizability of the transition metals, which is going along with the expansion of the d-orbitals. Nevertheless, the complexes  $[M^I, 5(\text{CH}_3\text{CN})]^+$  left to the line connecting  $\text{Sc} \rightarrow \text{Zr} \rightarrow \text{Nb} \rightarrow \text{W}$  remain coordination compounds, due to enthalpic reasons and under consideration of the primarily formed spin states.

Tungsten complexes with  $n = 5$  prefer a metallacyclic structure. However, the activation barriers increase with atomic number within one period.

DFT calculations identified  $[\text{W}^I, 5(\text{CH}_3\text{CN})]^+$  as a candidate for further spectroscopic experiments. However, due to its relatively high activation barrier of  $72.8 \text{ kJmol}^{-1}$  it is uncertain whether the intramolecular coupling reaction could be observed. The occurrence of this reaction strongly depends on the complexes' internal energy – respectively the temperature – which is not known exactly for the experiment.

For the identification of potential candidates for further spectroscopic studies the screening by means of DFT calculations has proven to be a helpful tool. Due to the acquired results, future experiments should focus on the complexes  $[\text{Ta}^I, 5(\text{CH}_3\text{CN})]^+$  and  $[\text{W}^I, 5(\text{CH}_3\text{CN})]^+$ .

## 8.5 References

- 1 S. Kobayashi and H. Ishitani, *Chemical Reviews* **99** (5), 1069 (1999).
- 2 B. N. Storhoff and H. C. Lewis, *Coord. Chem. Rev.* **23** (1), 1 (1977).
- 3 B. M. Trost and M. L. Crawley, *Chem. Rev.* **103** (8), 2921 (2003).
- 4 P. B. Armentrout, *Annu. Rev. Phys. Chem.* **52**, 423 (2001).
- 5 M. B. Knickelbein, *Annu. Rev. Phys. Chem.* **50** (1), 79 (1999).
- 6 S. R. Langhoff and C. W. Bauschlicher, *Annu. Rev. Phys. Chem.* **39** (1), 181 (1988).
- 7 K. Eller and H. Schwarz, *Chemical Reviews* **91** (6), 1121 (1991).
- 8 H. S. Diethard K. Böhme, *Angew. Chem.* **117** (16), 2388 (2005).
- 9 T. W. Coffindaffer, B. D. Steffy, I. P. Rothwell, K. Folting, J. C. Huffman, and W. E. Streib, *J. Am. Chem. Soc.* **111** (13), 4742 (1989).
- 10 C. G. Dewey, J. E. Ellis, K. L. Fjare, K. M. Pfahl, and G. F. P. Warnock, *Organometallics* **2** (3), 388 (1983).
- 11 G. F. P. Warnock and J. E. Ellis, *J. Am. Chem. Soc.* **106** (17), 5016 (1984).
- 12 F. A. Cotton, L. R. Falvello, and R. C. Najjar, *Inorg. Chem.* **22** (3), 375 (1983).
- 13 F. A. Cotton and W. J. Roth, *Inorg. Chem.* **22** (6), 868 (1983).
- 14 F. A. Cotton and W. J. Roth, *J. Am. Chem. Soc.* **105** (11), 3734 (1983).
- 15 F. A. Cotton, S. A. Duraj, and W. J. Roth, *J. Am. Chem. Soc.* **106** (17), 4749 (1984).
- 16 A. P. Sattelberger, R. B. Wilson, and J. C. Huffman, *J. Am. Chem. Soc.* **102** (23), 7111 (1980).
- 17 S. M. Rocklage and R. R. Schrock, *J. Am. Chem. Soc.* **104** (11), 3077 (1982).
- 18 S. M. Rocklage, H. W. Turner, J. D. Fellmann, and R. R. Schrock, *Organometallics* **1** (5), 703 (1982).
- 19 F. N. Tebbe, *J. Am. Chem. Soc.* **95** (17), 5823 (1973).
- 20 S. Datta and S. S. Wreford, *Inorg. Chem.* **16** (5), 1134 (1977).
- 21 D. R. Neithamer, L. Parkanyi, J. F. Mitchell, and P. T. Wolczanski, *J. Am. Chem. Soc.* **110** (13), 4421 (1988).
- 22 F. A. Cotton and W. T. Hall, *J. Am. Chem. Soc.* **101** (17), 5094 (1979).
- 23 M. A. Bruck, A. S. Copenhaver, and D. E. Wigley, *J. Am. Chem. Soc.* **109** (21), 6525 (1987).
- 24 C. Ting and L. Messerle, *J. Am. Chem. Soc.* **109** (21), 6506 (1987).
- 25 J. L. Templeton and R. E. McCarley, *Inorg. Chem.* **17** (8), 2293 (1978).
- 26 M. D. Curtis and J. Real, *Organometallics* **4** (5), 940 (1985).

- 27 E. J. Corey, R. L. Danheiser, and S. Chandrasekaran, *J. Org. Chem.* **41** (2), 260 (1976).
- 28 F. T. Ladipo, *Curr. Org. Chem.* **10** (9), 965 (2006).
- 29 V. Y. Kukushkin and A. J. L. Pombeiro, *Chemical Reviews* **102** (5), 1771 (2002).
- 30 R. A. Michelin, M. Mozzon, and R. Bertani, *Coord. Chem. Rev.* **147**, 299 (1996).
- 31 P. A. Finn, M. S. King, P. A. Kilty, and R. E. McCarley, *J. Am. Chem. Soc.* **97** (1), 220 (1975).
- 32 J. L. Cross, A. D. Garrett, T. W. Crane, P. S. White, and J. L. Templeton, *Polyhedron* **23** (17), 2831 (2004).
- 33 Y. C. Tsai, F. H. Stephens, K. Meyer, A. Mendiratta, M. D. Gheorghiu, and C. C. Cummins, *Organometallics* **22** (14), 2902 (2003).
- 34 R. Duchateau, A. J. Williams, S. Gambarotta, and M. Y. Chiang, *Inorg. Chem.* **30** (25), 4863 (1991).
- 35 F. A. Cotton and W. T. Hall, *Inorg. Chem.* **17** (12), 3525 (1978).
- 36 E. J. M. Deboer and J. H. Teuben, *J. Organomet. Chem.* **153** (1), 53 (1978).
- 37 B. M. Reinhard, A. Lagutschenkov, J. Lemaire, P. Maitre, P. Boissel, and G. Niedner-Schatteburg, *J. Phys. Chem. A* **108** (16), 3350 (2004).
- 38 E. Fluck, *Pure Appl. Chem.* **60** (3), 431 (1988).
- 39 R. Ahlrichs, M. Bar, M. Haser, H. Horn, and C. Kolmel, *Chem. Phys. Lett.* **162** (3), 165 (1989).
- 40 A. D. Becke, *J. Chem. Phys.* **98** (7), 5648 (1993).
- 41 A. Schafer, C. Huber, and R. Ahlrichs, *J. Chem. Phys.* **100** (8), 5829 (1994).
- 42 D. Andrae, U. Haussermann, M. Dolg, H. Stoll, and H. Preuss, *Theor. Chim. Acta* **77** (2), 123 (1990).
- 43 M. Sodupe, V. Branchadell, M. Rosi, and C. W. Bauschlicher, *J. Phys. Chem. A* **101** (42), 7854 (1997).
- 44 C. W. Bauschlicher, Jr., A. Ricca, P. H., and S. R. Langhoff, in *Recent Advances in Density Functional Theory Part II*, edited by D. P. Chong (World Scientific Publishing, Singapore, 1997).
- 45 J. N. Harvey, *Struct. Bonding (Berlin)* **112**, 151 (2004).
- 46 M. Reiher, O. Salomon, and B. A. Hess, *Theor. Chem. Acc.* **107** (1), 48 (2001).
- 47 O. Salomon, M. Reiher, and B. A. Hess, *J. Chem. Phys.* **117** (10), 4729 (2002).
- 48 R. J. Deeth and N. Fey, *J. Comput. Chem.* **25** (15), 1840 (2004).

- 49 T. Ziegler, *Canadian Journal of Chemistry-Revue Canadienne De Chimie* **73** (6), 743 (1995).
- 50 A. A. Radzig and B. M. Smirnov, *Reference Data on Atoms, Molecules and Ions*, (Springer-Verlag, 1985).
- 51 G. Schaftenaar and J. H. Noordik, *J. Comput.-Aided Mol. Des.* **14** (2), 123 (2000).
- 52 H. Schwarz, *Int. J. Mass Spectrom.* **237** (1), 75 (2004).

## Electron configuration of monocationic transition metals and their first promotion energies

Positive ion	<b>Sc<sup>+</sup></b>	<b>Ti<sup>+</sup></b>	<b>V<sup>+</sup></b>	<b>Cr<sup>+</sup></b>	<b>Mn<sup>+</sup></b>	<b>Fe<sup>+</sup></b>	<b>Co<sup>+</sup></b>	<b>Ni<sup>+</sup></b>	<b>Cu<sup>+</sup></b>	<b>Zn<sup>+</sup></b>
Ground state	$3d^1 4s^1 (^3D_1)$	$3d^2 4s^1 (^4F_{3/2})$	$3d^4 4s^0 (^5D_0)$	$3d^5 4s^0 (^6S_{5/2})$	$3d^5 4s^1 (^7S_3)$	$3d^6 4s^1 (^6D_{9/2})$	$3d^8 4s^0 (^3F_4)$	$3d^9 4s^0 (^2D_{5/2})$	$3d^{10} 4s^0 (^1S_0)$	$3d^{10} 4s^1 (^2S_{1/2})$
Excited state	$3d^1 4s^1 (^3D_2)$	$3d^2 (^3F) 4s^1 (^4F_{5/2})$	$3d^4 4s^0 (^5D_1)$	$3d^4 (^5D) 4s^1 (^6D_{1/2})$	$3d^5 (^6S) 4s^1 (^5S_2)$	$3d^6 (^5D) 4s^1 (^6D_{7/2})$	$3d^8 4s^0 (^3F_3)$	$3d^9 4s^0 (^2D_{3/2})$	$3d^9 (^2D_{5/2}) 4s^1 (^3D_3)$	$4p^1 (^2P^0_{1/2})$
Promotion energy / kJ/mol	0.8	1.1	0.4	143.1	113.3	4.6	11.4	18.0	262.3	579.9
Positive ion	<b>Y<sup>+</sup></b>	<b>Zr<sup>+</sup></b>	<b>Nb<sup>+</sup></b>	<b>Mo<sup>+</sup></b>	<b>Tc<sup>+</sup></b>	<b>Ru<sup>+</sup></b>	<b>Rh<sup>+</sup></b>	<b>Pd<sup>+</sup></b>	<b>Ag<sup>+</sup></b>	<b>Cd<sup>+</sup></b>
Ground state	$4d^0 5s^2 (^1S_0)$	$4d^2 5s^1 (^4F_{3/2})$	$4d^4 5s^0 (^5D_0)$	$4d^5 5s^0 (^6S_{5/2})$	$4d^5 5s^1 (^7S_3)$	$4d^7 5s^0 (^4F_{9/2})$	$4d^8 5s^0 (^3F_4)$	$4d^9 5s^0 (^2D_{5/2})$	$4d^{10} 5s^0 (^1S_0)$	$4d^{10} 5s^1 (^2S_{1/2})$
Excited state	$4d^1 (^2D) 5s^1 (^3D_1)$	$4d^2 (^3F) 5s^1 (^4F_{5/2})$	$4d^4 5s^0 (^5D_1)$	$4d^4 (^5D) 5s^1 (^6D_{1/2})$	$4d^6 5s^0 (^5D_4)$	$4d^7 5s^0 (^4F_{7/2})$	$4d^8 5s^0 (^3F_3)$	$4d^9 5s^0 (^2D_{3/2})$	$4d^9 (^2D_{5/2}) 5s^1 (^3D_3)$	$5p^1 (^2P^0_{1/2})$
Promotion energy / kJ/mol	10.1	3.8	1.9	140.9	41.4	18.2	28.7	42.3	468.5	527.9
Positive ion	<b>La<sup>+</sup></b>	<b>Hf<sup>+</sup></b>	<b>Ta<sup>+</sup></b>	<b>W<sup>+</sup></b>	<b>Re<sup>+</sup></b>	<b>Os<sup>+</sup></b>	<b>Ir<sup>+</sup></b>	<b>Pt<sup>+</sup></b>	<b>Au<sup>+</sup></b>	<b>Hg<sup>+</sup></b>
Ground state	$5d^2 6s^0 (^3F_2)$	$5d^1 6s^2 (^2D_{3/2})$	$5d^3 6s^1 (^5F_1)$	$5d^4 6s^1 (^6D_{1/2})$	$5d^5 6s^1 (^7S_3)$	$5d^6 6s^1 (^6D_{9/2})$	$5d^7 6s^1 (^5F_5)$	$5d^9 6s^0 (^2D_{5/2})$	$5d^{10} 6s^0 (^1S_0)$	$5d^{10} 6s^1 (^2S_{1/2})$
Excited state	$5d^2 6s^0 (^3F_3)$	$5d^1 6s^2 (^2D_{5/2})$	$5d^3 (^4F) 6s^1 (^3F_2)$	$5d^4 (^5D) 6s^1 (^6D_{3/2})$	$5d^4 6s^2 (^5D_0)$	$5d^6 (^5D) 6s^1 (^6D_{7/2})$	$5d^8 (^3F_4)$	$5d^8 (^3F) 6s^1 (^4F_{9/2})$	$5d^9 (^2D_{5/2}) 6s^1 (^3D_3)$	$5d^9 6s^2 (^2D_{5/2})$
Promotion energy / kJ/mol	12.2	36.5	12.3	18.2	164.8	42.9	27.1	57.3	179.9	424.8

From: A.A. Radzig and B.M. Smirnov, Reference Data on Atoms, Molecules and Ions, Springer-Verlag, 1985





## 9. Summary

Within this thesis a series of molecular species has been studied, with focus on hydrogen bonded species and on transition metal complexes. Experimental techniques such as FT-ICR-MS and IRMPD were combined with ab initio calculations for the determination of structure and reactivity of the aforementioned types of systems.

On the basis of high level electronic structure calculations of **neutral water clusters**  $(\text{H}_2\text{O})_n$  with  $n = 17\text{--}21$  a transitional size regime has been determined, where a structural stabilization between all-surface and interior configurations alternates with the addition or removal of a single water molecule. This behavior has been previously suggested based on the results with the TTM2-F interaction potential and it is qualitatively different from the results of the inappropriate yet popular TIP4P potential. Electronic structure calculations suggested that for  $n = 17$  and  $19$  the interior configuration would be energetically more stable than the all-surface one.

The analysis of the IR spectra in the intramolecular O–H stretching region ( $3000\text{--}4000\text{ cm}^{-1}$ ) revealed that the spectroscopic signature of the favorable structures in the  $n = 17\text{--}21$  cluster size regime is accompanied by an undulation in the position of the most red-shifted O–H stretching vibrations.

Further characterization of the most red-shifted vibrations confirmed previous findings regarding their origin. These modes are localized vibrations of the hydrogen bonded O–H stretch of a water molecule which acts as a donor in a strong hydrogen bond and which has a “free” O–H stretch.

The gas phase infrared spectrum ( $3250\text{ to }3810\text{ cm}^{-1}$ ) of the **singly hydrated ammonium ion**,  $\text{NH}_4^+(\text{H}_2\text{O})$ , had previously been recorded by photodissociation spectroscopy of mass selected ions and interpreted by means of ab initio calculations. Resolved rotational transitions became subject of symmetric top analysis. The present work provided additional information on the shape of the potential energy curves of  $\text{NH}_4^+(\text{H}_2\text{O})$  along the N–H distance on MP2/aug-cc-pVDZ level of theory yielding an anharmonic potential shape. The best agreement in the comparison of experimental and calculated spectra

was observed when frequencies are calculated on MP2-FC/aug-cc-pVDZ level of theory. However, the calculated relative band intensities were not reproduced in case of the  $\nu_3(\text{H}_2\text{O})$  band for which the observed value is about 20 times weaker than the calculated one. This mode specific fragmentation behavior could be explained by the analysis of the calculated anharmonic coupling constants in  $\text{NH}_4^+(\text{H}_2\text{O})$ . The coupling of the  $\nu_3(\text{H}_2\text{O})$  to other cluster modes is orders of magnitude weaker than the coupling of the  $\nu_1(\text{H}_2\text{O})$  mode. These findings together render a picture of a mode specific fragmentation dynamic that modulates band intensities in action spectra with respect to absorption spectra.

Calculation of potential energy curves of the O–H mode of the intramolecular hydrogen bond of various **dicarboxylic acids (oxalic to adipic acid)** revealed that the shapes of the potentials directly correlate to the size of the system and the resulting ring strain. The potentials are wide or even quartic in systems with strongly directional hydrogen bonds. The more the ring strain decreases, the wider the potential becomes. The shape of the potential is also influenced by the charge of the system. An oscillation of the strength of the hydrogen bond is observed between protonated and deprotonated dicarboxylic acids, with the protonated ones being weaker than the deprotonated ones.

Calculation of anharmonic frequencies based on the VPT2 approach lead to reasonable results in all systems with narrow potentials. In case of deprotonated adipic acid a good agreement with the experimental results is found. In case of the protonated adipic acid the agreement reasonable.

ESI-FT-ICR-MS spectra unambiguously determined the **nonheme iron(III) catecholate model complexes**  $[(\text{L-N}_4\text{Me}_2)\text{Fe}(\text{cat})]^+$  and  $[(\text{L-N}_4\text{Me}_2)\text{Fe}(\text{dbc})]^+$ . The  $\text{O}_2$ -adduct  $[(\text{L-N}_4\text{Me}_2)\text{Fe}(\text{dbc})\text{O}_2]^+$  has been successfully isolated in the ICR ion trap with an intensity that is sufficient for further spectroscopic studies. However, the structures of the intermediate  $\text{O}_2$ -adducts remain unknown. MS experiments did not yield unambiguous evidence for the exclusive existence of any of the possible isomers.

Preliminary quantum chemical calculations provided geometries and frequencies of the model complexes  $[(\text{L-N}_4\text{Me}_2)\text{Fe}(\text{cat})]^+$  and  $[(\text{L-N}_4\text{Me}_2)\text{Fe}(\text{dbc})]^+$  as well as an energy profile and calculated IR spectra of various possible isomers of their  $\text{O}_2$ -adducts. The MS experiments along with the calculated energetics and the rate constants of the catalytic

reaction observed in solution suggest isomers of the muconic type to be the most probable structures of the O<sub>2</sub>-adducts.

**IRMPD spectra** of complexes in the gas phase have been recorded for a series of vanadium oxide complexes with acetonitrile, methanol and ethanol. The experimental spectra were compared to calculated absorption spectra.

The **vanadium oxide acetonitrile** complexes [VC<sub>2</sub>H<sub>3</sub>NO]<sup>+</sup>, [VC<sub>4</sub>H<sub>6</sub>N<sub>2</sub>O]<sup>+</sup> and [VC<sub>4</sub>H<sub>6</sub>N<sub>2</sub>O<sub>2</sub>]<sup>+</sup> are assigned to coordination compounds in which the acetonitrile ligands are coordinated via the lone-pair of the nitrogen atom to VO<sup>+</sup> or VO<sub>2</sub><sup>+</sup>. The complexes can be described as the energetically most favored structures OV(NCCH<sub>3</sub>)<sup>+</sup>, OV(NCCH<sub>3</sub>)<sub>2</sub><sup>+</sup> and VO<sub>2</sub>(NCCH<sub>3</sub>)<sub>2</sub><sup>+</sup>. Strong evidence was found for a tricyclization reaction of three acetonitrile ligands in [VC<sub>6</sub>H<sub>9</sub>N<sub>3</sub>O<sub>2</sub>]<sup>+</sup> and [VC<sub>6</sub>H<sub>10</sub>N<sub>3</sub>O<sub>2</sub>]<sup>+</sup> yielding most likely structures that are best described as VO<sub>2</sub>(2,4,6-trimethyl-1,3,5-triazine)<sup>+</sup> and (HO)OV(2,4,6-trimethyl-1,3,5-triazine)<sup>+</sup>. Both the experimental IRMPD spectra and the ab initio computed IR absorption spectra of such structures agree well in this regard except for the high computed total energies of the predicted structures

IRMPD spectra of **vanadium oxide methanol** complexes have been assigned to a mixture of isomers in case of [VCH<sub>6</sub>O<sub>2</sub>]<sup>+</sup>. The recorded spectrum of [VC<sub>2</sub>H<sub>12</sub>O<sub>4</sub>]<sup>+</sup> resembles that of [VCH<sub>6</sub>O<sub>2</sub>]<sup>+</sup> leading to the conclusion that these two species should be of similar structure. The spectra of [VCH<sub>5</sub>O<sub>3</sub>]<sup>+</sup> and [VCH<sub>7</sub>O<sub>3</sub>]<sup>+</sup> differ significantly in number and position of bands from those of [VCH<sub>6</sub>O<sub>2</sub>]<sup>+</sup> and [VC<sub>2</sub>H<sub>12</sub>O<sub>4</sub>]<sup>+</sup>. The observed spectral features are due to a strong dependence on the formal oxidation state. Complexes with an odd number of H atoms appear to release the protonated formaldehyde or at least involve a methoxy group. This was not observed in the IRMPD spectra of complexes with even numbers of H atoms. The best matching isomer of [VCH<sub>5</sub>O<sub>3</sub>]<sup>+</sup> was found to be OV(OH)(HOCH<sub>3</sub>)<sup>+</sup>, while [VCH<sub>7</sub>O<sub>3</sub>]<sup>+</sup> can be assigned to (HO)V(OH<sub>2</sub>)(HOCH<sub>3</sub>)<sup>+</sup>. Both complexes lose neutral •OCH<sub>3</sub> upon irradiation.

The IRMPD spectrum of the **vanadium oxide ethanol** complex [VC<sub>2</sub>H<sub>6</sub>O<sub>2</sub>]<sup>+</sup> showed the expected loss of ethene as the main fragment. Based on the comparison of the experiment with the calculated spectra [VC<sub>2</sub>H<sub>6</sub>O<sub>2</sub>]<sup>+</sup> can be described as (C<sub>2</sub>H<sub>4</sub>)V(OH)<sub>2</sub><sup>+</sup>, which is the most stable isomer.

The systematic DFT study of the last chapter of this thesis identified potential candidates for **reductive nitrile coupling in cationic transition metal acetonitrile** complexes of the formal stoichiometry  $[M^I, n(\text{CH}_3\text{CN})]^+$ , with  $n = 4, 5$ .

On the basis of the calculated energetic preferences of the reaction enthalpies, of the activation energies, and under the assumption of spin conservation for the coupling reaction, the formation of metallacyclic structures in group 3 through 7 complexes  $[M^I, 4(\text{CH}_3\text{CN})]^+$  can be ruled out.

Solvation of the transition metal cation by five acetonitrile ligands leads to a coupling reaction in two types of complexes, namely those containing either niobium or tantalum.

Tungsten complexes with  $n = 5$  were also identified to prefer a metallacyclic structure. However, the activation barriers increase with atomic number within one period. Due to its relatively high activation barrier of  $72.8 \text{ kJmol}^{-1}$  it is questionable whether the intramolecular coupling reaction can be observed in experiments on  $[\text{W}^I, 5(\text{CH}_3\text{CN})]^+$ .

Guided by the obtained predictions, future IRMPD experiments should focus on the complexes  $[\text{Ta}^I, 5(\text{CH}_3\text{CN})]^+$  and  $[\text{W}^I, 5(\text{CH}_3\text{CN})]^+$ .

The combination of ab initio theory and contemporary gas phase experiments proved to be successful in the elucidation of structures and reactivities of hydrogen bonded species and transition metal complexes.

The results and spectral analysis of this present study will assist in future experiments on e.g. the predicted structural transition between all-surface and interior configurations in neutral water clusters.

The availability of IRMPD spectra with even higher resolution would ease structural assignment. This will be accomplished by a cooled ion trap, which is planned to be installed at the FT-ICR-MS setup at Orsay and at Kaiserslautern in the near future.

## 10. Zusammenfassung

Im Rahmen dieser Arbeit wurde eine Reihe von Systemen untersucht, welche entweder wasserstoffverbrückten Spezies oder der Gruppe der Übergangsmetallkomplexe zugeordnet werden können. Zur Bestimmung der Struktur und der Reaktivität dieser Systeme wurden unterschiedliche experimentelle Techniken wie FT-ICR-MS und IRMPD sowie quantenchemische Rechnungen eingesetzt. Im Folgenden werden die wichtigsten Resultate kurz zusammengefasst.

In **neutralen Wasserclustern  $(\text{H}_2\text{O})_n$  mit  $n = 17-21$**  wurde auf Grundlage von quantenchemischen Berechnungen ein Übergangsgrößenbereich bestimmt, in dem die stabilste Struktur zwischen "all-surface" und "interior" Konfigurationen bei Zugabe oder Entfernen eines einzelnen Wassermoleküls alterniert. Dieses Verhalten wurde zuvor auf Basis der Ergebnisse des TTM2-F Wechselwirkungspotentials beobachtet, welches sich qualitativ von den Ergebnissen des populären aber nicht angemessenen TIP4P Potentials unterscheidet.

Die Analyse der IR-Spektren im Bereich der intramolekularen O–H Streckschwingungen ( $3000 - 4000 \text{ cm}^{-1}$ ) weist für die bevorzugten Strukturen für  $n = 17-21$  einen mit der Struktur korrelierten Wechsel der Position der am stärksten rot-verschobenen O–H Streckschwingung auf. Die weitergehende Charakterisierung dieser Schwingungen bestätigt frühere Vermutungen bezüglich ihrer Herkunft. Diese Moden sind lokalisierte Schwingungen von wasserstoffverbrückten O–H Streckschwingungen eines Wassermoleküls, das als Donor in einer starken Wasserstoffbrücke agiert und eine freie O–H Streckschwingung besitzt.

Das Gasphasen Infrarotspektrum ( $3250$  bis  $3810 \text{ cm}^{-1}$ ) des **einfach hydratisierten Ammonium-Ions,  $\text{NH}_4^+(\text{H}_2\text{O})$** , das in einer früheren Arbeit durch Photodissoziationsspektroskopie an massenselektierten Ionen aufgenommen wurde, konnte durch ab initio Berechnungen interpretiert werden. Aufgelöste Rotationsübergänge wurden mit Hilfe des Modells des prolaten symmetrischen Rotators ausgewertet. Diese Arbeit liefert weitere Informationen bezüglich der Form der Potentialkurve entlang des N–H Abstandes der Wasserstoffbrücke in  $\text{NH}_4^+(\text{H}_2\text{O})$  auf MP2/aug-cc-pVDZ Niveau. Es wurde eine deutlich anharmonische Potentialkurve ermittelt. Die beste Übereinstimmung zwischen experimentellen und berechneten Spektren wurde auf MP2-FC/aug-cc-pVDZ Niveau

beobachtet. Lediglich die berechneten Intensitäten wurden speziell für die  $\nu_3(\text{H}_2\text{O})$  Bande nicht gut wiedergegeben. Diese sind im Experiment um den Faktor 20 schwächer als in den berechneten Spektren. Dieses modenspezifische Verhalten kann mit Hilfe der anharmonischen Kopplungskonstanten erklärt werden. Die Kopplung von  $\nu_3(\text{H}_2\text{O})$  an andere Clustermoden ist um Größenordnungen kleiner als die Kopplung der  $\nu_1(\text{H}_2\text{O})$  Mode. Zusammengenommen ergibt sich eine modenspezifische Fragmentationsdynamik, welche die Bandenintensitäten der IRMPD Spektren im Vergleich zu Absorptionsspektren widerspiegelt.

Die Berechnung der Potentialkurven entlang des O–H Abstandes der intramolekularen Wasserstoffbrücke verschiedener **Dicarbonsäuren (Oxal- bis Adipinsäure)** ergab eine direkte Korrelation der Form des Potentials mit der Größe des Systems und der daraus resultierenden Ringspannung. Die Potentiale sind breit oder sogar quartisch in Systemen mit starken direktionalen Wasserstoffbrückenbindungen. Je mehr die Ringspannung abnimmt, umso breiter wird das Potential. Die Form des Potentials wird außerdem durch die Ladung des Systems beeinflusst. In der Reihe der homologen Dicarbonsäuren wird eine Oszillation der Bindungsstärke zwischen jeweils den protonierten und deprotonierten Säuren beobachtet, wobei die H-Brücken der protonierten Säuren schwächer sind.

Die Berechnung von anharmonischen Frequenzen mittels VPT2 Ansatz liefert glaubwürdige Ergebnisse für alle Systeme mit schmalen bis mittleren Potentialformen. Im Fall der deprotonierten Adipinsäure sind die berechneten Banden in guter Übereinstimmung mit den experimentell beobachteten Banden. Im Fall der protonierten Adipinsäure kann die Übereinstimmung noch als ausreichend bezeichnet werden.

ESI-FT-ICR-MS Spektren der **Nicht-Häm Eisen(III) Catecholat Modell Komplexe**  $[(\text{L-N}_4\text{Me}_2)\text{Fe}(\text{cat})]^+$  und  $[(\text{L-N}_4\text{Me}_2)\text{Fe}(\text{dbc})]^+$  konnten eindeutig den entsprechenden Molekülionensignalen der beiden Komplexe zugeordnet werden. Das  $\text{O}_2$ -Addukt  $[(\text{L-N}_4\text{Me}_2)\text{Fe}(\text{dbc})\text{O}_2]^+$  konnte in ausreichender Intensität in der ICR-Zelle isoliert werden. Weitere spektroskopische Studien an diesem Addukt sind dadurch möglich. Bislang ist die Struktur des  $\text{O}_2$ -Addukts noch nicht bekannt, da allein auf Grundlage der massenspektrometrischen Experimente keine eindeutige Zuordnung zu einem der in Frage kommenden Strukturisomere getroffen werden kann.

Erste quantenchemische Berechnungen liefern Geometrien und Frequenzen der Modellkomplexe  $[(\text{L-N}_4\text{Me}_2)\text{Fe}(\text{cat})]^+$  und  $[(\text{L-N}_4\text{Me}_2)\text{Fe}(\text{dbc})]^+$ , sowie ein Energieprofil und berechnete IR-Spektren verschiedener  $\text{O}_2$ -Addukte dieser beiden Komplexe. Die energetisch

bevorzugten muconsäureartigen Isomere der O<sub>2</sub>-Addukte werden als die wahrscheinlichsten Isomere betrachtet. Die Ratekonstanten der katalytischen Reaktion in Lösung, sowie die beobachteten Fragmente in den MS-Spektren untermauern die berechnete Energetik.

**IRMPD Spektren** wurden für eine Reihe von Vanadiumoxid Komplexen mit Acetonitril, Methanol und Ethanol aufgenommen. Die experimentell erhaltenen Spektren wurden dann mit berechneten Absorptionsspektren verglichen.

Die **Vanadiumoxid-Acetonitril Komplexe** [VC<sub>2</sub>H<sub>3</sub>NO]<sup>+</sup>, [VC<sub>4</sub>H<sub>6</sub>N<sub>2</sub>O]<sup>+</sup> und [VC<sub>4</sub>H<sub>6</sub>N<sub>2</sub>O<sub>2</sub>]<sup>+</sup> sind energetisch begünstigte Koordinationsverbindungen, in denen die Acetonitril-Liganden über das freie Elektronenpaar des Stickstoffs an VO<sup>+</sup> bzw. VO<sub>2</sub><sup>+</sup> koordiniert vorliegen. Diese Komplexe können somit als OV(NCCH<sub>3</sub>)<sup>+</sup>, OV(NCCH<sub>3</sub>)<sub>2</sub><sup>+</sup> und VO<sub>2</sub>(NCCH<sub>3</sub>)<sub>2</sub><sup>+</sup> beschrieben werden. Die IRMPD Spektren sowie die berechneten IR Spektren von [VC<sub>6</sub>H<sub>9</sub>N<sub>3</sub>O<sub>2</sub>]<sup>+</sup> und [VC<sub>6</sub>H<sub>10</sub>N<sub>3</sub>O<sub>2</sub>]<sup>+</sup> deuten darauf hin, dass in diesen Komplexen eine Trizyklisierung dreier Acetonitril-Liganden zu Triazinen stattgefunden hat. Die Strukturen lassen sich als VO<sub>2</sub>(2,4,6-trimethyl-1,3,5-triazine)<sup>+</sup> und (HO)OV(2,4,6-trimethyl-1,3,5-triazine)<sup>+</sup> beschreiben.

IRMPD Spektren von **Vanadiumoxid-Methanol Komplexen** konnten im Fall von [VCH<sub>6</sub>O<sub>2</sub>]<sup>+</sup> durch eine Mischung von Isomeren erklärt werden. Das Spektrum von [VC<sub>2</sub>H<sub>12</sub>O<sub>4</sub>]<sup>+</sup> ähnelt demjenigen von [VCH<sub>6</sub>O<sub>2</sub>]<sup>+</sup> stark, woraus sich eine Ähnlichkeit der Struktur der beiden Komplexe herleiten lässt. Die Spektren von [VCH<sub>5</sub>O<sub>3</sub>]<sup>+</sup> und [VCH<sub>7</sub>O<sub>3</sub>]<sup>+</sup> unterscheiden sich in Anzahl und Lage der Banden von den Spektren von [VCH<sub>6</sub>O<sub>2</sub>]<sup>+</sup> und [VC<sub>2</sub>H<sub>12</sub>O<sub>4</sub>]<sup>+</sup>. Die beobachteten spektralen Merkmale der Komplexe hängen zudem stark vom formalen Oxidationszustand ab. In Komplexen mit einer ungeraden Anzahl an H-Atomen wird die Freisetzung von protoniertem Formaldehyd bzw. das Auftreten einer Methoxy(radikal)gruppe beobachtet. In Komplexen mit gerader Anzahl an H-Atomen ist dies nicht der Fall. [VCH<sub>5</sub>O<sub>3</sub>]<sup>+</sup> wird am besten durch OV(OH)(HOCH<sub>3</sub>)<sup>+</sup> beschrieben, während [VCH<sub>7</sub>O<sub>3</sub>]<sup>+</sup> als (HO)V(OH<sub>2</sub>)(HOCH<sub>3</sub>)<sup>+</sup> bezeichnet werden kann. Beiden gemein ist der Verlust eines neutralen •OCH<sub>3</sub> bei resonanter Absorption der FEL IR Strahlung.

Das IRMPD Spektrum des **Vanadiumoxid-Ethanol Komplexes** [VC<sub>2</sub>H<sub>6</sub>O<sub>2</sub>]<sup>+</sup> zeigt den erwarteten Verlust von Ethen als Hauptfragment. Basierend auf dem Vergleich des Experiments mit berechneten Spektren kann [VC<sub>2</sub>H<sub>6</sub>O<sub>2</sub>]<sup>+</sup> als (C<sub>2</sub>H<sub>4</sub>)V(OH)<sub>2</sub><sup>+</sup> beschrieben werden, das zudem das stabilste Isomer darstellt.

Die systematische DFT-Studie im letzten Kapitel dieser Arbeit identifizierte Kandidaten für die **reduktive Nitril-Kopplung in kationischen Übergangsmetall-Acetonitril Komplexen** der Zusammensetzung  $[M^I, n(\text{CH}_3\text{CN})]^+$ , mit  $n = 4, 5$ .

Auf der Grundlage der berechneten Reaktionsenthalpien und der Aktivierungsbarrieren, sowie unter Annahme der Spinerhaltung während der Kopplungsreaktion, kann die Bildung von metallazyklischen Strukturen für die Komplexe  $[M^I, 4(\text{CH}_3\text{CN})]^+$  der Gruppe 3 bis 7 ausgeschlossen werden.

Die Solvatisierung des Übergangsmetallkations durch fünf Acetonitril-Liganden führt zu einer Kopplungsreaktion in zwei der untersuchten Metall-Ligand Komplexe, und zwar in Niob- und Tantal-Acetonitril Komplexen. Wolfram-Acetonitril Komplexe mit  $n = 5$  weisen ebenfalls eine Präferenz für metallazyklische Strukturen auf. Mit zunehmender Ordnungszahl erhöhen sich jedoch auch die Aktivierungsbarrieren innerhalb einer Periode. Es ist fraglich, ob die intramolekulare Kopplungsreaktion im Experiment beobachtet werden kann, da in  $[W^I, 5(\text{CH}_3\text{CN})]^+$  die berechnete Aktivierungsbarriere mit  $72.8 \text{ kJ mol}^{-1}$  fast doppelt so hoch ist wie im Fall von  $[Ta^I, 5(\text{CH}_3\text{CN})]^+$ .

Mit Hilfe dieser Voraussagen können zukünftige IRMPD Experimente gezielt für die Komplexe  $[Ta^I, 5(\text{CH}_3\text{CN})]^+$  und  $[W^I, 5(\text{CH}_3\text{CN})]^+$  durchgeführt werden.

Die Kombination von ab initio Methoden und modernen Gasphasenexperimenten erweist sich als erfolgreiche Strategie zur Aufklärung der Struktur und Reaktivität wasserstoffverbrückter Spezies und von Übergangsmetallkomplexen.

Die in dieser Arbeit erhaltenen Ergebnisse, insbesondere die Spektralanalysen, werden als hilfreich für zukünftige spektroskopische Experimente erachtet, beispielsweise für den erwarteten alternierenden strukturellen Übergang zwischen den berechneten "all-surface" und "interior" Konfigurationen neutraler Wasserclustern der Größe  $n = 17-21$ .

Die Strukturaufklärung mittels IRMPD würde durch die Verfügbarkeit höher aufgelöster Spektren weiter vereinfacht. Dies wird demnächst mit Hilfe einer gekühlten Ionenfalle an den FT-ICR-MS Aufbauten in Orsay und Kaiserslautern möglich sein.



## List of Publications

- 2004 ***Reductive Nitrile Coupling in Niobium-Acetonitrile Complexes Probed by Free Electron Laser IR Multiphoton Dissociation Spectroscopy.***  
Reinhard, Bjoern M.; Lagutschenkov, Anita; Lemaire, Joel; Maitre, Philippe; Boissel, Pierre; Niedner-Schatteburg, Gereon  
Journal of Physical Chemistry A (2004), 108(16), 3350.  
<http://dx.doi.org/10.1021/jp037337i>
- 2004 ***Ab initio study of  $[Mg, nH_2O]^-$  reactive decay products: structure and stability of magnesium oxide and magnesium hydroxide water cluster anions  $[MgO, (n - 1)H_2O]^-$ ,  $[HMgOH, (n - 1)H_2O]^-$  and  $[Mg(OH)_2, (n - 2)H_2O]^-$ .***  
Reinhard, Bjoern M.; Lagutschenkov, Anita; Niedner-Schatteburg, Gereon  
Physical Chemistry Chemical Physics (2004), 6(17), 4268.  
<http://dx.doi.org/10.1039/b405747c>
- 2005 ***Structural, spectral and excited state features of water hydrogen bonding networks: Results of ab-initio calculations and interaction potentials.***  
Xantheas, Sotiris S.; Fanourgakis, George S.; Kowalski, Karol; Lagutschenkov, Anita; Niedner-Schatteburg, Gereon  
Abstracts of Papers, 229th ACS National Meeting, San Diego, CA, United States, March 13-17, 2005 (2005), PHYS-026.  
ISSN: 0065-7727
- 2005 ***The spectroscopic signature of the "all-surface" to "internally solvated" structural transition in water clusters in the  $n=17-21$  size regime.***  
Lagutschenkov, Anita; Fanourgakis, George S.; Niedner-Schatteburg, Gereon; Xantheas, Sotiris S.  
Journal of Chemical Physics (2005), 122(19), 194310.  
<http://dx.doi.org/10.1063/1.1899583>
- 2007 ***The Infrared Spectrum of  $NH_4^+(H_2O)$ : Evidence for Mode Specific Fragmentation.***  
Pankewitz, Tobias; Lagutschenkov, Anita; Niedner-Schatteburg, Gereon; Xantheas, Sotiris S.; Lee, Yuan T.  
Journal of Chemical Physics (2007), 126(7), 074307.  
<http://dx.doi.org/10.1063/1.2435352>

- 2008 *Energetics and reaction pathways of intramolecular reductive nitrile coupling of monocationic group 3 through 7 transition metal acetonitrile complexes.*

Lagutschenkov, Anita; Niedner-Schatteburg, Gereon

In preparation

- 2008 *Hula hoop like backbone twisting driven proton transfer and isomerization in protonated and deprotonated adipic acid ions and their O-H-O infrared spectra*

Min, Seung; Park, Mina; Nongmaithem, Jiten; Kim, Kwang; Jaberg, Stephanie; Pfeffer, Britta; Lagutschenkov, Anita; Niedner-Schatteburg, G.; Lemaire, Joel; Maitre, Philippe

In preparation

## Danke

Herrn Prof. Dr. Gereon Niedner-Schatteburg möchte ich für die Betreuung, die gute Zusammenarbeit und den mir eingeräumten Freiraum während meiner Arbeit danken. Nicht zu vergessen, für die Möglichkeit ein paar Monate in den USA zu arbeiten. Dankeschön.

Herrn Prof. Dr. Markus Gerhards danke ich für die Übernahme des Zweitgutachtens und Herrn Prof. Dr.-Ing. Stefan Ernst für die Übernahme des Kommissionsvorsitzes.

Dr. Sotiris S. Xantheas und seiner Familie danke ich ganz herzlich für die Möglichkeit am PNNL zu arbeiten und für alles, was sie außerhalb der Arbeit möglich gemacht haben.

Dr. Christoph Riehn, Prof. Dr. Christoph van Wüllen und Prof. Hans-Jörg Krüger danke ich für hilfreiche wissenschaftliche Diskussionen.

Björn, Stefan und Christophe möchte ich für Hilfe beim Start in der PC danken.

Britta und Steffi für's gemeinsame Leiden, Durchhalten und manchmal auch Jubeln.

Lars und Bernd für alles Mögliche, Unmögliches und noch mehr.

Heinrich für die tollen Bilder, tolle Partys und die schöne Alpenwanderung.

Tobias und Anna für die tolle Zusammenarbeit.

Christine, Fabian, Uli, Michael, Nicole, Stefan, Graziano, Sawa, Alex, Daubi, Tanja, Dr. Hartmut Schulze und Gabriel für all die gute Zusammenarbeit und viele schöne und lustige Erinnerungen.

Außerdem auch ein dickes Dankeschön an alle ehemaligen (Teil-)Praktikanten: Petra, Matthias, Lars, Paul, Christine, Sandra, Thomas und Driss.

Ganz besonderer Dank gilt auch der IT-Abteilung Elmar, Thomas und Markus, die immer hilfsbereit waren, wenn's bei mir mal wieder nicht ging.

Frau Krull, Frau Heieck und Frau Bressemer danke ich für die permanente Hilfe und Unterstützung im Papierkrieg.

Den Mitarbeitern am CLIO, insbesondere Philippe, Joel und Luke, danke ich für die unermüdliche Unterstützung während der Messungen.

Den Mitarbeitern am PNNL, besonders George, danke ich für die Hilfe und Gastfreundschaft während meines Aufenthaltes dort.

Collin, Mark, David, Matthias und Maciek danke ich für ihre Freundschaft. Danke, dass Ihr für mich da seid.

Zuletzt möchte ich meiner Familie danken.

Danke, dass Ihr immer für mich da seid und an mich glaubt.



**Curriculum Vitae**

Name	Anita Lagutschenkov
Date of birth	24. October 1977
Place of birth	Leutkirch im Allgäu

**Education**

1984 - 1988	Grundschule Wolfegg
1988 - 1990	Salvatorkolleg Bad Wurzach
1990 - 1997	Karolinengymnasium Frankenthal Abitur, June 1997
1997 - 2003	Universität Kaiserslautern Degree: Diplom Chemie, May 2003
2003 - 2008	PhD studies as member of the group of Prof. Dr. G. Niedner-Schatteburg, Physical Chemistry, Technische Universität Kaiserslautern



### **Eidesstattliche Erklärung**

Hiermit bestätige ich, Dipl.-Chem. Anita Lagutschenkov, dass die vorliegende Arbeit gemäß der Promotionsordnung des Fachbereichs Chemie der Technischen Universität Kaiserslautern selbständig und mit den angegebenen Hilfsmitteln und Quellen angefertigt wurde.

Kaiserslautern, im August 2008.

